MALDI Technology Development to Enable High Spatial Resolution Imaging Mass
Spectrometry and to Improve Lipidomic and Proteomic Coverage

By

Josiah C. McMillen

Dissertation

Submitted to the Faculty of the

Graduate School of Vanderbilt University

in partial fulfillment of the requirements

for the degree of

DOCTOR OF PHILOSOPHY

in

Chemistry

May 13th, 2022

Nashville, Tennessee

Approved:

Richard M. Caprioli, Ph.D.

John A. McLean, Ph.D.

Kevin L. Schey, Ph.D.

Renã A. S. Robinson, Ph.D.

To my mother, Carol Anne

ACKNOWLEDGEMENTS

TABLE OF CONTENTS

LIST OF TABLES

LIST OF FIGURES

ABBREVIATIONS

ACN: Acetonitrile

AGE: Advanced glycation end product

cDHA: (*E*)-4-(2,5-dihydroxyphenyl)but-3-en-2-one

CE: Cholesterol ester

Cer: Ceramide

CID: Collision induced dissociation

CHCA: α-cyano-4-hydroxycinnamic acid

DAN: 1',5'-diaminonaphthalene

DG: Diacylglycerol

DHA: 2',5'-dihydroxyacetophenone

ESI: Electrospray ionization

FT-ICR: Fourier transform ion cyclotron resonance

GRAVY: Grand average of hydropathy

H&E: Hematoxylin and eosin

HexCer: Hexosylceramide

IAPP: Islet amyloid polypeptide

IMS: Imaging mass spectrometry

ITO: Indium tin oxide

LC: Liquid chromatography

LPC: Lysophosphatidylcholine

LPE: Lysophosphatidylethanolamine

m/z: mass-to-charge ratio

MALDI: Matrix-assisted laser desorption/ionization

MALDI-1: MALDI

MALDI-2: MALDI with laser post-ionization

MG: Monoacylglycerol

MS: Mass spectrometry

MS/MS: Tandem mass spectrometry

MW: Molecular weight

NOR: Norharmane

PC: Phosphatidylcholine

PE: Phosphatidylethanolamine

PI: Phosphatidylinositol

PG: Phosphatidylglycerol

PMF: Peptide mass fingerprint

ppm: parts per million

PS: Phosphatidylserine

PTM: Post translational modification

SEM: Standard error of the mean

S/N: Signal-to-noise ratio

SM: Sphingomyelin

TG: Transmission geometry *or* triacylglycerol

TMA: Tissue microarray

TOF: Time of flight

CHAPTER I

INTRODUCTION

This chapter was in part adapted from *Matrix-Assisted Laser Desorption/Ionization Imaging Mass Spectrometry: Technology and Applications published in Toxic Chemical and Biological Agents. NATO Science for Peace and Security Series A: Chemistry and Biology* and has been reproduced with the permission of the publisher and my co-authors William J. Perry, Kavya Sharman, Katerina V. Djambazova, and Richard M. Caprioli.

> McMillen J.C., Perry W.J., Sharman K., Djambazova K.V., Caprioli R.M. (2020) Matrix-Assisted Laser Desorption/Ionization Imaging Mass Spectrometry: Technology and Applications. In: Sindona G., Banoub J.H., Di Gioia M.L. (eds) Toxic Chemical and Biological Agents. NATO Science for Peace and Security Series A: Chemistry and Biology. Springer, Dordrecht. https://doi.org/10.1007/978-94-024-2041-8_7

OVERVIEW

Biological imaging is commonly used for the characterization of healthy and diseased tissues, but each modality has trade-offs in the areas of spatial resolution, molecular coverage, and specificity. Stained tissue microscopy provides a high spatial resolution view of tissue morphologies and cellular structure but little molecular information. Although it requires *a priori* information, immunohistochemistry provides additional specificity using antibodies to mark antigens of predefined cell types. Matrix-assisted laser desorption/ionization (MALDI) imaging mass spectrometry (IMS) allows for the untargeted detection of hundreds to thousands of molecular species within a single experiment.[1,2] IMS enables the detection of a wide range of biological species at increased molecular coverage with high spatial resolution and sensitivity.

Historical background

Scientific imaging technologies have been advancing rapidly since Robert Hooke's discovery and drawing of cells from a thin section of the cork plant in 1665.[3] Stains for tissue sections were developed and allowed for visualization of sub-cellular compartments such as the nucleus as described by Joseph von Gerlach in 1858 using a dilute solution of carmine, followed by the development of a combination of hematoxylin and eosin (H&E) stains to visualize the cytoplasm and nucleus, respectively (1896).[4] These chemical stains allowed for finer optical characterization of tissue, but little chemical information could be obtained. Separately, one year

after H&E staining was developed, J. J. Thomson first described the separation of ions based on their mass and charge using a cathode ray tube (1897), thereby setting the groundwork for modern mass spectrometry (MS).[5] Since these first MS experiments, many discoveries have been made to enable modern biological mass spectrometry, most notably the development of electrospray ionization (ESI)[6,7] and matrix-assisted laser desorption/ionization (MALDI).[8–10]

Mass spectrometric instrumentation continued to improve and in 1997, Richard Caprioli et al. analyzed thin tissue sections using a mass spectrometer to obtain chemical information in the form of ion images.[1] The spatial resolution, or pixel size, of these first ion images from tissue using MALDI was approximately 25 μm. Since then, attempts have been made to achieve higher spatial resolution images with higher sensitivity using MALDI imaging mass spectrometry (IMS) to better characterize the molecular composition of tissues and organs, in a spatially resolved manner, to understand human disease.

Matrix-assisted laser desorption/ionization

The MALDI process relies on the presence of a matrix with an analyte prior to irradiation with a laser to generate ions in the gas phase (**Figure 1.1**).[11,12] An ideal matrix functions to dilute the sample and prevent aggregation, absorb energy from laser irradiation, and impart the energy to the analyte to efficiently ionize with minimal fragmentation.[12] The function of the matrix absorbing laser irradiation serves multiple purposes. First, the analytes and sample surface are spared from excessive energy that would cause analyte heating and fragmentation. It is important that the analyte does not fragment upon ionization so that the identity of the ion can be determined. Secondly, the matrix absorbs the laser irradiation and desorbs from the sample surface, forming the MALDI plume of ions and neutral molecules thereby converting the sample into the gas phase.[12] Thirdly, the matrix molecules excited by the energy from the laser is thought to help with ionization of analyte molecules by charge transfer.[11]
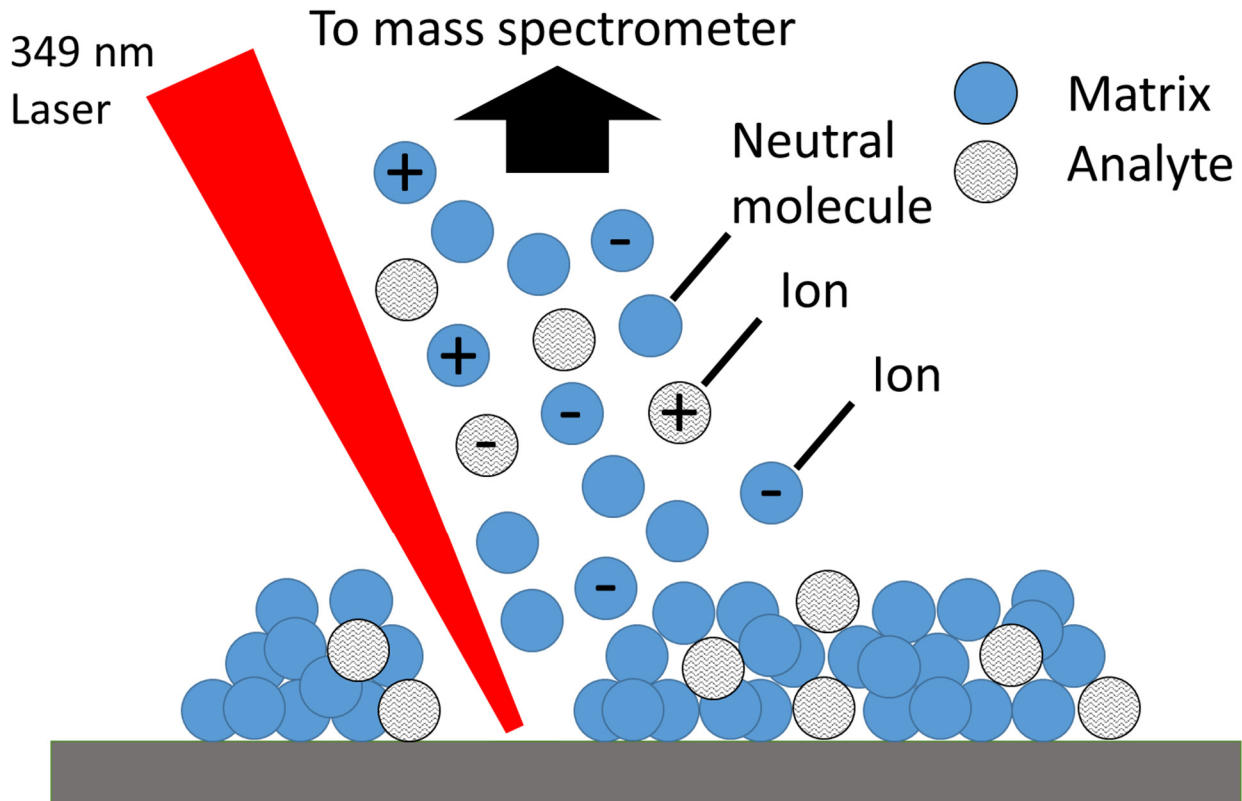
Figure 1.1. Schematic of MALDI process. Matrix is applied to a sample for co-crystallization with analytes. Upon irradiation with an ultraviolet laser, the mixture is ablated, and analytes enter the gas phase. Ions (positively and negatively charged) are generated in this process and are directed to the mass spectrometer for detection.

MS analyzers used for imaging applications

   Once ions are generated, they can be directed to a mass spectrometer for analysis, where different mass analyzers have their own strengths and drawbacks. Time-of-flight (TOF) mass analyzers separate ions based on flight times in a high-vacuum flight tube and are commonly used for IMS (**Figure 1.2**).[13] The kinetic energy equation is shown in **Equation 1** where KE is the kinetic energy, m is mass, and v is velocity (also equal to distance/time), z is the number of charges of the ion, and e is the electron charge. **Equation 1** is rearranged to form **Equation 2** (for MALDI ions that are typically all singly charged) to show that ions that travel a set distance in the flight tube and that have similar kinetic energy (KE) will differentiate based on their mass where smaller ions reach the detector faster than larger ions. Therefore, ions with different masses are separated as a consequence of their distribution of velocities.

Equation 1:
$$KE = \frac{1}{2}mv^2 = zeV_s$$

Equation 2:
$$t = \frac{d}{\sqrt{\frac{2*zeV_S}{m}}}$$

The resolving power of a mass analyzer is defined in **Equation 3** where m is the mass of the ion and Δm is the width of the peak measured at 50% peak height. Most TOF instrument have moderate resolving powers but benefit because of their high throughput of analysis at up to about 100 pixels per second.[14] Higher resolving power analyzers allow for separation of molecules that have very similar *m/z* values and is especially useful for complex mixtures such as those from tissue.

Equation 3:
$$R = \frac{m}{\Delta m}$$
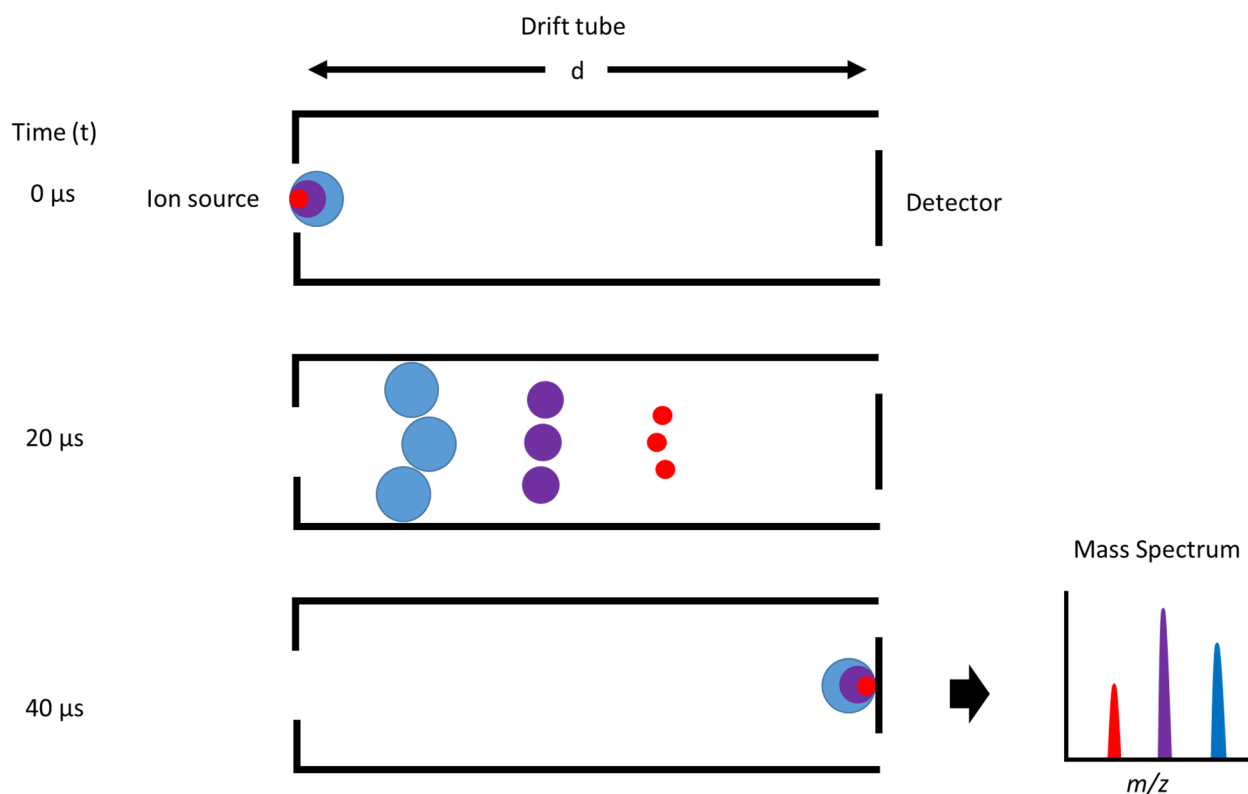
Figure 1.2. Schematic of ions travelling through the field free drift tube of a time of flight (TOF) mass analyzer. Ions are imparted with a large amount of kinetic energy in the ion source, travel through the drift tube, and separate in time based on their mass (if all singly charged). Ions of different mass (and therefore different velocities) reach the detector at different times and the resulting mass spectrum is generated.

Another type of mass spectrometer detects ions based on the resonance frequency of ions in the presence of a magnetic or electric field to generate an image current of the ion motion. The image current measured in the time domain can then be translated to the frequency domain using a Fourier transform and a mass spectrum is generated after calibration of known ions to their corresponding frequency (**Figure 1.3**). Examples include the Fourier Transform ion cyclotron resonance instruments (FT-ICRs) and Orbitraps. These instruments have variable mass resolution that is based on an adjustable transient length and the ability of the ions to maintain their trajectory inside the cell. Increased transient length allows for mass resolution of many hundreds of thousands at *m/z* 400 for both FT-ICRs and Orbitraps. In an FT-ICR, packets of ions cycle within a uniform magnetic field and initially have random orbital phases. Upon excitation, the orbital radius of the ion packet increases to achieve coherence and the resonance frequency can therefore be detected as an image current.[15] In an Orbitrap analyzer, ions are injected and oscillate along a central spindle-shaped electrode to produce an image current. This image current is transformed into the frequency domain and converted to *m/z*, like with the FT-ICR. The frequency of the ions is independent of the kinetic energy and is related to the ratio of *m/q* where q is the total charge of the ion ($q = ze$ where e is the electron charge and z is the number of charges of an ion).[16,17] One benefit of the high-vacuum environment for FT instruments is that chemical noise can be significantly reduced. Here, ions traverse a very long mean free path (many kilometers) in a coherent motion for detection whereas background or metastable ions that do not have coherent motion will be counted as part of the background.[16] The acquisition times for FT instruments are typically longer than for TOFs, but FTs allow for sensitive detection of ions with a wide dynamic range and high mass resolution for elucidation of the composition of complex chemical mixtures.
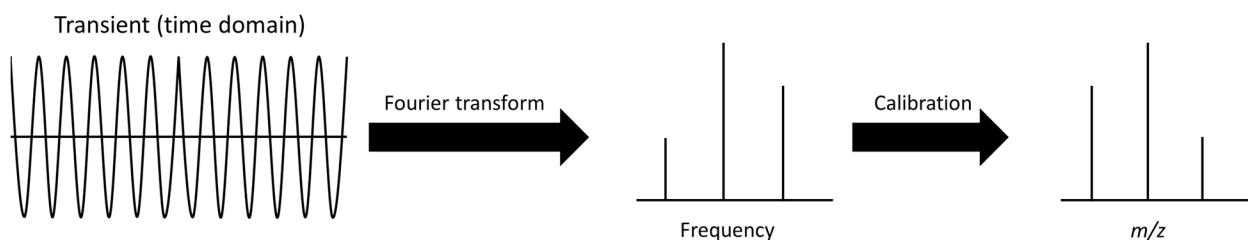
Figure 1.3. Simulated processing of data obtained from FT analyzers. The image current in the time domain is transformed to the frequency domain using a Fourier transformation and subsequently calibrated to obtain the corresponding mass spectrum.[18]

MALDI imaging mass spectrometry

To perform a MALDI IMS experiment from tissue, the tissue is sectioned thinly (~10 µm) and mounted onto a glass slide with a conductive coating (**Figure 1.4**). The small molecule matrix is applied homogeneously to the surface typically using sublimation or a robotic sprayer. The matrix-coated sample is loaded into the mass spectrometer and a focused laser is used to irradiate the MALDI matrix layer to produce ions. The sample is moved in a grid pattern, the laser irradiates the sample at each new position, and a mass spectrum is generated for each position. After acquisition, peaks that correspond to biomolecules are integrated, and the peak intensities of each location are displayed to produce heat maps based on ion intensity variation at different positions within the tissue, thereby generating ion images.
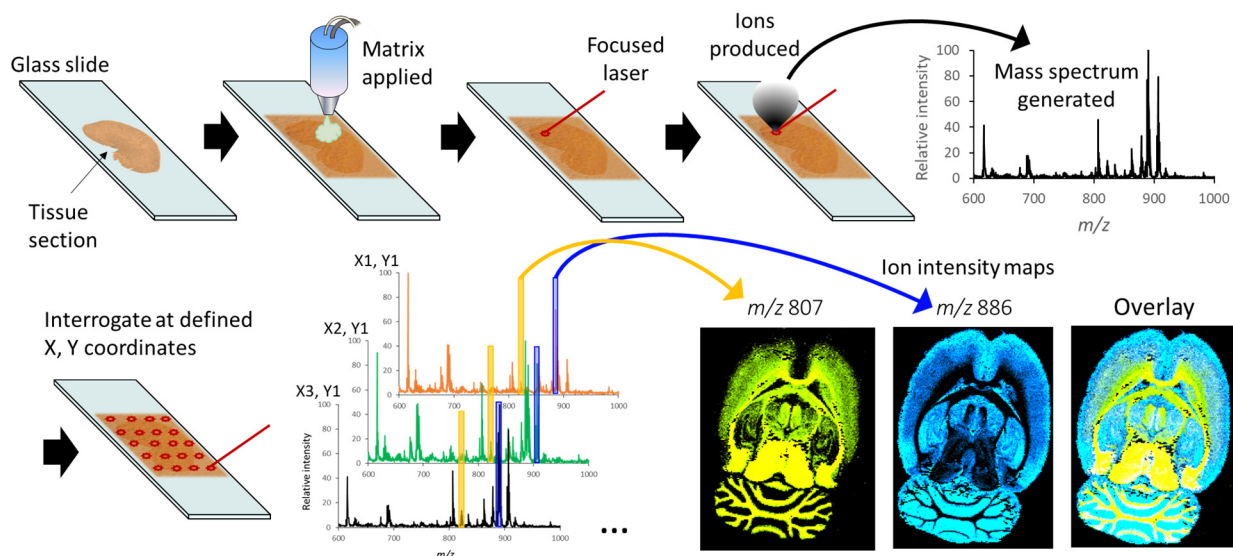
Figure 1.4. MALDI IMS workflow. Tissue is sectioned thinly and thaw-mounted onto a conductive glass slide. Matrix is applied homogeneously to the surface. The sample is irradiated to produce ions and a mass spectrum is generated at each position throughout the tissue. After acquisition, ions are selected in imaging software to generate ion images based on intensity at different positions within the tissue.

High spatial resolution MALDI IMS instrumental considerations

Spatial resolution is an important consideration of a MALDI IMS experiment as it determines the level of structural detail visible in the resulting ion images. Many instrumental parameters determine spatial resolution in a MALDI IMS experiment including the step size of the sample stage, or pitch, and the area of the laser spot on target (**Figure 1.5 A, B**). Both the laser ablation diameter and pitch need to be reduced to achieve higher spatial resolution, but most

commercial IMS instruments are limited to approximately 20 μm laser ablation diameter, as determined by the laser focusing optics.

A tightly focused laser beam for high spatial resolution IMS is achieved using objective lenses placed above a sample surface (**Figure 1.6**, front-side geometry). However, high power objectives can interfere with ion transmission to the mass analyzer. An ablation diameter below 5 μm is possible with special modifications of the laser optics.[19,20] One reported approach uses a drilled hole in the center of the final focusing lens that is positioned between the mass analyzer and the sample.[21] The lens is then brought close above the sample while allowing ion transmission through the lens hole. Another approach to achieve a small ablation diameter is to place a high numerical aperture objective behind the sample, and this optical arrangement is termed transmission geometry (**Figure 1.6**, transmission geometry). A sample placed on an optically transparent substrate results in the generation of ions unimpeded by laser optics so a much smaller ablation diameter can be achieved versus front-side geometry .[22,23]

Spatial resolution considerations for MALDI IMS instrumentation

A)

Laser spot size   Pitch

B)

50 μm   20 μm

Ion image   Mass spectrum   Ion image   Mass spectrum

- 50 μm pixel size
- Low spatial resolution
- Good signal

- 20 μm pixel size
- Higher spatial resolution
- Lower signal
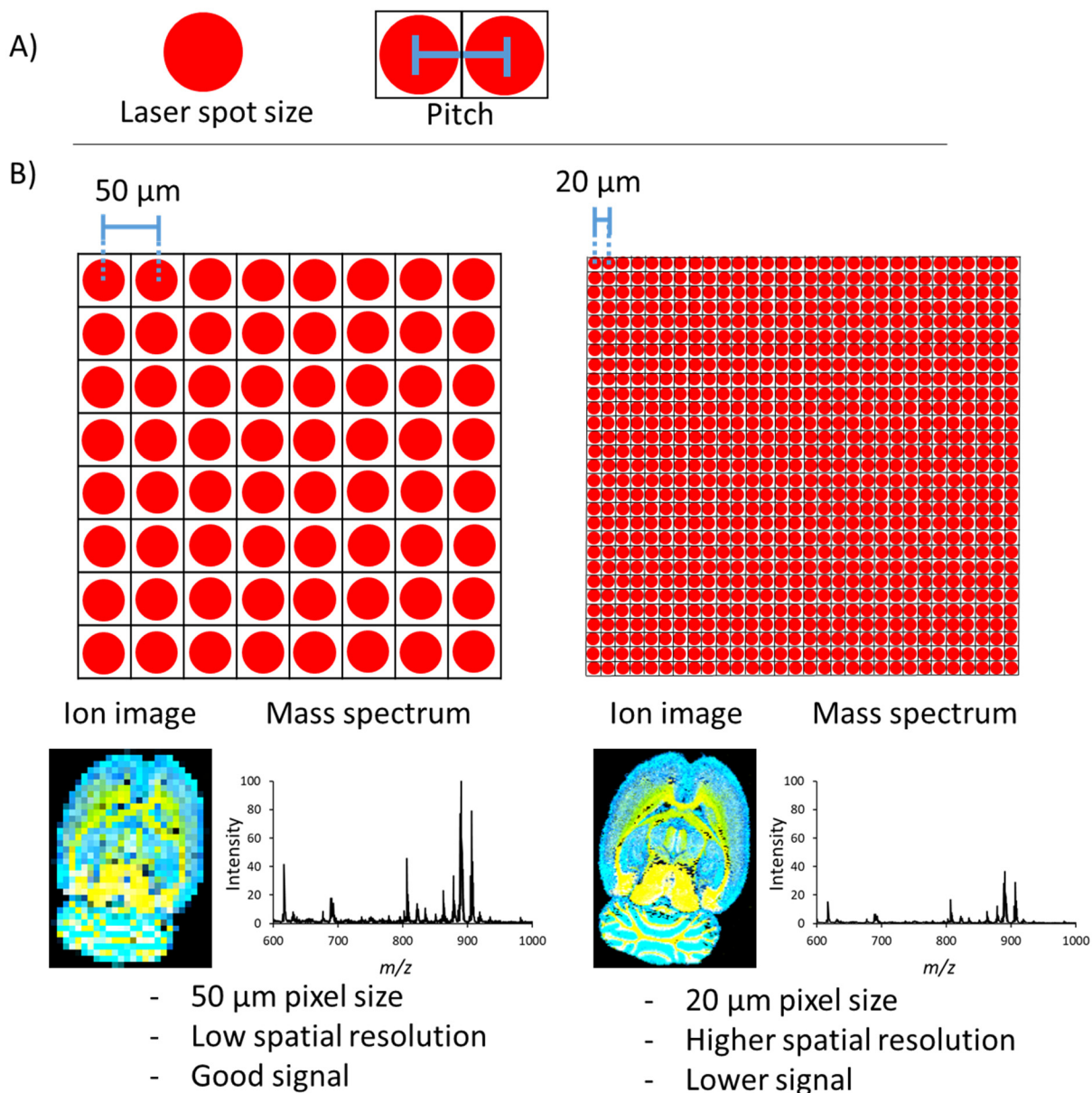
Figure 1.5. Spatial resolution considerations for MALDI IMS instrumentation include laser spot size and the distance between pixels, or pitch (**A**). Simulated examples of different spatial resolution MALDI IMS of a rat brain sample are shown in (**B**) where large laser spot size and pitch (200 μm) results in a low spatial resolution image where no distinct regions in the brain can be visualized. Higher spatial resolution IMS with 50 μm size pixels allows for visualization of different regions of the brain including differentiation between white and grey matter regions of the cerebellum. At higher spatial resolution the sampling area is smaller so there is less signal overall as shown in the representative averaged mass spectra.
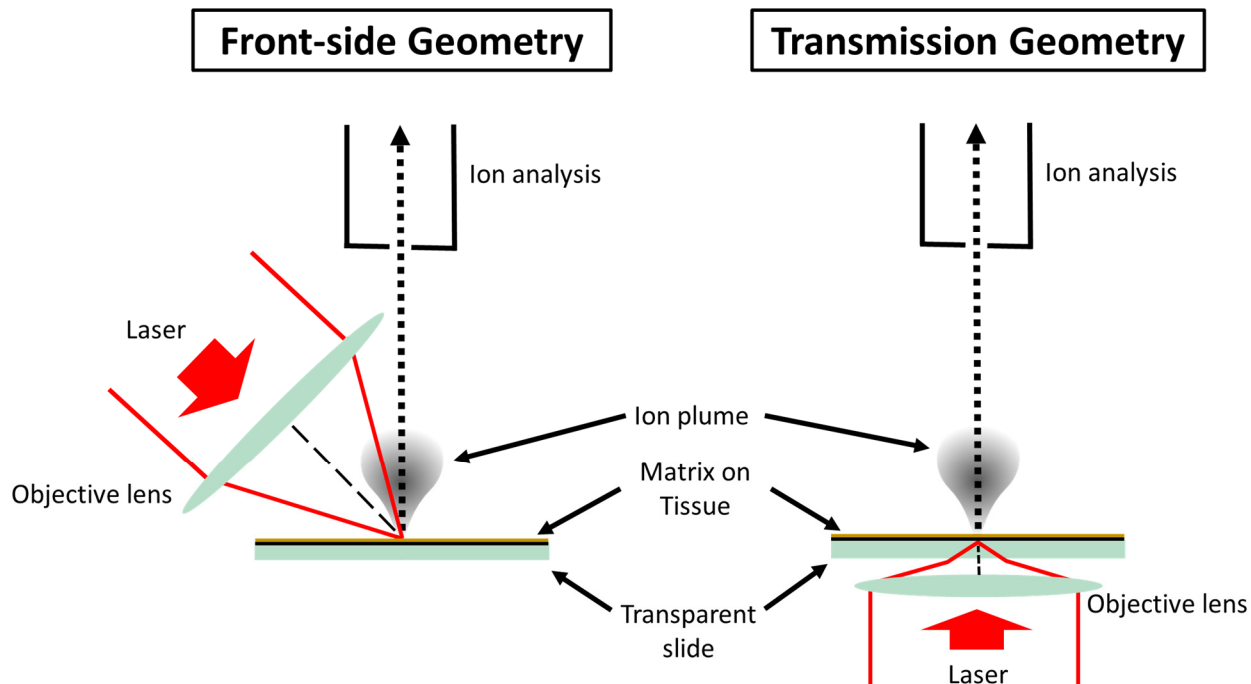
Figure 1.6. MALDI ion sources available on commercial instruments (front-side geometry) typically allow for a laser ablation diameter down to 20 μm. A smaller ablation diameter can be achieved with objective lenses closer to the sample. The transmission geometry optical path allows for use of high numerical aperture lenses (e.g., 0.95 N.A.) close to the sample such that the laser can travel through a transparent substrate and can be focused on the sample to achieve an ablation diameter of approximately 1 μm. Reprinted by permission from Springer Nature, Matrix-Assisted Laser Desorption/Ionization Imaging Mass Spectrometry: Technology and Applications, McMillen, J.C. *et al.* © 2020.

Increasing ion intensity for high spatial resolution IMS

While high spatial resolution increases the detail within an ion image, ion intensities are decreased due to the smaller amount of material sampled. One approach to increase ion intensity for high spatial resolution IMS is to use post-ionization to irradiate the MALDI plume and produce more ions. In the laser irradiated plume, the ratio of neutral molecules to ions is high.[24] Common post-ionization strategies include irradiation with either plasma, an ESI beam as with MALDESI, or with a secondary, 266 nm UV laser.[25–27] Using a secondary UV laser for post-ionization is termed MALDI-2.[28–30] Here, post-ionization is delayed temporally after the initial MALDI event (also called MALDI-1) to irradiate the MALDI plume that is generated above the sample (**Figure 1.7**). MALDI-2 has been shown to provide a 100-fold increase in intensities for some classes of biomolecules including lipids, metabolites, and peptides[29,31,32]. The intensity increase provided by

MALDI-2 allows for higher spatial resolution experiments while maintaining a comparable signal-to-noise ratio to MALDI-1 performed at a lower spatial resolution.[31,33]
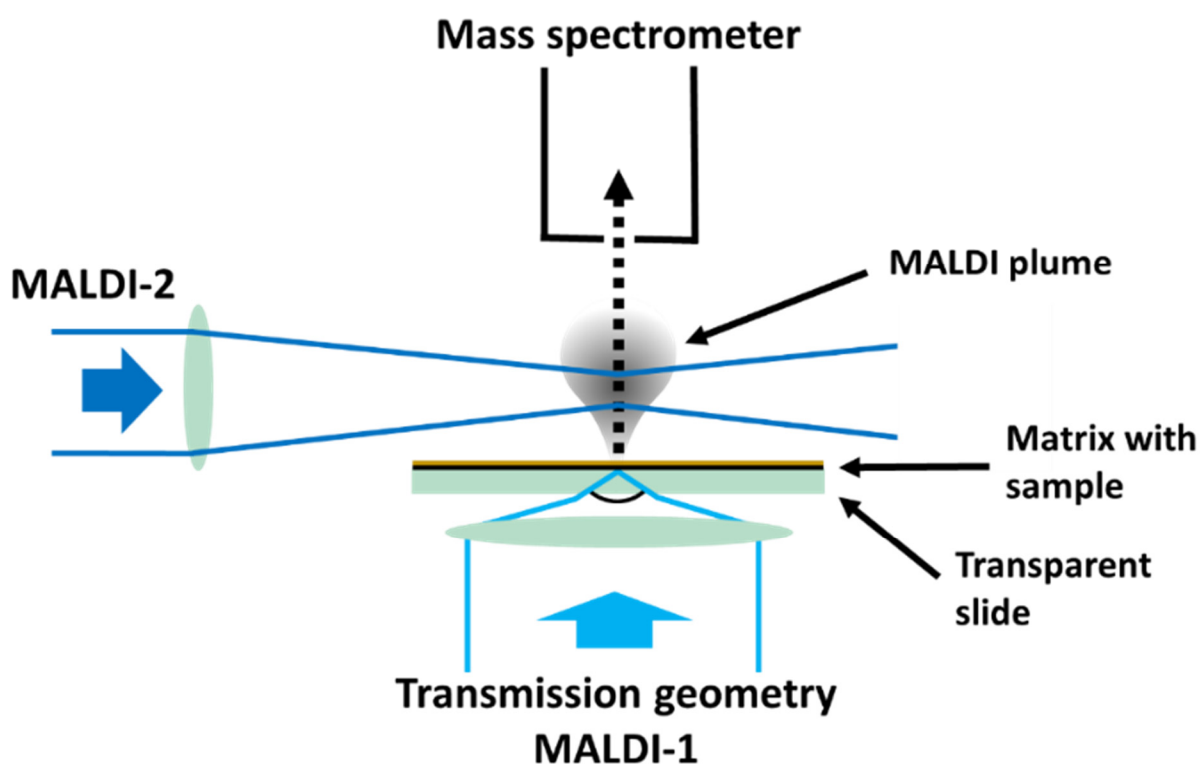
Figure 1.7. MALDI-2 post-ionization shown with a transmission geometry optical setup for the primary MALDI event. The MALDI-2 laser beam is focused orthogonally to the sample surface above the sample. The lasers are synchronized such that MALDI-2 irradiates immediately following the MALDI plume formation. Reprinted by permission from Springer Nature, Matrix-Assisted Laser Desorption/Ionization Imaging Mass Spectrometry: Technology and Applications, McMillen, J.C. *et al.* © 2020.

Sample preparation for IMS

IMS is highly dependent on the quality of sample preparation.[34] An example workflow consists of tissue sectioning, an optional washing procedure, matrix application, and an optional recrystallization procedure is shown in **Figure 1.8**. The primary goal of any sample preparation is to achieve crisp, accurate images with minimal analyte delocalization and degradation while maximizing sensitivity.[35] Sample preparation protocols are typically developed for specific tissue types, analytes of interest, and desired spatial resolution, although common methods and protocols can be established.[36–40]
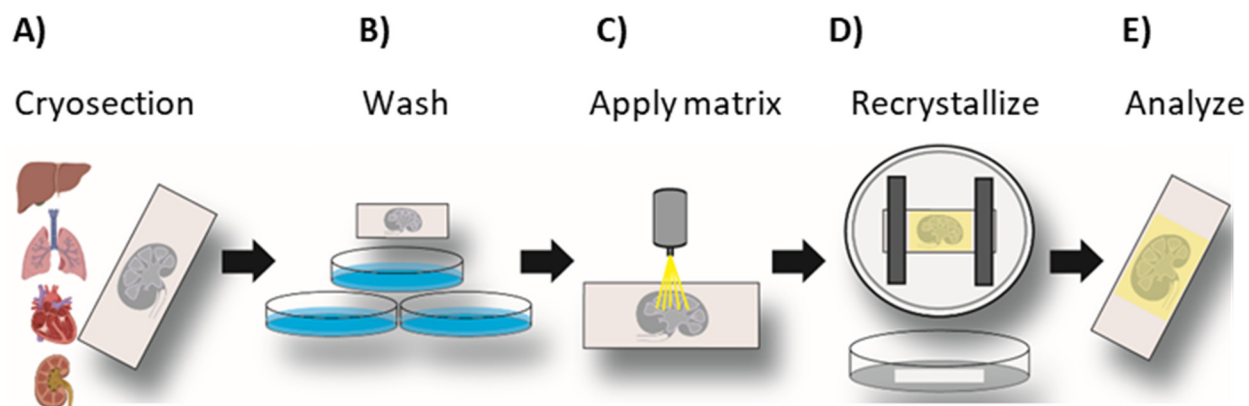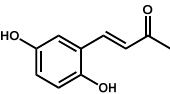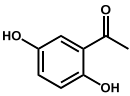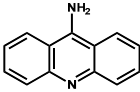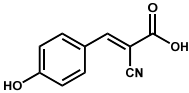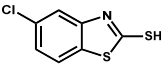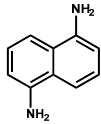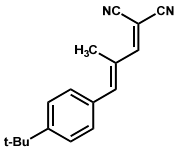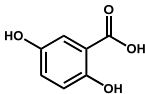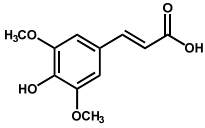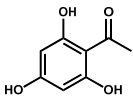
Figure 1.8. MALDI IMS sample preparation workflow. A) Biological tissues are thinly sectioned, and thaw mounted onto conductive microscope slides. **B)** Sections may undergo optional washing protocols to select for analytes of interest or lessen chemical interferences. **C)** MALDI matrix is homogenously applied to a sample using a robotic aerosol sprayer. **D)** An optional recrystallization procedure can be applied to samples when needed to ensure analyte-matrix layer co-crystallization. **E)** Prepared samples are ready when needed for IMS analysis. Reprinted by permission from Springer Nature, Matrix-Assisted Laser Desorption/Ionization Imaging Mass Spectrometry: Technology and Applications, McMillen, J.C. *et al.* © 2020.

For fresh frozen samples, tissue is cryosectioned prior to thaw mounting onto the slide. Tissue washing protocols can remove potential chemical interferences and select for specific analytes (**Figure 1.8 B**).[35,41–43] Ammonium formate buffer is used to remove salts from tissue for the analysis of lipids.[41] In the positive ion mode, protonated ions dominate the spectra after ammonium formate tissue washing. Decreased salt presence also increases sensitivity in the negative ion mode. Sensitivity for intact proteins can be increased by removing both lipids and salts from tissue using Carnoy's solution (ethanol, chloroform, and acetic acid), water, and ethanol.[35] Washes may delocalize some analytes so care and validation are required.

MALDI matrix selection and application

MALDI matrices are chosen based on their ability to provide sufficient ionization efficiency for a given analyte class (*e.g.,* low molecular weight metabolites, lipids, proteins, polymers, or organometallics). A MALDI matrix is typically a small organic molecule consisting of a UV absorbing chemical moiety. Differences in observed analyte sensitivities can be attributed to the physical properties of a matrix such as molecular structure, pH, proton affinity, and peak wavelength absorbance.[23,44–51] However, studies have successfully employed various inorganic materials such as nanoparticles or thin layers of metals.[52] 2,5-dihydroxybenzoic acid (DHB) is widely employed as a MALDI matrix, offering sufficient sensitives for many analyte classes in

positive ion mode MS analysis.[50,53–56] 9-Aminoacridine (9AA) is often used for the analysis of metabolites in negative ion mode and 1,5-diaminonaphthalene (DAN) for lipids with high sensitivity in both polarities.[45,51] However, the energy transferred during the ablation process can result in analyte modification or fragmentation, complicating data interpretation.[53,57] Vapor pressure is also a consideration when selecting a MALDI matrix because the matrix layer must remain on the tissue surface under high vacuum conditions for lengthy acquisition times (hours). 2,5-Dihydroxyacetophenone (2,5-DHA) is an excellent matrix for MS analysis of multiple analyte classes; however, its high volatility limits acquisition times.[23] (E)-4-(2,5-dihydroxyphenyl)but-3-en-2-one (2,5-cDHA) is a vacuum stable matrix providing high sensitivity for lipids, peptides, and intact proteins.[44] **Table 1.1** lists many commonly used matrices.

Table 1.1. MALDI matrices and analyte applications

Matrix	Other Names	Chemcial Structure	Application
(E)-4-(2,5-dihydroxyphenyl)but-3-en-2-one	2,5-cDHA		Lipids Peptides Proteins Positive and Negative Ionization Modes
2,5-dihydroxyacetophenone	2,5-DHA		Lipids Peptides Proteins Positive and Negative Ionization Modes
9-Aminoacridine	9-AA		Low Molecular Weight Metabolites Lipids Negative Ionization Mode
α-Cyano-4-hydroxycinnamic acid	CHCA		Peptides Proteins Positive Ionization Mode
5-Chloro-2-mercaptobenzothiazole	CMBT		Lipids Peptides Positive and Negative Ionization Modes
1-5,Diaminonapthalene	DAN		Lipids Positive and Negative Ionization Modes
trans-2-[3-(4-tert-Butylphenyl)-2-methyl-2-propenylidene]malononitrile	DCTB		Carbohydrates Polymers Inorganic Materials Organometallics Positive and Negative Ionization Modes
2,5-Dihydroxybenzoic acid	DHB		Low Molecular Weight Metabolites Pharmacuticals Lipids Positive Ionization Mode
3,5-Dimethoxy-4-hydroxycinnamic acid	Sinapic Acid		Peptides Proteins Positive Ionization Mode
2',4',6'-Trihydroxyacetophenone	THAP		Carbohydrates Nucleic Acids Lipids Peptides Positive and Negative Ionization Modes

The protocol for application of a MALDI matrix to a tissue sample can dictate matrix layer homogeneity, matrix crystal size, analyte extraction, and analyte delocalization (**Figure 1.8 C**). MALDI matrices are commonly applied by either aerosol spray or sublimation. Aerosol application can be accomplished using a hand airbrush sprayer or more homogenously and reproducibly using a robotic pneumatic sprayer. Spray parameters including temperature, gas flow, and solvent composition can influence analyte extraction and unwanted delocalization. Ideally, matrix application is 'wet' enough to ensure analyte extraction without promoting analyte delocalization. Crystal size of the matrix can be assessed using optical or scanning electron microscopy methods as matrix crystal size is an important factor when performing high spatial resolution IMS due to the need for crystals to be much smaller than the incident laser diameter.[23] Matrix application by sublimation has been shown to produce small crystal sizes[58]. However, sublimation typically does not provide the level of analyte extraction achieved by aerosol spray. A recrystallization procedure was developed to achieve efficient extraction after matrix application by sublimation (**Figure 1.8 D**).[35] One potential issue with sublimation is the lack of reproducible deposition of the matrix over multiple replicates. As such, sublimation is generally not commonly used for comparing large sample cohorts where reproducibility is crucial.[23,35,41,59] Sample preparation and matrix selection are important considerations when developing a method for IMS analysis.

Biological example to illustrate developed technology: Diabetes and the pancreas

Diabetes is a disease that induces molecular changes that correspond to decreased function of many organs including the pancreas and subsequent dysregulation of blood sugar levels that further damage the body.[60–62] There are two classifications of diabetes where type 1 diabetes is an autoimmune disease and type 2 diabetes (T2D) is a metabolic disease (**Figure 1.9**). Management of diabetes is possible by frequent testing of blood sugar, dietary restriction, and sometimes injection of synthetic human insulin into the body. Modern developments such as insulin pumps allow for more technology-based approach to the management of diabetes.[63] Despite the study of diabetes occurring since ancient times[64], the molecular underpinnings and progression of T2D is poorly understood.[65] A comprehensive molecular understanding of diabetes progression and its effects on the pancreas may allow for prevention of the disease overall or lead to better approaches to treatment and management of the disease.
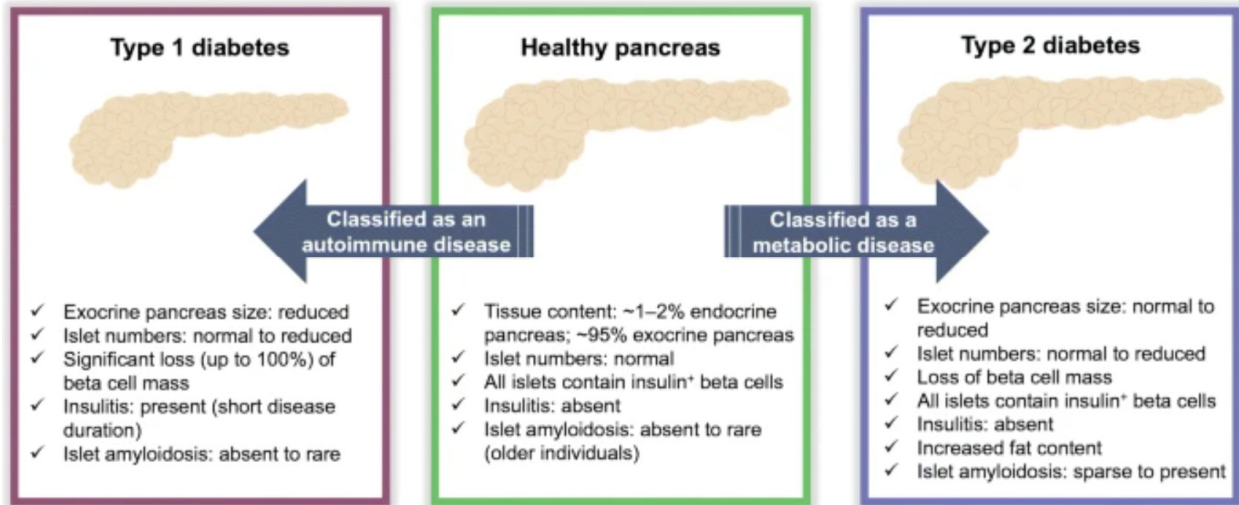
Figure 1.9. Differences among a healthy pancreas versus one from an individual with type 1 diabetes or T2D. T2D is classified as a metabolic disease where islet amyloidosis is often present. Reprinted by permission from Springer Nature Customer Service Centre GmbH: Springer, Diabetologia, Organisation of the human pancreas in health and in diabetes Atkinson, M.A., Campbell-Thompson, M., Kusmartseva, I. *et al.* © 2020.

The pancreas is a complex organ containing enzyme-producing tissue including endocrine tissue (islets) that is composed of many cell types that secrete enzymes including insulin, glucagon, and somatostatin that help regulate blood sugar (**Figure 1.10**).[60] Islets in the pancreas are numerous, (approximately one million)[66] yet these small structures (approximately 150 μm in diameter) are dispersed. Decreased islet functionality and β cell death leads to insulin resistance, hyperinsulinemia, reduced capacity to produce insulin, as well as formation of amyloid plaques in the islets.[67–70] Bulk tissue analysis techniques such as homogenization are often used to study the molecular profile of the pancreas, but spatial information is lost. Additionally, tissue homogenization may dilute islet-specific signals below the limit of detection of some assays. MALDI IMS allows for both untargeted analysis while maintaining spatial localization of islets within the tissue.[71]
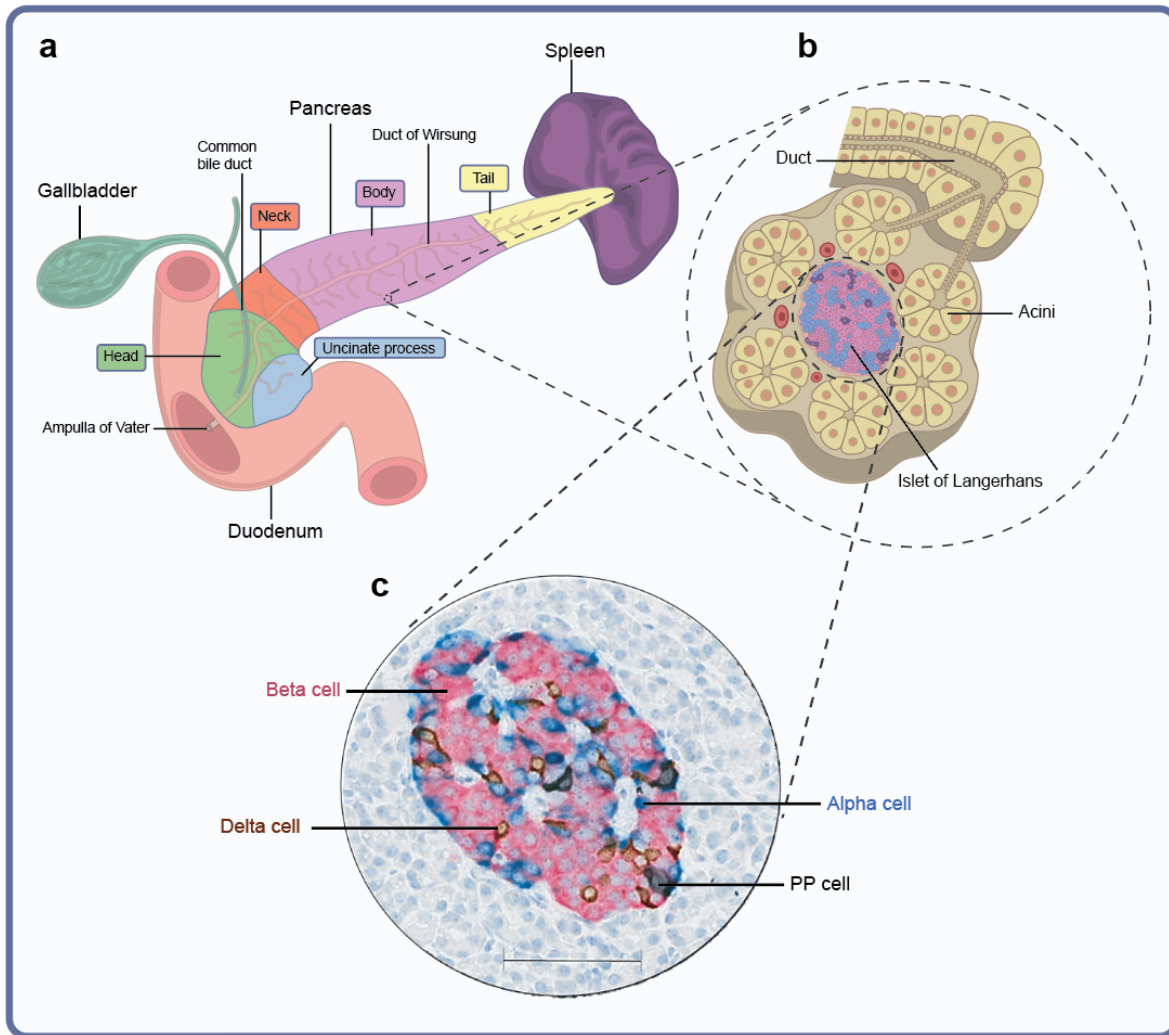
Figure 1.10. The human pancreas in relation to other organs in the body including the small intestines, gallbladder, and spleen (A) with insets showing exocrine tissue (Acini) as well as endocrine tissue (Islet of Langerhans) (B). Islets are composed of multiple cell types including α cells, β cells, δ cells, and PP (pancreatic polypeptide) cells (C). Reprinted by permission from Springer Nature Customer Service Centre GmbH: Springer, Diabetologia, Organisation of the human pancreas in health and in diabetes Atkinson, M.A., Campbell-Thompson, M., Kusmartseva, I. *et al.* © 2020.

Compared to a non-diabetic (ND) pancreas, in T2D there is a loss of β cell mass, increased fat content, and often, amyloid plaques form that can harm the insulin-producing β cells in islets.[60,72–74] The amyloid plaques are primarily composed of islet amyloid polypeptide (IAPP) aggregates. IAPP is a 37 amino acid peptide that is naturally co-secreted with insulin in a 1:100 ratio but the mechanism of formation and exact molecular composition of these amyloid plaques is unknown or poorly understood.[72,73,75,76] Recently, non-enzymatic modifications to IAPP have been shown to increase aggregation properties *in vitro*.[77–79] A more complete understanding of the

aggregation of islet amyloid polypeptide to form amyloid plaques could help in determining approaches to prevention or treatment of type 2 diabetes.

SUMMARY OF CHAPTERS

Spatial resolution and sensitivity for MALDI IMS were improved through instrument modification and implementation of new technology. First, modifications to a TOF instrument were made to allow for high precision stage motion down to a 20 nm step size using microstepping drivers. Additionally, ion source and laser optics modifications to allow for high spatial resolution transmission geometry sampling down to 1.5 µm ablation diameter. These modifications enabled routine IMS of tissue sections at 1-2 µm spatial resolution while maintaining a high rate of acquisition (80 pixels/second). The transmission geometry technology was implemented on an Orbitrap Elite platform to enable high mass resolution to elucidate the complex mixtures of tissue at high spatial resolution. A new transmission geometry source was fabricated and laser optics including a high numerical aperture objective (0.95 N.A.) was installed to achieve a 1 µm ablation diameter. Additionally, a secondary laser was implemented on the custom source to enable MALDI-2 post-ionization for increased sensitivity of lipids and metabolites. A 7-fold increase in overall lipid signal was detected for a spotted rat brain homogenate analyzed using the transmission geometry system with MALDI-2. MALDI-2 post-ionization is a relatively new technology for enhanced sensitivity for MALD IMS and there are differences in signal enhancement based on lipid class. Therefore, to characterize the performance of MALDI-2 for different lipid classes, four common MALDI matrices (DHA, DHB, CHCA, NOR) were evaluated. The highest number of lipids identified was found with DHB matrix and MALDI-2 for positive ion mode. Then, this sample preparation protocol was applied to study the lipid differences between ND and T2D pancreata. The utility of MALDI-2 for other biomolecular classes such as tryptic peptides had not been evaluated. Here, tryptic peptide signal from human kidney tissue was shown to significantly increase with MALDI-2. This resulted in a 3-fold increase of proteins identified compared to MALDI alone after matching to peptides generated by LC-MS/MS. Unlike for lipids and tryptic peptides, protein signal did not change with MALDI-2 irradiation. Intact protein analysis was performed using a 15T FT-ICR for spatial proteomic analysis of ND and T2D pancreata. Proteoforms of islet amyloid polypeptide elevated in the T2D donor were discovered that have not been previously characterized by spatial proteomic approaches. These modifications

and technology developments have allowed for significant improvement in lipidomic and proteomic coverage from MALDI IMS of tissue sections, ultimately allowing for significantly more comprehensive molecular, spatially resolved analysis of tissue.

CHAPTER II

IMPLEMENTATION OF MICROSTEPPING DRIVERS TO ENABLE HIGH THROUGHPUT, HIGH SPATIAL RESOLUTION TRANSMISSION GEOMETRY IMAGING MASS SPECTROMETRY

INTRODUCTION

Matrix assisted laser desorption ionization imaging mass spectrometry (MALDI IMS) enables the direct mapping of molecular distributions in tissue samples.[1] An important parameter of an IMS experiment is the spatial resolution, which determines the level of structural detail visible in the resulting image.[80–82] Spatial resolution is a consequence of the beam size of the focused laser on the sample and the step size between sampling areas, or pitch.[21,83]

Over the past 10 years, there has been increased interest in improving spatial resolution as most commercial MALDI instruments are limited to laser diameters of approximately 20 μm.[84,85] This limit is due to the long focal length needed with conventional laser optics systems to allow for an unobstructed ion beam. Focusing optics with shorter focal lengths allow for higher numerical aperture objectives that enable a more tightly focused laser beam and therefore smaller spot size, thereby enabling high spatial resolution MALDI IMS.[22,25] One method for improving this spatial resolution is by focusing the laser using a centrally bored objective in line with the ion beam. This allows for a short focal length while maintaining ion beam flow through the objective center to the mass analyzer and has allowed for an ablation diameter of 1.4 μm on tissue.[21,86] Precise machining of such an objective requires expertise, can add greatly to the expense of the source and may induce source-to-source variability among designs. Other approaches to minimizing the laser ablation diameter while not interfering with ion transmission include the implementation of a pinhole within the laser optical path for spatial filtration of the laser beam.[87] A third approach to minimize ablation diameter is to direct the laser to the rear of the sample through a transparent substrate, in a laser optical configuration termed transmission geometry (TG).[22,88–90] In TG the focusing objective is placed opposite the mass analyzer so that the laser passes through a conductive glass slide transparent to laser wavelength and ablates the sample. This configuration allows for a short focal length and implementation of a high numerical aperture objective to achieve tight laser focus thereby enabling high spatial resolution imaging.

High spatial resolution IMS experiments also require stage raster step sizes (i.e., the pitch) of distances equal to or smaller than the desired spatial resolution. For example, to obtain images with pixels on the order of one micron, distance between sampling areas must be one micron. As most instrument stages are limited by the motion drivers to send current pulses equating to approximately 5 μm pitch and are not designed for precise movement, modifications to decrease stage pitch are required.

We have modified a commercial MALDI TOF MS to perform high spatial resolution IMS using microstepping motor operation to improve stage precision in TG. We have also implemented a method for facile adjustment of the TG MALDI objective, greatly improving the speed and accuracy with which the objective position can be calibrated. These modifications have enabled more routine high spatial resolution IMS of rat brain and rat testis tissues from the instrument's original 50 μm limit down to 1.0 μm.

EXPERIMENTAL

Materials and sample preparation

The MALDI matrix (E)-4-(2,5-dihydroxyphenyl)but-3-en-2-one (2,5-cDHA) was used as previously described[44]. Ethyl acetate, toluene, and ammonium formate were purchased from Fischer Scientific (Waltham, MA). Rat brain was purchased from BioreclamationIVT (Baltimore, MD). Frozen tissue was sectioned at 7 μm thickness using a cryostat (Cryostar NX70, Thermo Scientific, Waltham, MA), thaw-mounted onto indium tin oxide (ITO) coated glass slides (Delta Technologies, Loveland, CO), washed with 50 mM ammonium formate solution, and dried in a vacuum desiccator. Matrix 2,5-cDHA was prepared at a concentration of 3 mg/mL in a 1:1 ethyl acetate/toluene mixture and sprayed at 90°C using a robotic TM Sprayer (HTX Technologies, Chapel Hill, NC). After MALDI IMS, matrix was removed with methanol and the tissue section was stained with hematoxylin and eosin (H&E) and ablation diameters were measured using a Nikon microscope (Eclipse 90i, Nikon Instruments Inc., Melville, NY).

Instrument modification

Instrument modifications to a MALDI TOF system (SimulTOF 200 Combo, Virgin Instruments, Marlborough, MA) were performed in addition to those described previously[22]. Briefly, in addition to the front-side laser, the instrument was fitted with an open-frame stage to

allow for TG optics. To reduce step size of the stage and reduce jitter in the motor, programmable microstepping motion drivers (AutomationDirect STP-DRV-4850) were introduced to the stage control which bypasses the original stepper driver control board (**Figure 2.1**). The drivers can be programmed from 200 to 51200 steps per revolution using SureStep PRO software. A retriggerable monostable multivibrator (SN74123N, Texas Instruments) was implemented before the microstepping driver to ensure stepper signal fidelity for the stage motors in the x and y direction.
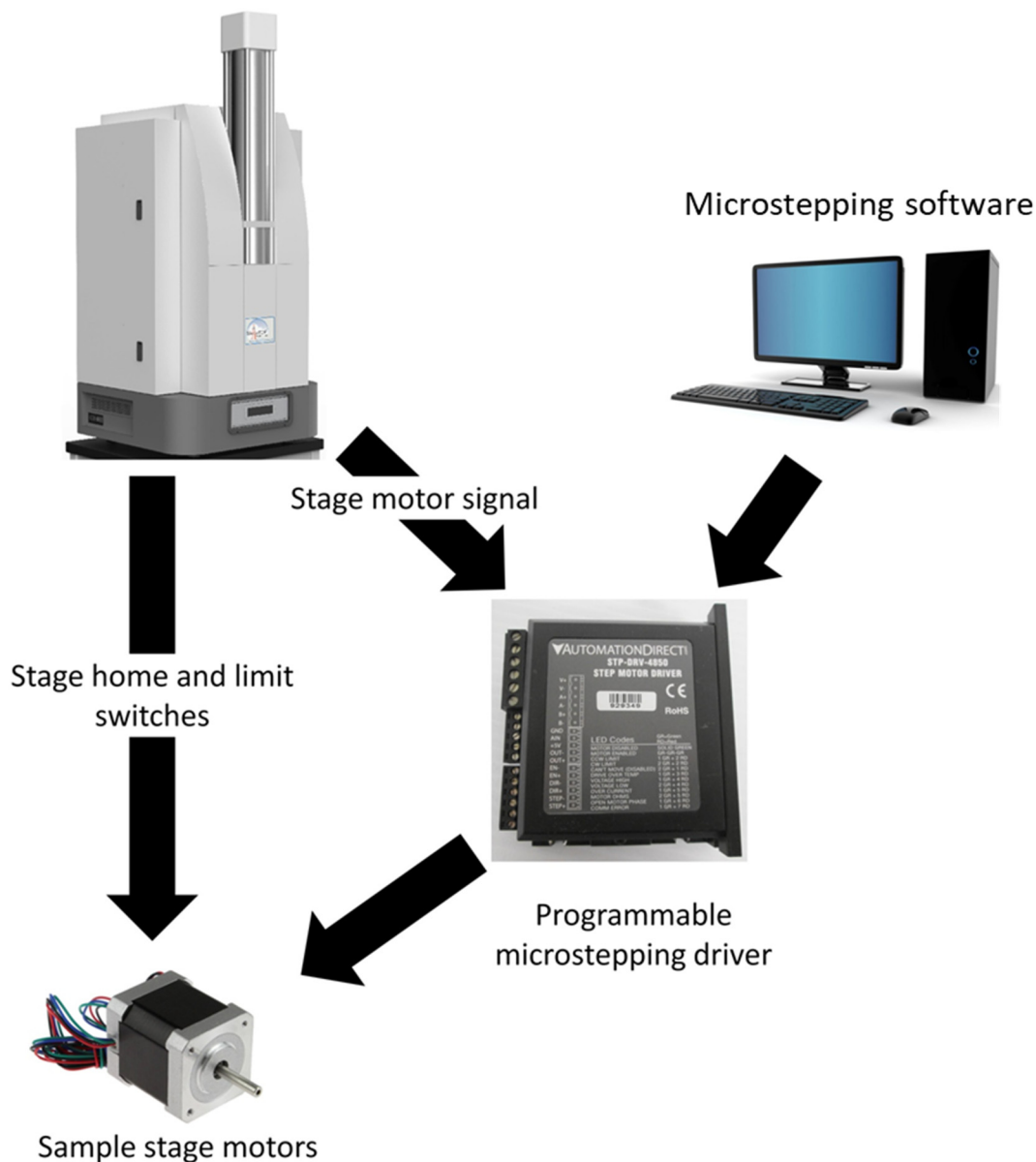
Figure 2.1. Implementation of microstepping drivers with sample stage motors of SimulTOF 200 instrument for high spatial resolution analysis.

The laser focusing objective and its z-axis motor were mounted on an x, y-translational plate so that the TG laser ablation area can be adjusted to be co-axial with the front-side ablation area (**Figure 2.2**). The translation plate provides for adjustment of the focusing objective while source is under vacuum, which reduces the time required for focusing alignment from ~1 hour to a few seconds. Aligning the front-side and TG ablation areas ensures that ion beam produced from either MALDI experiment is appropriately focused with the source ion optics. When switching between front-side and TG modes typically only requires retuning of the pulsed ion extraction timing, due to the fact that the MALDI plume dynamics can vary between front-side and TG[90].
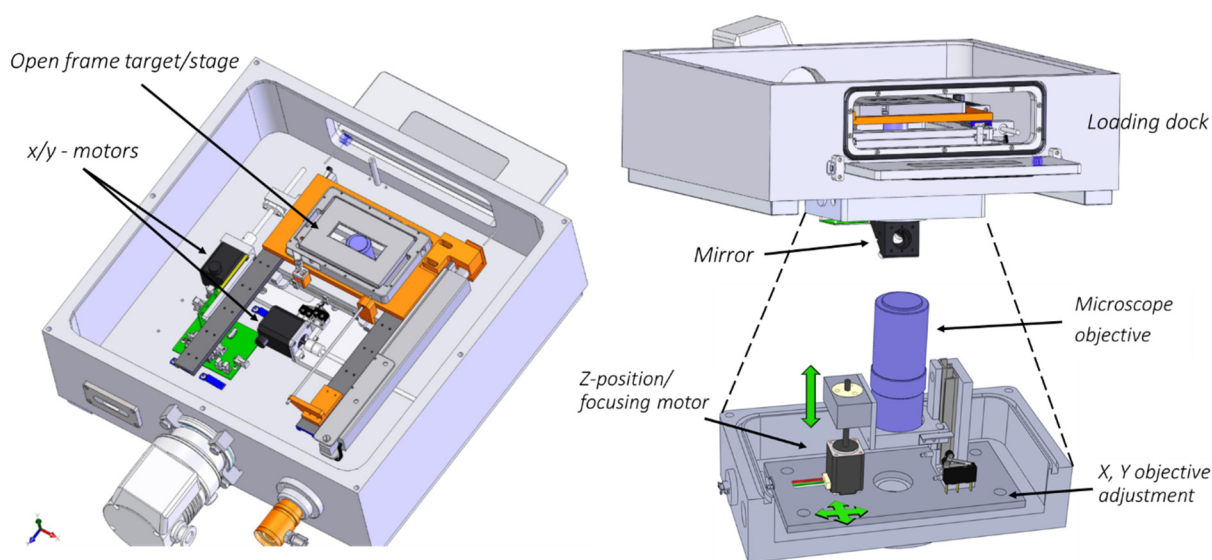
Figure 2.2. Source modifications on SimulTOF 200 instrument to allow for TG laser optics. The TG optics are mounted on an x, y adjustment stage and has a motor for z-position adjustment. Modifications did not affect the typical laser optical path.

A single laser shot per sampling area (i.e., pixel) was acquired by matching the real stage speed with the laser frequency. This coordination was completed by calculating the distance the stage has traveled between laser shots based on a constant stage speed in relation to the laser frequency. Appropriate adjustment of the microstepping parameters is described in Equation 1 for a desired spatial resolution, or pitch.

Equation 1:
$$Pitch\ (\mu m) = \frac{scan\ speed\ \left(\frac{mm}{s}\right)*1000\ \mu m/mm}{Laser\ repetition\ rate\ (Hz)}$$

RESULTS

In a previous report detailing the TG optical configuration on the SimulTOF 200 Combo instrument, the achieved 2.5 µm step size was limited by the stage motion driver.[23] In order to decrease stage step size, microstepping drivers were spliced into the existing motor control lines, bypassing the instrument motion control boards while maintaining continuity of the stage limit switches. Microstepping drivers can be used in place of the original motion drivers to divide the full step and corresponding current pulse into multiple microsteps. This is completed by sending partial current pulses to move the motor in smaller increments that, when added together, are equivalent to one full step of the motor. Microstepping increases the number of steps per motor revolution allowing for increased step precision while maintaining use of the original stage motors. A monostable multivibrator was implemented in-line prior to the microstepping drivers to decrease electronic noise and errant motion signal such that motor motion can be precisely controlled throughout the imaging run. The original motor motion drivers limited the stage motors to 400 steps per revolution resulting in a minimum 2.5 µm step size, whereas microstepping now allows for 51200 steps per revolution enabling a 20 nm theoretical step size. In addition to decreasing the step size well below the 2.5 µm standard instrument stage capability, increasing the number of motor steps between acquisition areas also allows for increased precision in the stage movement by reducing mechanical jitter. Without microstepping, a single motor step per acquisition area causes mechanical jitter that leads to a non-uniform ablation pattern (**Figure 2.3 A**). Scanning the sample surface at 2.0 µm (i.e., below the 2.5 µm stage limit) causes the instrument stage to rescan every 5th acquisition line to account for the discrepancy between the acquisition setting and minimum allowable stage pitch. A much more uniform ablation pattern is achieved with microstepping and stage pitch is improved to allow for higher spatial resolution imaging (**Figure 2.3 B**). The increase in the number of steps between each ablation position noticeably smooths out mechanical stage jitter.
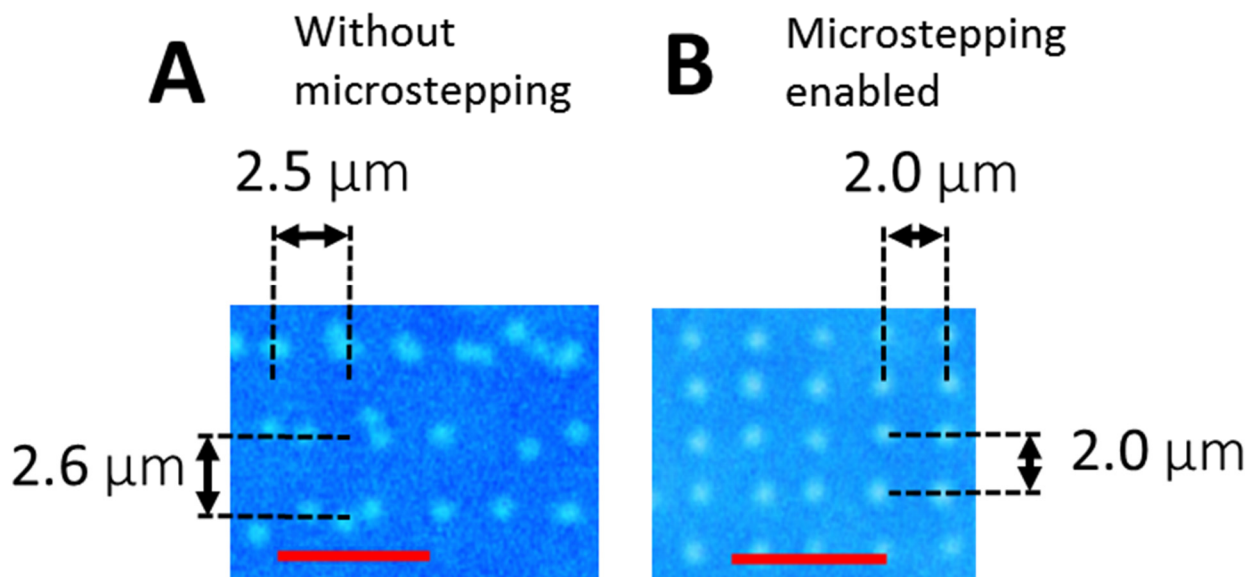
Figure 2.3. Example of microstepping benefit with ablation pattern on reference material, distance between ablation spots set to 2 µm in both cases. Red scale bar is 5 µm. **A)** Ablation pattern without microstepping. Distance between ablation areas is about 2.5 µm which matches the smallest pitch the original drivers allow. Mechanical jitter causes non-linear ablation pattern and non-uniform distance between ablation areas. **B)** Ablation pattern with microstepping enabled. Distance between ablation areas 2.0 µm as desired with improved stage movement resolution for more uniform distance between sampling areas.

The MALDI matrix cDHA was used as it was specifically developed in our lab to overcome the challenges of high spatial resolution IMS in high vacuum ion sources.[44] Higher spatial resolution acquisition of a given region allows for higher fidelity of spatial distribution of molecules within a tissue but there are tradeoffs in the forms of lower signal, larger data file sizes, and longer acquisition times. As such, some matrices may sublimate off in high vacuum sources during long acquisition times resulting in signal fading over the acquisition time and eventually a complete loss of signal. To remedy this, a matrix with a very low vapor pressure, cDHA, was chosen. Additionally, matrix application was previously optimized to allow for crystal sizes of approximately 1 µm with minimal analyte delocalization. Minimal matrix mass loss was detected, even after 24 hours, when stored in a similar high vacuum ion source.[44] The matrix also allowed for sensitive detection of lipids to counteract the loss in signal from smaller sampling areas with high spatial resolution IMS.

MALDI IMS acquisition parameters were optimized for TG high spatial resolution analysis. In reflection geometry acquisition, the laser fires at one pixel for many tens to thousands

of times and analyte signal is obtained with subsequent laser shots. Labs have previously demonstrated that sample is ablated after one laser shot, but it was not clear if there was a corresponding loss in signal for subsequent laser shots.[89] To test this, tissue was analyzed in transmission geometry in drill mode and the number of laser shots per pixel was varied from 1, 2 and 4 shots per pixel and a similar number of pixels was averaged for each acquisition.. With an increased number of laser shots, the overall lipid signal decreased (**Figure 2.4**). Next, one pixel was interrogated with subsequent laser shots and the resulting spectra were recorded (**Figure 2.5**). The first laser shot generated all the detectable lipid signal (**Figure 2.5 A**) whereas the second laser shot generated no signal (**Figure 2.5 B**). Subsequent laser shots were obtained (to 5 shots per pixel) but the data were like the second laser shot (no lipid signal) and was not included here. These data indicate that one laser shot should be fired per pixel because the matrix is ablated from that region.

Number of laser shots averaged per pixel

A) 1 shot

B) 2 shots

C) 4 shots
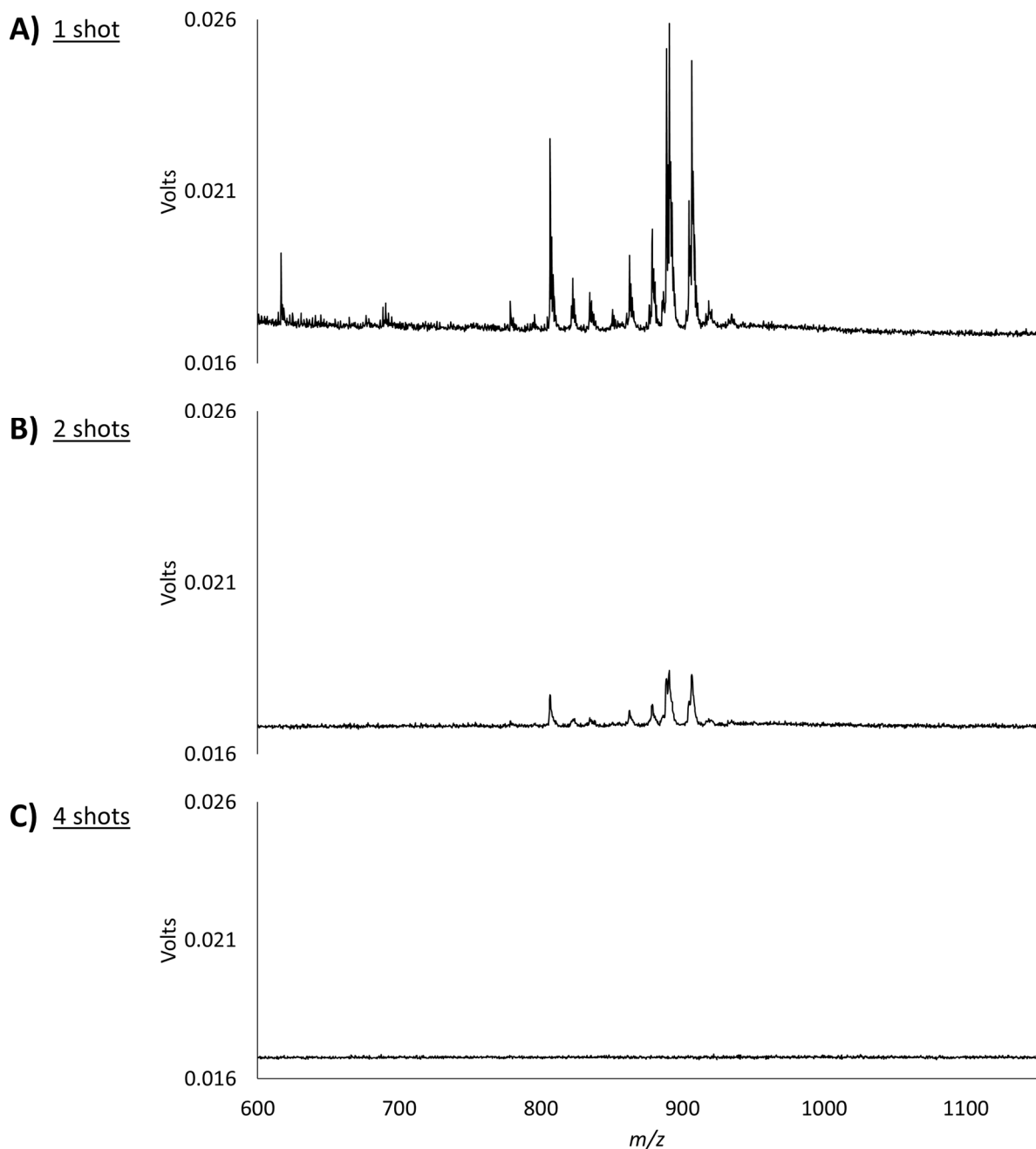
Figure 2.4. Lipids signal from tissue as a function of number of laser shots averaged per ablation area. One laser shot per pixel (**A**) allows for the highest signal-to-noise ion image to be obtained. Increasing the number of laser shots per pixel using "drill mode" to two (**B**) decreases the averaged signal. Averaging more laser shots per pixel such as four (**C**) decreases the average signal further such that it is indistinguishable from the instrumental noise. This indicates that the optimal analysis will be performed with one laser shot per ablation area for the SimulTOF 200 system in TG.

A)

1st shot

B)

2nd shot
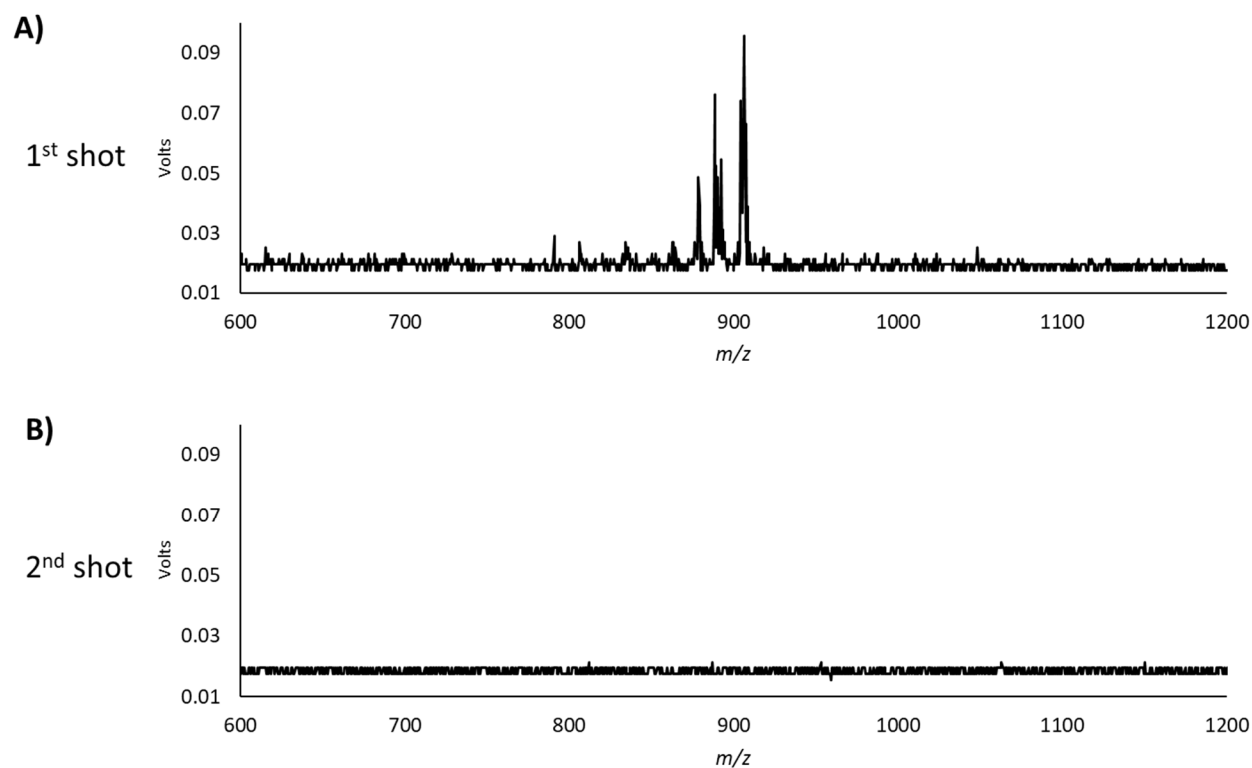
Figure 2.5. Transmission geometry analysis with subsequent laser shots. The first laser shot contains majority of lipid signal for TG MALDI IMS. The same pixel was analyzed with subsequent laser shots and the corresponding spectra were recorded. Single shot spectra from a rat brain section demonstrates that the majority of signal is obtained from the first laser shot (**A**) whereas no signal is obtained from the second laser shot for one IMS pixel (**B**). Therefore, ion images should be based on single laser shots per ablation area for TOF platforms, else noise will be averaged into the spectrum of each pixel and will lower the S/N of resulting data.

High spatial resolution IMS of rat testis tissue

High spatial resolution ion images were acquired in TG using stage microstepping. The stage speed and laser repetition rate were adjusted per Equation 1 to obtain the desired pitch. Rat testis was imaged using an 80-Hz laser frequency and a stage speed matched to acquire one laser shot[89] every 2 μm (Figure 2.4). The microstepping driver was set to 6400 steps per revolution resulting in 156 nm step size and 12.8 steps per laser shot. The number of microsteps was not an integer value so there may be some variability in pitch between ablation areas, but variability below 10% (microsteps above 5 ± 0.5 per laser shot) was accepted. The ablation diameter on tissue after acquisition was measured using an optical microscope and found to be, on average, ~1.5 μm. Lipid images showed numerous substructures in the tissue, including seminiferous tubule regions and interstitial Leydig cells. For example, *m/z* 795 localizes throughout the large, circular seminiferous

27

tubule structures (**Figure 2.6 A**) and *m/z* 885 localizes to the interstitial Leydig cells surrounding seminiferous tubules (**Figure 2.6 C**). The lipid at *m/z* 809 also localizes to seminiferous tubules but may reflect different developmental stages compared to *m/z* 795 because it is more concentrated in the outer ring of the tubules, where spermatozoa are more mature (**Figure 2.6 B**). The identity of the lipid at *m/z* 795 has been reported in literature to be a sulfated glyceroglycolipid, seminolipid (16:0, 16:0), *m/z* 809 was reported as seminolipid (17:0, 16:0), and *m/z* 885 as PI (diacyl-18:0/20:4).[91–94] An H&E stain of the tissue following acquisition confirmed the identification of these tissue areas (**Figure 2.6 D**). The spermatozoa flagella are stained dark purple and are located at the center of some seminiferous tubules.
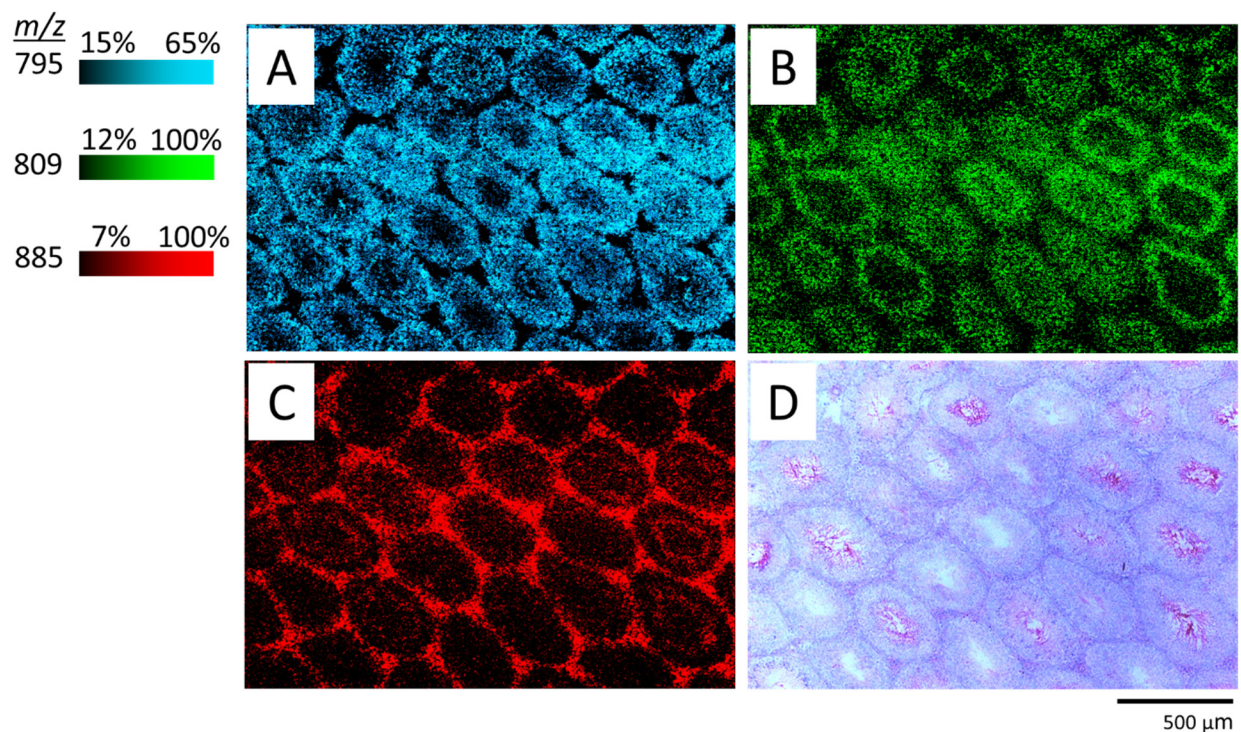
Figure 2.6. Rat testis imaged at 2 μm spatial resolution in negative ion mode with selected ions shown (**A-C**) as well as the H&E stain of the tissue section after acquisition (**D**). **A**) Ion image of *m/z* 795 shown in blue localizes throughout the seminiferous tubule (circular structure). **B**) Ion image of *m/z* 809 shown in green localizes to seminiferous tubule differently from *m/z* 795, seeming to correspond to different developmental stages with a ring of this lipid around tubule during spermatozoa maturation (compare to dark central regions of tubule in H&E). **C**) Ion image of *m/z* 885 in red localized to interstitial Leydig cells. **D**) H&E stain of tissue after ion image acquisition showing histology matching with ion images and demonstrating that ample tissue is left after imaging acquisition, an indication that there is no oversampling.

Another test tissue, rat brain cerebellum, was used to acquire ion images in TG at different spatial resolutions (2 µm, 1 µm, and 700 nm) to determine performance at higher spatial resolutions and the ion images matched to corresponding tissue sections stained with H&E. For all analyses, acquisition parameters were set to the smallest laser ablation diameter of ~1.5 µm. For the ion image of spatial resolution 2 µm, the microstepping stage and laser settings were such that 2 shots were acquired per pixel (**Figure 2.7**). High spatial resolution IMS allowed us to visualize fine structural detail within the cerebellum region. Next, a 1 µm ion image was obtained with 1 laser shot per pixel. The laser ablation diameter was larger than the pitch, so some oversampling of the tissue occurred, and the detrimental effects are thought to be seen as grainy ion images (**Figure 2.8**). Additionally, there is a decrease in signal as evidenced by lower contrast in the ion images. At even higher spatial resolution (700 nm), there is significant oversampling and there is a corresponding decrease in sensitivity such that *m/z* 885 is no longer detected and there are few distinguishing features in the ion image (**Figure 2.9**). The averaged spectra from the ion images obtained at different spatial resolutions are shown in **Figure 2.10 A-C** and there is a corresponding decrease in signal (voltage) at higher spatial resolution.

500 µm

m/z 2% 75%
885
888
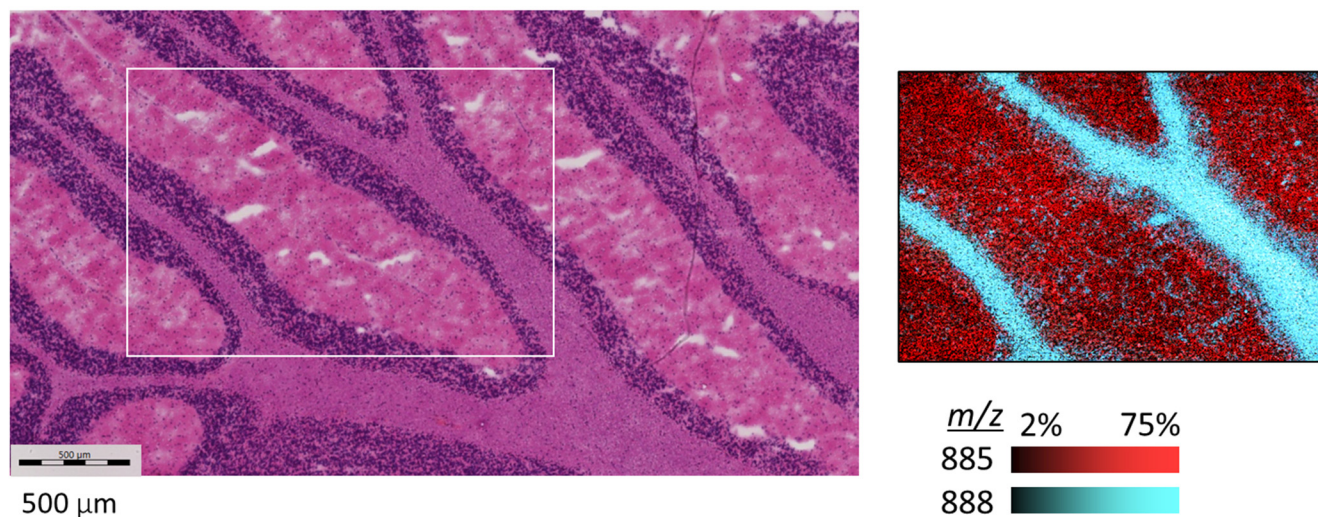
Figure 2.7. Rat brain cerebellum tissue section analyzed at 2 µm spatial resolution in negative ion mode using TG laser optics. Ions were selected based on their localization to white and grey matter within the cerebellum. A serial section of tissue was stained with H&E for comparison and a region corresponding to approximate IMS region was outlined in white. No oversampling was observed across the area of acquisition and tissue ablation diameter was approximately 1.5 µm.
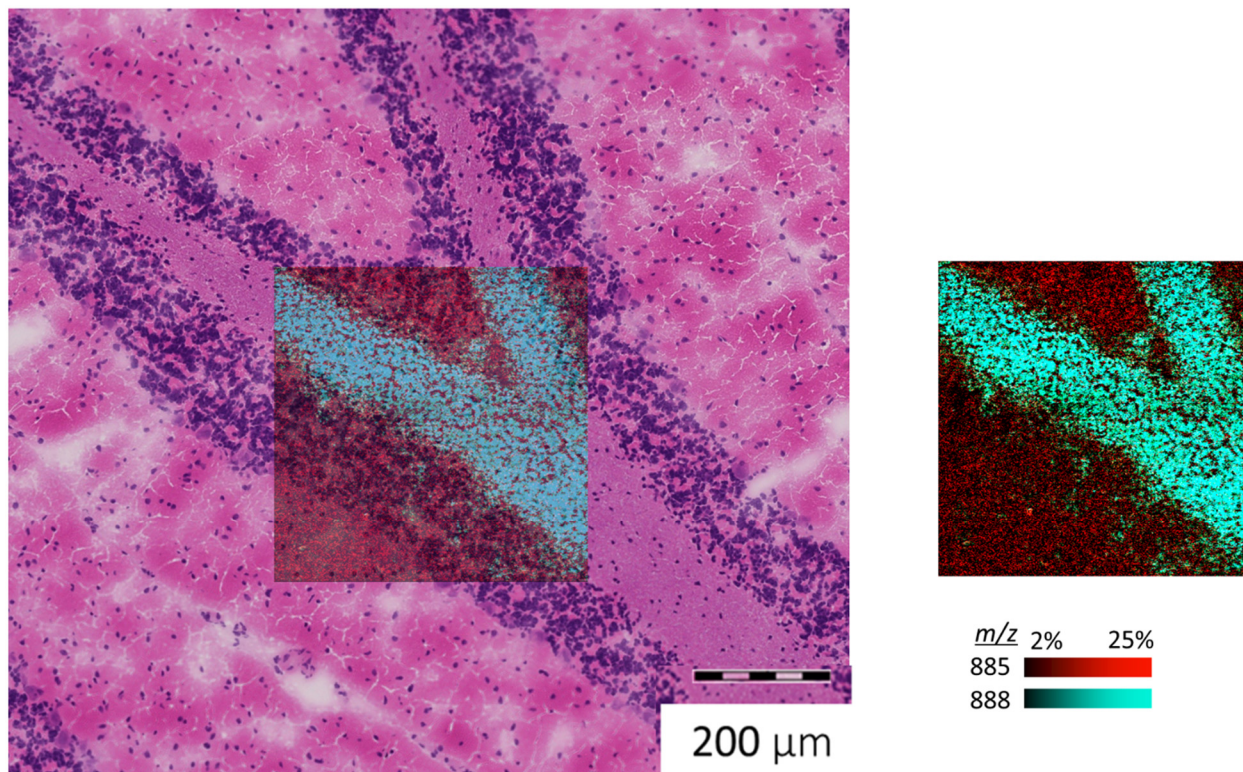
Figure 2.8. Overlay of rat brain images of MALDI IMS obtained in negative ion mode at 1 µm spatial resolution compared to a serial section of tissue stained with H&E. The ion image on right was made transparent and overlaid onto the H&E section approximating the region of IMS. Signal is relatively low for *m/z* 885, but still allows for contrasting ion images to be represented along with *m/z* 888.
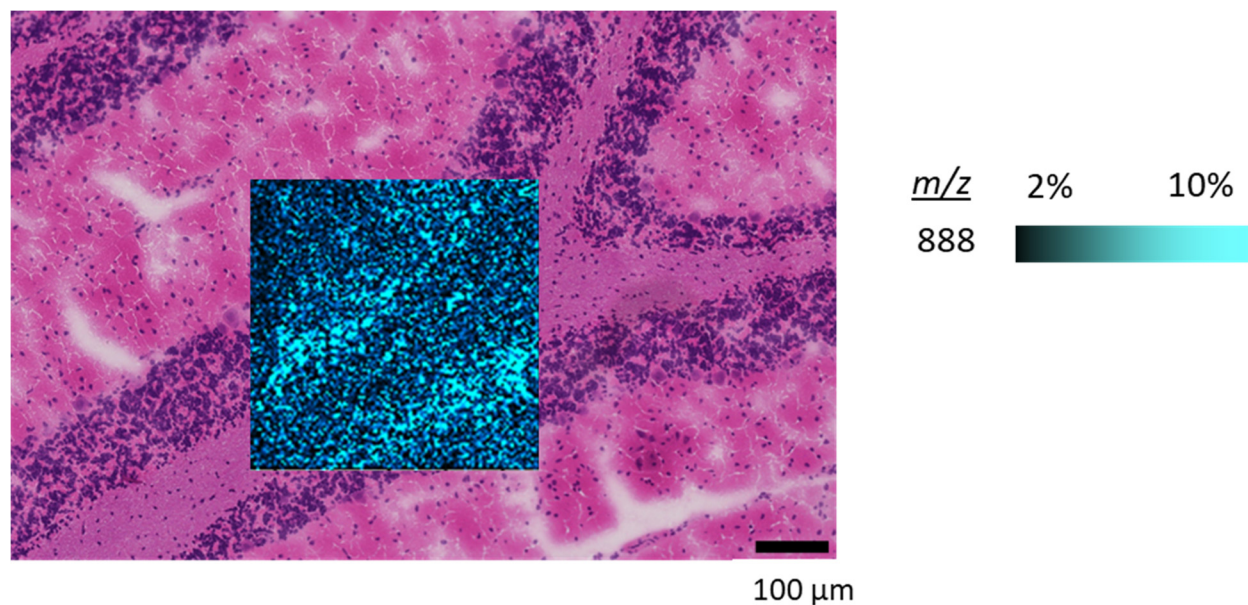
Figure 2.9. Rat brain cerebellum imaged at 700 nm spatial resolution in negative ion mode in TG overlaid onto an H&E-stained serial section of tissue. Multiple lipids were detected in the mass spectrum averaged over the entire imaging region and the lipids had similar distributions within the tissue. Only the ion at *m/z* 888 is displayed and the scale bar in black is 100 μm in length.
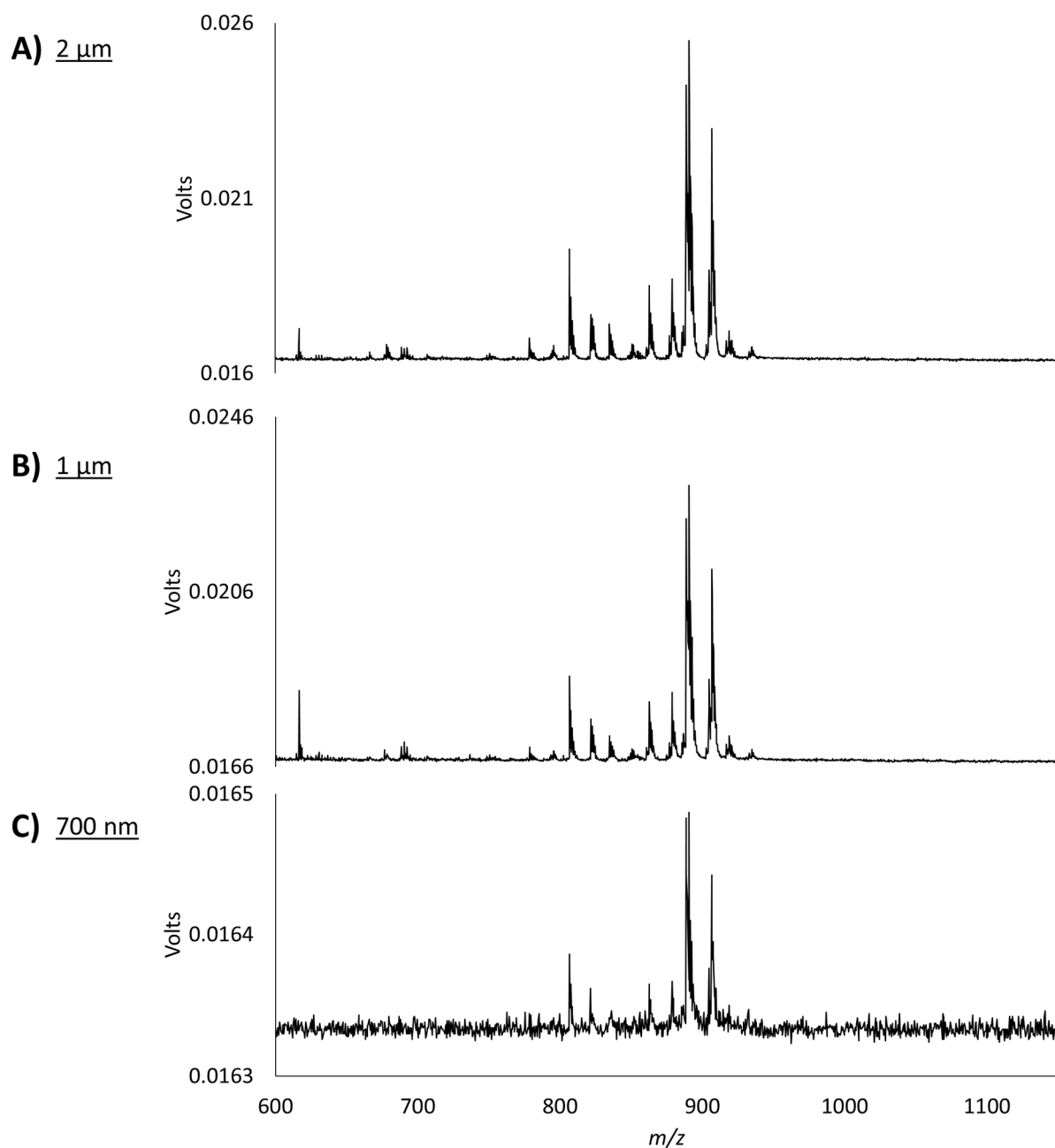
Figure 2.10. Signal comparison at various spatial resolution for analysis of rat brain tissue sections with a TG MALDI source. Averaged mass spectra are shown for ion images obtained at spatial resolutions of 2 μm (**A**), 1 μm (**B**) and 700 nm (**C**) of lipids in negative ion mode. Signal decreases slightly between 2 μm and 1 μm (**B**) indicating that the ablation diameter is slightly larger than 1 μm and that there is some oversampling. Additionally, at higher spatial resolution, the averaged signal at 700 nm is significantly decreased compared to that at 1 μm indicating that there is significant oversampling.

TG IMS of rat brain hippocampus

Rat brain hippocampus ion images were acquired in TG with a 1 µm pitch. Stage speed for 1 µm IMS was set to half that as compared to the 2 µm acquisition parameters. Microstepping was set to 6400 steps per revolution resulting in 156 nm step size and 6.4 steps per laser shot. Ion images were overlaid onto the same tissue section that was subsequently stained with H&E after IMS acquisition (**Figure 2.11 A**). The overlaid images show the dentate gyrus of the hippocampus, and they demonstrate the structural consistency between histological image and the ion images. The ion at *m/z* 885 localizes to the dentate gyrus of the hippocampus whereas *m/z* 888 localizes to surrounding structure. Average spectrum shown (**Figure 2.11 B**) demonstrates that numerous lipids were detected. A single pixel spectrum (**Figure 2.11 C**) shows signal from a single sampling area with good signal-to-noise.
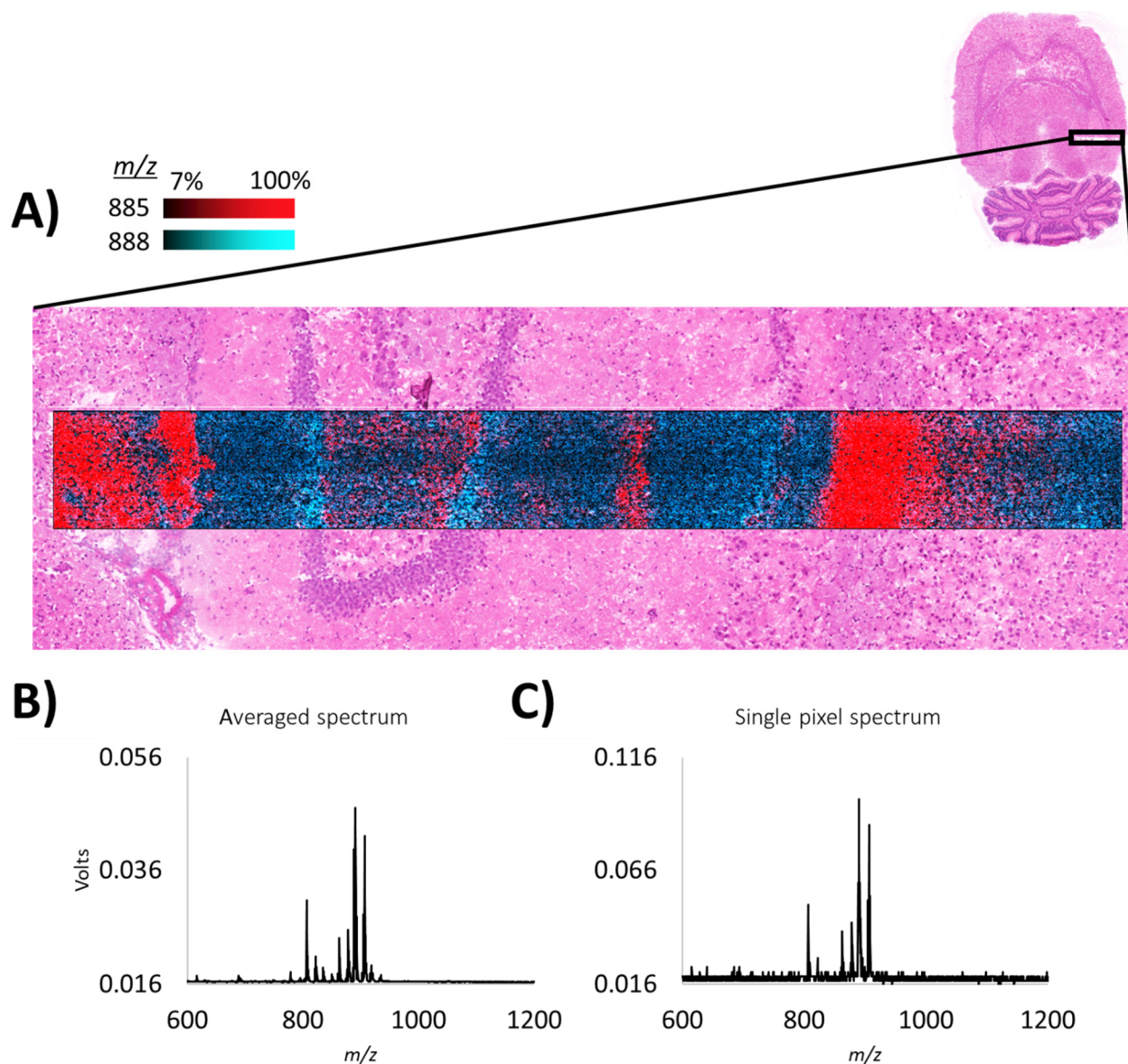
Figure 2.11. Rat brain hippocampus ion images obtained at 1 μm spatial resolution acquisition settings. After acquisition, the MALDI matrix was removed, and the tissue section was stained with H&E to visualize the morphological details of the tissue. **A)** Detail of imaged hippocampus region overlaid onto H&E-stained tissue. Two lipid ions of *m/z* 885 in red and *m/z* 888 in turquoise are displayed. **B)** Average spectrum (~5000 pixels) of red region showing strong lipid signal at high spatial resolution imaging. **C)** Single-pixel spectrum from ion image showing that multiple ions are detected from one pixel.

Other tissues analyzed by transmission geometry include rat retina and *Staphylococcus aureus*-infected mouse kidney (**Figures 2.12, 2.13**). High spatial resolution is needed for analysis of the single-celled layer of the retinal pigment epithelium implicated in the development of macular degeneration.[95] As the layer is approximately 10 μm wide, high spatial resolution IMS is

required to differentiate that layer from the surrounding tissue. The RPE layer was not detectable in this analysis, but greater sensitivity would allow for its detection. Murine model systems are ideal for studying the effects of antibiotic resistant bacteria and the formation of bacterial colonies in organs.[96] An bacteria-induced abscess was selected for analysis (**Figure 2.13**) at 2µm spatial resolution. The abscess itself was devoid of signal but the surrounding tissue and tubules could be visualized based on numerous lipid species that had different localizations within the tissue.
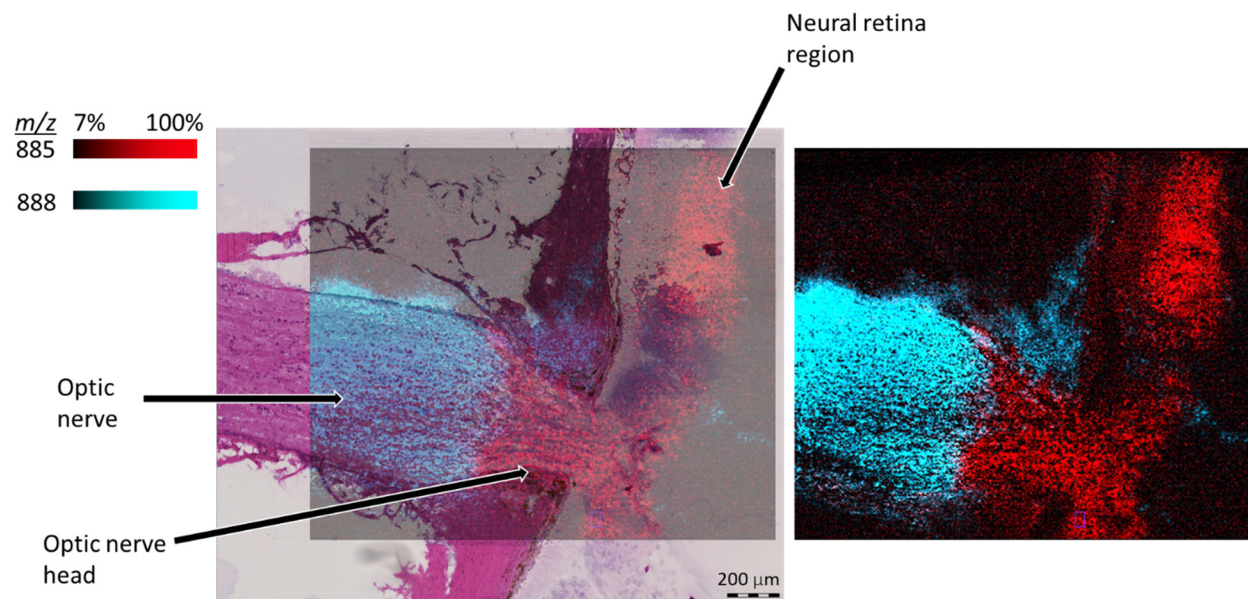
Figure 2.12. A rat retina was analyzed using the TG source at a spatial resolution of 2 µm in negative ion mode. The ion image (right) was set to 50% transparency and was overlaid onto the H&E stain of the same tissue section. Ion images show the transition of lipid species between the optic nerve and the optic nerve head regions of the rat retina.
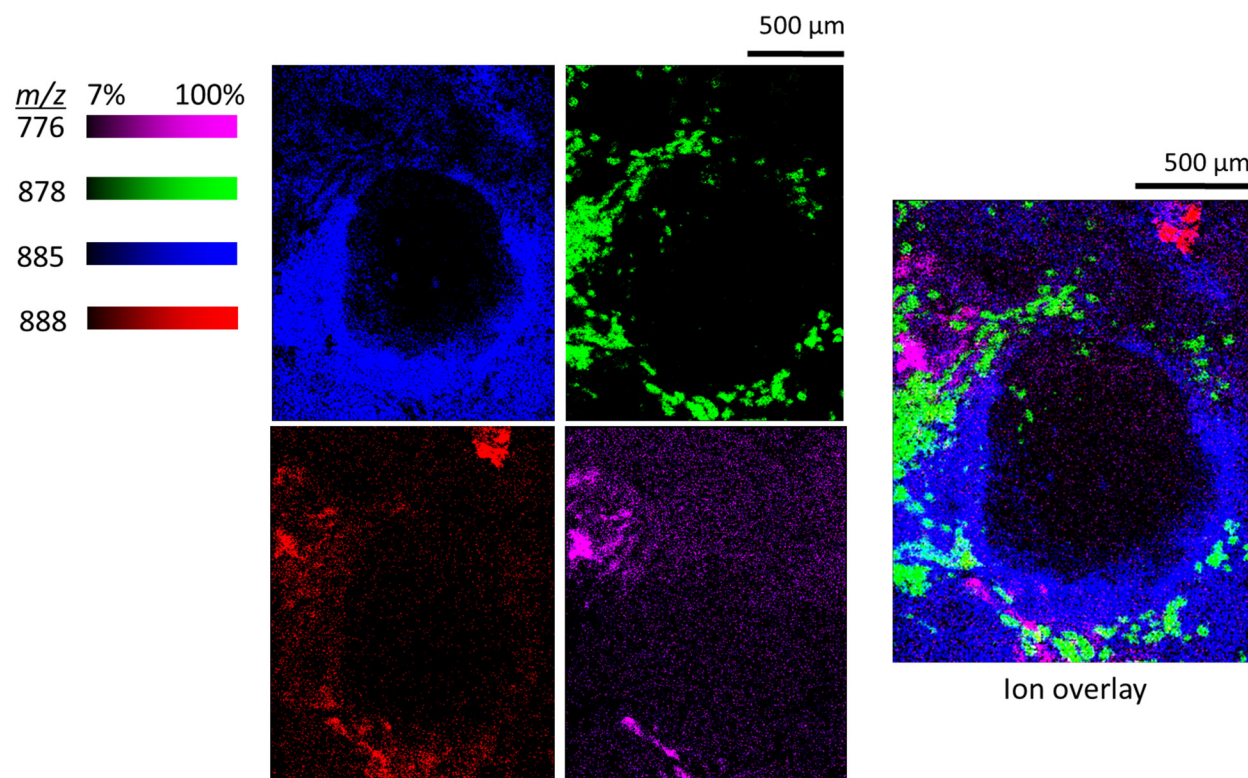
Figure 2.13. MALDI IMS ion images of *Staphylococcus aureus*-infected mouse kidney imaged at 2 μm spatial resolution using the TG source. Imaged region includes *S. aureus* abscess (central dark portion) and surrounding tissue with the false color images of numerous lipids shown as purple (*m/z* 776), green (*m/z* 878), red (*m/z* 888) and other tissue in blue (*m/z* 885). The ion overlay is a combination of the four individual ions.

Even though the tissue regions selected were small to moderate, the high spatial resolution meant that the number of pixels acquired per acquisition was between 750k and 1 million. Even though the laser was firing at 80 Hz and 1 laser shot per pixel was obtained, the actual acquisition time for these ion images were much longer than expected. At the end of each ion image row, the instrument stopped and processed data. Instead of taking hours, some of these ion images took tens of hours to acquire. This limitation in real acquisition speed was based on the limited data processing capabilities of the digitizer that interfaced between the instrument and the computer. The digitizer did not have the processing power to transfer and save the spectra at the rate of acquisition (80 spectra/sec) instead, the real acquisition rate was estimated to be 40 spectra/sec. Future work would be to implement a more powerful digitizer to allow for faster rates of saving of data and ion image acquisition.

CONCLUSIONS

The TOF instrument allowed for a relatively high sampling rate that is useful for these large ion images (500k - 1 MM pixels) that can take a long time to acquire at high spatial resolution. Microstepping drivers enabled very precise, fine movement of the sample stage without having to modify the existing motors and without the purchase of other expensive, high-precision stage motors. Ion images with high spatial resolution were acquired in a routine manner. Some drawbacks of this system were that the mass resolution was relatively poor (~4000 at *m/z* 760) so there were likely many isobaric lipids in a given peak in the mass spectrum. Additionally, there was a significant loss of signal at very high spatial resolutions such as at 1 μm and at 700 nm. To fully characterize the lipidome of complex tissue samples in a spatially resolved manner, higher mass resolution and higher sensitivity will be of greater value.

Acknowledgements

CHAPTER III

CUSTOM TRANSMISSION GEOMETRY SOURCE FABRICATION AND IMPLEMENTATION OF MALDI-2 ALLOW FOR HIGH SPATIAL RESOLUTION SURFACE ANALYSIS AND SIGNIFICANT ENHANCEMENT OF SOME LIPID SIGNALS ON AN ORBITRAP INSTRUMENT

This chapter is in part adapted from Combining MALDI-2 and transmission geometry laser optics to achieve high sensitivity for ultra-high spatial resolution surface analysis published in the Journal of Mass Spectrometry and has been reproduced with the permission of the publisher and my co-authors Eric C. Spivey, Daniel J. Ryan, Jeffrey M. Spraggins, and Richard M. Caprioli.

OVERVIEW

A transmission geometry (TG) optical configuration allows for a smaller laser spot size to facilitate high resolution MALDI mass spectrometry. This increase in spatial resolution (i.e., smaller laser spot size) is often associated with a decrease in analyte signal. MALDI-2 is a post-ionization technique that irradiates ions and neutrals generated in the initial MALDI plume with a second orthogonal laser pulse and has been shown to improve sensitivity. We have modified a commercial Orbitrap mass spectrometer to incorporate a transmission geometry MALDI source with MALDI-2 capabilities to improve sensitivity at higher spatial resolutions.

INTRODUCTION

Matrix-assisted laser/desorption ionization (MALDI) mass spectrometry (MS) is a technology that enables the spatial analysis of tissues with a high degree of molecular specificity, enabling new approaches for understanding biology and medicine.[97–99] Tissue interrogation by MALDI is performed by either collecting individual spectra from discrete foci as a histology guided profiling experiment [4,5] or by a raster of the sample to collect spectra over an area of the sample to generate ion images.[6,7] In either case, cell-scale interrogation of the sample (<10 μm) is desired to differentiate among cell types for complete characterization of a tissue.[59] For

commercial MALDI platforms, the sizes of the foci are typically limited (often to ~20 μm) by the resolving power of the optics used to focus the laser onto the sample.[22] Commercial systems implement a front-side geometry optical configuration where the laser optics and ion optics of the instruments are on the same side of the sample, resulting in long focal length lenses to avoid having the laser optics interfere with the ion optics. The long focal length required with front-side geometry MALDI instruments limits the resolving power of the focusing optics used, as approximated by the equation:

$$D_f \cong \frac{4\lambda * f}{\pi * D_0}$$

where D_f is the beam waist diameter in μm at the focal length (determines spatial resolving power), f is the focal length of the lens in mm, λ is the wavelength of the laser in μm, and D_0 is the collimated beam diameter in mm at the lens. It is worth noting here that parameters other than the focused beam diameter also affect the ultimate spatial resolution of a MALDI measurement, the sensitivity of the instrument, the type of matrix used, the matrix application method, and most importantly stage step size. However, the focused beam diameter is a critical parameter affecting MALDI resolution.

Transmission geometry MALDI platforms have been developed in order to use higher resolving power focusing optics.[9,10] For TG, the laser and focusing lens are placed on the opposite side of the sample, irradiating the back side of a slide. The sample and its substrate are sufficiently thin and optically transparent to allow the passage of the laser beam through to the matrix layer. This arrangement allows the use of much shorter focal length optics, including the use of lens stacks in the form of microscope objectives. These high numerical aperture objectives (0.95 N.A.) have very short effective focal lengths that can permit submicron spatial resolution. The trade-off, however, is that these objectives often have very short working distances. This can require that samples be mounted on thinner substrates in order to be analyzed.

Although TG MALDI has been successfully applied to achieve subcellular imaging, sensitivity constraints are a challenge and often only the more abundant species are detected in an acquisition. Several strategies have been developed in order to improve the signal-to-noise ratio (S/N) in IMS, including instrument design[104] and improved sample preparation methods.[12,13] Recently, a laser-based post-ionization approach, referred to as MALDI-2, has been developed for

improved sensitivity.[29] Briefly, MALDI-2 is performed by irradiating the plume of molecules and matrix generated by a primary MALDI ablation event with a second post-ionization UV laser beam that is orthogonal to the primary ionization plume.[30] MALDI-2 has been shown to improve sensitivity up to 100-fold for some lipid species by ionizing neutral molecules generated in the MALDI process.[29] These initial studies focused on applications for front-side geometry optical path MALDI instruments with a beam diameter between 5-10 μm.

We have combined TG and MALDI-2 post-ionization to demonstrate the synergistic potential of the two techniques. Because MALDI-2 improves signal without altering any pre-ionization aspect of the TG system, we effectively compensate for the loss of signal that occurs when sampling small areas during high spatial resolution experiments. We show that in certain cases, we recover most if not all of the signal that was lost by improving spatial resolution, and that we can detect species in the sample that are below the detection limit of the TG MALDI system alone.

METHODS

Sample preparation and mass spectrometry

Lipid standard 1,2-dielaidoyl-*sn*-glycero-3-phosphocholine was purchased from Avanti Polar Lipids (Alabaster, AL, USA), acetonitrile and methanol were purchased from Fisher Scientific (Waltham, MA, USA), 2,5-dihydroxyacetophenone (DHA) was purchased from Sigma-Aldrich (St. Louis, MO, USA), and water was purified to 18.2 MΩ via Milli-Q Reference Water Purification System (Millipore Sigma, Burlington, MA, USA). Rat liver was obtained from BioreclamationIVT (Baltimore, MD, USA) and indium tin oxide (ITO)-coated (8-12 Ω) glass coverslips were obtained from SPI Supplies (West Chester, PA, USA). A solution of DHA was prepared in 90:10 acetonitrile/water (15 mg/ML) for MS analysis. For standard experiments, matrix was mixed with the lipid standard and reconstituted in methanol to a 1:1 ratio and spotted (0.5 mL) onto an ITO coverslip. Rat liver (20 mg wet weight) was homogenized in 1 mL methanol, centrifuged, and supernatant was spotted 1:1 with matrix solution as above. Spot size measurements were obtained from a thin film of a reference material, ink from a permanent marker (black fine point Sharpie Classic, Sanford Brands, Oak Brook, IL, USA), on coverglass. Ablation diameters from measurements taken at ionization threshold were acquired at 100x magnification using a Nikon microscope (Eclipse 90i, Nikon Instruments Inc. Melville, NY, USA). Mass analysis

was completed on an Orbitrap Elite mass spectrometer operated with a resolution of 60,000 at *m/z* 400, 1 microscan, and an *m/z* range of 200-2000.

Transmission geometry source

A commercially available MALDI ion source (Spectroglyph LLC, Richland, WA, USA) was modified to include TG optics (**Figure 3.1**). The existing vacuum chamber back plate with a micro-positioning stage was replaced with a customized back plate that includes an adjustable lens system and an open aperture stage. A custom-built lens holder is attached to a high-precision, piezo motor-driven linear stage (Model Q-545, Physik Instrumente, Auburn, MA, USA), which is enclosed in a vacuum-tight box within the main vacuum chamber. A 63x magnification, 0.95 numerical aperture microscope objective (EC Plan-Neofluar Corr M27, Carl Zeiss Microscopy, LLC, Thornwood, NY, USA) is attached to a lens holder to focus the 349 nm MALDI laser (Explorer, Spectra Physics, Santa Clara, CA, USA) on the sample. A custom-built stage constructed from acrylic plastic was installed in the vacuum chamber lid to hold the sample near the entrance of the ion funnel of the mass spectrometer. The stage is manually actuated and uses a magnetic couple to transmit movements from a positioner on the front of the lid. Laser optics (ThorLabs, Newton, NJ, USA) were affixed to the outside of the vacuum chamber custom back plate and aligned to direct the laser beam from the laser head to the back aperture of the objective.
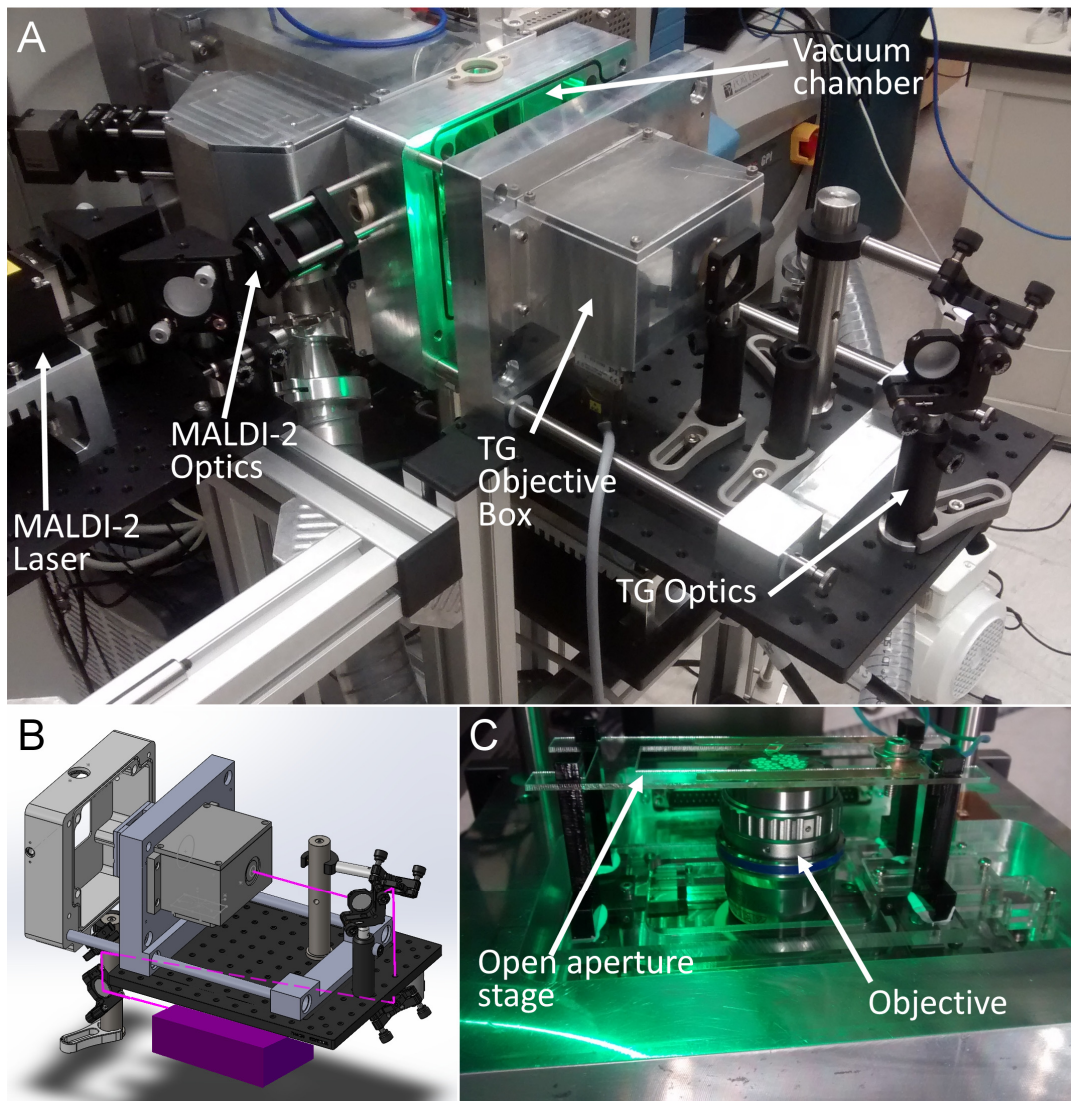
Figure 3.1. Transmission geometry MALDI-2 ion source. (**A**) Image of the custom ion source installed on an Orbitrap Elite mass spectrometer. The MALDI-2 laser and optics can be seen at the left side of the image. The vacuum chamber is open, and the lid (which contains the open aperture stage) is mounted on rails with the optics breadboard and optics. (**B**) Drawing of assembled source parts with approximate laser path. Laser light is emitted from the stock laser mounted under the source (purple box) and picked off by a periscope which reflects it to an upward-facing mirror under the end of the breadboard. The beam passes through a hole in the breadboard to a pair of steering mirrors used to align the beam to the optical axis of the objective lens, before entering the source through a window on the outside of the box containing the focusing stage and the objective. (**C**) Objective and stage as seen inside the source. The objective projects into the source from the focusing stage (not seen), and through the open aperture of the manually actuated stage. The stage holds a sample at the correct position relative to the Orbitrap funnel. The magnetic couple for the stage can be seen at the right side of the image.

The new TG system is designed to operate with minimal disruption to the stock front-side geometry source. No stock parts were disassembled or materially altered to install the TG system. The MALDI-2 laser of 266 nm wavelength (FQSS266-200-STA, CryLaS GmbH, Berlin, Germany) is aligned to irradiate the MALDI plume generated after the MALDI-1 event. Lasers were set to 60 Hz each with 100 μs delay between the MALDI-1 and MALDI-2 laser pulses. The MALDI-2 laser beam was aligned with the MALDI-1 spot and positioned ~1 mm above the surface. Longer delay time between MALDI-1 and MALDI-2 pulses as well as greater distance between the sample and MALDI-2 focus were used as compared with front-side geometry previously reported in literature.[14,15] Adjustment of the stock MALDI laser optics was obviated by intercepting the beam as it left the laser head. The beam was intercepted for the TG optics via a magnetically mounted mirror, which simplifies switching between the two modes of operation (*i.e.,* front-side and TG operation).

RESULTS AND CONCLUSIONS

The capability of the custom TG MALDI source to achieve ultra-high spatial resolution ablation patterns is demonstrated using a homogenous reference material (i.e., Sharpie ink). An analysis of ablation patterns shows over 200-fold decrease in the ablation area at ionization threshold when using TG MALDI (**Figure 3.2**) with an ablation diameter of 17 μm using front-side geometry laser optics down to 1 μm with our custom TG MALDI source. These results indicate the potential for high resolution imaging MS applications using this platform. Given the precise optical alignment required between the laser and the objective, and the vulnerability of the laser optics to movement and vibration, we are pleased to note that only minor adjustment of the optics is required between samples. The stability of the current optical setup for TG analysis provides the basis for future experiments.
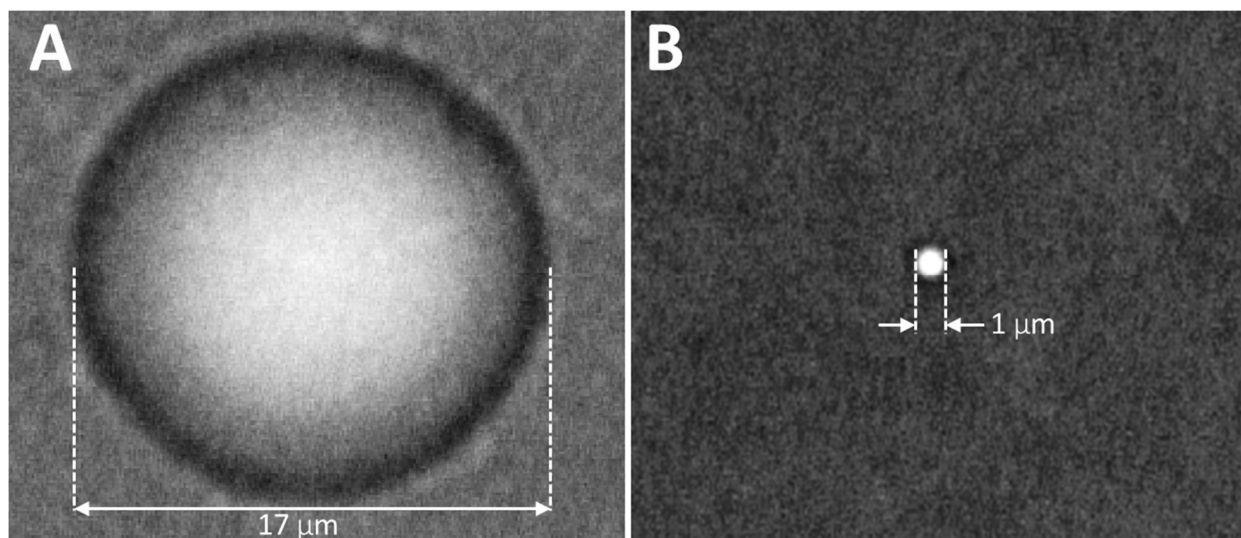
Figure 3.2. Ablation of thin-film reference material via (**A**) front-side geometry laser and (**B**) transmission geometry at tissue homogenate/lipid standard ionization threshold. Spot size of laser used for front-side geometry is 17 µm in diameter. Transmission geometry spot size is 1 µm in diameter. An over 200-fold decrease in ablation area is realized with transmission geometry as compared to front-side geometry.

An aim of the development work is to offset losses in signal from the smaller TG mode ablation regions, with improved sensitivity using the MALDI-2 system. We measured a 10-fold increase in signal intensity between transmission geometry MALDI intensity (as tested with lipid standard and tissue homogenate), when MALDI-2 was employed (**Figure 3.3**). Lipid standards analyzed with TG MALDI only (**Figure 3.3 A**) and with TG MALDI-2 (**Figure 3.3 B**) showed a 12-fold increase in intensity of the potassiated species of the standard with post-ionization. No lipid signal was detected with only MALDI-2 laser firing which indicates that the MALDI-2 laser is orthogonal to our sample, i.e., the MALDI-2 beam does not irradiate the sample surface and no ions are produced from MALDI-2 alone. Thus, any increase in signal with MALDI-2 originates from species ionized from the ion plume. Rat liver tissue homogenate was also analyzed, and MALDI-2 provided an increase of ~7-fold for most lipid species (**Figure 3.3 C, D**). Noise did not appreciably increase with increases in signal, so there was a significant improvement in the signal-to-noise ratio (S/N) of multiple ions (**Figure 3.4**).
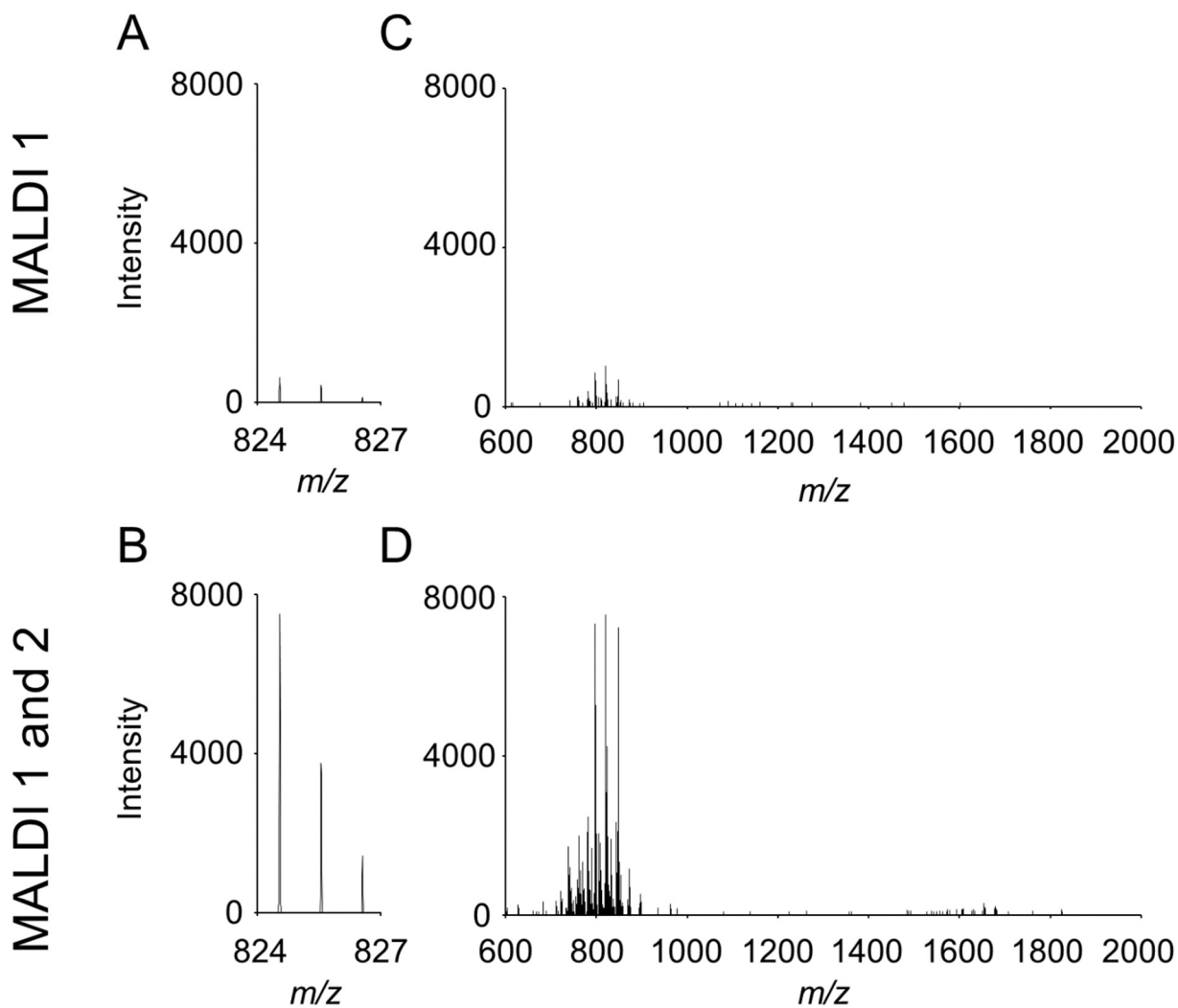
Figure 3.3. MALDI lipid spectra of spotted standard and from rat liver tissue homogenate analyzed with TG with and without MALDI-2 post-ionization. **A)** Lipid standard with MALDI 1. **B)** Lipid standard with post-ionization **C)** Rat liver homogenate mass spectrum at ionization threshold without MALDI-2 showing low S/N ratio. **D)** Rat liver homogenate mass spectrum with MALDI 1 and MALDI-2 resulting in ~7x increase in lipid signal.
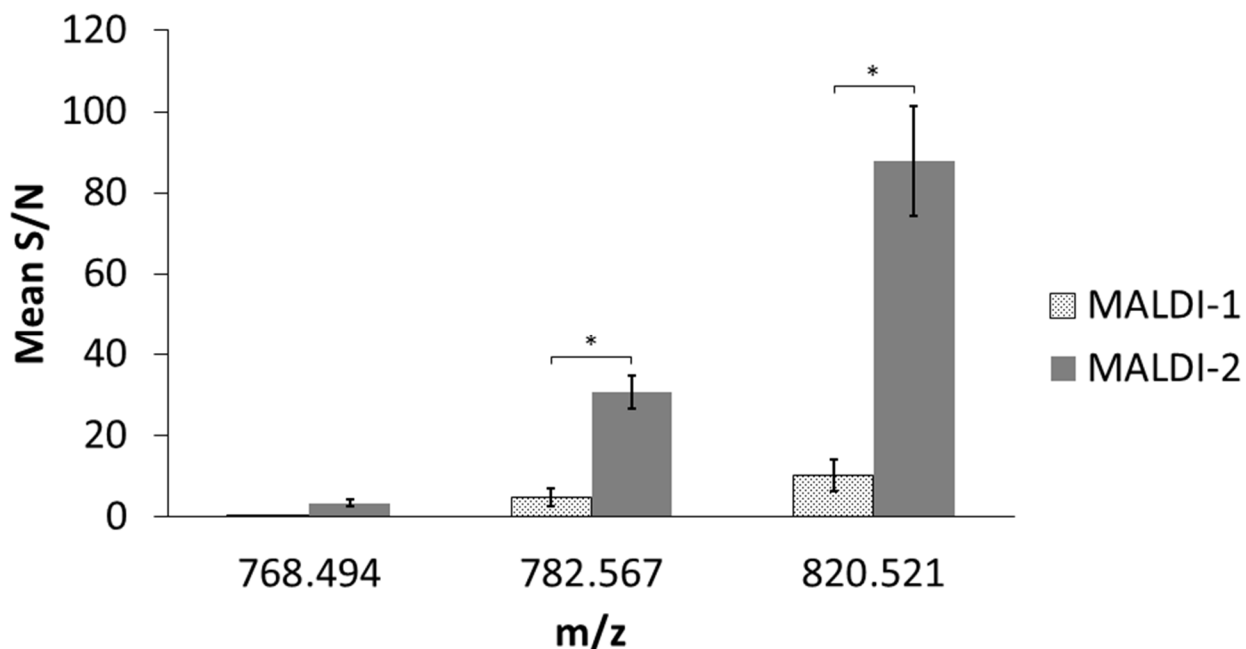
Figure 3.4. Comparison of S/N with MALDI only (MALDI-1) and of MALDI with MALDI-2 (MALDI-2). Five measurements were acquired from homogenized rat liver and the S/N was recorded for peaks at *m/z* 768.494, 782.567 and 820.521. Bars show the mean S/N value at each peak, error bars denote the standard deviation of the mean S/N (n=5). No signal was detected at *m/z* 768.494 without the use of MALDI-2. MALDI-1 and MALDI-2 were compared at peaks *m/z* 782.57 and 820.53 using a 2-tailed, 2-sample t-test assuming unequal variances. (*) denotes α<0.001.

The major advantage of coupling TG and MALDI-2 is recovery of signal lost by smaller ablation areas. The combination promises to provide an unprecedented pairing of spatial resolution and sensitivity, opening new possibilities for imaging MS at cellular resolution. By designing and implementing a modified MALDI source with an open-aperture sample stage and laser optics positioned for back-side, transmission geometry, we can achieve much smaller ablation patterns. Improvements in spatial resolution can often lead to a loss of ion signal in MALDI IMS acquisitions, due primarily to a reduction in the total amount of material desorbed from the sample. We show MALDI-2 improves sensitivity of TG measurements through a second, post-ionization event of the MALDI-1 generated ion plume.

These initial experiments with a custom source established the proof-of-principle for TG on an Orbitrap platform so the source was modified further with high-precision piezoelectric stage motors to allow for IMS. Compact linear stages with ultrasonic piezoelectric motors (U-521 PILine® Linear Stage) were acquired from Physik Instrumente, stacked to allow for x, y motion

of the stage, and an open-back sample holder was attached to the top stage. Stage motor movement timing was based on contact closure connection and fill time of the instrument. The center of the TG stage and TG laser optics were positioned to be at the center of the MALDI-1 ablation area from the Spectroglyph source for comparison between TG and front-side ablation modes. The objective holder was modified to allow for use of a Mitutoyo M Plan Apo NUV 100x, 0.5 numerical aperture, infinity corrected objective that has a longer focal length (compared to the 0.95 N.A. objective). This allowed for the use of the thicker ITO-coated glass slides rather than samples on the thin, brittle coverslips.

IMS capabilities of the TG source on the Orbitrap Elite system were demonstrated using tissue sections from rat testes. Rat testes were sectioned at 7 µm thickness, thaw-mounted onto ITO-coated glass slides, coated with DAN matrix and analyzed at 3 µm spatial resolution in positive ion mode using the TG MALDI source (**Figure 3.5**). Good S/N was achieved with the Orbitrap system allowing for ion images with excellent contrast. Numerous ion species were detected with good S/N as evidenced in the averaged mass spectrum (**Figure 3.6**). At 3 µm spatial resolution there was no oversampling as determined by the tissue morphology stained with H&E after IMS acquisition (**Figure 3.7**). The ablation diameter was approximately 2.5 µm and the optical image showed the uniformity of the ablation area which was afforded by the high-precision piezoelectric stages. Ion images were obtained at 2 µm as well but there appeared to be significant oversampling artifacts that presented as black lines or pixels with poor lipid signal (**Figure 3.8**). Finally, the performance of the TG configuration with front-side configuration was tested (Figure 3.9). TG allows for a much more detailed ion image whereas the front-side acquisition allows for significantly better signal (by an order of magnitude). The signal is approximately proportional to the ablation area for each acquisition mode.
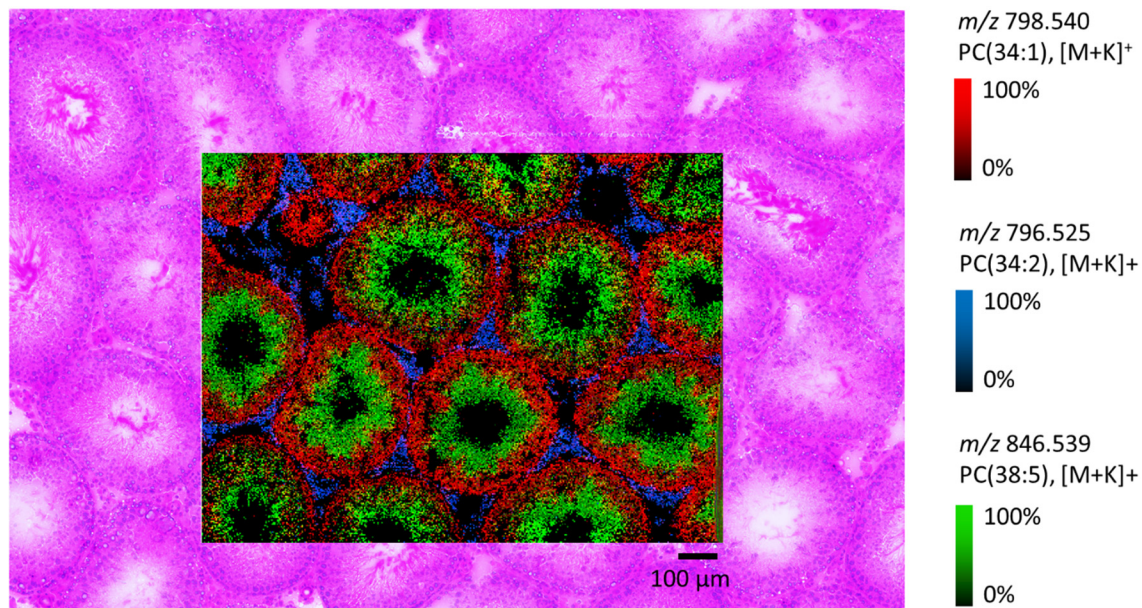
Figure 3.5. Ion image of rat testis obtained using transmission geometry platform at 3 µm spatial resolution. Ion image is overlaid onto tissue section stained with H&E after IMS acquisition. Large round structures outlined by *m/z* 798.540 (identified by accurate mass [<1.3 ppm error] as potassiated PC(34:1)) represent cross sections of the structures corresponding to maturation of spermatozoa, the seminiferous tubules. The interior of the seminiferous tubules corresponds to the localization of *m/z* 846.539, identified by accurate mass (<2.4 ppm error) as potassiated PC(38:5), and this region is where spermatozoa mature as they transition from the exterior of the seminiferous tubule to the interior based on their stages of maturation. Surrounding the seminiferous tubules are the interstitial Leydig cells. The ion at *m/z* 796.525, identified by accurate mass (<0.4 ppm error) as potassiated PC(34:2) localizes to regions of Leydig cells. High spatial resolution IMS at 3 µm and higher spatial resolution allows for more accurate differentiation between cellular regions of distinct biochemical composition such as the Leydig cells and seminiferous tubules that are separated by a single cellular layer.
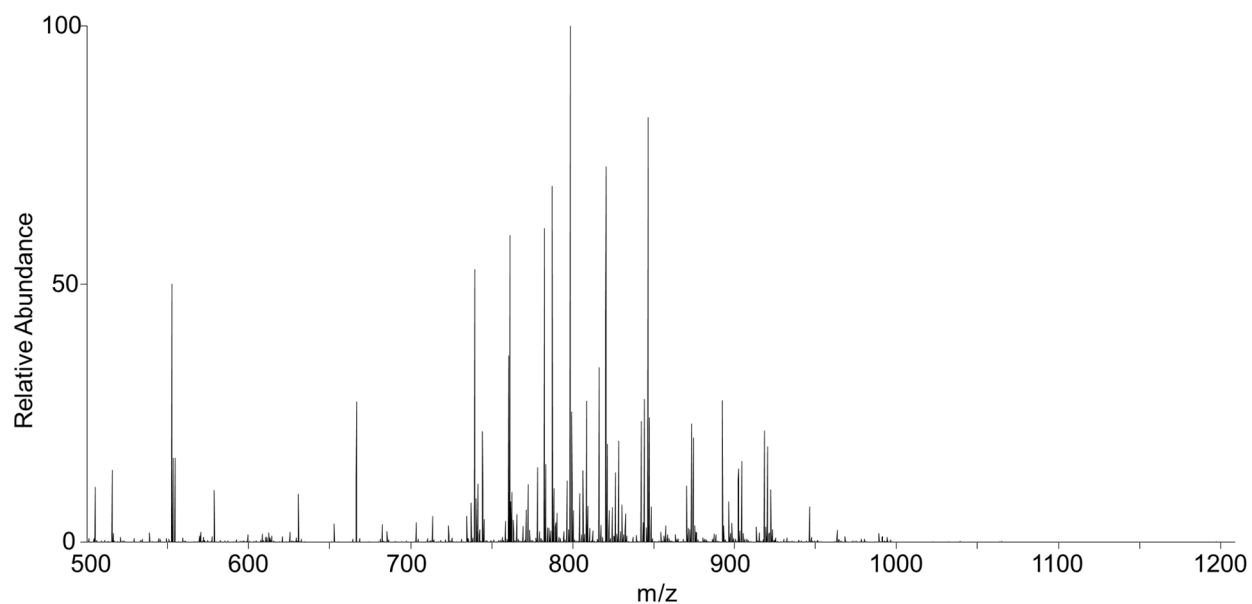
Figure 3.6. Mass spectrum averaged from the rat testis tissue analyzed at 3 μm spatial resolution in transmission geometry. After deisotoping the data, there are 255 peaks above a signal-to-noise threshold of 3. High spatial resolution IMS allows for fine structural detail in resulting ion images by analyzing small regions of tissue, but smaller sampling areas often lead to lower overall signal-to-noise. Here, even though we obtain high spatial resolution IMS, the number of species detected on a high mass resolution platform allows for many ion images with different localization and/or high signal-to-noise.
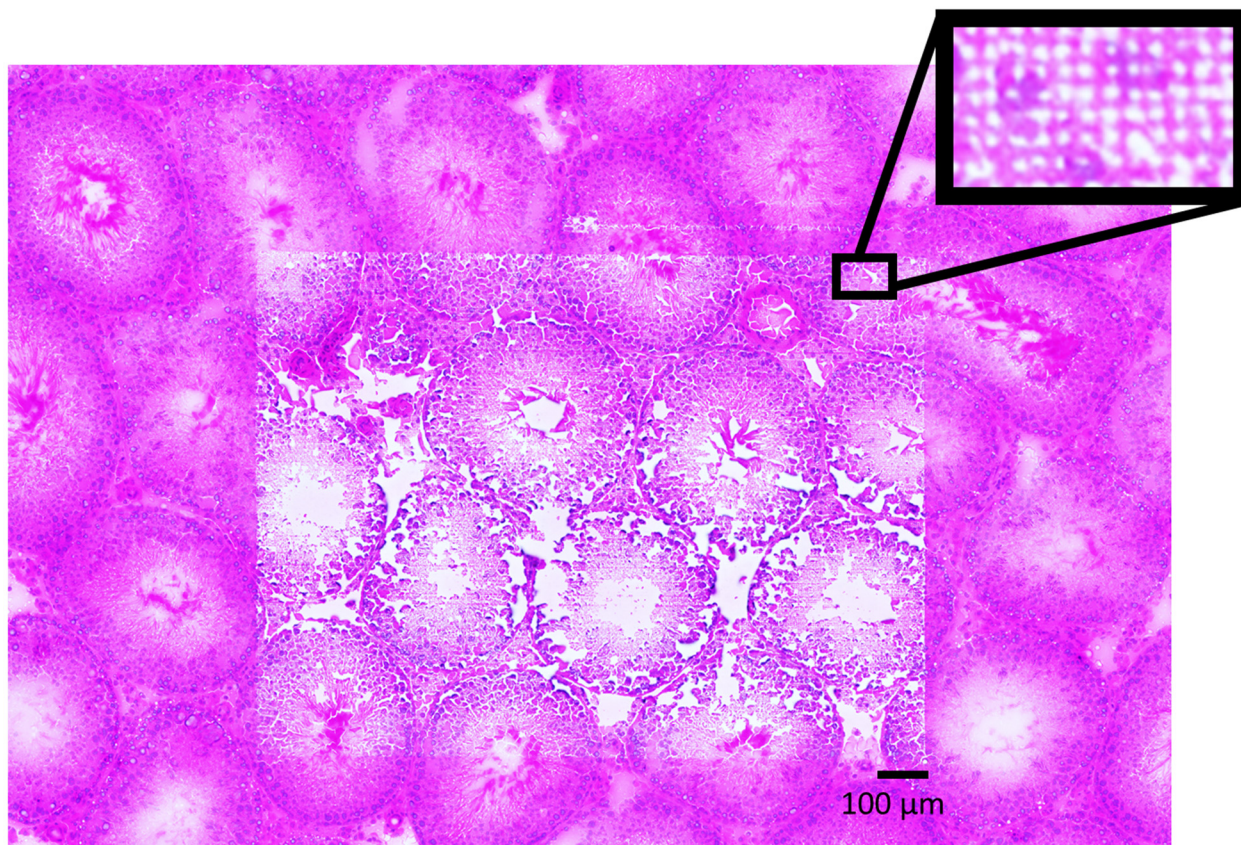
Figure 3.7. Rat testis tissue section after IMS acquisition at 3 µm spatial resolution with transmission geometry MALDI source, stained with H&E to visualize nuclei and cytoplasm, respectively. After IMS acquisition, MALDI matrix was removed, and the tissue section was stained with H&E. Inset shows ablation area after acquisition. Ample tissue is present after acquisition and ablation regions indicating that the laser ablation diameter is below 3 µm. Ablation marks are in a uniform grid pattern which highlights the capabilities of the high precision piezoelectric motors that allow for fine control of sample stage movement.
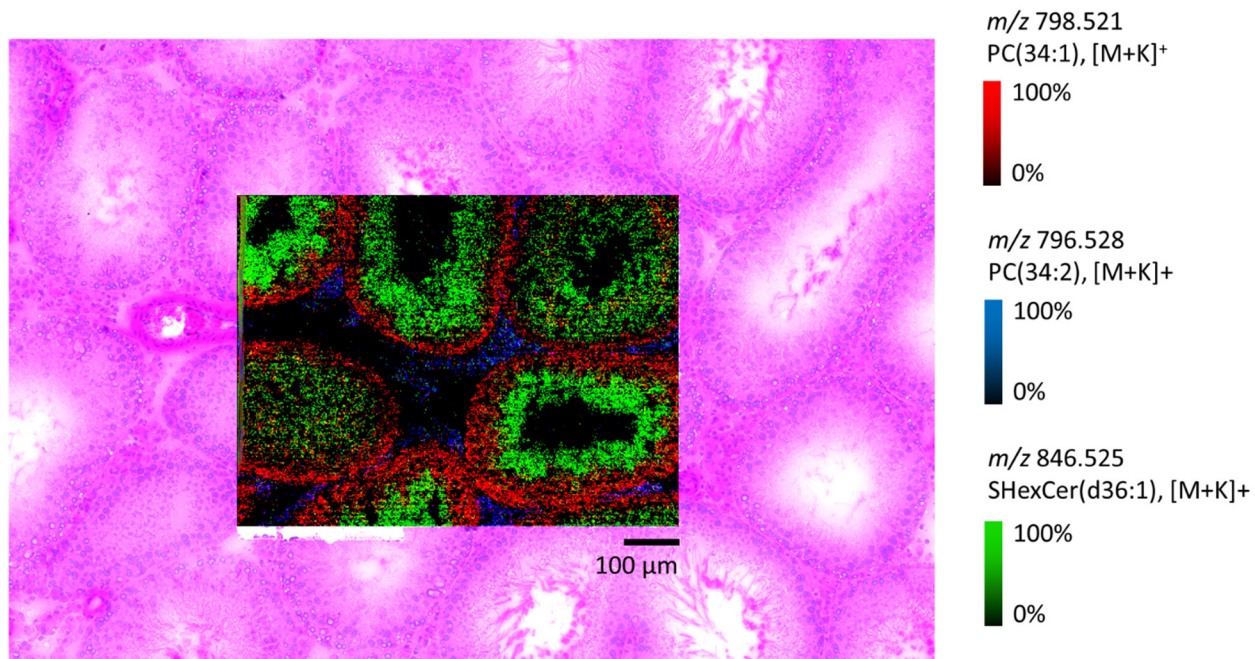
Figure 3.8. Rat testis tissue imaged at 2 µm spatial resolution using transmission geometry MALDI ion source. At 2 µm spatial resolution, finer image detail may be obtained compared with 3 µm IMS, but under these acquisition parameters (laser focus, laser energy) some oversampling artifacts are observed. The ion image has ~50% lower spectral intensity for lipids compared to that obtained at 3 µm, which is also an indication of oversampling. Nevertheless, high spatial resolution IMS at 2 µm is feasible with the custom transmission geometry source on a high mass resolution Orbitrap instrument.

A) 3 µm spatial resolution **B)** 10 µm spatial resolution

100 µm

m/z 798.540, 1.3 ppm error
PC(34:1), [M+K]⁺

100%

0%

m/z 796.525, 0.4 ppm error
PC(34:2), [M+K]+

100%

0%

m/z 846.539, 2.4 ppm error
PC(38:5), [M+K]+

100%

0%
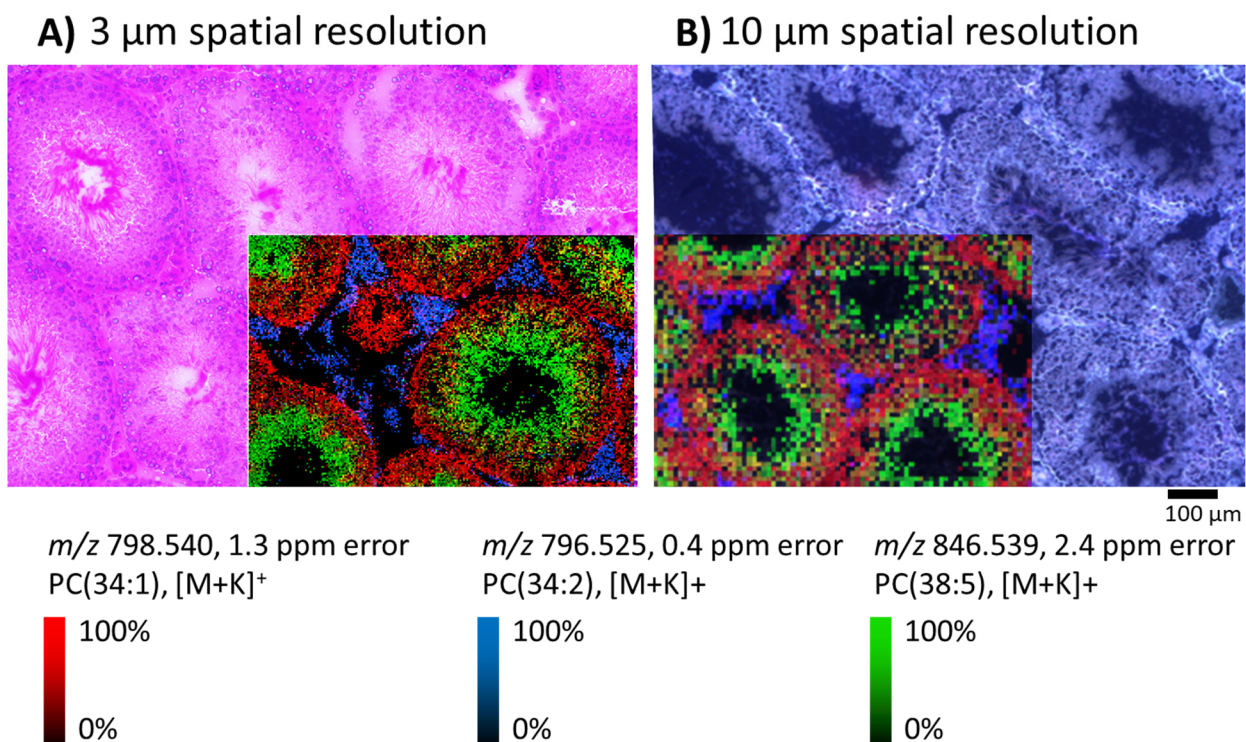
Figure 3.9. Comparison of spatial resolution between MALDI IMS acquisition at 3 µm spatial resolution using the custom transmission geometry ion source (**A**) and acquisition at 10 µm spatial resolution without oversampling using the front-side source (Spectroglyph LLC) (**B**) on the same instrument (Orbitrap Elite, Thermo). Ion images are overlaid onto the same tissue used for IMS either stained with H&E after acquisition (**A**) or overlaid onto the autofluorescence image obtained prior to MALDI acquisition (**B**). There is noticeable increase in ion image sharpness at 3 µm compared to acquisition at 10 µm spatial resolution. At 10 µm, the border between the seminiferous tubules (ion in red) and the interstitial Leydig cells (ion in blue) is indistinct (**B**) but acquisition at high spatial resolution using the transmission geometry source allows for us to see that there is a clear molecular difference between those two tissue regions for ions identified by accurate mass as potassiated PC(34:1) (*m/z* 798.540, 1.3 ppm error) and potassiated PC(34:2) (*m/z* 796.525, 0.4 ppm error) (**A**).

TG was developed for the Orbitrap system to allow for high spatial resolution and high mass resolution capabilities with MALDI-2 for good sensitivity. The Orbitrap was capable of a resolving power of up to 480k at *m/z* 400 and the TG source modifications allowed for sampling down to 1 µm in diameter. MALDI-2 was shown to increase signal significantly for lipids and may counteract the decrease in signal of high spatial resolution analysis. While MALDI-2 was beneficial for lipid signal enhancement, the enhancement seemed to be lipid class-dependent, so more research is needed to characterize the effect of MALDI-2 signal enhancement of lipids.

Acknowledgements

CHAPTER IV

EFFECT OF MALDI MATRICES ON LIPID ANALYSES OF BIOLOGICAL TISSUES USING MALDI-2 POST-IONIZATION MASS SPECTROMETRY

This work is adapted from Effect of MALDI matrices on lipid analyses of biological tissues using MALDI-2 postionization mass spectrometry published in the Journal of Mass Spectrometry and has been reproduced with the permission of my co-authors Jarod Fincher, Dustin Klein, Jeffrey Spraggins, and Richard Caprioli.

McMillen, JC, Fincher, JA, Klein, DR, Spraggins, JM, Caprioli, RM. Effect of MALDI matrices on lipid analyses of biological tissues using MALDI-2 postionization mass spectrometry. J Mass Spectrom. 2020; 55:e4663. https://doi.org/10.1002/jms.4663.

OVERVIEW

Laser post-ionization (MALDI-2) was developed for increased ion yield and sensitivity at high spatial resolution for lipids on a Orbitrap Elite instrument fitted with a custom transmission geometry source. However, the dependence of MALDI-2 performance on the various lipid classes is largely unknown. To understand the effect of the applied matrix on MALDI-2 analysis of lipids, samples including an equimolar lipid standard mixture, various tissue homogenates, and intact rat kidney tissue sections were analyzed using the following matrices: α-cyano-4-hydroxycinnamic acid (CHCA), 2',5'-dihydroxyacetophenone (DHA), 2',5'-dihydroxybenzoic acid (DHB), and norharmane (NOR). Lipid signal enhancement of protonated species using MALDI-2 technology varied based on the matrix used. From the four matrices tested, NOR provided the greatest increase in sensitivity for neutral lipids (triacylglycerol, diacylglycerol, monoacylglycerol, cholesterol ester) and DHB provided the highest overall number of lipids detected using MALDI-2 technology. DHB matrix was used to analyze pancreas sections from human non-diabetic and type 2 diabetic donors.

INTRODUCTION

Attempts to increase sensitivity of MALDI IMS have led to the development of multiple targeted and untargeted technologies. Targeted methods such as chemical tagging using photocleavable mass tags or in-source reactive tags have allowed for up to 40-fold increase in ion

yields.[107–110] Nevertheless these methods are targeted and only provide improvements for molecules with specific chemical functionality. Instrumental approaches to increase in signal in MALDI experiments include the continuous accumulation of selected ions (CASI) prior to detection as well as selected ion ejection (SIE) in an FT-ICR instrument.[111] Non-tagging approaches to increase sensitivity include the development of novel matrices,[44,112,113] the incorporation of chemical additives to matrices, removal of interfering species from tissue sections by organic solvents and aqueous washes[105,106], and use of laser wavelengths that better match the absorption bands of the matrices.[114] As an example, adding 2-hydroxy-5-methoxybenzoic acid to 2,5-dihydroxybenzoic acid (DHB) allowed for a 3-fold increase in signal-to-noise (S/N) for oligosaccharides compared to DHB alone.[115]

While MALDI allows for high spatial resolution sampling of tissue surfaces with good sensitivity, mostly neutral molecules are desorbed with low overall ion yields.[24,116,117] To address this, a technology termed laser post-ionization (MALDI-2) capitalizes on the abundance of neutrals in the initial MALDI desorption plume to generate additional ions.[29] For clarity, we will term the traditional MALDI event MALDI-1 and the combination experiment of MALDI-1/MALDI-2 simply as MALDI-2. Briefly, the MALDI-2 process utilizes a secondary laser aligned ~ 400 μm above the primary MALDI-1 ablation surface so that the secondary laser pulses intersect the primary MALDI-1 desorption plume at a given delay time, resulting in ionization of some of the desorbed neutrals.[26,27,30,118–122] The MALDI-2 ionization process is thought to result from a two-photon ionization threshold mechanism that gives rise primarily to protonated species.[29,30,33,123] MALDI-2 has been shown to improve ion yields by more than two orders of magnitude for some, but not all, lipid classes.[29,30,33] Additionally, the increase in ion intensity has enhanced conditions needed for ultra-high spatial resolution MALDI imaging applications.[27]

Although the enhanced performance observed with MALDI-2 has been reported, much more needs to be done to further characterize this technology. For example, the difference in the overall molecular coverage between MALDI-1 and MALDI-2 has not yet been fully studied. Thus far, MALDI-2 has proven to improve sensitivity for certain molecular classes including liposoluble vitamins, mono- and oligosaccharides, certain lipid classes, and exogenous drugs.[26,27,29–31,120–124] Lipid classes that have been shown to have dramatically increased ion intensities in positive ion mode include hexosylceramides (HexCers), phosphatidylethanolamines (PEs),

phosphatidylinositols (PIs), phosphatidylglycerols (PGs), phosphatidylserines (PSs), triacylglycerols (TGs), and cholesterol esters (CEs).[29] Interestingly, other classes of lipids such as phosphatidylcholines (PCs) were not shown to increase significantly with MALDI-2. In addition, recent work by Boskamp and Soltwisch has demonstrated ion suppression and ion promotion effects among different lipid classes with MALDI-2.[123] Overall, these data suggest a significant lipid-class dependence for MALDI-2 experiments.

The choice of matrix is known to affect desorption/ionization upon laser ablation for MALD-1 analyses, but no studies have been reported that systematically investigate the influence of various matrices with MALDI-2 for lipid analyses. Matrices that have been used most commonly for MALDI-2 analysis include α-cyano-4-hydroxycinnamic acid (CHCA), 2',5'-dihydroxyacetophenone (DHA), 2',5'-dihydroxybenzoic acid (DHB), and norharmane (NOR). To understand the effect of matrix on detection of lipid classes with MALDI-2, we examined sensitivity and lipid coverage using a variety of samples: an equimolar lipid standard mixture, rabbit adrenal gland, rat brain, rat kidney, and rat liver tissue homogenates. The four matrices listed above were used for these analyses, and each sample was analyzed both with MALDI-1 and MALDI-2. This study lays the groundwork for improved, standardized methods for MALDI-2 analysis and the findings allow for tuning of matrix choice to maximize sensitivity for specific lipid classes.

METHODS

Materials and methods

Lipid standards were purchased from Avanti Polar Lipids (Alabaster, AL, USA) as EquiSPLASH LIPIDOMIX Quantitative Mass Spec Internal Standard containing a methanol solution of 100 µg/mL of each of thirteen deuterated lipids of following lipid classes: phosphatidylcholine (PC), lysophosphatidylcholine (LPC), phosphatidylethanolamine (PE), lysophosphatidylethanolamine (LPE), phosphatidylglycerol (PG), phosphatidylinositol (PI), phosphatidylserine (PS), triacylglycerol (TG), diacylglycerol (DG), monoacylglycerol (MG), cholesterol ester (CE), sphingomyelin (SM), and ceramide (Cer). Ammonium formate and the MALDI matrices DHA, DHB, CHCA, and NOR were purchased from MilliporeSigma (Burlington, MA, USA). The matrices DHA, DHB, and CHCA were purified via recrystallization in-house prior to use. Acetonitrile (ACN) and methanol (MeOH) were purchased from Fisher

Scientific (Pittsburgh, PA, USA) and water (H_2O) of 18.2 MΩ·cm resistivity was obtained from a Milli-Q Reference Water Purification System (MilliporeSigma, Burlington, MA, USA). The lipid standard mixture was prepared by mixing 100 µL lipid solution with 4 mg matrix in 1 mL MeOH for each of the four matrices. The matrix and lipid combination was sprayed onto indium-tin oxide (ITO)-coated glass slides (Delta Technologies, Loveland, CO, USA) using the TM Sprayer (HTX Technologies, Chapel Hill, NC, USA) with a solvent flow rate of 0.05 mL/minute, 16 passes, 1350 mm/s velocity, and 60°C nozzle temperature.

Tissue samples of rabbit adrenal gland, rat brain, rat kidney, and rat liver were obtained from BioIVT (Baltimore, MD, USA). Tissue homogenates were prepared as described by Groseclose and Castellino.[55] Tissue sections and tissue homogenates were stored frozen at -80°C, sectioned at 10 µm thickness at -20°C (Leica CM3050, Leica Biosystems, Buffalo Grove, IL, USA), thaw-mounted onto ITO-coated glass slides, washed in a solution of 50 mM ammonium formate for 30 seconds, and dried under a stream of nitrogen.[41] Matrix solutions for coating tissue homogenates were prepared for CHCA (5 mg/mL, 80:20, ACN:H_2O), DHA (15 mg/mL, 90:10, ACN:H_2O), DHB (20 mg/mL, 90:10, MeOH:H_2O), and NOR (5 mg/mL, 90:10, MeOH:H_2O) and sprayed with the TM Sprayer with a solvent flow rate of 0.05 mL/minute, 16 passes, 1350 mm/s velocity, and 60°C nozzle temperature. Autofluorescence microscopy images were obtained prior to matrix application with EGFP, DAPI and DsRed filters using a Zeiss AxioScan Z1 slide scanner (Carl Zeiss Microscopy GmbH, Germany).

Instrument/acquisition parameters

Samples were analyzed using an Orbitrap Elite (Thermo Scientific, San Jose, CA) mass spectrometer equipped with a Spectroglyph MALDI-1 ion source (Spectroglyph LLC., Kennewick, WA). The Spectroglyph source was equipped with a MALDI-2 laser for post-ionization as described previously.[31] Briefly, the MALDI-2 laser (266 nm, FQSS266-200-STA, CryLaS GmbH, Berlin, Germany) is aligned parallel to the sample surface to irradiate the MALDI-1 plume at ~400 µm above the sample surface. A delay time was set to be 20 µs between the MALDI-1 and MALDI-2 laser pulses. MALDI-2 energy was set to 150 µJ. The mass spectrometer was operated at a resolving power of 120,000 at *m/z* 400 with 1 microscan. IMS of a tissue homogenate and rat kidney tissue section were obtained with 20 µm spatial resolution with a mass range of *m/z* 400-1500. Spectra for lipid standards were obtained in full profile mode where 20

spectra were averaged from line scans at 20 μm spatial resolution. Grids of ~500 pixels were obtained with MALDI-1 and MALDI-2 from adjacent regions of the tissue homogenates for comparison. An averaged spectrum generated from the grid above was used for subsequent lipid identification based on accurate mass measurement. Technical replicates of tissue homogenates were prepared and analyzed on separate days.

Data analysis

Thermo RAW files were opened in Xcalibur Qual Browser and the spectra over the time of the image were averaged and imported into the spectral processing software mMass (mmass.org,).[125] A signal-to-noise (S/N) threshold was manually set to 3x above the baseline noise level observed for each experiment. Tissue homogenate spectra were processed by removing isotopes and linearly recalibrating the mass axis. Spectra were annotated and lipids were identified by accurate mass measurements using a mass accuracy of +/- 2 ppm based on a custom reference mass list including PC, LPC, PE, LPE, SM, CE, Cer, HexCer, Cholesterol, MG, DG, TG, PA, PG, PI, and PS lipid classes. Identified lipids and their intensities were exported via the "Analysis Report" feature and were compared using Microsoft Excel (Version 1902, Redmond, WA, USA). IMS data of rat kidney tissue was converted to vendor-neutral imzML data format using ImageInsight (Spectroglyph, LLC., Kennewick, WA, USA) and imported to SCiLS (2019c, Bruker Daltonics, Billerica, MA) for visualization of ion images. Processing of ion images in SCiLS included hotspot removal and RMS normalization.

RESULTS AND DISCUSSION

Analysis of lipid standards

To explore the effect of the MALDI matrix on the ionization of different lipid classes by MALDI-2, an equimolar mixture of deuterated lipid standards, each of which represents a different lipid class, was analyzed by both MALDI-1 and MALDI-2 in positive ion mode. The lipid mixture contained PC(15:0/18:1 d7), PE(15:0/18:1 d7), PS(15:0/18:1 d7), PG(15:0/18:1 d7), PI(15:0/18:1 d7), LPC(18:1 d7), LPE(18:1 d7), CE(18:1 d7), MG(18:1 d7), DG(18:1 d7), TG(18:1 d7), SM(18:1/18:1 d7), and Ceramide (d18:1 d7/15:0). Matrices CHCA, DHA, DHB, and NOR were chosen for this study as they comprise the majority of matrices used in published reports of MALDI-2 analyses.[27,29,30,126] For MALDI-1, the spectra were typically dominated by PC, LPC,

and SM lipid classes as demonstrated in the overview spectra, as is typical for MALDI-1 analysis as the PC and SM head groups are positively charged and are detected readily in positive ion mode.[123,127] For MALDI-2, protonated lipid species show the greatest increase in signal intensity, whereas most of the sodium- and potassium-adducted lipids do not dramatically increase. Therefore, our analysis is focused on enhancement of protonated forms of lipids. **Figures 4.1** and **4.2** show expanded MALDI-1 (black) and MALDI-2 (red) spectra for protonated PC, PE, PG, PI, and TG lipid standards. Intensity comparisons among matrices show CHCA and DHB give similar intensity profiles for MALDI-2 spectra (within 3x) (**Figures 4.1** and **4.3**). MALDI-1 and MALDI-2 lipid intensity profiles are similar using DHA and NOR for most lipid standards except for non-polar species. None of the non-polar lipid standards (TG, DG, MG and CE) were detected with DHA using either MALDI-1 or MALDI-2. On the other hand, all were detected using MALDI-2 with NOR (**Figures 4.2** and **4.4**).
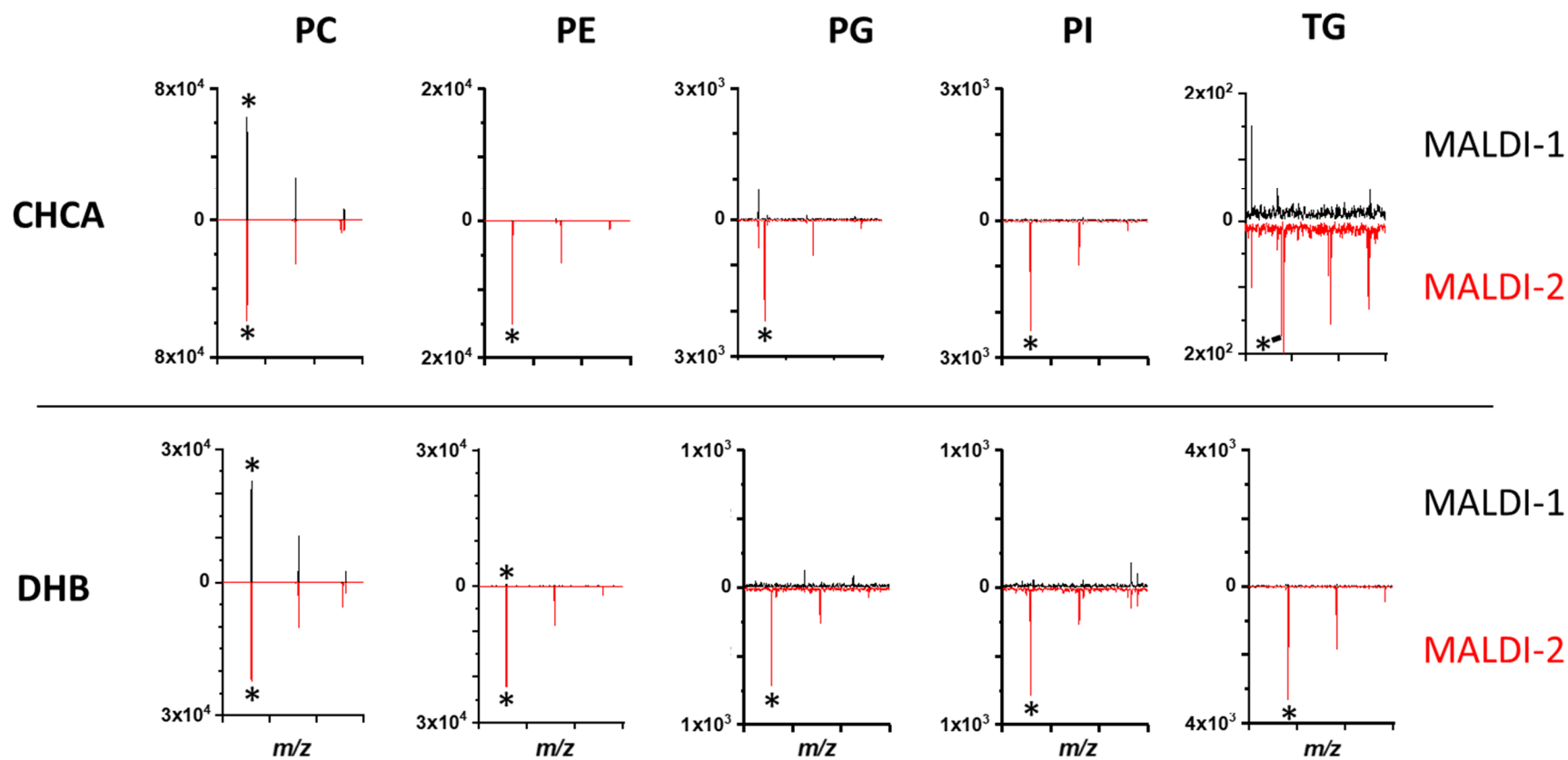
Figure 4.1. Spectra of the lipid standard mixture expanded to show enhancement of protonated species for deuterated PC, PE, PG, PI, and TG lipid standards for CHCA and DHB matrices. MALDI-1 spectra are shown in black traces (top), MALDI-2 are the red traces (bottom), and the intensity scale is the same for each pair of MALDI-1 and MALDI-2 spectra. The presence of an asterisk indicates that the lipid standard was detected. The absence of an asterisk means lipid was not detected with S/N value greater than 3 (see also **Table 4.1**)
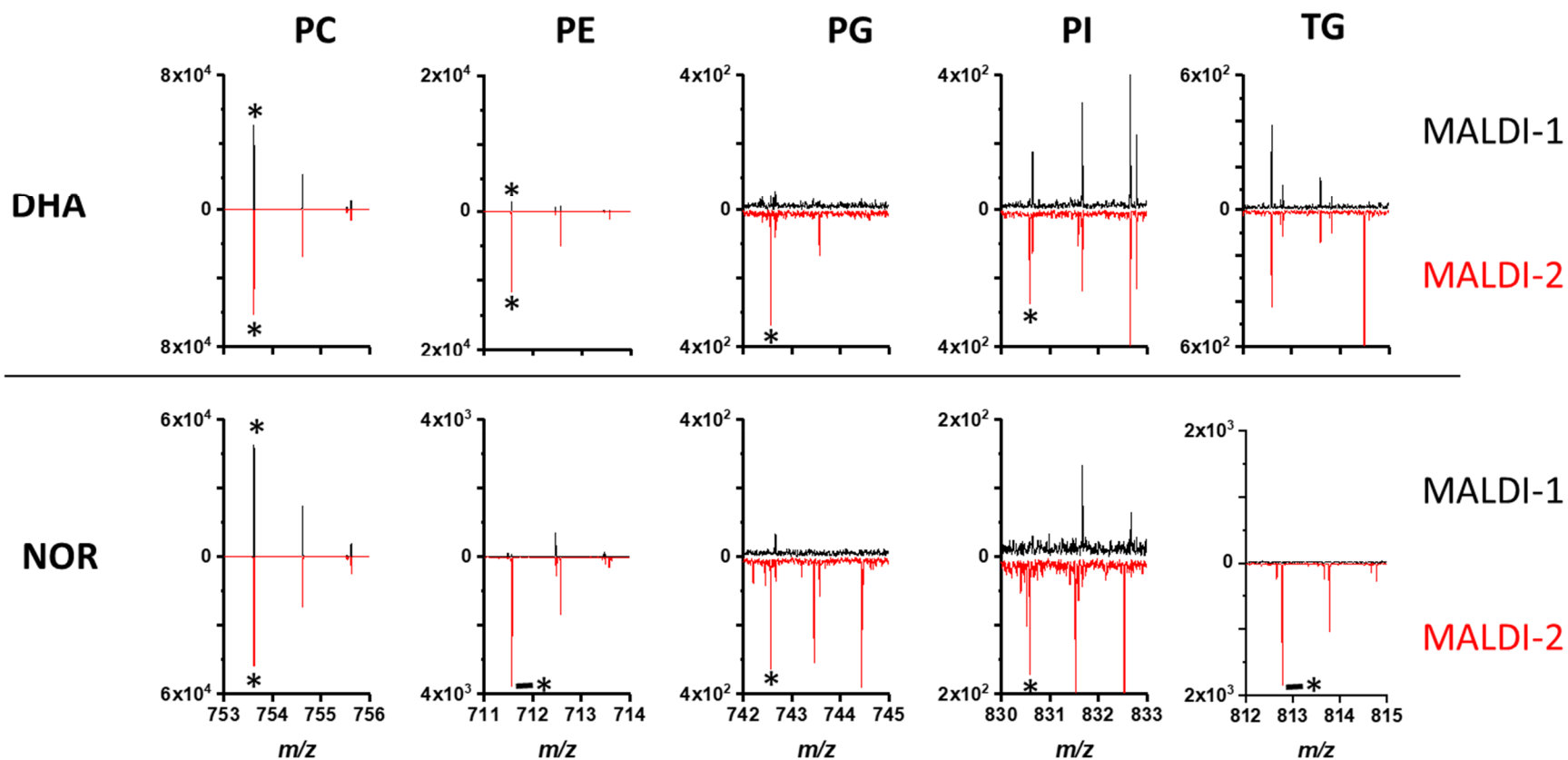
Figure 4.2. Spectra of the lipid standard mixture expanded to show enhancement of protonated species for deuterated PC, PE, PG, PI, and TG lipid standards for DHA, and NOR matrices. MALDI-1 spectra are shown in black traces (top), MALDI-2 are the red traces (bottom), and the intensity scale is the same for each pair of MALDI-1 and MALDI-2 spectra. The presence of an asterisk indicates that the lipid standard was detected. The absence of an asterisk means lipid was not detected with S/N value greater than 3 (see also **Table 4.1**)
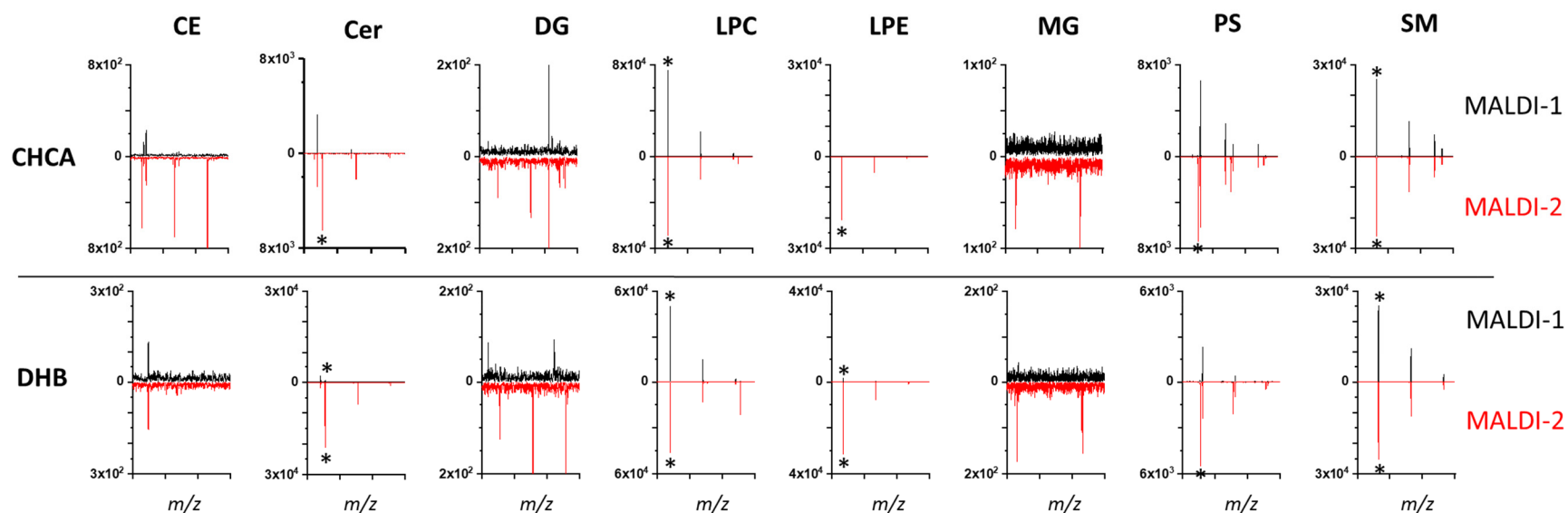
Figure 4.3. Spectra of lipid standard mixture expanded to show enhancement of protonated species for deuterated CE, Cer, DG, LPC, LPE, MG, PS, and SM lipid standards for CHCA and DHB matrices. MALDI-1 spectra are the black traces (top), MALDI-2 are the red traces (bottom), and the intensity scale is the same for each pair of MALDI and MALDI-2 spectra. The presence of an asterisk indicates that the lipid standard was detected. The absence of an asterisk means lipid was not detected with S/N value greater than 3 (see also **Table 4.1**).
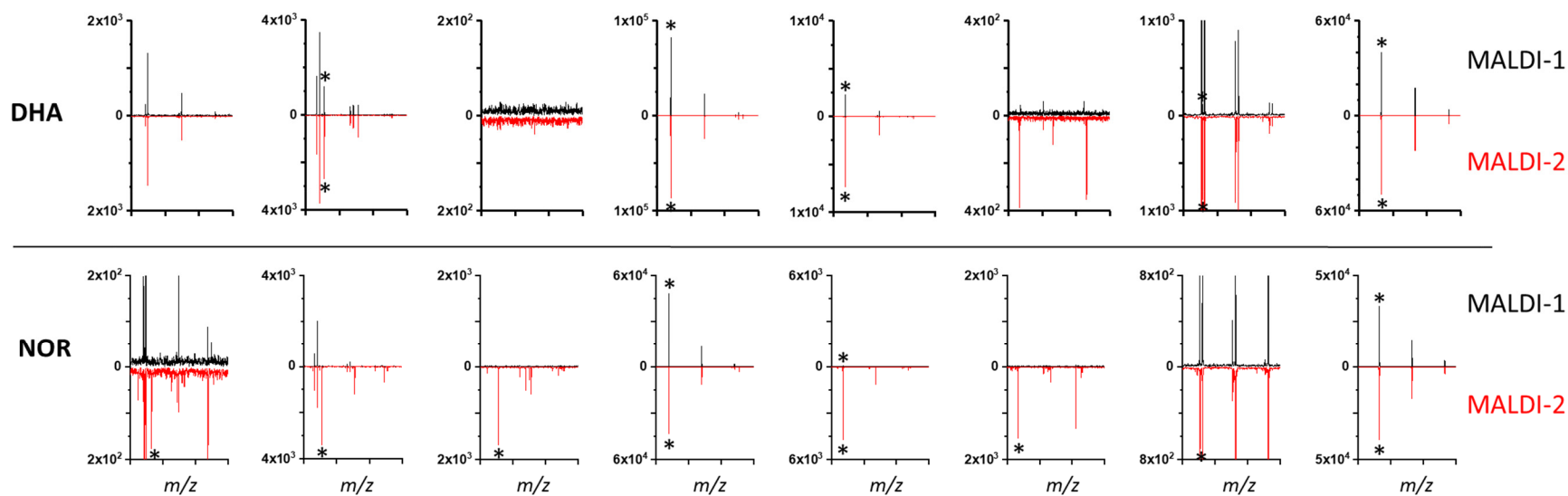
Figure 4.4. Spectra of lipid standard mixture expanded to show enhancement of protonated species for deuterated CE, Cer, DG, LPC, LPE, MG, PS, and SM lipid standards for DHA and NOR matrices. MALDI-1 spectra are the black traces (top), MALDI-2 are the red traces (bottom), and the intensity scale is the same for each pair of MALDI and MALDI-2 spectra. The presence of an asterisk indicates that the lipid standard was detected. The absence of an asterisk means lipid was not detected with S/N value greater than 3 (see also **Table 4.1**).

Overall, MALDI-2 was found to have significantly increased molecular coverage for most protonated lipids for all matrices tested (CHCA, DHA, DHB, and NOR). Lipid classes such as PI, PS, and PG were detected as the protonated form with MALDI-2 for all matrices. Additionally, MALDI-2 enabled the detection of protonated TG using CHCA, DHB, and NOR (**Figures 4.1** and **4.2**) and protonated forms other non-polar species (MG, DG, and CE) with NOR (**Figure 4.4**). This contrasts with MALDI-1 analysis where neutral lipid classes are typically detected as sodiated adducts in positive ion mode. Improvements in sensitivity from MALDI-2 were matrix- and lipid class-dependent for the lipid standards and results are summarized in **Table 4.1**. Data presented in **Table 4.1** indicate the S/N fold change between MALDI-1 and MALDI-2 for lipids detected in both cases. Species that are only detected with MALDI-2 are noted with an asterisk (*) and lipids not detected with either MALDI-1 or MALDI-2 are denoted with "ND".

The standards of PC, LPC, and SM lipid classes had no significant difference in intensity with MALDI-2. In contrast, all other lipid classes detected showed a significant increase in intensity when MALDI-2 was activated. One benefit of positive ion mode analysis by MALDI-2 is the detection of lipid species typically only observed in negative ion mode only such as PI, PS, PG. Recent work by Boskamp and Soltwisch has shown that MALDI-2 may correct for ion suppression effects to enable detection of these protonated species.[123] MALDI-2 increased protonated lipid coverage with all matrices but the species detected with MALDI-2 varied based on the matrix. The TG species, for example, was detected only with MALDI-2 for CHCA, DHB, and NOR but was not detected with DHA. Note, although the intact molecular ions for protonated TGs, DGs, and MGs were detected in certain cases, we do detect $[DG+H-H_2O]^+$ and $[MG+H-H_2O]^+$ with greater intensity. These ions are likely the result of MALDI-induced fragmentation of the corresponding protonated TGs and DGs. Lipids DG, MG, and CE were only detected with NOR matrix with MALDI-2. In contrast, species such as PG and PI were detected for all matrices, but only with MALDI-2.

Table 4.1. Fold change intensity increase (numbers in cells) with MALDI-2 for protonated lipid standards in mixture. Fold change spans from lowest (red cells) to highest (green cells). "ND" in a white cell denotes detected neither with MALDI-1 nor with MALDI-2. An asterisk (*) denotes species only detected with MALDI-2.

Fold change increase for MALDI-2

Lipid Standard	Matrix			
	CHCA	DHA	DHB	NOR
PC(15:0/18:1) d7[M+H]+	1	1	1	1
LPC(18:1) d7[M+H]+	1	1	1	1
PE(15:0/18:1) d7[M+H]+	*	8	47	*
LPE(18:1) d7[M+H]+	*	3	20	44
PG(15:0/18:1) d7[M+H]+	*	*	*	*
PI(15:0/18:1) d7[M+H]+	*	*	*	*
PS(15:0/18:1) d7[M+H]+	*	7	*	*
TG(15:0/18:1) d7[M+H]+	*	ND	*	*
DG(15:0/18:1) d7[M+H]+	ND	ND	ND	*
MG(18:1) d7[M+H]+	ND	ND	ND	*
CE(18:1) d7[M+H]+	ND	ND	ND	*
SM(d18:1/18:1) d9[M+H]+	1	1	1	1
C15 Ceramide-d7[M+H]+	*	2	30	*

Fold change increase with MALDI-2

1   47

ND = not detected
* = Only detected with MALDI-2

From the study of lipid standards, NOR provided the broadest coverage for protonated lipids with MALDI-2 whereas DHB provided for the largest fold change increase for PE lipids. One explanation for the discrepancy in performance among matrices may be based on their absorption profile. Initial experiments by Soltwisch et al. show that PE lipid signal is laser wavelength- and pulse energy-dependent.[29] Note, the MALDI-2 laser pulse energy for our studies is lower than what has been used recently by the Ellis group (150 µJ vs. 500 µJ), as limited by the maximum energy output for the laser.[33] Early studies showed that a dramatic increase in signal could be produced with MALDI-2 while operating MALDI-1 energy at or below the ionization threshold,.[30,31] Here, we operated the MALDI-1 laser well above the ionization threshold to obtain maximum lipid signal without MALDI-2. Therefore, any increase in number lipids detected with MALDI-2 activated are in addition to what is already detectable with MALDI-1 alone.

Improved lipid intensity using MALDI-2 was observed for all matrices in the analysis of standards, but the lipid class coverage was matrix dependent. NOR was the only matrix that enabled all classes in the lipid standard to be detected in the protonated form using MALDI-2. While the lipid standards mixture analysis provides confirmation that MALDI-2 enhances sensitivity for lipid classes that are not typically detected in their protonated form (PG, PI, PS, TG, MG, DG), it does not accurately represent the complex mixture of lipids detected during tissue analysis. Tissue homogenates from rabbit adrenal gland, rat brain, rat kidney, and rat liver were analyzed to obtain representative results from tissue.

Lipidomic comparisons across multiple tissue types

To evaluate the performance of matrices with MALDI-2 for a complex, broad range of lipids, homogenates of various tissues were analyzed. Tissue homogenates help to reduce possible spatial heterogeneity while maintaining the overall lipid, protein, and salt compositions of tissues. As a result, tissue homogenates are commonly used for generating calibrations curves that enable *in situ* quantitative analysis, and as a means to optimize tissue IMS sample preparation.[128–133] For the studies described herein, tissue homogenates were used to minimize variability between MALDI-1 and MALDI-2 for each of the tested matrices and tissue types. Tissue and tissue homogenates were washed with ammonium formate to reduce salt content and to increase overall lipid signal for MALDI-1 and MALDI-2. Examples of the results of washing are shown in **Figure 4.5** with washed and unwashed rat testis tissue sections analyzed by MALDI-1 and MALDI-2. Intensity of protonated lipid species increase in positive ion mode while the salt adducted species decrease in intensity after washing.

Spectral comparisons of MALDI-1 and MALDI-2 are shown for washed rat brain and rat kidney homogenates for each of the four matrices (**Figure 4.6**). Spectral data from rabbit adrenal gland and rat liver tissue can be found in **Figure 4.7**. Average spectra for MALDI-1 alone are the black traces on the top of each pair and MALDI-2 average spectra are inverted along the x-axis (red traces). The intensity for each panel is scaled to the most intense peak from the pair of spectra for a given matrix and tissue homogenate combination. In general, MALDI-1 spectra for the tissue homogenates are dominated by PC and SM lipids and this is reflected in the spectral profiles as they are relatively similar among the matrices for MALDI-1 alone. In comparison with MALDI-2, MALDI-1 spectra for CHCA and DHA matrices have comparable signal intensity and spectral

66

features, and MALDI-2 does increase the number of species detected, but many of these species are relatively low in signal. In contrast, MALDI-2 for DHB and NOR show dramatic increases in both signal intensity and spectral complexity. MALDI-2 with NOR has been shown to produce many lipid-matrix adducts here and has been reported by others.[30] Here, we also observe intense lipid-NOR adducts between *m/z* 800-900 (**Figure 4.6**, NOR, brain and **Figure 4.7**) but matrix adducts are only minimally detected in spectra with the other matrices tested. Spectra were compared to a lipid reference list to determine total number of identified lipids for each experiment, based on accurate mass measurements within +/- 2 ppm error.
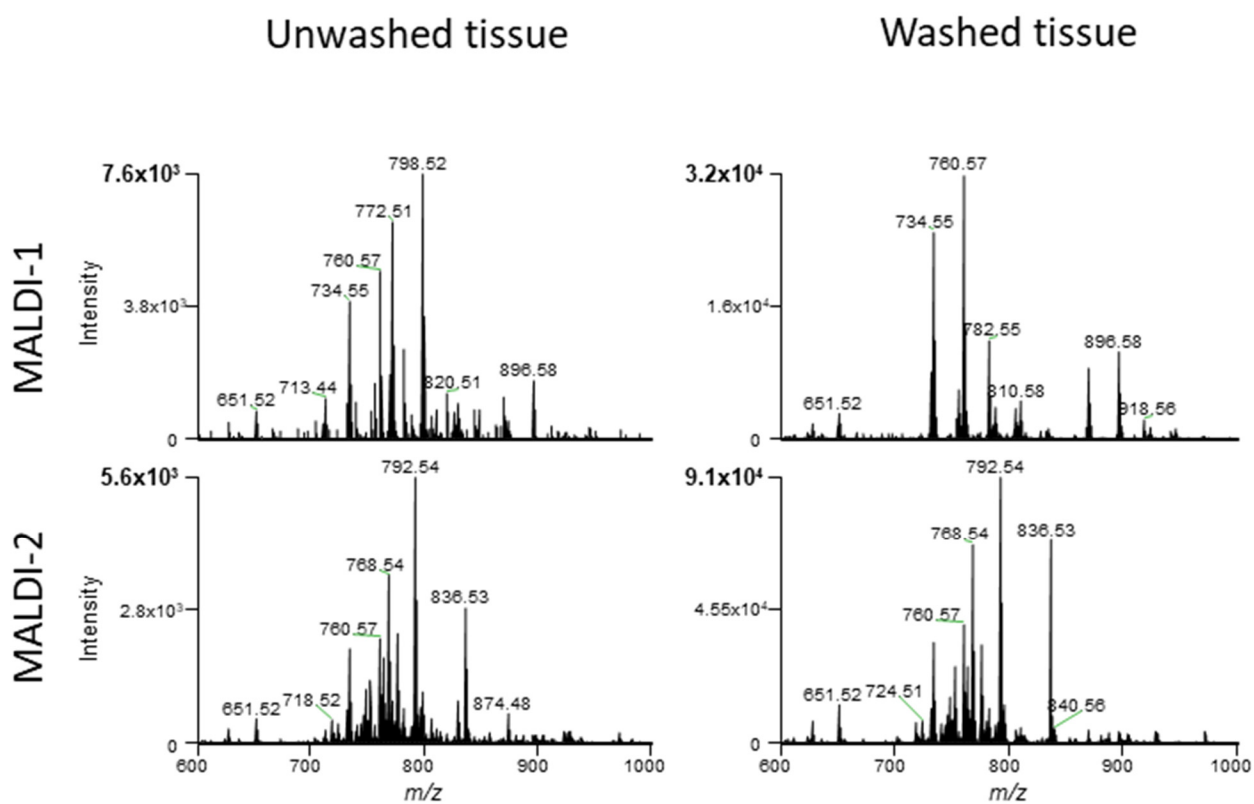
Figure 4.5. Mass spectra from rat testis that have either been washed with ammonium formate or unwashed, analyzed with MALDI-1 alone or with MALDI-2. Tissue washing allows for increased lipid signal by desalting to enhance the detection of protonated species and MALDI-2 allows for increased intensity of numerous lipids of various classes. Together, they afford a 12-fold increase in overall lipid signal compared to MALDI-1 of unwashed tissue.
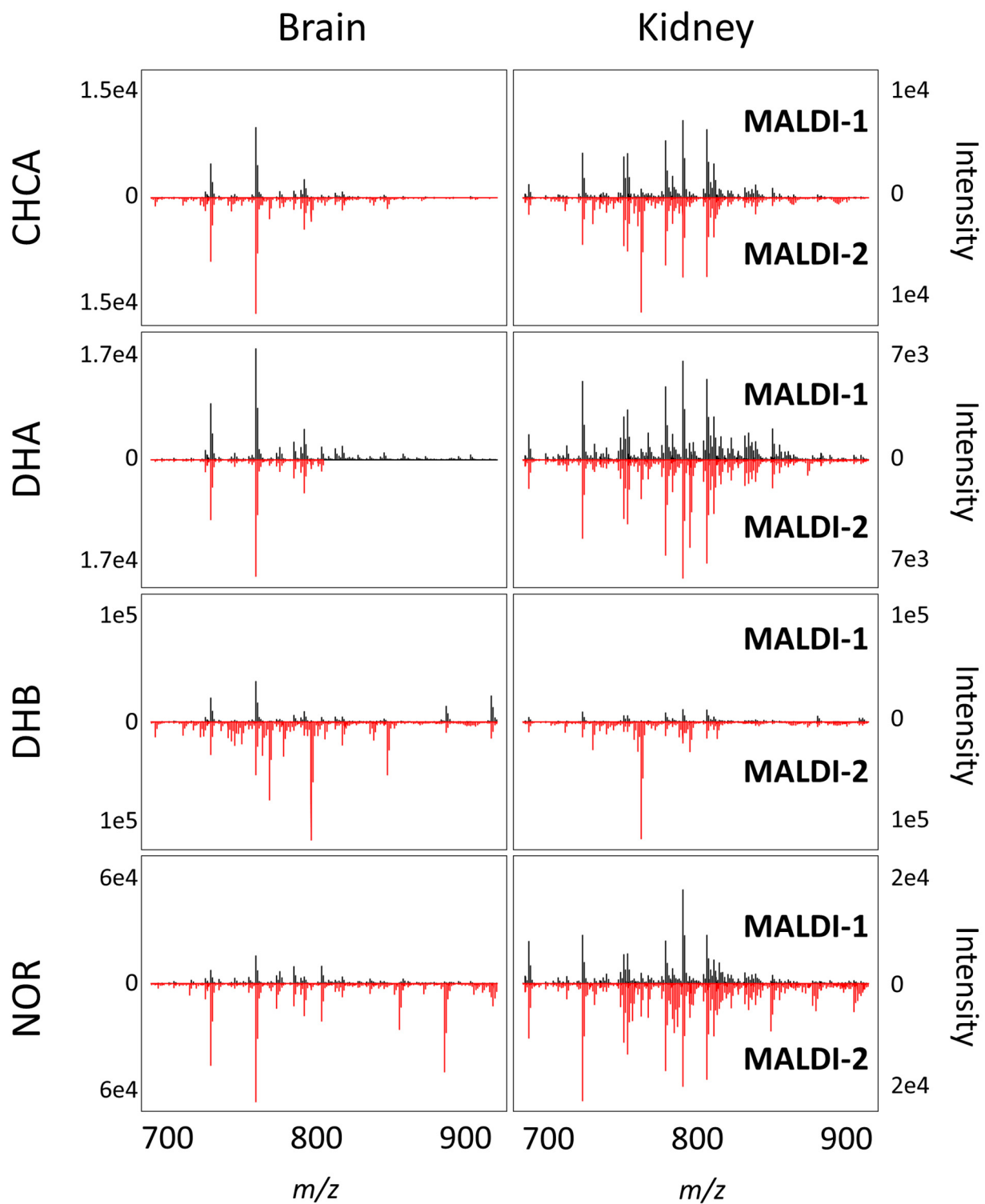
Figure 4.6. Overview spectra of rat brain and rat kidney tissue homogenates analyzed with MALDI-1 (black, top) and MALDI-2 (red, bottom) with CHCA, DHA, DHB, NOR matrices. Intensity is scaled to the base peak of MALDI-1 or MALDI-2 for each pair of spectra. Dramatic increases in lipid intensity are shown for MALDI-2.
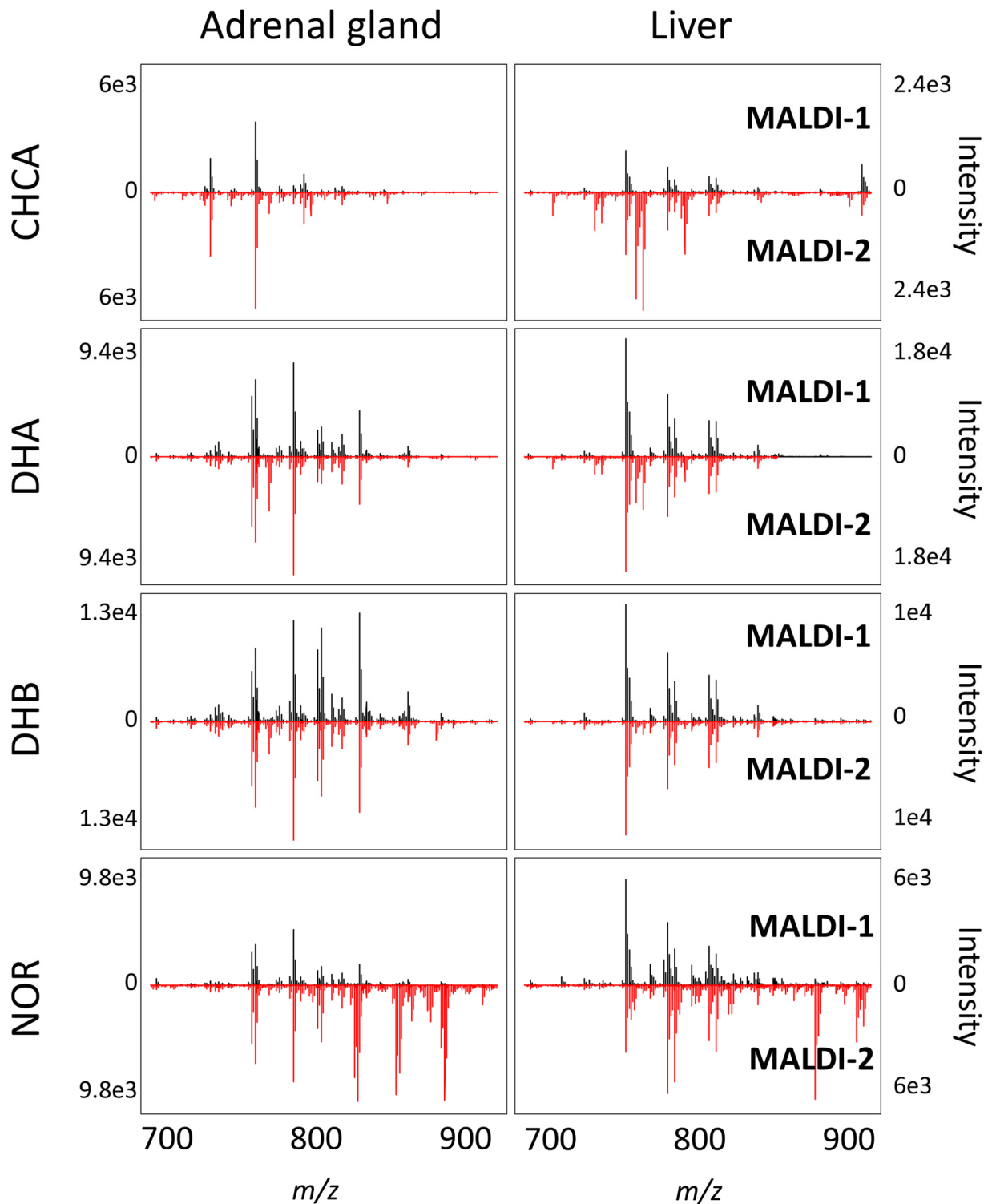
Figure 4.7. Overview spectra of rabbit adrenal gland and rat liver tissue homogenates analyzed with MALDI (black, top) and MALDI-2 (red, bottom) with CHCA, DHA, DHB, and NOR matrices. Intensity is scaled to the base peak of MALDI or MALDI-2 for each pair of spectra. Dramatic increases in lipid intensity with MALDI-2.

The total number of identified protonated lipids for each matrix and tissue homogenate was calculated as an average of the three technical replicates and is shown in **Figure 4.8** for MALDI-1 (blue bars) and MALDI-2 (red bars). Error bars represent the standard deviation for the three replicates. The matrices CHCA and DHB both provided larger average increases in number of identified lipids with MALDI-2 (65 ± 23 and 76 ± 12, respectively) compared to DHA and NOR (32 ± 13 and 27 ± 22, respectively). Note, these values were calculated by taking the average increase in the lipids detected for each matrix across all tissue types. These results indicate that the spectral complexity observed in the overview spectra with MALDI-2 is not simply a result of fragmentation or chemical noise but, at least in part, corresponds to an increase in sensitivity for lipids not commonly detected with MALDI-1 alone.

With more complex samples as with tissue homogenates, ion suppression effects based on lipid class may affect ion yield.[123] While NOR performed well with MALDI-2, DHB had the highest increase in lipids detected with MALDI-2 from the tissue homogenates compared with other matrices. The number of lipids detected in each lipid class for CHCA and DHA is displayed in **Figures 4.9** and **4.10**. Data from DHB and NOR matrices are shown in **Figure 4.11** and **4.12**. These data show the dramatic differences in ionization efficiency between the matrices. For example, MALDI-1 analysis of liver homogenate with DHB detects all lipid classes presented in **Figure 4.11** but with NOR only 6/13 lipid classes are detected (**Figure 4.12**). With MALDI-2, NOR provides a significant increase in most neutral lipid classes (CE, MG, DG, TG), as expected based on performance of lipid standard mixture. DHB provides greatly improved sensitivity for phospholipids (PC, PE, PS, PI, PA, LPC, LPE). This global comparison of lipidomic profiles from various tissue types for each of the MALDI-1 matrices tested suggests that DHB and NOR are best suited for MALDI-2 studies, depending on lipid classes of interest. Further, differences in MALDI-2 lipid profiles show that specific matrices can be chosen to improve sensitivity for specific lipid classes. For the matrices tested here, NOR is optimal for non-polar lipid studies and DHB is better applied to increase sensitivity of phospholipids.
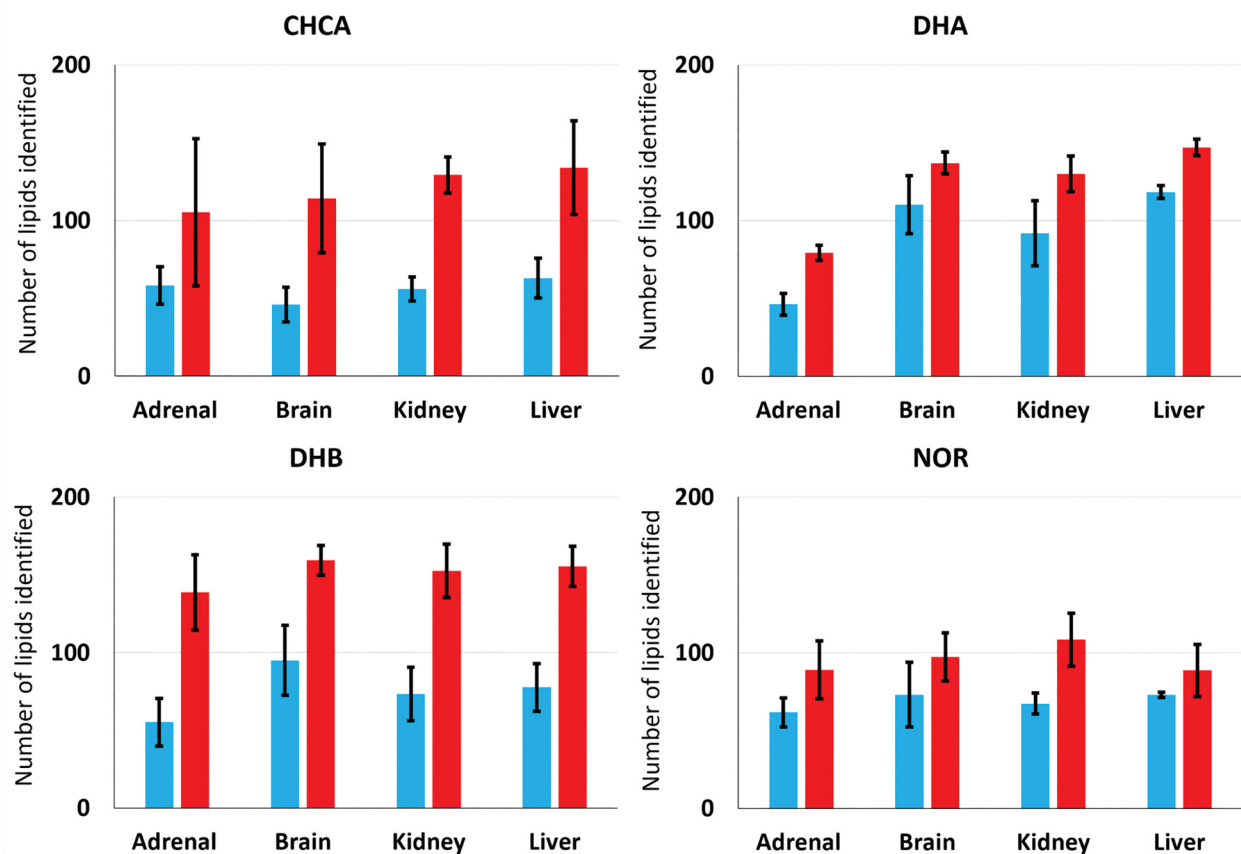
Figure 4.8. Bar graphs of total protonated lipids identified with MALDI-1 (blue bars) and MALDI-2 (red bars) for the CHCA, DHA, DHB, NOR matrices and rabbit adrenal gland, rat brain, rat kidney, and rat liver tissue homogenates. Error bars represent the standard deviation of three technical replicate experiments.
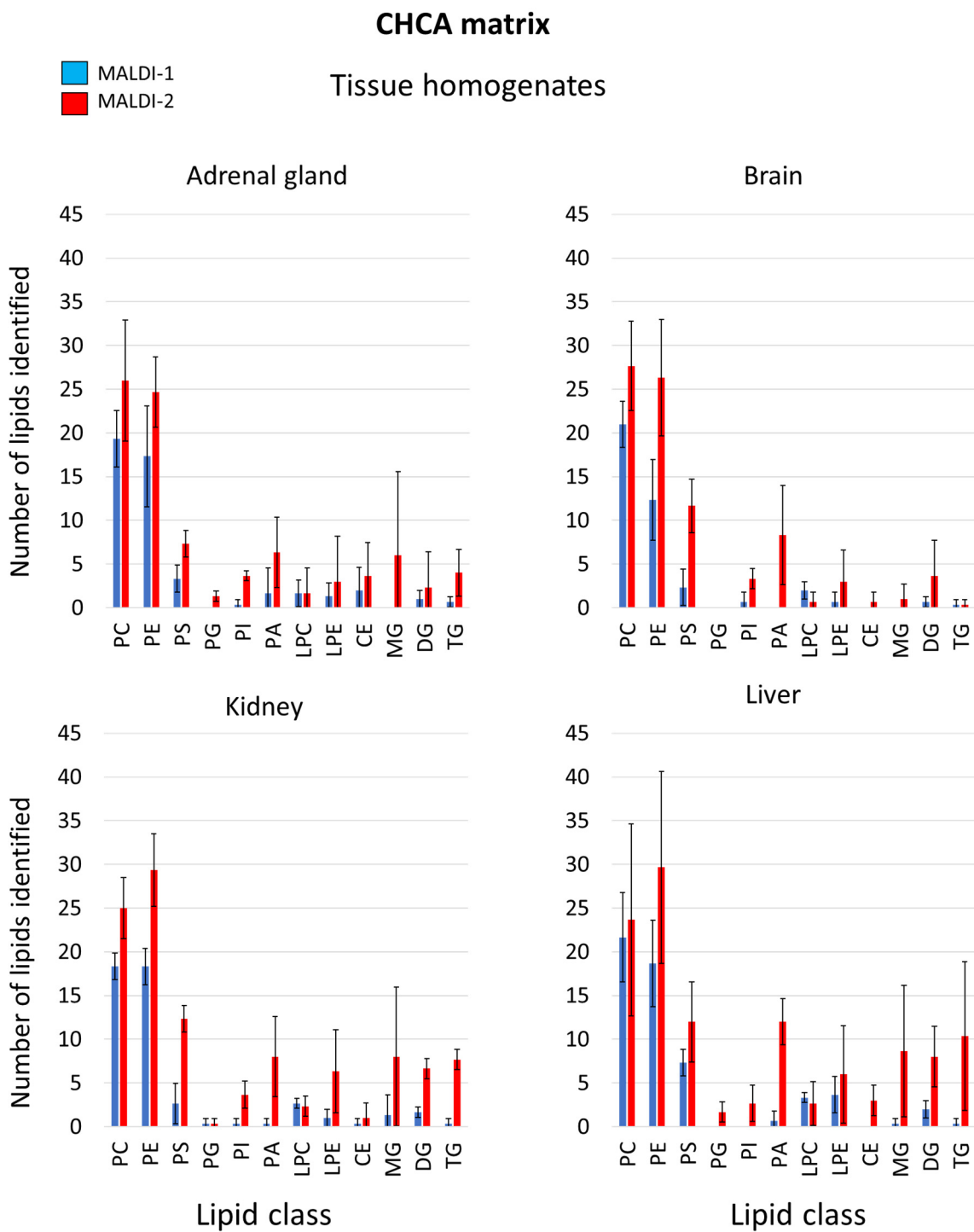
Figure 4.9. Number of protonated lipids identified per lipid class for CHCA matrix for each of four tissue homogenates analyzed with MALDI-1 (blue bars) and MALDI-2 (red bars). Error bars represent the standard deviation of three technical replicate experiments. Identifications were made by accurate mass measurements matched within 2 ppm error of a database of lipids.

DHA matrix

Tissue homogenates
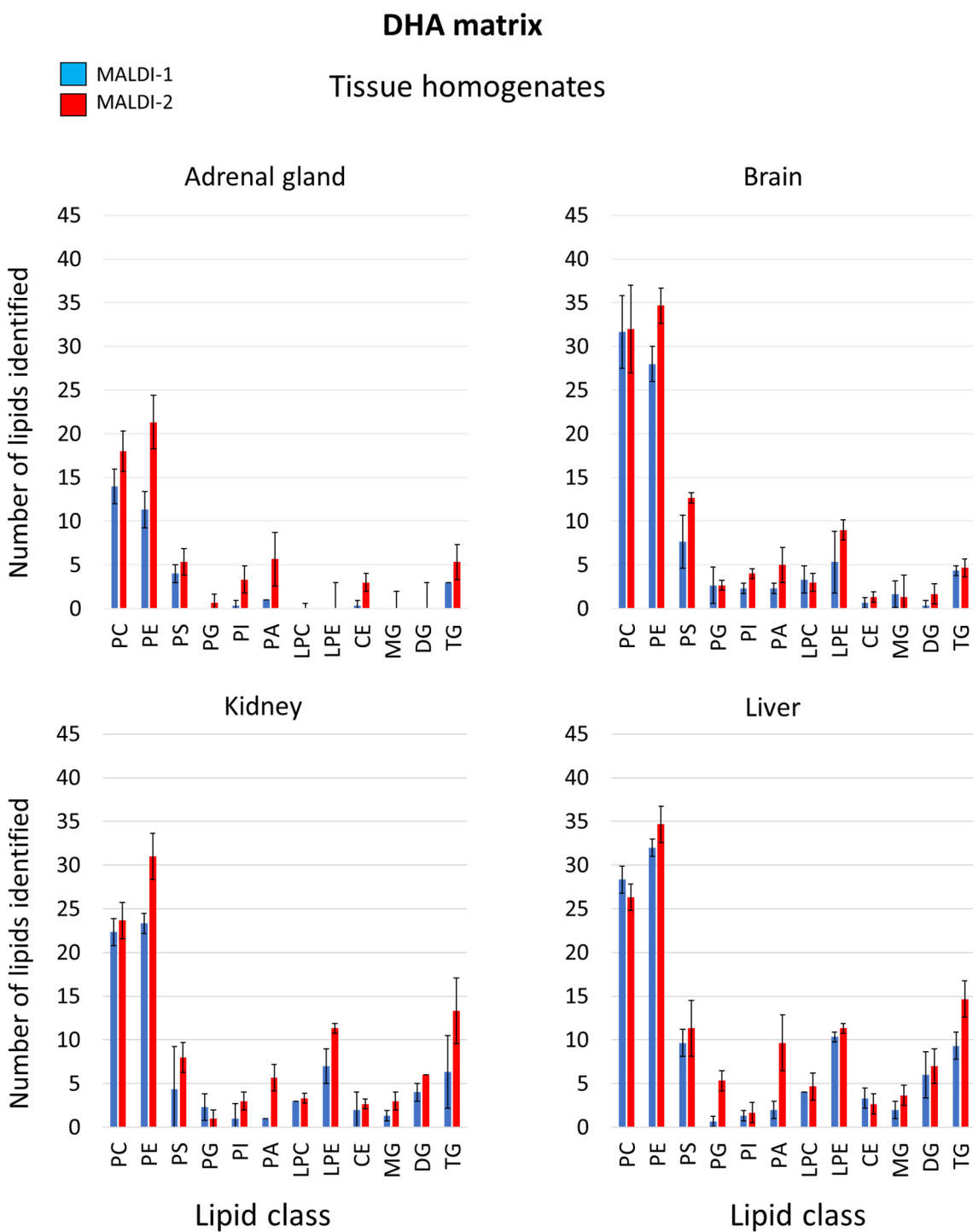
Figure 4.10. Number of protonated lipids identified per lipid class for DHA matrix for each of four tissue homogenates analyzed with MALDI-1 (blue bars) and MALDI-2 (red bars). Error bars represent the standard deviation of three technical replicate experiments. Identifications were made by accurate mass measurements matched within 2 ppm error of a database of lipids.
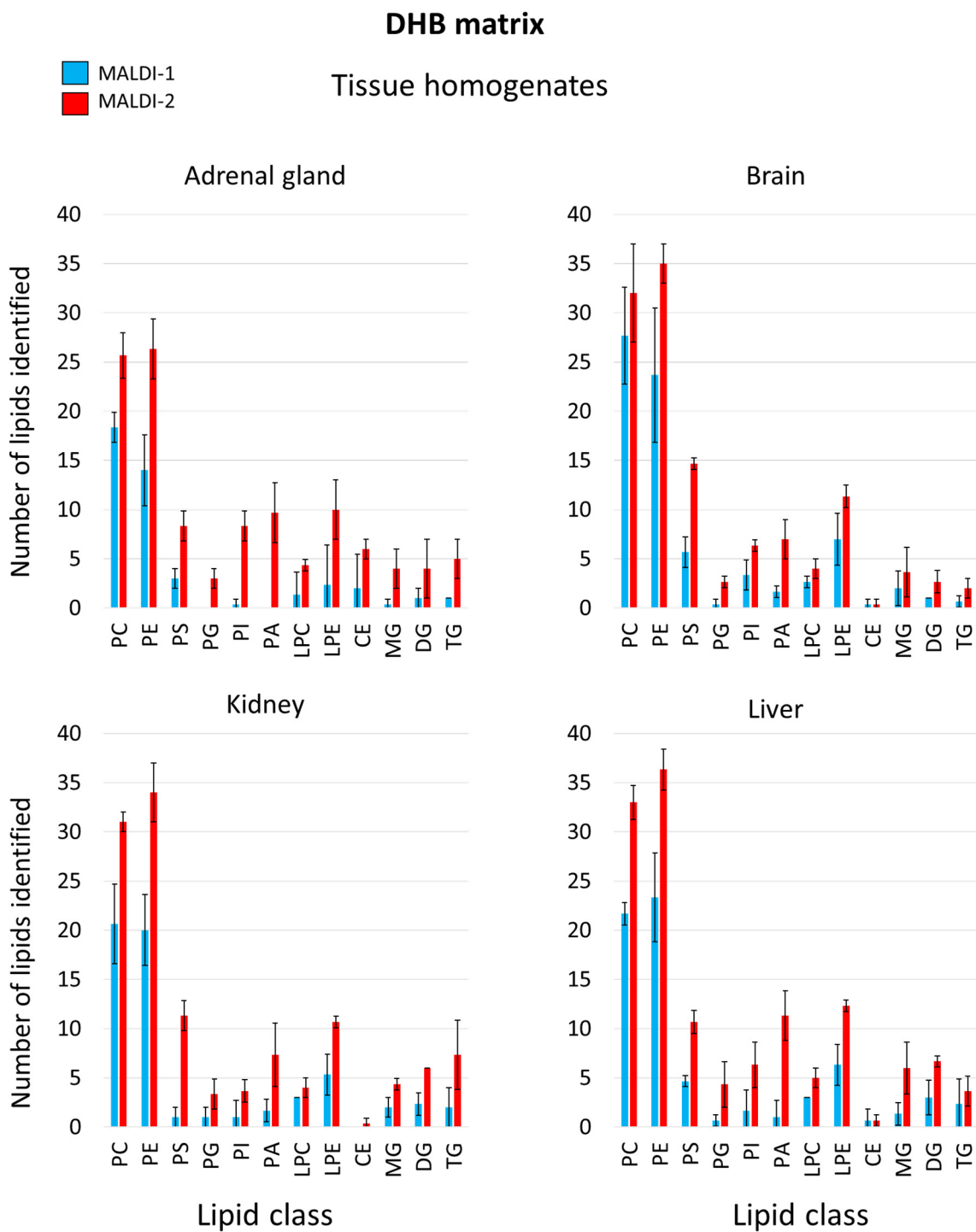
Figure 4.11. Number of protonated lipids identified per lipid class for DHB matrix for each of four tissue homogenates analyzed with MALDI-1 (blue bars) and MALDI-2 (red bars). Error bars represent the standard deviation of three technical replicate experiments. Identifications were made by accurate mass measurements matched within 2 ppm error of a database of lipids.
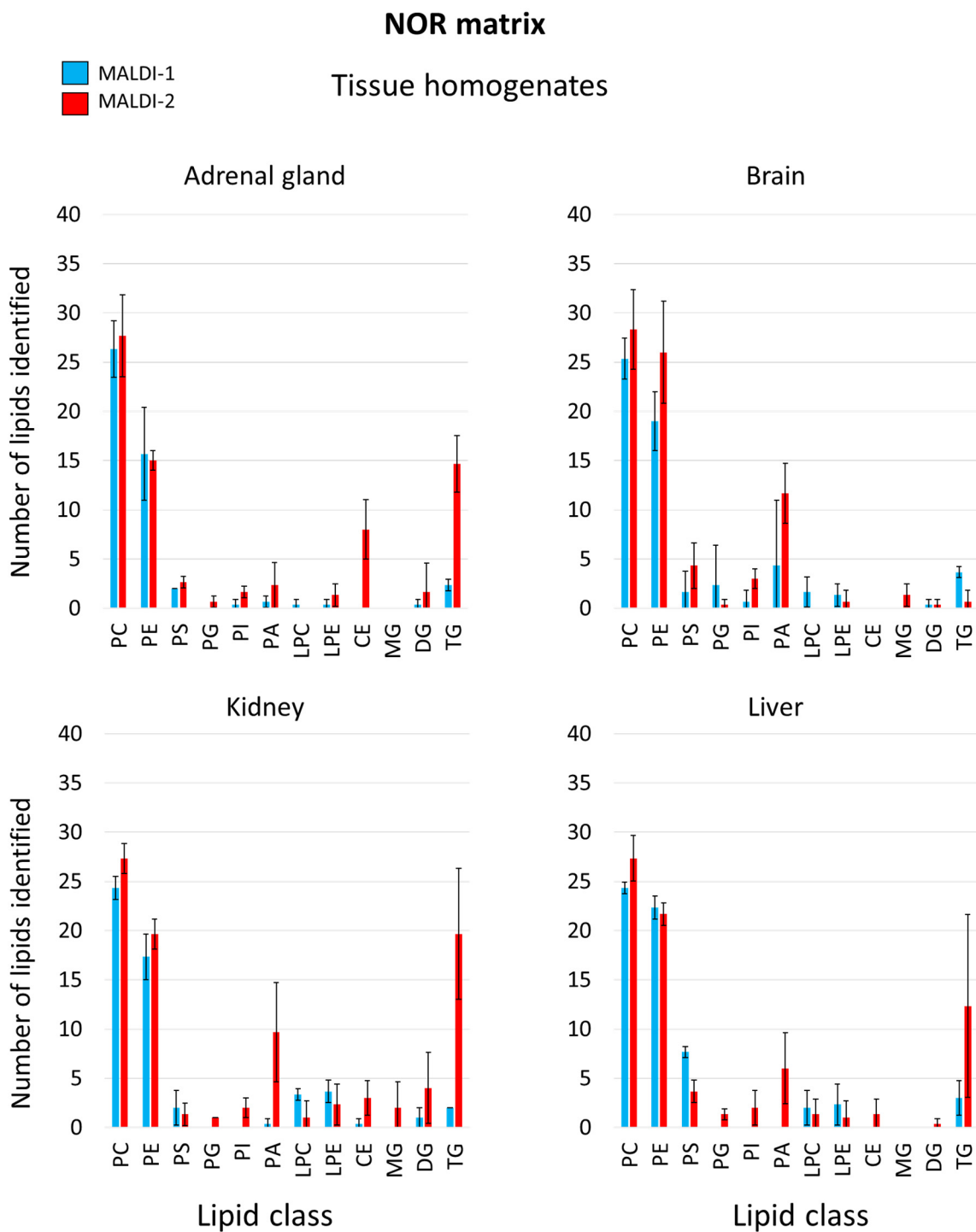
Figure 4.12. Number of protonated lipids identified per lipid class for NOR matrix for each of four tissue homogenates analyzed with MALDI-1 (blue bars) and MALDI-2 (red bars). Error bars represent the standard deviation of three technical replicate experiments. Identifications were made by accurate mass measurements matched within 2 ppm error of a database of lipids.

High spatial resolution MALDI-2 IMS: Improved phospholipid sensitivity using DHB

Based on the number of lipids identified by accurate mass (< 2 ppm error) from tissue homogenates, DHB was selected to demonstrate improved imaging performance of phospholipids using MALDI-2. Defined regions from a single rat kidney tissue section were selected for analysis with and without MALDI-2 activated. Prior to IMS, the tissue was imaged using autofluorescence microscopy to provide a high spatial resolution morphological image.[134] The autofluorescence microscopy image clearly shows the various anatomical regions of the kidney including the renal pelvis, medulla, inner cortex and outer cortex (**Figure 4.13 A**). Specified areas of the tissue were defined for MALDI-1 (white, top) and MALDI-2 (red, bottom) analysis. Averaged spectra of the acquired image regions were annotated similarly to the tissue homogenate experiments using mass accuracy (< 2 ppm mass tolerance). Compared with the rat kidney tissue homogenate, the MALDI-1 spectra had a comparable number or lipids identified (73 for homogenate, 72 for tissue) but the number of lipids identified with MALDI-2 for tissue were lower than for the homogenate (162 for homogenate, 125 for tissue). The number of lipids detected per lipid class for rat kidney tissue is shown in **Figure 4.14**. One explanation for lower number of identifications for the tissue section may be that there is greater variation in lipid concentrations from pixel-to-pixel within the intact tissue imaging experiment compared with the tissue homogenate. Still, a greater number of lipid species were detected with MALDI-2 compared with MALDI-1 alone and the overall image quality was dramatically improved for many of the phospholipid species (**Figure 4.13 B-E**). Of the examples shown, the PS, PE, and PI lipids were detected with much greater sensitivity with MALDI-2 as compared to MALDI-1. In many cases no discernable image was detected with MALDI-1 but ion images with good S/N and spatial fidelity were generated with MALDI-2 activated. Briefly, $[PE(38:5)+H]^+$ localizes to the medulla and, less so, the cortex. The species $[PS(36:4)+H]^+$, which is only detected with MALDI-2, was found specifically in the medulla, renal pelvis, and the glomeruli that appear as punctate regions within the cortex of the kidney. In contrast, $[PS(38:4)+H]^+$ is found at higher abundance in the inner and outer cortex. The species at *m/z* 887.564, identified as $[PI(38:4)+H]^+$, was observed more ubiquitously throughout the kidney with seemingly higher abundance in the renal pelvis and inner cortex. Overall, DHB provided for a dramatic increase in sensitivity, molecular coverage, and image quality for phospholipid species. No signal improvements were observed for non-polar lipid species. These results corroborate our lipid standards and tissue homogenate experimental data.
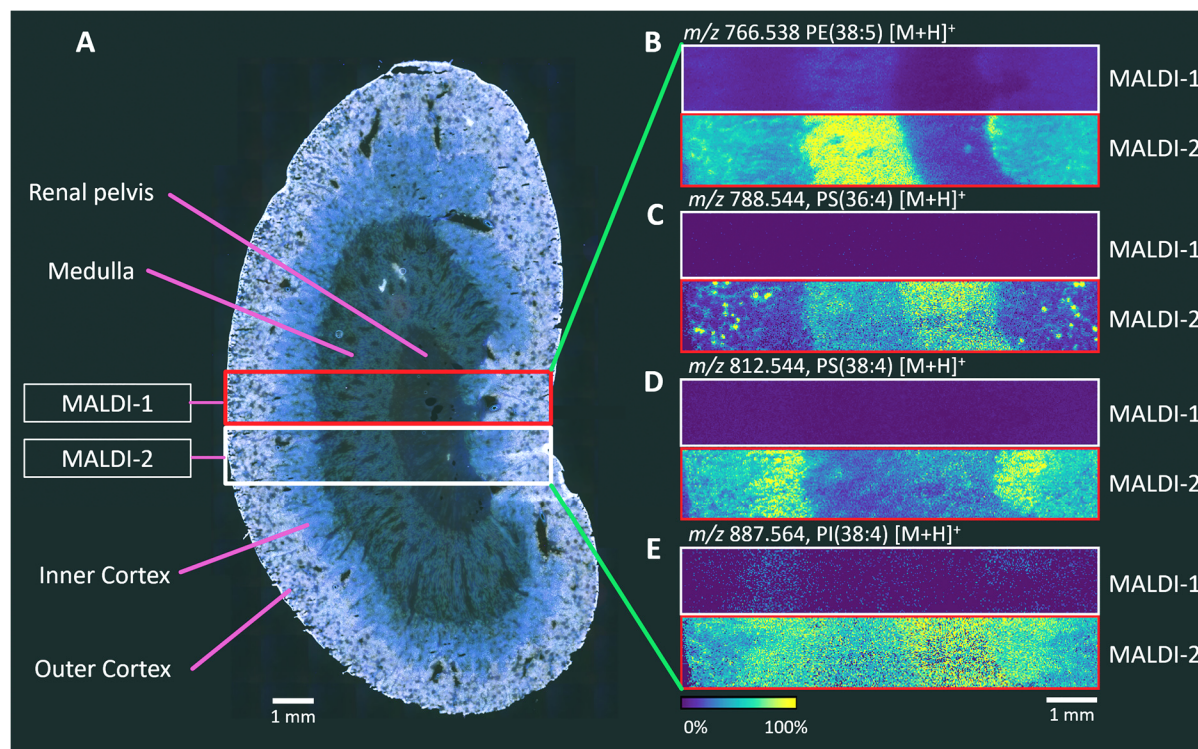
Figure 4.13. Rat kidney tissue analyzed with DHB matrix with and without MALDI-2. **A)** Autofluorescence image of rat kidney tissue with annotated substructures, and boxed regions indicating where MALDI-1 (white) and MALDI-2 (red) IMS data were collected. MALDI-1 and MALDI-2 IMS selected ion images for **B)** m/z 766.538 ((PE 38:5), [M+H]$^+$), **C)** m/z 788.544 (PS(36:4) [M+H]$^+$), **D)** m/z 812.544 ((PS 38:4), [M+H]$^+$), and **E)** m/z 887.564 ((PI 38:4), [M+H]$^+$). Ion intensity is relatively scaled from 0% (purple) to 100% (yellow). Ions were identified based on exact mass measurements (<2 ppm mass accuracy), even-number carbon chain, and on lipid classes known to increase with MALDI-2 in the lipid standard. Scale bars represent 1 mm in length.
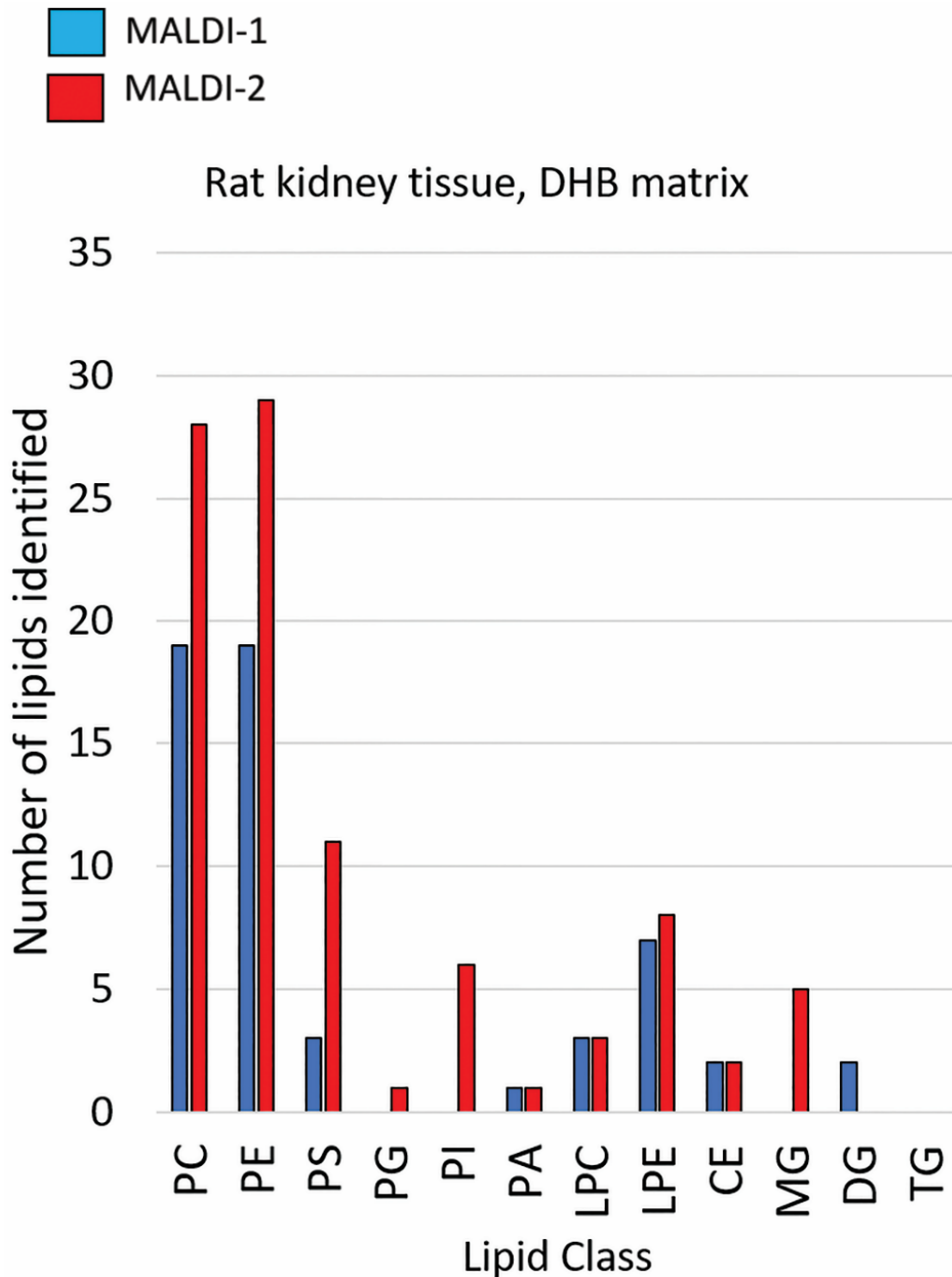
Figure 4.14. Number of protonated lipids identified by accurate mass measurement (<2 ppm error) per lipid class for rat kidney tissue section coated with DHB matrix, analyzed with MALDI-1 (blue bars) and MALDI-2 (red bars). Lipids were annotated from the averaged spectrum from each ion image using the same workflow as with the tissue homogenate data.

This study provides a systematic comparison of molecular coverage and sensitivity of protonated lipids between MALDI-1 and MALDI-2 for the matrices CHCA, DHA, DHB, and NOR. From MALDI-2 analysis of the equimolar, deuterated lipid standard mixture, NOR provided the broadest lipid coverage with all protonated forms of neutral lipids (TG, DG, MG, CE) detected, and DHB provided the greatest fold change increase with MALDI-2 for species already detected with MALDI-1. DHB provided the combination of greatest increase in the number of lipids detected as well as the greatest number of lipids detected with MALDI-2 for tissue homogenates and these results were confirmed in high resolution imaging experiments of rat kidney tissue.

LIPID ANALYSIS OF PANCREATA FROM NON-DIABETIC AND TYPE 2 DIABETIC DONORS USING MALDI-2

Laser-based post-ionization (MALDI-2) allows for enhancement of signal for numerous lipid classes. Here, I applied DHB matrix to sections of pancreata from ND and T2D donors for lipid analysis. Data were acquired on a prototype MALDI trapped ion mobility (TIMS) platform (timsTOF Pro) modified with a second laser to allow for analysis using MALDI-2.

Methods

Pancreata from a ND donor and a T2D donor, were obtained through agreements with the International Institute for Advancement of Medicine (IIAM), National Disease Research Interchange (NDRI), and local organ procurement organizations. These donors were screened for criteria reflective of a representative pancreas including limited ICU/hospital stay, absence of pancreatitis, and no history of congestive heart failure or end stage renal disease. Pancreata were received within 18 hours from cross clamp and maintained in cold preservation solution on ice until processing. Pancreata were then cleaned from connective tissue and fat, measured and weighed. Multiple cross-sectional slices of pancreas with 2-3 mm thickness were obtained from the head, body and distal tail. Pancreatic slices were further divided into four quadrants and then either snap frozen or processed for cryosections. Pancreatic tissue was flash frozen in liquid nitrogen and stored at -80°C until further use. Serial 10 μm cryosections were cut for MALDI IMS and stored in vacuum-sealed bags at -80°C.

Sections were prepared for MALDI IMS by removing from storage at -80°C and warming to room temperature in a vacuum desiccator for 30 minutes. A MALDI matrix solution of DHB

was prepared at a concentration of 30 mg/mL in tetrahydrofuran including 20 μL of N,N-Dimethyl formamide. The matrix solution was applied to the samples using an M5 TM Sprayer from HTX Technologies that included a heated stage. Sprayer conditions were set to 60°C for the nozzle and stage, 4 passes in CC pattern, flow rate of 0.05 mL/minute, nozzle head velocity of 1350 mm/minute, track spacing of 2 mm, nitrogen pressure of 8 psi, and dry time of 2 seconds between passes.

A prototype MALDI timsTOF Pro instrument, with additional modifications for a secondary (MALDI-2) laser, was used for analysis. The MALDI-2 laser was an Ekspla NL 204, Nd:YAG 266nm, frequency quadrupled laser with a measured output of ~500 μJ, operated at 1000 Hz. The MALDI-2 laser was positioned ~500 μm above the sample surface to irradiate the plume from the primary MALDI event, and the timing was set to a 40 μs delay after the MALDI-1 laser. The timsTOF instrument was operated in qTOF mode and acquisition parameters were as follows: 250 laser shots per pixel, 1000 Hz frequency for both MALDI-1 and MALDI-2 lasers, the pressure of the "TIMS in" funnel was maintained at 2.5 mBar with a Dry Temp of 150 °C, Focus Pre TOF transfer time: 100 μs, Pre Pulse Storage time: 5 μs. Ion images were set to a 16 μm 'scan range' setting in x and y with a Resulting Field Size of 20 μm with beam scan on and the Smart Beam set to Single M2. Each ion image had an approximate size of 10,000 pixels. Data were obtained by setting up the ion images for ND and T2D samples for MALDI-2 first, then obtaining MALDI-1 for both samples as the MALDI-2 laser needs time to equilibrate prior to acquisition. For the T2D donor, MALDI-1 and MALDI-2 were obtained on adjacent regions of the same tissue but for the ND donor there were issues with sample adhesion on the slide surface. As such, similar regions were analyzed on serial sections of tissue that were on the same slide and were prepared the same way.

Data analysis

The four ion images were opened together in SCiLS 2022a (Bruker) software for processing. Averaged spectra of each tissue (~10,000 pixels each) were exported as a .csv file and the data were imported into mMass (mmass.org) for further processing. Peak picking was performed using a cutoff of 3x the noise level for each ion image. Post-acquisition calibration was performed using a list of common lipids detected in tissues: PC(32:0) ([M+H$^+$], *m/z* 734.5694), PC(34:1) ([M+H$^+$], *m/z* 760.5851), PC(34:1) ([M+Na$^+$], *m/z* 782.5670), PC(36:1) ([M+H$^+$], *m/z*

788.6164), PC(34:1) ([M+K$^+$], *m/z* 798.5410), PC(38:4) ([M+K$^+$], *m/z* 810.6007), PC(38:4) ([M+Na$^+$], *m/z* 832.5827), PC(38:4) ([M+K$^+$], *m/z* 848.5566). The peak picked and calibrated lists were imported into LIPID MAPS (lipidmaps.org/tools/ms/lm_mass_form.php) and searched based on the following parameters: ion adducts of [M+H]$^+$, even chain lipids only, and a mass tolerance of +/- 0.01 *m/z*. Resulting lipid matches were copied and further processed in Excel. The list of lipids was combined with the results from Bowman et al. of lipids detected from rat liver tissue coated with DHB using MALDI-2 and duplicate species between the two lists were removed.[33] Using this comprehensive list, a reference list for annotation in mMass was generated and the corresponding mMass file (references.xml) in the "configs" mMass folder was modified to include the comprehensive list of lipids for annotation. In mMass, spectra were annotated using the Mass Filter tool and selecting the comprehensive reference list from the dropdown menu. The reference list was matched to the peak list using a 5.0 ppm tolerance and the spectra were annotated. Annotations for each spectrum were exported under the "File → Analysis Report…" feature and were copied into Excel for further processing. The measured *m/z* was compared to the comprehensive reference list and the closest match was used where there was more than one annotation for a given peak. As a practical example, in Excel the measured *m/z* was in column M and the reference list was in column N, rows 3:804, (**Figure 4.15**) so the closest theoretical *m/z* was generated by the formula:

"=INDEX(N$3:N$804,MATCH(MIN(ABS(N$3:N$804-M3)),ABS(N$3:N$804-M3),0))"

and for each species in the reference list in column N where the identity is listed in column P, a similar equation was used to query the identity for each *m/z*:

"=INDEX(P$3:P$804,MATCH(MIN(ABS(N$3:N$804-Q3)),ABS(N$3:N$804-Q3),0))".

Figure 4.15. Extract of excel sheet showing equations used to match MALDI peak lists (column M) with *m/z* values of lipids from a lipid database (column N). Lipid names for matched species were extracted using a similar equation in column R. Lipids were identified by accurate mass measurement within 2 ppm error.

M	N	O	P	Q	R
Measured *m/z*	Reference list	Lipid class	Reference lipid	Closest m/z to reference	Lipid match
457.237	312.1207	LPC	LPC(3:1)	=INDEX(N$3:N$804,MATCH(MIN(ABS(N$3:N$804-M3)),ABS(N$3:N$804-M3),0))	=INDEX(P$3:P$804,MATCH(MIN(ABS(N$3:N$804-Q3)),ABS(N$3:N$804-Q3),0))
459.251	370.1625	PC	PC(6:0)	=INDEX(N$3:N$804,MATCH(MIN(ABS(N$3:N$804-M4)),ABS(N$3:N$804-M4),0))	=INDEX(P$3:P$804,MATCH(MIN(ABS(N$3:N$804-Q4)),ABS(N$3:N$804-Q4),0))
480.3458	395.2557	LPA	LPA(P-16:0)	=INDEX(N$3:N$804,MATCH(MIN(ABS(N$3:N$804-M5)),ABS(N$3:N$804-M5),0))	=INDEX(P$3:P$804,MATCH(MIN(ABS(N$3:N$804-Q5)),ABS(N$3:N$804-Q5),0))
483.2504	400.3421	CAR	CAR(16:0)	=INDEX(N$3:N$804,MATCH(MIN(ABS(N$3:N$804-M6)),ABS(N$3:N$804-M6),0))	=INDEX(P$3:P$804,MATCH(MIN(ABS(N$3:N$804-Q6)),ABS(N$3:N$804-Q6),0))
487.2826	419.2557	CPA	CPA(18:1)	=INDEX(N$3:N$804,MATCH(MIN(ABS(N$3:N$804-M7)),ABS(N$3:N$804-M7),0))	=INDEX(P$3:P$804,MATCH(MIN(ABS(N$3:N$804-Q7)),ABS(N$3:N$804-Q7),0))
504.3469	426.3578	CAR	CAR(18:1)	=INDEX(N$3:N$804,MATCH(MIN(ABS(N$3:N$804-M8)),ABS(N$3:N$804-M8),0))	=INDEX(P$3:P$804,MATCH(MIN(ABS(N$3:N$804-Q8)),ABS(N$3:N$804-Q8),0))
518.3243	428.3734	CAR	CAR(18:0)	=INDEX(N$3:N$804,MATCH(MIN(ABS(N$3:N$804-M9)),ABS(N$3:N$804-M9),0))	=INDEX(P$3:P$804,MATCH(MIN(ABS(N$3:N$804-Q9)),ABS(N$3:N$804-Q9),0))
522.3577	438.2979	LPE	LPE(P-16:0)	=INDEX(N$3:N$804,MATCH(MIN(ABS(N$3:N$804-M10)),ABS(N$3:N$804-M10),0))	=INDEX(P$3:P$804,MATCH(MIN(ABS(N$3:N$804-Q10)),ABS(N$3:N$804-Q10),0))
524.3734	454.3891	CAR	CAR(20:1)	=INDEX(N$3:N$804,MATCH(MIN(ABS(N$3:N$804-M11)),ABS(N$3:N$804-M11),0))	=INDEX(P$3:P$804,MATCH(MIN(ABS(N$3:N$804-Q11)),ABS(N$3:N$804-Q11),0))
535.3018	457.235	LPA	LPA(20:5)	=INDEX(N$3:N$804,MATCH(MIN(ABS(N$3:N$804-M12)),ABS(N$3:N$804-M12),0))	=INDEX(P$3:P$804,MATCH(MIN(ABS(N$3:N$804-Q12)),ABS(N$3:N$804-Q12),0))
542.3242	459.2506	LPA	LPA(20:4)	=INDEX(N$3:N$804,MATCH(MIN(ABS(N$3:N$804-M13)),ABS(N$3:N$804-M13),0))	=INDEX(P$3:P$804,MATCH(MIN(ABS(N$3:N$804-Q13)),ABS(N$3:N$804-Q13),0))
542.4935	478.3374	HexSph	HexSph(t18:1)	=INDEX(N$3:N$804,MATCH(MIN(ABS(N$3:N$804-M14)),ABS(N$3:N$804-M14),0))	=INDEX(P$3:P$804,MATCH(MIN(ABS(N$3:N$804-Q14)),ABS(N$3:N$804-Q14),0))
544.3411	480.3448	LPC	LPC(O-16:1)	=INDEX(N$3:N$804,MATCH(MIN(ABS(N$3:N$804-M15)),ABS(N$3:N$804-M15),0))	=INDEX(P$3:P$804,MATCH(MIN(ABS(N$3:N$804-Q15)),ABS(N$3:N$804-Q15),0))
546.3555	480.3531	HexSph	HexSph(t18:0)	=INDEX(N$3:N$804,MATCH(MIN(ABS(N$3:N$804-M16)),ABS(N$3:N$804-M16),0))	=INDEX(P$3:P$804,MATCH(MIN(ABS(N$3:N$804-Q16)),ABS(N$3:N$804-Q16),0))

Intensity values (column G) were summed for each annotation (column J) matched to the reference list identifications (column P) using the equation:

"=SUMIF(J$3:J$210,"*"&P3&"*",G$3:G$210)" where the first dataset spanned rows 3-210.

In a separate Excel sheet, the intensity values (already filtered to be above a S/N threshold of 3) were used to determine if the species was detected using the equation "=IF(T3=0,0,1)" where T3 is a queried intensity value such that if it was detected, a "1" would be listed and if not detected, a "0" would be listed. The total number of lipids detected per class were calculated using the equation: "=SUMIF(G$3:G$786,"*"&Q4&"*",C$3:C$787)" where C3:C787 are the possible lipids for one sample (column C), cell Q4 and below contains the abbreviation for the desired lipid class (e.g., PC), and column G contains the lipid classes for each associated lipid of the reference list. Total number of lipids identified from each ion image were obtained by calculating the sum of those values.

RESULTS AND DISCUSSION

Characterizing the lipid and metabolite composition differences between pancreata of ND donors and T2D donors is an important component in understanding disease progression for future treatment and prevention approaches. Here, a pilot study was conducted to evaluate the performance of MALDI-2 for the enhancement of signal of lipids and other metabolites in the comparison between ND and T2D pancreatic tissue. As demonstrated previously in this chapter, samples coated with the MALDI matrix DHB and analyzed with MALDI-2 provided the broadest lipid coverage compared to CHCA, DHA, and NOR matrices for rabbit adrenal gland, rat brain, rat kidney, and rat liver tissue. Since DHB was shown to be most effective for lipid detection with MALDI-2 for multiple tissue types, it was chosen as the matrix for analysis of pancreas tissue.

MALDI IMS was performed on tissue sections from ND and T2D donors using MALDI-1 and MALDI-2 for comparison of detection of lipids. Representative spectra are shown in **Figures 4.16 and 4.17** where the averaged spectrum for MALDI-1 is shown on top in blue and MALDI-2 is shown mirrored, below, in green. Autofluorescence images of the tissue are displayed in **Figure 4.18** with the IMS regions overlaid onto them. The spectral differences between the two are significant. Some typical intensity differences between MALDI-1 and MALDI-2 are observed such as the detection of the α-tocopherol (Vitamin E) radical at *m/z* 430.383 with MALDI-2. Here,

Vitamin E signal was below the limit of detection for MALDI-1 but was detected with MALDI-2 at arbitrary intensities of 600 and 1000 in the ND and T2D donor tissue, respectively (**Figure 4.19**). Other typical signal enhancement with MALDI-2 was observed such as with PE lipids. One example is the protonated PE lipid [PE(38:4), PE(O-38:5(OH)), or PE(P-38:4(OH))] detected at *m/z* 768.555 (1.7 ppm error, filtered for protonated, even chain lipids) enhanced ~8-fold with MALDI-2. Signal enhancement of liposoluble vitamins has been demonstrated with MALDI-2 by other groups and by our lab in various tissue types.[29,135,136] Vitamin E from rabbit adrenal gland homogenate was previously analyzed and fragmented using collision-induced dissociation (CID) on an Orbitrap Elite mass spectrometer equipped with a MALDI source from Spectroglyph LLC and a MALDI-2 laser for post-ionization as shown in **Figure 4.20**. Other differences in the MALDI-2 spectrum include enhanced detection of triglyceride (TG) species in the range of *m/z* 880-910.
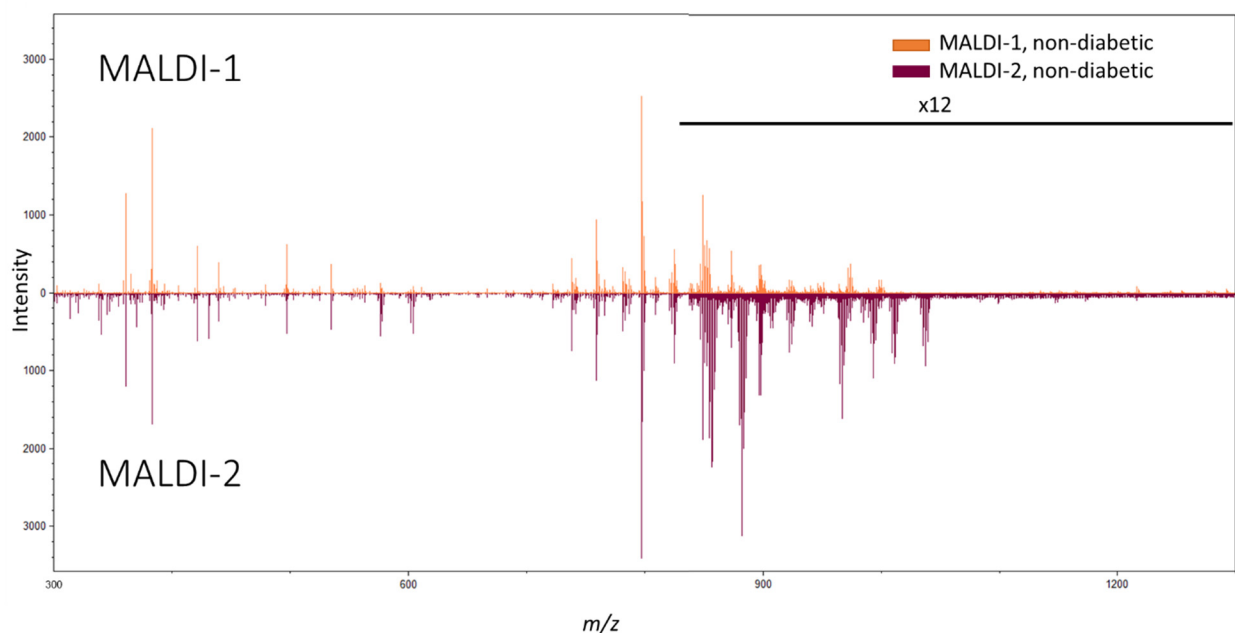
Figure 4.16. Averaged mass spectra of human ND pancreas tissue analyzed with MALDI-1 in orange (top) and MALDI-2 in red (bottom). Approximately 10,000 pixels were averaged for each spectrum. MALDI-2 provides for enhanced signal of many lipids from the human pancreas.
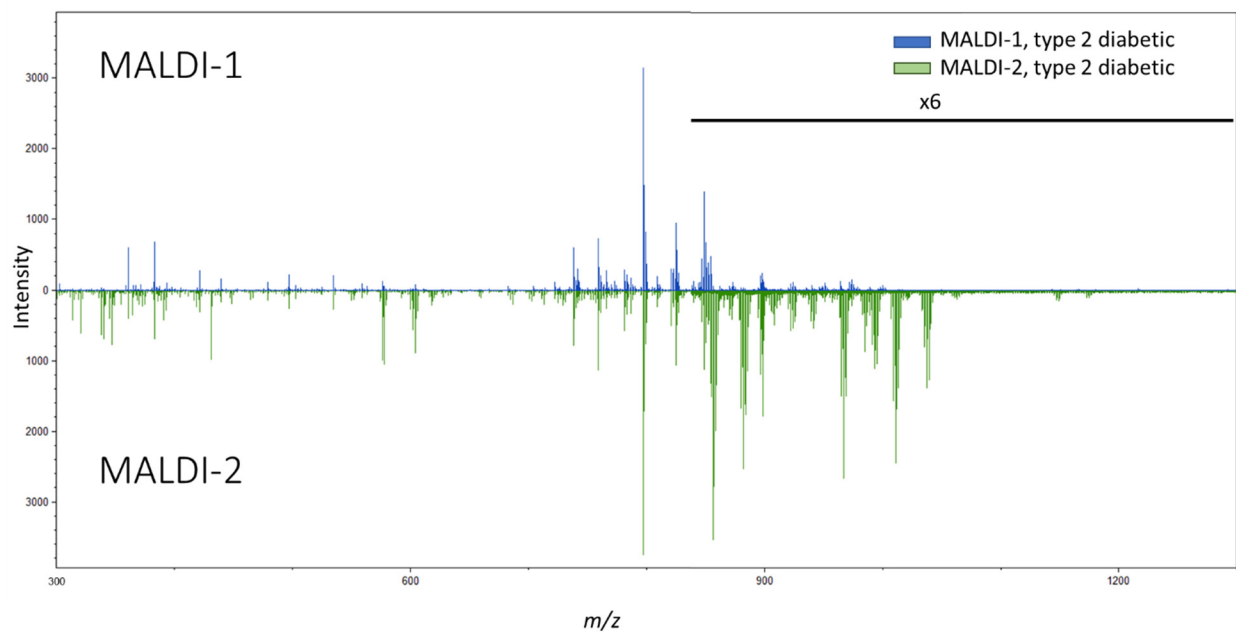
Figure 4.17. Averaged mass spectra of human T2D pancreas tissue analyzed with MALDI-1 in blue (top) and MALDI-2 in green (bottom). Approximately 10,000 pixels were averaged for each spectrum. Note the significant increase in intensity of numerous species above *m/z* 850 for MALDI-2 and higher signal compared to non-diabatic samples, above.
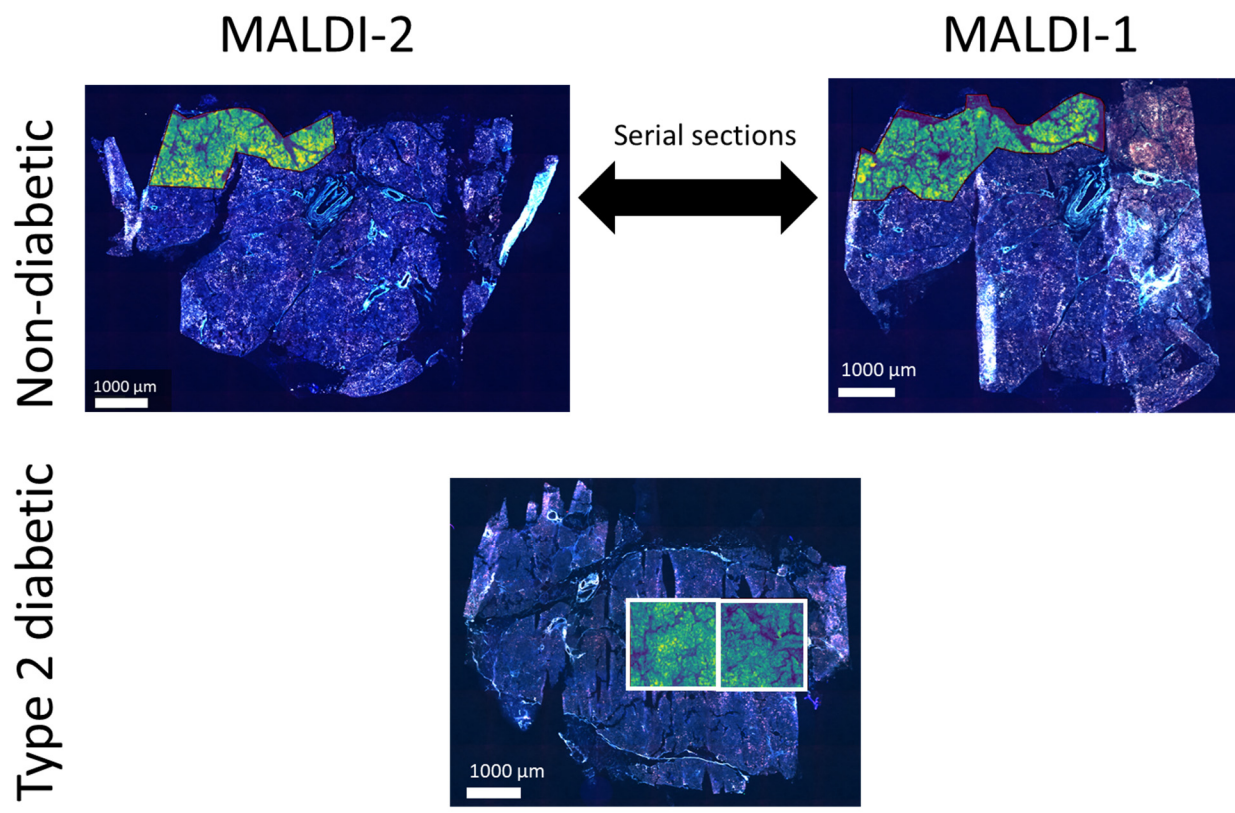
Figure 4.18. Autofluorescence images of pancreatic tissue from ND donor (top) and T2D donor (bottom) with IMS acquisition regions overlaid onto them. The ND donor tissue was analyzed by MALDI-1 and MALDI-2 as serial sections. Adjacent regions of one tissue section from the T2D donor tissue was analyzed by MALDI-1 (right) and MALDI-2 (left).
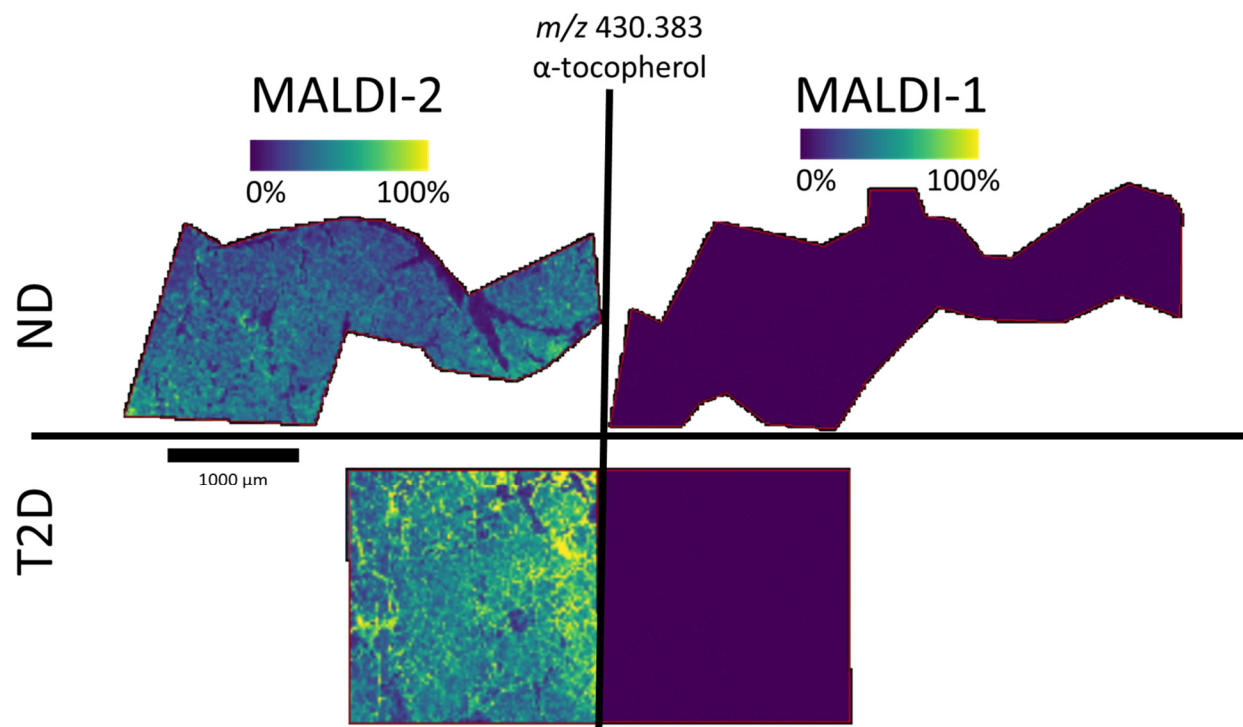
Figure 4.19. Ion images of α-tocopherol (Vitamin E) for ND (top) and T2D (bottom) donor obtained with MALDI-1 (right) and MALDI-2 (left). Vitamin E is not detected with MALDI-1 but is readily detected with MALDI-2 and seems have elevated intensity in the T2D donor. Ion image intensities are scaled to show the best contrast for MALDI-1 and MALDI-2.
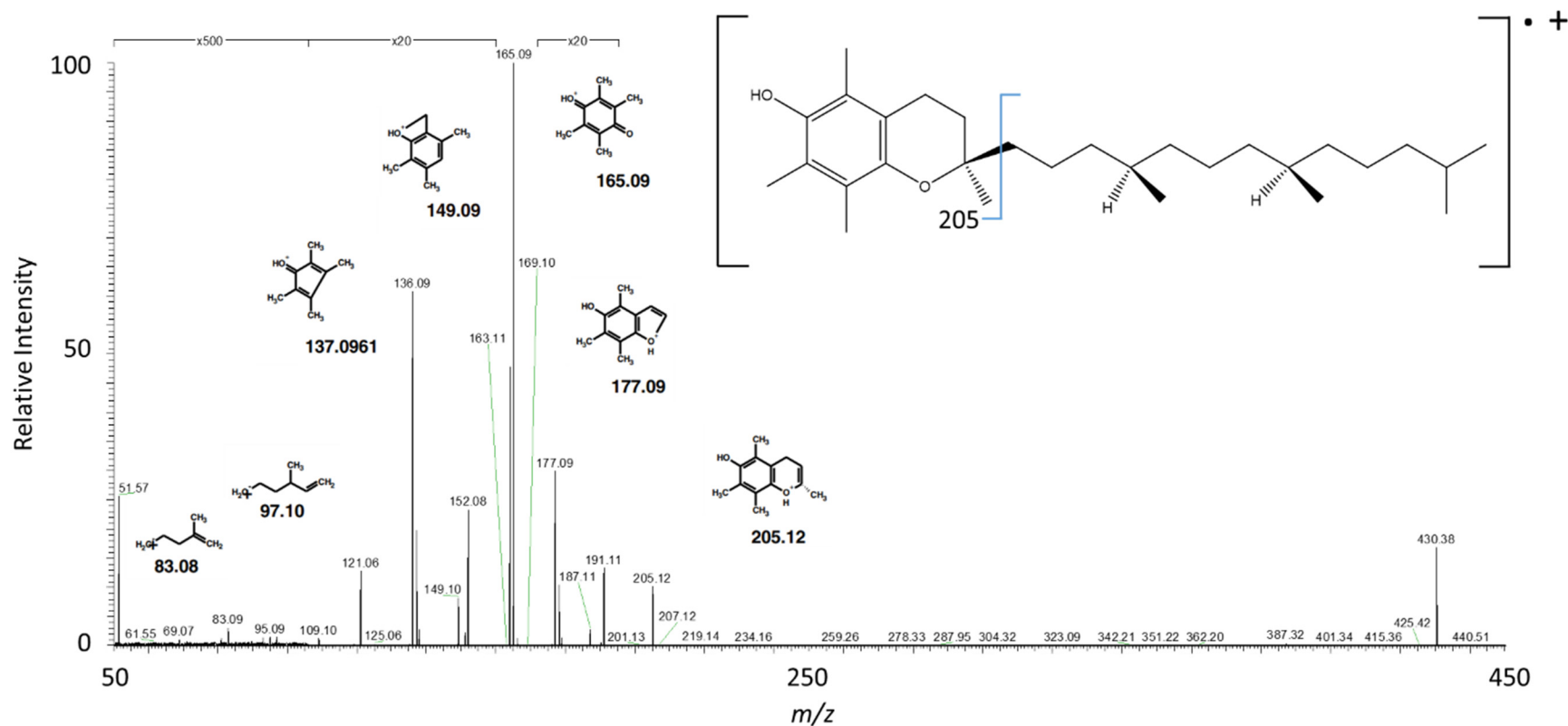
Figure 4.20. CID fragmentation spectrum of α-tocopherol (Vitamin E) obtained on the Orbitrap Elite instrument from rabbit adrenal gland tissue. Vitamin E is a common liposoluble metabolite that is readily ionized and detected in a typical MALDI-2 experiment. Structures of fragment ions were obtained from the fragmentation pathway of tocopherols published by Jiang et al. [137]

MALDI-2 has been shown to increase signal for many TG lipids in other tissue types and tissue homogenates, and this enhancement is observed from human pancreas tissue as well. One lipid that is enhanced with MALDI-2 and differs significantly between ND and T2D donors is *m/z* 881.761 which was identified by CID fragmentation as TG(16:0_18:1_20:4) (**Figure 4.21 A, B**). Pancreata from T2D donors have previously been shown in literature to have altered TG content, specifically a 23% increase in triglycerides compared to ND donors.[68] The data from MALDI analysis show similar results between these donors as well where TG content is elevated in the T2D donor compared to the ND donor, one example being TG(16:0_18:1_20:4) MALDI-2 plays an important role in the detection of TGs such that the difference in signal between ND and T2D donors can be represented and compared versus detection of TGs with MALDI-1. With MALDI-1 alone, the signal of this TG is very low at an arbitrary intensity of 6 for the ND donor and of 7 for the T2D donor (17% higher signal of T2D donor). With MALDI-2, the TG signal is 421 arbitrary intensity (a.i.) for T2D donor and 264 a.i. for the ND donor (59% higher signal of T2D donor). This species represents just one of 26 lipids identified by accurate mass measurement (≤5 ppm error) as TGs that were not detected with MALDI-1 but are detected using MALDI-2 in the T2D donor tissue. In the analysis of a lipid standard shown in previously in this chapter, DHB matrix was the only one that showed both high S/N for TGs (compared to CHCA) and minimal lipid-matrix adducted species (compared to norharmane). Interestingly, the TG standard fell below the limit of detection for MALDI-1 with DHB (and all other matrices tested) whereas from tissue, TGs are readily detected even with MALDI-1. Difference such as TG concentration and ionization suppression could account for the difference in performance of MALDI-1 between the lipid standard mixture and tissue. Both from lipid standard mixture and from human pancreas tissue, MALDI-2 allows for increased signal of TG lipids.
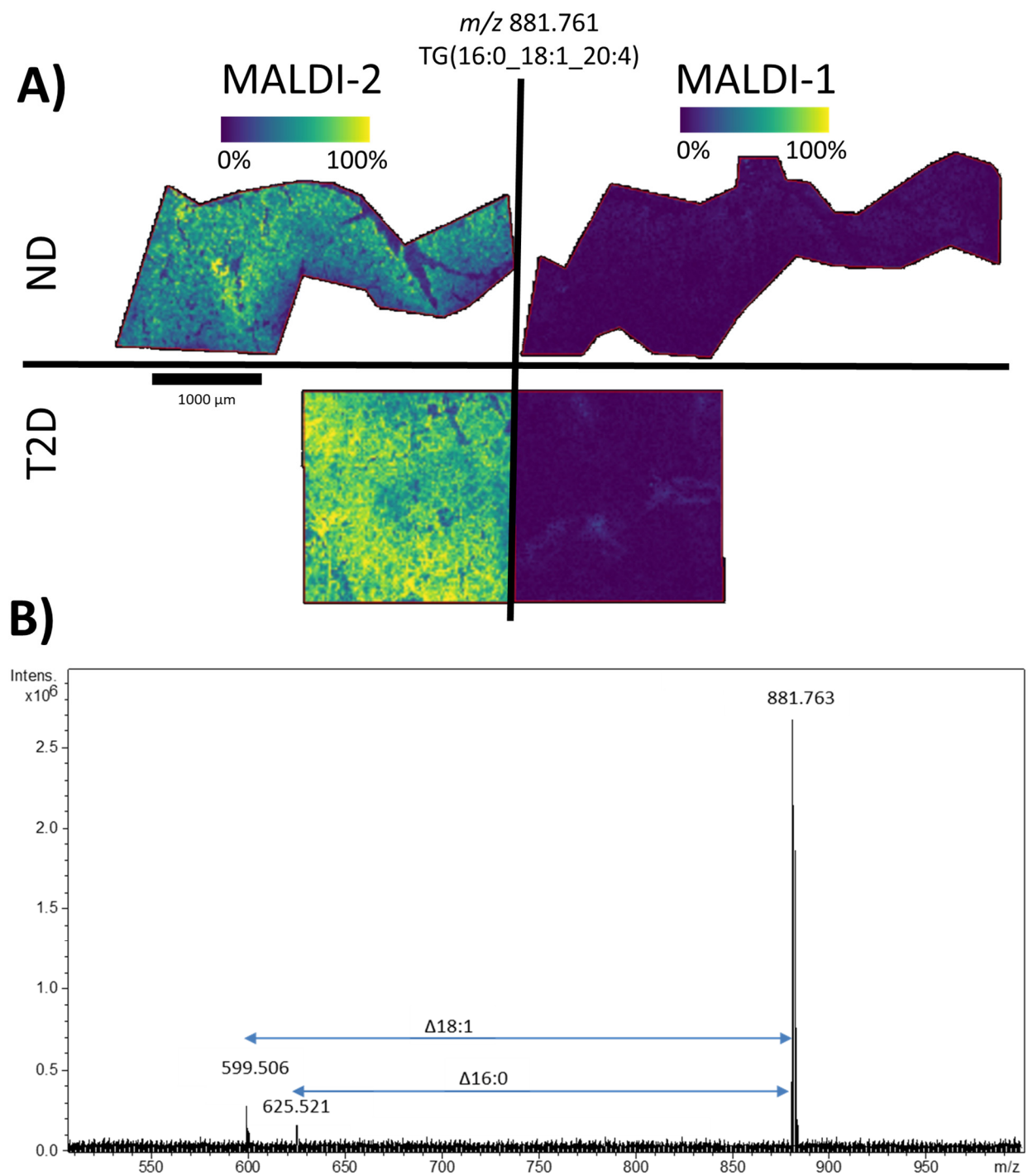
Figure 4.21. Ion images (**A**) of TG(16:0_18:1_20:4) for the ND (top) and T2D (bottom) donor using MALDI-1 (right) and MALDI-2 (left). The TG is detected with MALDI-1 in both donors at low levels, but the signal is poor and ion image quality is low. In contrast, MALDI-2 allows for detection of TG with good signal intensity and high ion image quality. CID fragmentation spectrum shown in **B**.

Two examples above show significant enhancement with MALDI-2 (Vitamin E) and differences between ND and T2D donors with lipids that are already detected with MALDI-1 [TG(16:0_18:1_20:4)] but there are examples of lipids only detectable with MALDI-2 that are significantly more intense in the T2D donor. One such example is at *m/z* 774.565 identified by accurate mass measurement as PS(O-36:2) or PS(P-36:1) (0.9 ppm mass error, **Figure 4.22 A**). With analysis on a 15T FT-ICR at a mass resolution ~190,000, the mass was detected at 774.56414 with 0.20657 ppm mass error that gives a molecular formula of $[C_{42}H_{80}NO_9P +H]^+$ (**Figure 4.22 B**). In the MALDI-1 ion image, the signal falls below the S/N threshold (3x noise level) with MALDI-1 for both the ND and T2D donors. MALDI-2 allows for signal enhancement and detection of this ion for both ND and T2D donors but there is an over 5-fold difference in intensities between the two (20 vs. 104 a.i. for ND and T2D donors, respectively).
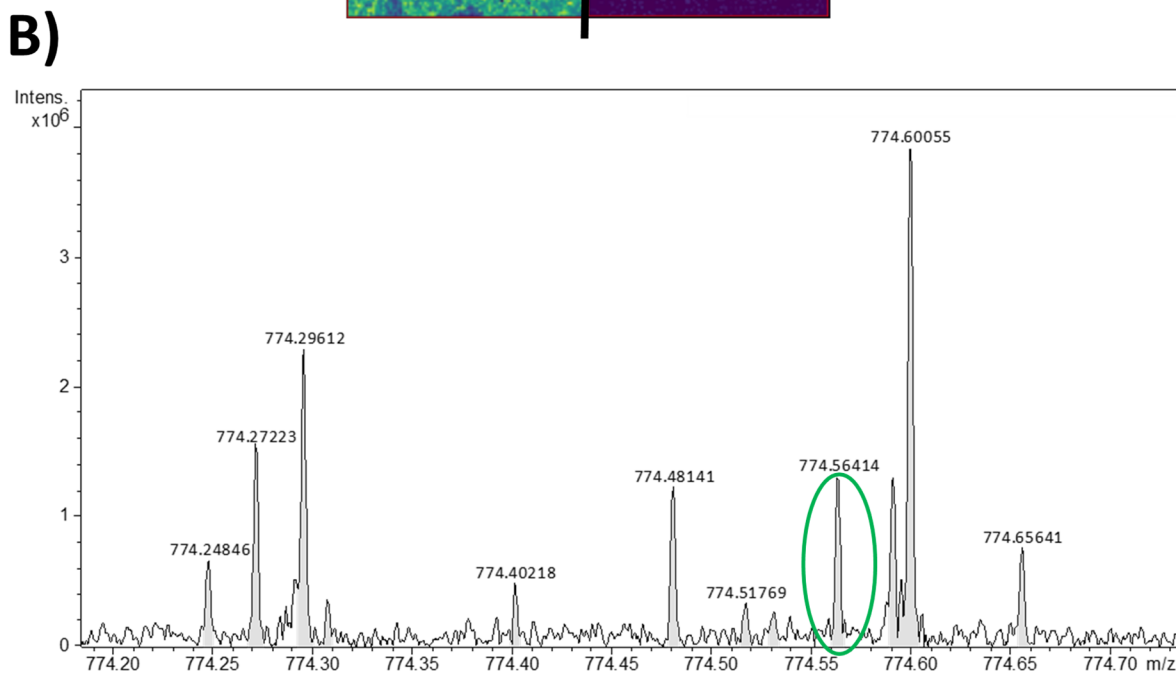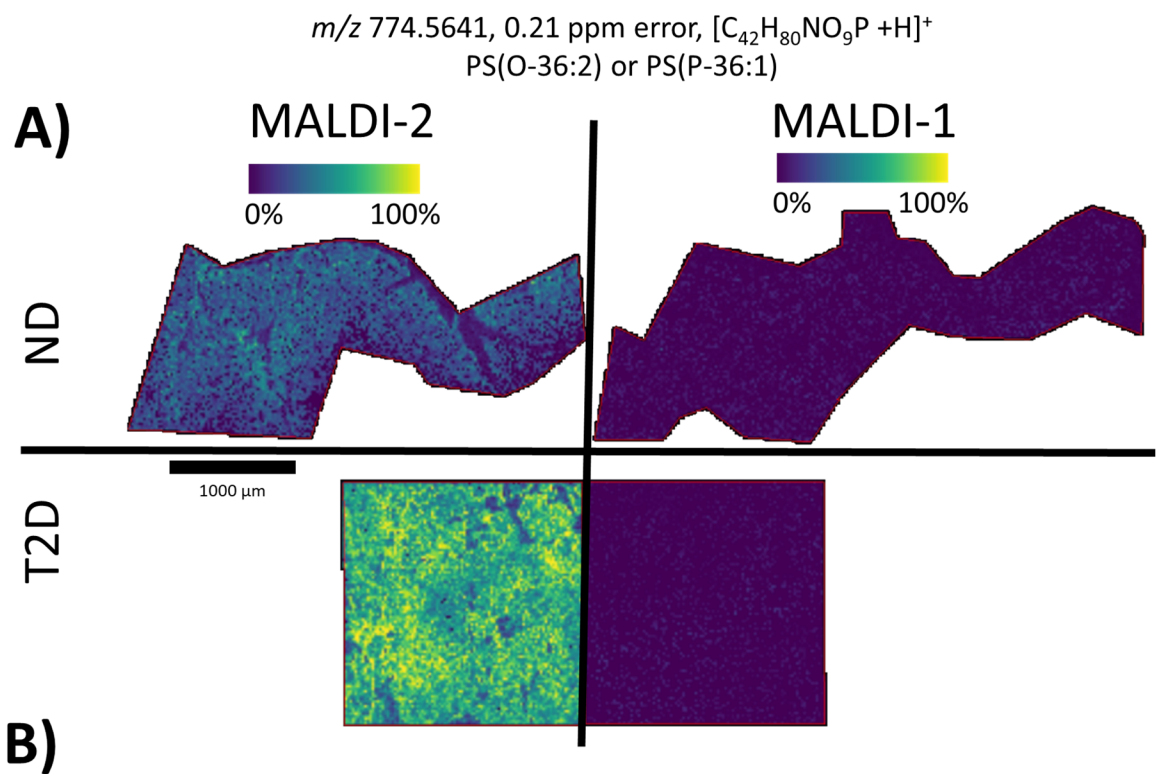
Figure 4.22. Ion images (**A**) of PS(O-36:2) or PS(P-36:1) lipid for the ND (top) and T2D (bottom) donor using MALDI-1 (right) and MALDI-2 (left). This ion is not detected in either donor with MALDI-1 whereas with MALDI-2 it is detected in both donors. Of note is the significant enhancement of signal in the T2D donor compared to the ND donor. This species may a be part of the metabolic dysregulation process that is characteristic in T2D patients. Mass spectrum (**B**) obtained on 15T FT-ICR showing isobaric ions within ~0.5 Da window so isolation for fragmentation of this ion (green oval) was not feasible, but confident identification was made by accurate mass measurement (0.21 ppm error).

Even though there are numerous differences in intensity between MALDI-1 and MALDI-2, some species and lipid classes have similar intensities between the two acquisition modes. One exemplary lipid class is PC where the associated lipid signal was not significantly different between modalities. The increase in signal with MALDI-2 is thought to correct for species that ionize poorly or that experience extensive signal suppression. But lipid classes such as PCs and SMs are readily protonated or have a permanent positive charge and are therefore readily detected in positive ion mode in MALDI and would not experience significant ion suppression. An example of MALDI-2 performance for PC lipids is shown in **Figure 4.23 A** identified by CID as PC(34:2) (**Figure 4.23 B**). For this ion, there is no significant difference in intensity difference between MALDI-1 and MALDI-2 or between the ND and T2D tissues. The PC lipid localizes to the tissue such that fine cracks in the tissue can be distinguished and little analyte delocalization is detected.

Although tissue washing can increase signal by removing salts and promoting detection of the protonated lipid species in positive ion mode, it can also induce analyte delocalization. An additional complication of tissue washing is that tissue sections may detach from the slide and the mixing of cellular components can contribute to delocalization. This delocalization is typically not a concern for most tissue types, but the pancreas contains numerous islets, which are ~150 μm in diameter, scattered throughout the tissue. As such, maintaining spatial distribution of analytes is important, even at the expense of signal intensity. Therefore, pancreas sections were not washed prior to matrix application to minimize delocalization of analytes and maintain tissue integrity. **Figure 4.17 A** demonstrates that by not washing, tissue integrity and analyte localization can be maintained throughout the process of coating a sample with matrix using a robotic sprayer.
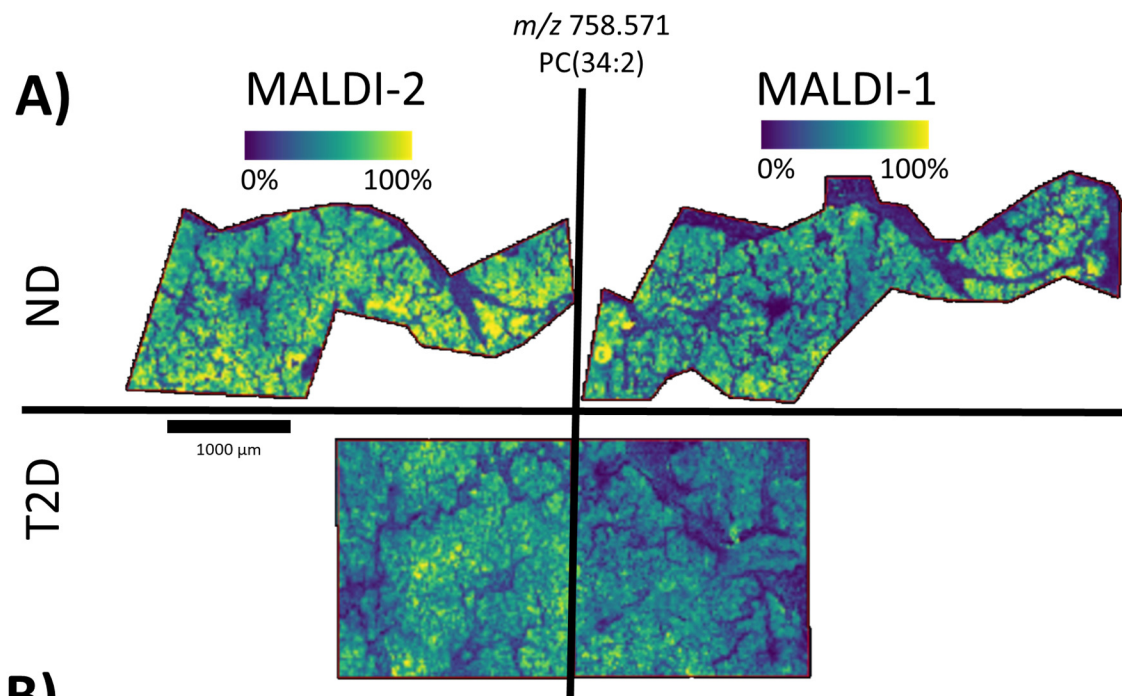
Figure 4.23. Ion images (**A**) of ND and T2D human pancreas tissue sections with traditional MALDI alone (MALDI-1) and with post-ionization (MALDI-2) for PC(34:2). The ion corresponding to the protonated form of PC(34:2) (*m/z* 758.571) is shown. Similar intensities are detected for this PC lipid with MALDI-1 as with MALDI-2, which would be expected for the PC lipid class. Here, the tissue morphology can be readily visualized, and this ion localizes to the tissue. CID fragmentation spectrum (**B**) of lipid showing characteristic PC headgroup loss.

One feature of the data from MALDI-2 analysis on the timsTOF instrument is the amount of spectral noise that is present. This noise presents as humps in the mass spectrum, often slightly offset from the main ions of interest, but are difficult to deconvolute. The result is that some peaks that appear to be real signal but are below the "noise" level go undetected, as is the case for the species identified by accurate mass measurement as PE(36:0) (1.3 ppm error). Even though the signal increased 3x from MALDI-1 to MALDI-2, the "noise" level increased ~7x and therefore there was a decrease in S/N. Yet when comparing MALDI-1 with MALDI-2 data from a high mass resolving power instrument such as the Orbitrap Elite, the noise level between MALDI-1 and MALDI-2 was comparable. Additionally, between MALDI-1 and MALDI-2 of the ND sample there was an uncharacteristic decrease in the number of peaks detected in the averaged mass spectrum. Therefore, it is hypothesized that the noise that increases with MALDI-2 on the timsTOF instrument may simply be other analytes that are enhanced with MALDI-2 that are not resolved on the TOF platform but may be resolved using higher mass resolution instruments.

CONCLUSIONS

These proof-of-concept experiments demonstrate the feasibility of using MALDI-2 technology for the enhancement of lipid and metabolite signal from ND and T2D pancreatic tissue. The MALDI matrix DHB allows for signal enhancement from human pancreas tissue with performance similar to that from sections of tissue homogenates and rat kidney tissue. MALDI-2 allows for detection of lipids and metabolites not detected with MALDI-1 alone as well as enhancement of signals already detected using MALDI-1. As such, MALDI-2 allowed for the comparison of lipids significantly elevated in the T2D donor compared to the matched control. Future experiments that include a larger cohort of tissue from matched ND and T2D donors will allow for robust lipid and metabolite analysis. This will help establish the biological significance of these candidate lipids for characterization of the metabolic differences between ND and T2D donors and will help assess efficacy of therapeutic treatment.

Acknowledgments

ENHANCEMENT OF TRYPTIC PEPTIDE SIGNALS FROM TISSUE SECTIONS USING MALDI-2 IMS

This chapter is adapted from Enhancement of Tryptic Peptide Signals from Tissue Sections using MALDI IMS Post-ionization (MALDI-2) published in the Journal of the American Society for Mass Spectrometry and has been reproduced with the permission of the publisher and my co-authors Danielle B. Gutierrez, Audra M. Judd, Jeffrey M. Spraggins, and Richard M. Caprioli.

OVERVIEW

The utility of MALDI-2 for signal enhancement of tryptic peptides has not been reported. We demonstrate signal enhancement of proteolytic peptides from thin tissue sections of human kidney by conventional MALDI (MALDI-1) augmented using a second ionizing laser (MALDI-2). Proteins were digested *in situ* using trypsin prior to IMS analysis and the MALDI-1 and MALDI-2 results were matched to a database of peptides from LC-MS/MS analysis. Protein identifications requiring two or more peptides per protein resulted in 276 ± 20 proteins with MALDI-1 and 401 ± 60 with MALDI-2. These results demonstrate that MALDI-2 provides enhanced sensitivity for the spatial mapping of tryptic peptides and significantly increases the number of proteins identified in IMS experiments.

INTRODUCTION

The spatial mapping of peptides and proteins is crucial for understanding the underlying molecular drivers of tissue biology and pathology.[1,138] Protein distributions in tissue are highly dependent on expression within cell types and on molecular changes in the tissue microenvironment.[139,140] Peptides and proteins are often identified by mass spectrometry technologies from bulk tissue homogenates, but spatial information is not typically retained with these methods. In contrast, immunohistochemical imaging allows for sensitive analyte detection and high spatial resolution mapping but requires *a priori* knowledge of the analyte of interest and is limited by the number of targets that can be imaged in a single experiment.

Matrix-assisted laser desorption/ionization imaging mass spectrometry (MALDI IMS) of peptides and proteins combines the advantages of both MS and immunohistochemistry by providing high sensitivity and specificity for analyte detection as well as untargeted, multiplexed mapping of hundreds-to-thousands of peptides and proteins from a single experiment.

Protein IMS has been reported for the intact detection of large proteins up to 200 kDa[141] but the practical upper mass limit is ~50 kDa.[104] High performance mass analyzers (e.g. FT-ICR and Orbitrap) provide superior mass resolving power and accuracy but have limited ion transmission efficiency at high m/z and analyses are typically limited to <30 kDa for protein IMS experiments.[142,143] To access larger proteins, a bottom-up approach is employed by applying a proteolytic enzyme such as trypsin to the tissue surface and imaging the resulting peptides.[37,144,145] Identifications were made using mass accuracy (≤5 ppm error) and the colocalization of tryptic peptides from the same protein.[144–147] However, because different peptides are generated by MALDI and electrospray ionization (ESI),[148–150] this approach is limited. To address this challenge, proteomic coverage can be increased for the IMS experiment by including multiple, complementary enzymes for *in situ* digestion.[151] On the other hand, more comprehensive protein databased generated by liquid chromatography tandem mass spectrometry (LC-MS/MS) can be made more comprehensive by including subsequent *in silico* digestion products of each identified protein.

Although peptide and protein IMS workflows are routine, proteomic coverage and sensitivity remain as challenges. Strategies to improve sensitivity through sample preparation approaches have included development of novel MALDI matrices[152] and tissue washes to remove interfering lipid and metabolite species that suppress peptide signal.[106] One common method to increase sensitivity is to use a method called antigen retrieval wherein proteins are denatured using high temperature. This allows the trypsin access to more sites for digestion thereby increasing proteomic coverage.[37] Digestion condition variables such as time, temperature, and humidity have also been optimized to improve digestion efficiency while maintaining peptide localization within a tissue section.[153,154] Nevertheless, increased sensitivity is needed to improve proteomic coverage for bottom-up IMS experiments.

Many instrumental technologies can be employed to improve sensitivity for IMS experiments.[111] One technology that has been shown to dramatically increase signal for MALDI IMS for some analytes is laser-based post-ionization.[24,29,155] Post-ionization by MALDI-2 employs a secondary laser positioned parallel to, and above the sample and irradiates the plume generated by the initial MALDI event (Figure

1.7), thereby increasing the fraction of molecules that are ionized. MALDI-2 has been recently shown to increase ion intensity up to 100-fold for lipids and increase the number of identified species by a factor of two. MALDI-2 post-ionization has been demonstrated to increase intensity for many classes of biologically relevant analytes including lipids,[29,124,155] saccharides,[29] liposoluble vitamins,[29] N-linked glycans,[156] certain pharmaceutical compounds,[124] and some protein complexes.[157] However there have been no reports of increased intensity of peptides with MALDI-2 post-ionization. Here, we demonstrate the use of MALDI-2 post-ionization for the enhancement of tryptic peptides from human kidney tissue sections and improved proteomic coverage for imaging experiments.

RESULTS AND DISCUSSION

MALDI IMS spectral data was compared between MALDI-1 and MALDI-2 of adjacent sections of the same section of human kidney tissue, performed in triplicate. Representative averaged, deisotoped mass spectra are displayed in **Figures 5.1 and 5.2** which show an increase in intensity and molecular coverage of tryptic peptides analyzed with MALDI-2. Analysis with MALDI-1 resulted in 474 ± 49 peaks whereas MALDI-2 allowed for detection of $1,278 \pm 161$ peaks based on a S/N level of 10. The overall spectral intensity was greater with MALDI-2 (2.6×10^3) as compared to MALDI-1 (8.0×10^2). These data indicate that there are significant signal and molecular coverage improvements for peptide IMS experiments with MALDI-2.
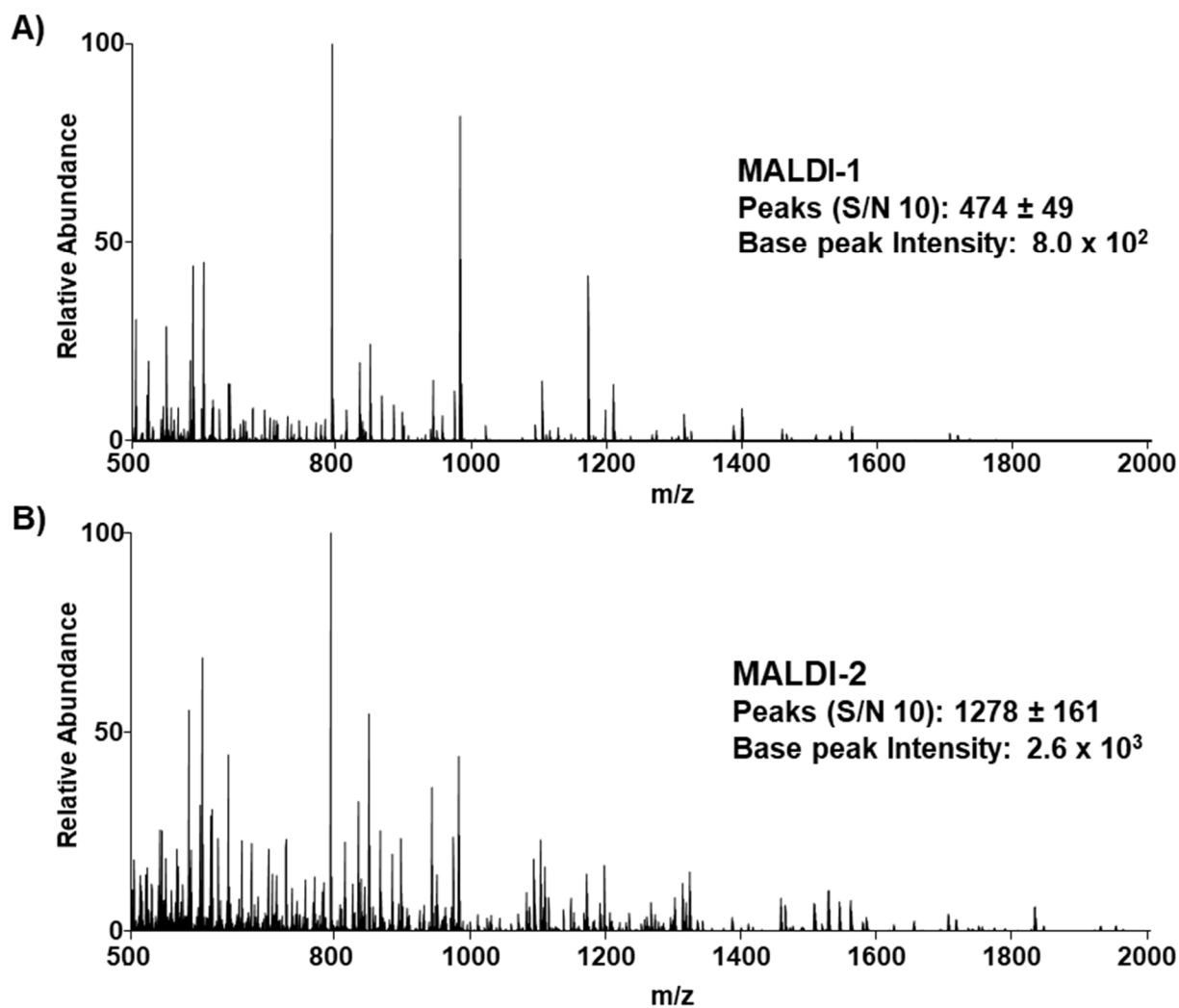
Figure 5.1. Representative averaged, deisotoped mass spectra of peptide ion images with MALDI-1 (**A**) and MALDI-2 (**B**) from IMS of human kidney section digested *in situ*. Number of peaks for MALDI-1 (474 ± 49) and MALDI-2 (1278 ± 161) are based on a signal-to-noise ratio of 10 to highlight the increase in S/N with MALDI-2. Spectra are scaled to their base peak of 8.0×10^2 for MALDI-1 and 2.6×10^3 for MALDI-2. Some matrix-related ions with high intensity decrease with MALDI-2.

LC-MS/MS peptides matched to IMS data

The increase in peptide signal and molecular coverage with MALDI-2 allows for more comprehensive proteomic coverage for tissue imaging experiments. To demonstrate this, MALDI peak lists were matched against a list of peptides from proteins identified by LC-MS/MS. Identification of proteins from IMS data was based on peptide mass fingerprinting (PMF) using 5 ppm mass error for peptides, 2 peptides per protein, and similar localization of peptides for each protein determined by manual review. The resulting number of peptides from identified proteins for MALDI-1 was 17 ± 1 and

57.7 ± 2 for MALDI-2. These identified peptides correspond to 9 ± 1 and 26 ± 1 proteins identified for MALDI-1 and MALDI-2, respectively. Further, MALDI-2 resulted in enhanced signal for all peptides (57.7 ± 2) identified using the criteria defined above.

Prior to acquisition, tissue sections were imaged optically using autofluorescence (**Figure 5.2 A**) to visualize the major functional tissue units of the kidney. Highlighted ion images were selected to provide examples of peptides that localize to these regions and throughout the tissue (**Figure 5.2 B-E**) including the cortex (**Figure 5.2 B**), medulla (**Figure 5.2 E**), and glomeruli (**Figure 5.2 C**). Many peptides not detected with MALDI-1 alone were detected with MALDI-2 (**Figure 5.2 C**), and MALDI-2 provided improved sensitivity for many ions already detectable with MALDI-1 (**Figure 5.2 B, D, E**). In many cases, a protein was identified from the IMS data sets with MALDI-2 only, and these proteins may provide insight into biological functions and disease states. One example is aminopeptidase N, a protein that is overexpressed in many types of cancer and is a target for cancer chemotherapy.[158,159] With IMS, we are able to visualize the localization of peptides of aminopeptidase N to the cortex of the kidney (**Figure 5.3 A-C**). Validation of this protein was performed using anti-aminopeptidase N antibody (**Figure 5.3 D**). Immunofluorescence shows aminopeptidase N localized to similar regions as the peptides detected by MALDI-2 (**Figure 5.3 B, C**). The secondary antibody control does not significantly fluoresce (**Figure 5.3 E**). MALDI-2 enhances peptide signal to allow for identification of this protein that otherwise would have remained undetected by IMS. Examples of other significant proteins identified with MALDI-2 in this analysis include alpha-enolase[160], zinc-alpha-2-glycoprotein[161], and phosphoglycerate kinase 1[140], proteins that have been found to be elevated in some cancers and tumors.
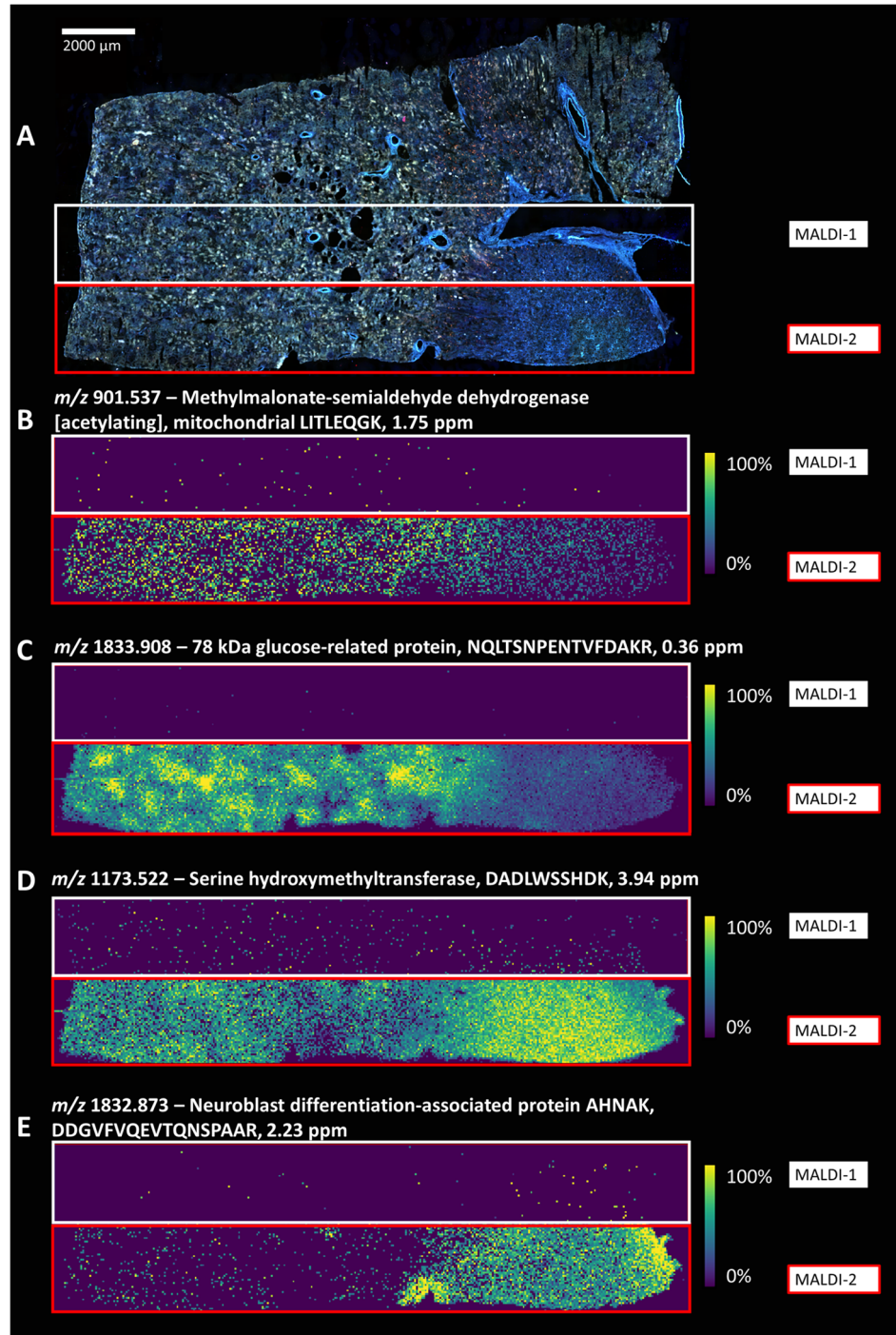
Figure 5.2. Autofluorescence image of human kidney (**A**) and ion images of peptides that localize to different tissue functional units of the kidney. Ion images were obtained via MALDI-1 (white outline, above) and MALDI-2 (red outline, below). Some species showed little change in intensity between MALDI-1 and MALDI-2 (**B**) while many species dramatically increased with MALDI-2 (**C-E**). Values are listed of ion *m/z*, protein designation, amino acid sequence of peptide, and mass error. Assignments are based on accurate mass measurements matched to the LC-MS/MS digest data within ± 5 ppm error for each peptide.
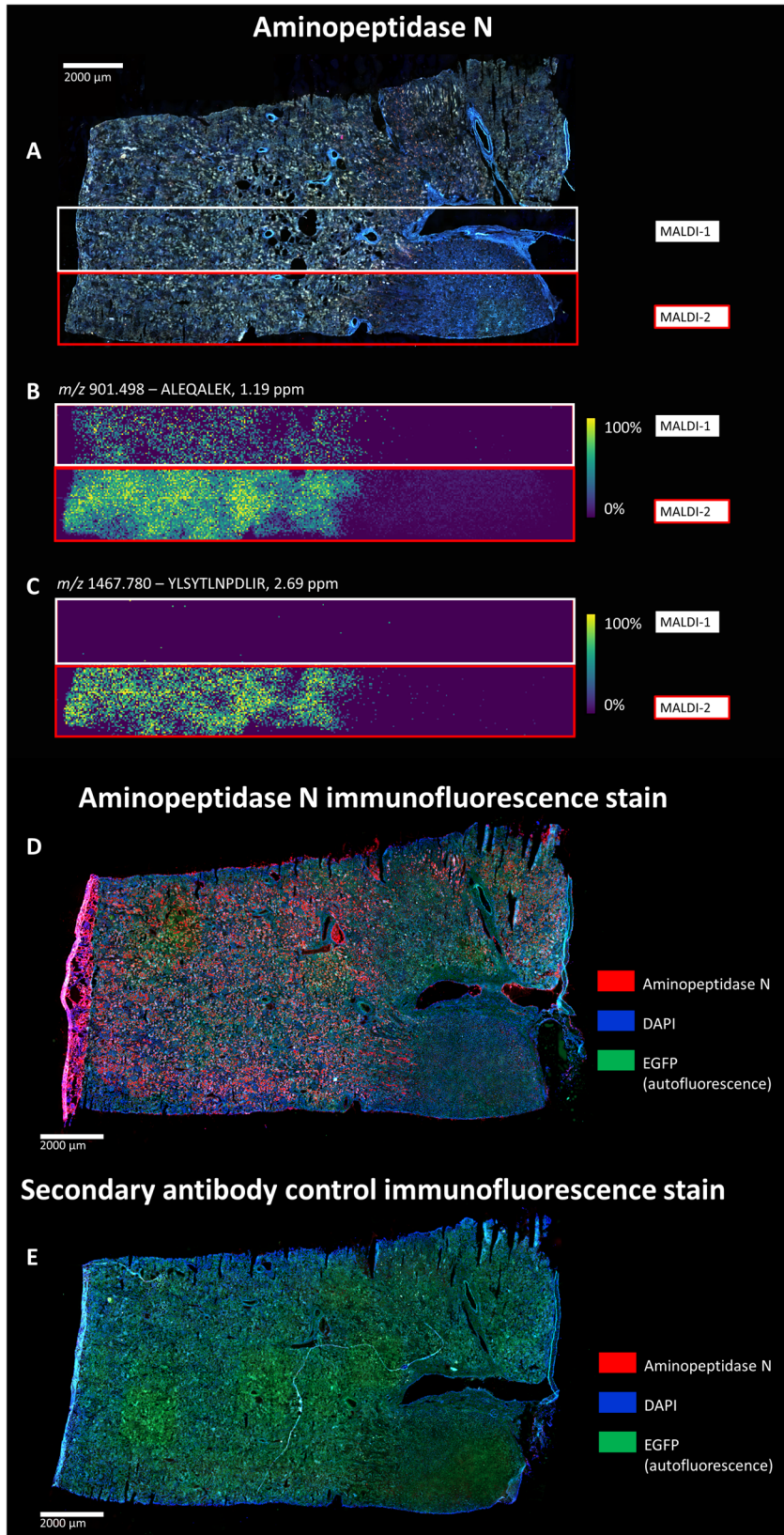
Figure 5.3. Autofluorescence image of human kidney (**A**) and ion images (**B, C**) show multiple peptide matches to the protein aminopeptidase N. Two peptides were detected that correspond to this protein and both species increase in signal with MALDI-2 analysis. The amino acid sequence, the measured *m/z*, and the ppm error of each peptide are listed above the ion image. Peptides localized similarly in the tissue which is expected from species relating to the same identified protein. Validation was performed by immunofluorescent staining of tissue with an anti-aminopeptidase N antibody (**D**) and it localized to similar regions of the tissue as with the ion images (**B, C**). A serial section was stained as a control and shows that there was no significant non-specific binding of the secondary antibody (**E**).

Some unannotated peptides decreased with MALDI-2 but were either below the S/N threshold or were not matched to an identified protein. This decrease in signal may be caused by matrix adduct formation or selective photoionization as observed in lipids analysis.[30] Other peaks that decrease with MALDI-2 were matrix-related and were detected in all IMS pixels, including areas away from the tissue. This decrease in matrix cluster signal was demonstrated previously with infrared post-ionization and is evidenced here with MALDI-2.[121] All peptides identified in MALDI-1 were also identified in MALDI-2 indicating that the decrease in signal did not affect the identified peptides to the extent that they would fall below the limit of detection. Fragmentation by collision-induced dissociation was performed on peptides over a range of *m/z* values to determine if increase in signal was related to matrix adduct formation but no loss of matrix was observed. Fragmentation of peptides from a serial section of tissue was performed to provide sequence information but the fragmentation results were poor due to low charge states formed by MALDI, and no conclusive data was generated.

The increase in peptide signals could possibly originate from fragmentation of larger proteins outside of the detectable mass range of the instrument. A 266 nm laser has been shown to dissociate singly protonated peptides, but the post-ionization laser energy used for the experiments reported herein is significantly lower (150 µJ vs. 3 mJ) than what was reported in these studies, both with nanosecond-scale pulse widths.[162] A bovine serum albumin tryptic digest was spotted with matrix and analyzed with MALDI-1 and MALDI-2 but interestingly, no significant change in spectra was observed with MALDI-2 – neither increase in species nor fragmentation of peptides was observed. This stands in contrast to spotted lipid standards that were enhanced with MALDI-2 as shown in our lab and by others.[136,163] Nevertheless, the use of MALDI-2 for tissue analysis allows for significant enhancement of peptide coverage by IMS.

To determine if certain amino acids or molecular characteristics affect MALDI-2 of peptides, amino acid composition analysis was performed (**Figure 5.4**). Significant differences in amino acid composition were discovered but no correlation in specific amino acid characteristics such as acidity/basicity, polarity, or charge was found. Additionally, peptide hydropathy values for each peptide were calculated based on peptide grand averages of hydropathy using amino acid hydropathy (GRAVY) values from Kyte and Doolittle[149,164] but no difference in distribution of GRAVY was observed (**Figure 5.5**). One limitation of these analyses is that the statistical power is hindered by the number of peptides identified. Still, these results are consistent with the ionization mechanisms previously proposed for

MALDI-2. It is thought that MALDI-2 proceeds through multiphoton ionization of matrix to form charged radicals that transfer charge to neutral analytes.[120,155,163] This may result in a reversal of ion suppression effects for some analytes, previously demonstrated for analysis of lipids and certain classes of phospholipids with MALDI-2.[123,136]
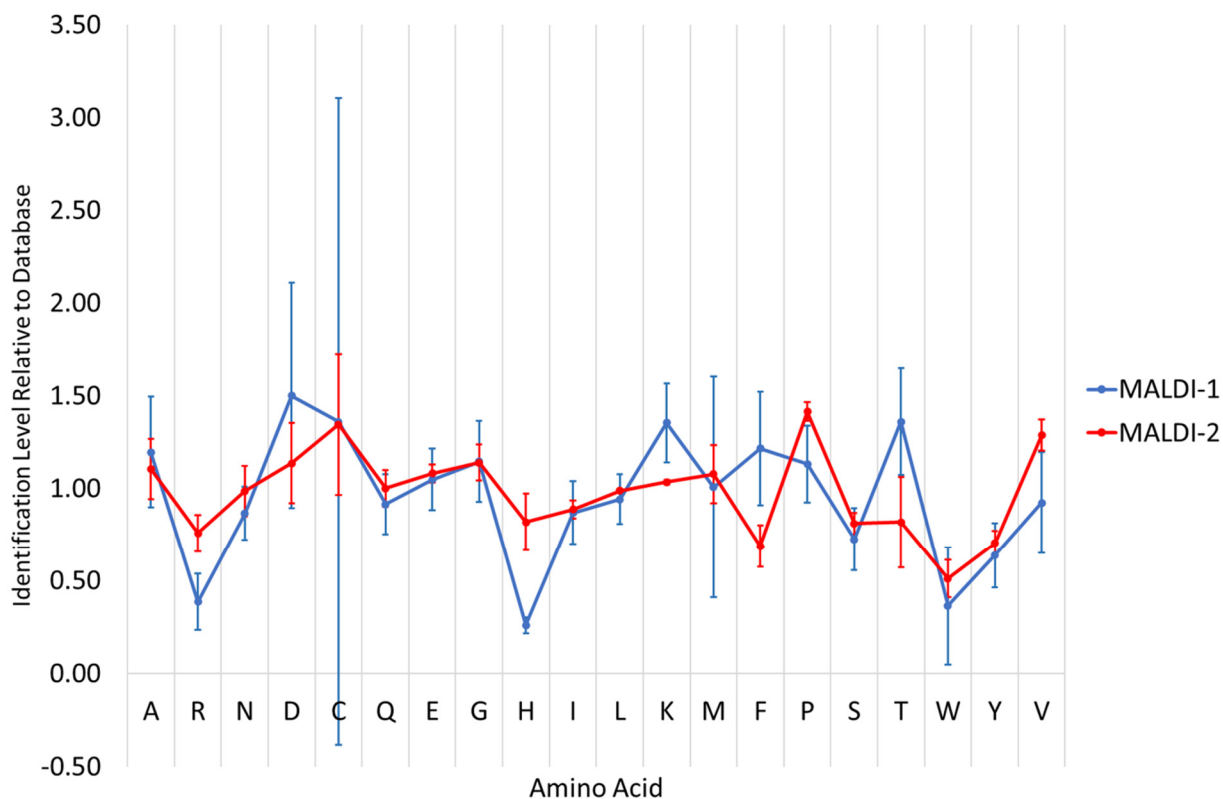
Figure 5.4. Amino acid composition analysis of unique peptides from proteins identified from ESI and IMS analysis for three technical replicates comparing MALDI-1 and MALDI-2. Amino acid frequency was compared to average values from SwissProt database. (MALDI-1: 17 ± 1.4, MALDI-2: 57.7 ± 2.4 peptides). The identification level of some amino acids was significantly different between MALDI-1 and MALDI-2 but they did not correspond to a certain class of amino acids.
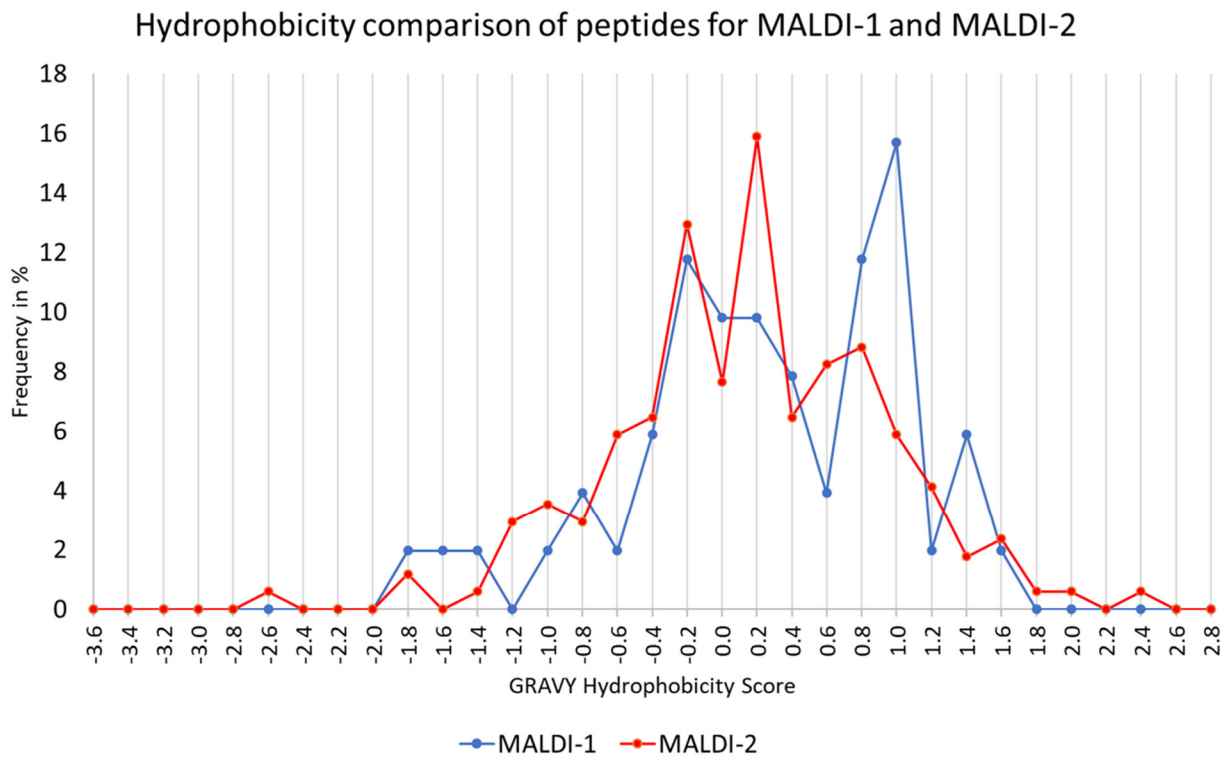
Figure 5.5. Grand average of hydropathy (GRAVY) distribution of unique peptides from proteins identified from ESI and IMS analysis, as a percentage of detection frequency, for MALDI-1 and MALDI-2 using hydropathy values from Kyte and Doolittle (1982). (MALDI-1: n= 57, MALDI-2: n=173). No difference was observed in the average hydropathy values of peptides detected with MALDI-1 compared with those detected by MALDI-

Generation of peptides in silico *matched to IMS data*

Many peptides in the IMS data remained unannotated after matching to LC-MS/MS data, and differences in observed peptides by ESI and MALDI is well established.[148–150] Additionally, there may be peptides detected with MALDI-2 that are not detected during LC-MS/MS analysis. To broaden the scope of the peptides searched, *in silico* digestion of proteins identified from LC-MS/MS was performed to generate a database of all theoretical peptides in the protonated form. This allows for annotation of peptides detected by MALDI-1 and MALDI-2 that may have gone undetected during LC-MS/MS analysis. Recently, this has been developed into a program called HIT-MAP by others.[165] In other work, reference databases for the identification of peptides from MALDI images were created from 33 tissue microarrays that were prepared in a similar manner to the imaged tissue.[166] We chose an alternative approach to increase the confidence of our assignments. Since individual tissue blocks or TMAs can vary greatly in their morphology (e.g., the percentage of cortex versus medulla) and therefore, in their protein content (as demonstrated in the above study), we chose to obtain our reference list of peptides from the same patient block of human kidney tissue that was used for MALDI IMS.[146] Ideally, these would be serial sections to get the closest histological match possible. Secondly, since it is established that correlation of peptides observed by MALDI and ESI is poor[148–150], we expanded the list of peptides available to match to MALDI IMS peptides by performing an *in silico* digest of the proteins identified by LC-MS/MS. Lastly, we matched MALDI IMS peptides within a mass tolerance of 5 ppm to the theoretical *m/z* and required at least two peptides per protein be identified in the MALDI IMS dataset in an approach similar to previously published work.[146]

Table 5.1. Number of unique proteins and matched to MALDI-1 and MALDI-2 data (n=3 replicates of human kidney tissue IMS) comparing *in silico* approach to LC-MS/MS PMF. Charge was accounted for and carbamidomethyl was subtracted from the mass of LC-MS/MS peptides, as this would not be present in the MALDI data.

	A) *Matched to in-silico* digest		B) *Matched to LC-MS/MS*	
	MALDI-1	MALDI-2	MALDI-1	MALDI-2
Unique Peptides	1337 ± 96	2076 ± 362	178 ± 5	445 ± 79
Unique Proteins	584 ± 27	703 ± 50	153 ± 5	358 ± 64
Unique Proteins, ≥2 peptides	276 ± 20	401 ± 60	9 ± 1	26 ± 1
MALDI peaks IDed (at ≥ 2 peptides/protein level)	1071 ± 97	1835 ± 392	42 ± 9	148 ± 56

Overall, IMS with MALDI-2 and subsequent protein identification by PMF allowed for identification of 2,076 ± 362 unique peptides (equivalent to 77% ± 0.5% of the deisotoped peaks) and 401 ± 60 proteins that were identified by 2 or more peptides, based on triplicate measurements.[153,167] 703 ± 50 proteins were identified by one peptide only; while these do not meet our criteria for identification, proteins of interest from this list could be validated in the future. In comparison, MALDI-1 alone led to approximately 30% fewer proteins identified with 2 or more peptides (**Table 1**). These numbers represent an average of proteins identified in each replicate. Many peaks in each spectrum were identified; however, additional peptide identifications may be possible when common MALDI adducts such as sodium and potassium are considered. The database constructed by *in silico* digestion contained 144,619 unique peptides from the 1,361 LC-MS/MS proteins to compare with IMS data. While this could potentially increase the number of false positives for proteins, this approach allows for identification of peptides detected by MALDI-1 and MALDI-2 that have gone undetected during LC-MS/MS analysis. These data also provide a starting point to enable discovery of potential molecular markers that can be further identified and validated using orthogonal methods.

METHODS

Tissue handling and preparation for MALDI IMS

Human kidney tissues were collected as part of normal non-neoplastic portions of nephrectomy samples.[168] Tissue blocks were frozen using an isopentane/dry ice slurry, embedded

in carboxymethyl cellulose, and cryo-sectioned at 10 μm thickness onto indium-tin oxide coated glass slides (Delta Technologies, Loveland, CO, USA).[169,170] Six serial sections were placed onto three slides and each slide was analyzed in triplicate as technical replicates. Sections were optically imaged using autofluorescence to obtain tissue morphological information from the same section used for IMS.[134] Sections were washed to remove the carboxymethyl cellulose embedding material using ethanol and water[171] followed by Carnoy's solution wash protocol to remove salts and lipids. Antigen retrieval was performed to thermally denature the proteins prior to the application of trypsin with a pneumatic sprayer, as previously described[134] and samples were digested *in situ* at 37°C overnight in a humidity oven (Espec North America, Hudsonville, MI, USA) set to 100% relative humidity. The MALDI matrix (α-cyano-4-hydroxy-cinnamic acid [CHCA]) was applied by pneumatic sprayer (HTX Technologies LLC, Chapel Hill, NC, USA) at 0.1 mL/min. flow rate for 8 passes with a nozzle temperature of 85°C. Matrix concentration was 5 mg/mL in 90% acetonitrile with 0.1% trifluoroacetic acid.[37] Sample preparation for peptides was optimized to maximize signal for MALDI-1 and to maintain the spatial localization of peptides.

Immunofluorescent staining

Immunofluorescent staining for aminopeptidase N was performed by fixing tissue in 4% paraformaldehyde in phosphate buffered saline (PBS) for 10 minutes. The tissue was covered with blocking buffer (0.5% Tween 20 and 1% bovine serum albumin in PBS) 1 hour at room temperature. The primary antibody (Recombinant anti-CD13 antibody, Abcam, ab7417, lot number: GR3388979-2 [0.423 gm/mL]) was diluted 1:500 using the blocking buffer. The solution was placed on the tissue and was incubated overnight at 4°C in a humidity chamber. The primary antibody was removed by washing twice with PBST followed by once with PBS. The secondary antibody (goat anti-mouse, cy5) was diluted 1:500 in PBS and tissue was incubated in it, protected from light. Tissue was washed 2x with PBST, 1x with PBS. A coverslip was mounted onto the slide using a water-soluble mounting media containing DAPI (DAPI Fluoromount-G, SouthernBiotech).

IMS analysis

Tissue section analysis by MALDI IMS was performed in positive ion mode using an Orbitrap Elite instrument equipped with a MALDI ion source (Spectroglyph LLC, Kennewick,

WA, USA), which included a second laser for MALDI-2 functionality (266 nm, CryLaS GmbH, Berlin, Germany) as described previously.[136] The instrument was operated with a range of *m/z* 500-2000 and was calibrated with calibration mix using the ESI inlet of the Spectroglyph source prior to acquisition. The MALDI-2 beam was positioned 430 μm above the MALDI-1 ablation region and lasers were operated at 60 Hz each and irradiation was offset temporally by 20 μs. Lasers were operated at 5 μJ for MALDI-1 and 150 μJ for MALDI-2. Spectra were acquired with AGC off and a fill time of 250 ms to obtain a constant 15 laser shots per IMS pixel. Samples were analyzed at spatial resolution of 50 μm with an ablation diameter of 25 μm for MALDI-1. Similar and adjacent regions of the same section were analyzed with MALDI-1 and MALDI-2, and the ion images contained ~15,000 pixels in each region. For image visualization, ion images were converted to vendor-neutral imzML format using ImageInsight software (Spectroglyph) and imported into SCiLS software (Bruker, version 2019b). Comparable regions of tissue were outlined using SCiLS software, averaged spectra were exported as .csv files, and then were imported into mMass (mmass.org, Version 5.5.0) for further processing. The IMS data were processed with root mean square normalization prior to image generation. Example ions and their localization were compared to the optical autofluorescence image of tissue.

LC-MS/MS proteomic workflow

A tissue homogenate of the same tissue used for IMS was analyzed using bottom-up LC-MS/MS proteomic protocols. Full experimental details including sample preparation and data search parameters are described on the Protocols.io website.[172–174] The sample was analyzed on a Thermo Scientific Orbitrap Fusion Tribrid mass spectrometer in line with a Thermo Scientific Easy-nLC 1000 UHPLC system. Tissue sections were homogenized in a Tris, 1% NP-40 buffer, and 100 μg of precipitated protein was digested with trypsin. After desalting, the sample was dried down. Prior to analysis, the sample was reconstituted in 0.1% formic acid at 1 μg/μL. Sample, 2 μL, was injected via the autosampler and loaded onto a fused silica pulled-tip C18 column (100 μm i.d. x 350 mm length,) packed with Waters C18 BEH resin (1.7 μm particle size, 130 Å pore size), with 0.1% formic acid in water (mobile phase A). Peptides were separated over a 127-minute gradient with 0.1% formic acid in water and 0.1% formic acid in acetonitrile (mobile phase B), and eluted peptides were ionized via positive mode nESI. The top 17 MS1 peaks were chosen in data dependent acquisition mode. Data were analyzed using MaxQuant version 1.6.7. The output

included 1,361 proteins identified by two or more unique peptides after removal of reverse hits, potential contaminants, and peptides identified by modified sites only. The proteomics data from this publication have been deposited to the ProteomeXchange Consortium[175] [http://www.proteomexchange.org/] via the PRIDE partner repository[176] with the dataset identifier PXD023877.

Identification of MALDI-generated peptides using LC-MS/MS

The list of peptides from the LC-MS/MS workflow was compared to the MALDI-1 and MALDI-2 peak lists from the averaged spectra for protein identification by peptide mass fingerprinting (PMF). Averaged spectra were generated in SCiLS by selecting comparable regions of tissue in MALDI-1 and MALDI-2 ion images and exporting the averaged spectrum as .csv file format. Averaged spectra were imported into mMass, deisotoped, and peak picked at 50% FWHM with a signal-to-noise ratio (S/N) threshold of 3. To ensure accurate peptide annotations, mass calibration post-acquisition was performed. The mMass reference file was modified to include potassiated CHCA clusters ([4M+K]$^{+}$, [5M+K]$^{+}$, [6M+K]$^{+}$ at *m/z* 795.1335, 984.1761, and 1173.2187, respectively) for a 3-point linear calibration.[177] The peak list from the averaged, recalibrated spectra were matched (± 5 ppm mass error) to the peptide closest in theoretical *m/z* from proteins identified in the LC-MS/MS data. Next, MALDI ions with two or more peptides matched to a protein were selected to generate ion images. A calibration curve was generated to align the calibrated mMass data to the uncalibrated IMS data in SCiLS using the 3-point linear calibration described above. To match the calibrated peak list to the uncalibrated, graphs were generated with *m/z* on the y-axis and spectral bin number on the x-axis. Linear best fit line equations for the uncalibrated and recalibrated spectra were used to back-calculate the *m/z* values for the peptides of interest in the SCiLS datasets (workflow shown in **Figure 5.6**). Those peak lists were imported into SCiLS to generate ion images which were grouped based on their annotated protein and the ion images were reviewed to verify that there were at least two ion images of peptides that localize to similar regions of the tissue. If the peptides did not localize to similar regions, the peptides and protein were removed from the list of identifications.
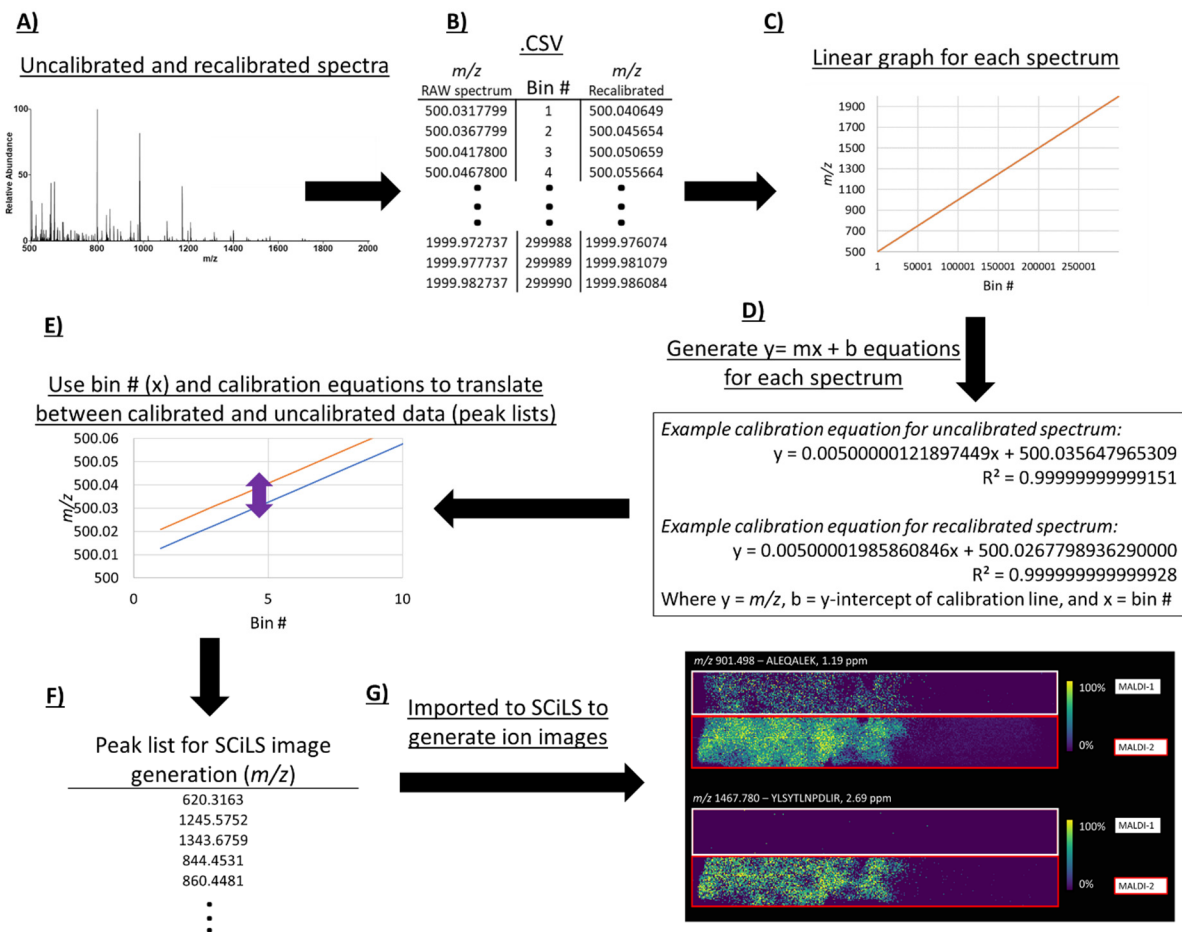
Figure 5.6. Detailed workflow showing the comparison between the calibrated peak list to uncalibrated data for ion image generation for a single IMS acquisition (repeated for MALDI-1 and MALDI-2, in triplicate). This is needed to rectify the data used for peptide identification (recalibrated) with the RAW data used for ion image generation (uncalibrated). Averaged spectra of tissue regions obtained by IMS (**A**) are converted to .csv format to extract the bin # for each *m/z* point of calibrated and uncalibrated spectra (**B**). Graphs of *m/z* vs. bin # are generated for each spectrum (**C**) to obtain the lines of best fit along with its corresponding linear equation (**D**), as well as to serve as a visual representation of the uncalibrated and recalibrated data. Values for "m" and "b" in the equations (**D**) are shown to 10+ decimal places to ensure fidelity between calibrated and uncalibrated values. The calibration equations are used to translate between calibrated and uncalibrated data. Peak list of identified peptides (not shown) can then be "uncalibrated" (**F**) and imported into SCiLS to generate ion images for the corresponding peptide ions of interest (**G**).

Identification of MALDI-generated peptides from in silico *digestion of proteins*

The proteins identified via LC-MS/MS were digested *in silico* using a local install of Protein Prospector to obtain a database of all possible tryptic peptides. Parameters were as follows: database = SwissProt revised September 18, 2019; digestion enzyme = trypsin; instrument = ESI-FT-ICR-CID; minimum digestion fragment = 400; maximum digestion fragment = 4,000 Da; minimum digestion fragment length = 5; maximum hits = 1,000,000; maximum missed cleavages = 2; variable modifications = acetylation N-term, Met-loss N-term, Met-loss N-term and acetylation N-term, oxidation of methionine. PMF was used to match within 5 ppm deisotoped IMS peaks from MALDI-1 and MALDI-2 analyses (with S/N of 3 or greater) to the theoretical *m/z* values of peptides resulting from *in silico* digestion of LC-MS/MS proteins. PMF is typically used with nearly purified proteins, where digestion of the sample results in many peptides that can distinguish the protein of origin. In the case of in-situ tissue digestion, the sample is molecularly complex, and hundreds of proteins will require identification.

To deal with multiple PMF matches to a single MALDI ion, a simple scoring system was implemented that 1) ranked proteins in the LC-MS/MS dataset using sequence coverage and the number of identified peptides per protein normalized to molecular weight, and 2) ranked the mass accuracy of the MALDI-to-peptide matches as well as the number of potential peptides per protein for each match. The scoring system also considered the number of potential matches with the same mass difference. For mass accuracy, matches with a smaller difference between the theoretical peptide *m/z* and the IMS *m/z* value positively affected the score. Additionally, a smaller number of matches (and thereby less uncertainty) had a positive effect. Likewise, the LC-MS/MS protein rank was higher, and positively affected the score of a match, when there was more sequence coverage and peptides (normalized to MW). This identification strategy needs further validation as it is possibly biased toward higher molecular weight proteins. It was implemented here to provide protein identifications to further compare MALDI-1 and MALDI-2.

CONCLUSIONS

Here, we demonstrated that MALDI-2 IMS increases sensitivity and molecular coverage for peptides from *in situ* bottom-up proteomic analysis of thin tissue sections. These improvements enabled ~3x increase in identification of proteins using the following criteria: 1) protein is matched

to LC-MS/MS data with two or more peptides, 2) peptide is within 5 ppm error, 3) and the peptides colocalize in tissue. Additionally, *in silico* digestion of proteins allowed for identification of peptides detected in MALDI data that were not detected by ESI-MS/MS. These proof-of-concept experiments demonstrate the utility of MALDI-2 for enhanced detection of peptides from tissue sections for bottom-up protein IMS. This technology will be beneficial for future studies to obtain both protein identity and corresponding spatial distribution of clinically relevant peptide and protein species. These technical improvements are also critical for providing more robust and complete molecular imaging capabilities for large-scale tissue mapping projects as well as combining these results with serial sections of tissue analyzed with MALDI-2 for supplementary lipidomic analysis. This way, a more complete molecular understanding of non-diseased and diseased tissue can be used to characterize disease states and inform both the development and the efficacy of therapeutic treatments.

Acknowledgements

CHAPTER VI

PROTEIN MALDI IMAGING MASS SPECTROMETRY REVEALS NUMEROUS MODIFICATIONS OF IAPP IN HUMAN T2D AMYLOID PLAQUE-CONTAINING ISLETS

INTRODUCTION

Diabetes is a widespread disease characterized by the loss of insulin-producing β cell function and mass in the pancreas, but the exact cause is yet to be determined.[69] Over 90% of patients with type 2 diabetes (T2D) have amyloid plaques in the pancreas, a phenomenon hypothesized as a causative factor of β cell death.[72,178,179] Amyloid plaques are primarily composed of aggregates of a small peptide, the 37 amino acid islet amyloid polypeptide (IAPP).[77,78] The IAPP peptide is secreted by β cells in a 1:100 ratio with insulin under normal conditions[70] and is thought to be involved in gastric emptying and regulating satiety.[180] The mechanism of IAPP aggregation to form amyloid plaques is incompletely understood. Still, recent research has investigated the roles of post-translationally modified forms of proteins that localize to the islets.[181,182]

Proteins frequently undergo a series of modifications after translation to become functional. This process is called post-translational modification (PTM) and can occur by an enzymatic process. PTMs are important to T2D as they have been shown to localize to islets by immunohistochemical analysis.[182] Examples of non-enzymatic PTMs include the formation of advanced glycation end products (AGEs) such as N^ε-(carboxymethyl) lysine (CML), N^ε-(carboxyethyl) lysine (CEL), and pyrraline.[183–185]. Formation of AGEs can occur by the reaction of a protein with glucose to produce a Schiff base that can rearrange to form the Amadori product.[186,187] The Amadori product can undergo subsequent non-enzymatic reactions to form AGEs.[188] An alternative pathway for AGE formation is through the generation of many reactive dicarbonyl compounds including glyoxal, methylglyoxal, and deoxyglucosones through oxidation of glucose and subsequent reaction with a protein to form CML, CEL, and pyrraline, respectively.[187,188] AGEs have been shown to be detrimental to β cell health, bind to the receptor for AGEs (RAGE),[189,190] modify protein folding,[191] affect IAPP aggregation,[78] and have been a recent focus for its role in facilitating plaque formation in islets of T2D patients[77,78]. There is a need to characterize the PTMs of IAPP present in amyloid plaques in the islets of T2D patients to

understand the mechanistic role of modified IAPP in the development of islet dysfunction leading to diabetes.

The pancreas is a complex organ where islets comprise ~1% of the pancreatic mass. [192,193] Islets are the primary location of aggregation of IAPP, but standard methods to analyze the protein composition of the pancreas include homogenization of whole tissue. Because islets comprise such a small fraction of the entire tissue, homogenization methods dilute islet-specific analytes to such a degree that they may fall below the detection limit. An additional drawback of tissue homogenization is that the information on the location of analytes within the tissue is lost. Proteomic techniques with a spatial component are needed for the molecular characterization of islets and plaque-specific analytes. Spatially targeted approaches such as liquid extraction surface analysis allow the extraction of intact proteins with an extraction diameter (~1 mm) larger than the diameter of a typical islet (100-200 μm).[194] Small tissue regions can also be targeted using laser capture microdissection, but other technologies to analyze small tissue regions are still being developed.[195] Methods of molecular imaging of pancreatic sections include chemical and immunofluorescent staining, which can provide very high spatial resolution images with high sensitivity. The high chemical specificity requires targeted analysis and is often limited in the number of analytes multiplexed in a single imaging experiment. Recent advances in multiplexing of immunofluorescent tags have allowed tens of proteins to be mapped to a single tissue section with high spatial resolution using technologies such as co-detection by indexing (CODEX). However, these technologies still rely on *a priori* knowledge for targeted analysis. [196] Furthermore, there is a lack of PTM-specific validated antibodies such that modified forms of proteins are often indistinguishable.

MALDI IMS allows for the multiplexed, untargeted detection of hundreds to thousands of analytes from a single IMS experiment in a spatially resolved manner. MALDI-2 post-ionization has been shown to enhance signal of metabolites, lipids, and tryptic peptides but its effect on intact proteins is unknown. We use MALDI-1 and MALDI-2 IMS for the untargeted, multiplexed, sensitive analysis of intact proteins in human pancreas sections from six ND and five T2D donors. Sections of the pancreas were analyzed by immunofluorescence and staining for amyloid plaques and were compared to MALDI IMS analysis of serial sections of tissue. Using MALDI IMS, multiple PTMs, including AGEs, were shown to localize with the unmodified form of the protein

in amyloid plaque-containing islets. Chemical stains show the presence or absence of amyloid plaque. Still, the sensitivity and wide dynamic range of MALDI IMS allow for detecting IAPP at baseline levels in the ND donor and elevated levels in islets containing amyloid plaque.

MALDI-2 FOR ENHANCEMENT OF INTACT PROTEIN SIGNAL FROM TISSUE

The utility of MALDI-2 technology for significant signal enhancement has demonstrated numerous biomolecular classes including lipids and tryptic peptides, but enhancement of protein signal has not been demonstrated. Here, we used the timsTOF Pro instrument with a MALDI source to allow for a MALDI-2 laser as described in Chapter V. In this study, tissue sections from ND and T2D donors were prepared for protein analysis with MALDI-1 and MALDI-2 to evaluate the feasibility of using MALDI-2 on the modified timsTOF Pro instrument for protein analysis of pancreatic tissue sections.

METHODS

Sample preparation

Previous experience using MALDI-2 for enhancement of tryptic peptides guided part of the sample preparation and acquisition for these tissues. The MALDI matrix CHCA has been previously shown with MALDI-2 to enhance lipid and tryptic peptide signal, compared with MALDI-1 alone, so it was used for protein analysis. The tissue sections were washed with a Carnoy wash protocol consisting of 70% ethanol (30 sec), 100% ethanol (30 sec), Carnoy's solution (6:3:1 ethanol/chloroform/acetic acid, 2 min), 100% ethanol (30 sec), water (30 sec), 100% ethanol (30 sec) and dried for 30 minutes in a benchtop vacuum desiccator. CHCA matrix was applied using a pneumatic, robotic sprayer (TM Sprayer M3, HTX Technologies) to obtain a homogeneous layer of matrix. Matrix solution was prepared as 5 mg/mL CHCA in 90% acetonitrile, 0.1% trifluoroacetic acid. Sprayer conditions were 85°C nozzle temperature, 10 psi nitrogen, 8 passes in CC pattern, 700 mm/minute nozzle speed, 2 mm track spacing, no dry time, 40 mm distance between nozzle and stage, solvent pushed at 0.1 mL/minute with 90% acetonitrile.

MALDI IMS

Ion images were acquired on a timsTOF Pro modified with a MALDI source and inclusion of a laser for MALDI-2. The MALDI-2 laser (Ekspla NL 204 Nd:YAG frequency quadrupled 266

nm) was positioned to irradiate 500 µm above the sample surface, operated at a frequency of 1000 Hz, and set to irradiate 40 µs after the MALDI-1 laser. The instrument was operated in qTOF mode and was set to acquire from 1000 – 10,000 *m/z* at 50 µm spatial resolution with beam scan on using the Smart Beam setting of Single M2. Focus Pre TOF settings were 200 µs for the Transfer Time and 25 µs for the Pre Pulse Storage. Under the Tune tab and Processing, the Absolute Threshold (per 1000 sum.) was set to 10 to allow for detection of low-intensity ions. The TIMS In pressure was set to its lowest setting of 1.5 mBar and the instrument was calibrated using red phosphorus clusters. After acquisition, ion images were opened together in SCiLS 2022 for ion image generation and averaged spectrum export. Spectra were imported into mMass for calibration and further processing.

Results and discussion

Intact proteins were detected from human pancreas tissue up to *m/z* 7000 (**Figure 6.1**). Signals were relatively sparse over the *m/z* range and most signals localized to islets. Species such as insulin and glucagon were detected and identified by accurate mass measurements (<20 ppm error) (**Figures 6.2 and 6.3**). Multiple ions localized to the islet regions (colocalized with insulin and glucagon) but neither IAPP (*m/z* 3904) nor any of its post-translationally modified forms were detected. The sensitivity for intact proteins was relatively low as there was a large baseline and low S/N for most proteins other than insulin. In contrast with the enhancement of lipid and tryptic peptide signals in **Chapters III**, **IV**, and **V**, there was no enhancement of signal for intact proteins from human pancreas sections coated with CHCA and analyzed using MALDI-2.
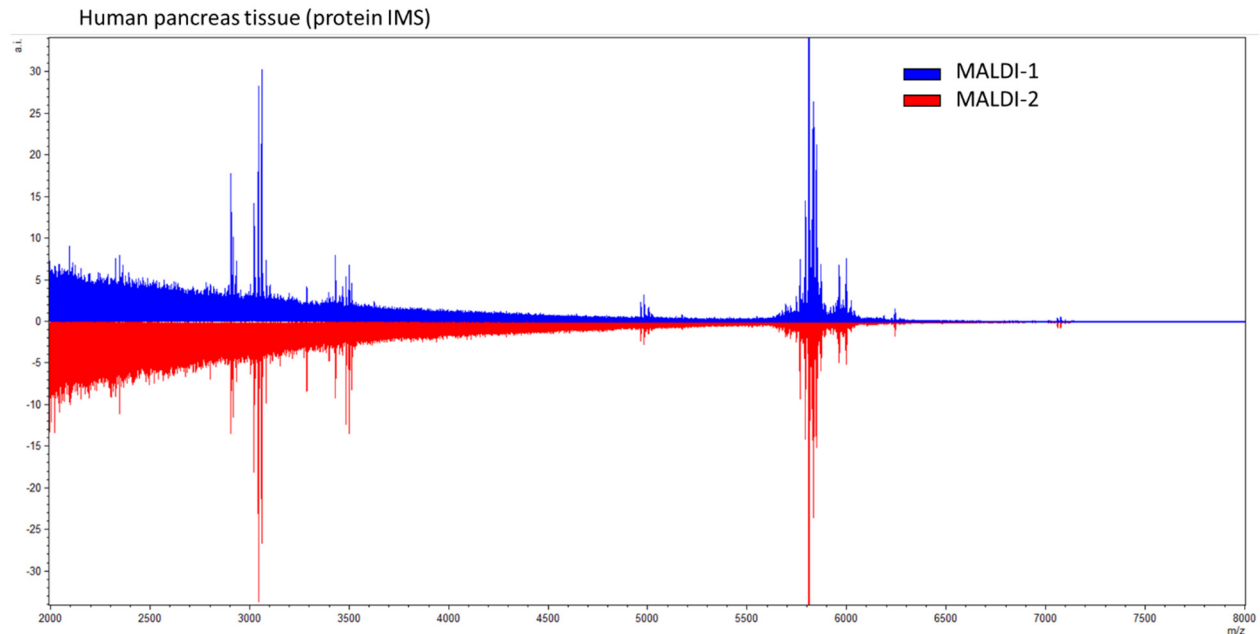
Figure 6.1. Representative mass spectra from human pancreas tissue analyzed with MALDI-1 and MALDI-2 prepared with CHCA for intact proteins. The spectrum is enhanced to show lower intensity ions while the insulin peak (*m/z* 5808) was much more intense at ~200 arbitrary intensity (a.i.). There was no significant protein signal difference between MALDI-1 and MALDI-2.

PROTEIN IMS OF ND AND T2D PANCREATIC TISSUE USING A 15T FT-ICR

MALDI-2 did not allow for signal enhancement of intact proteins on the TOF platform, as indicated in the previous section. Additionally, intact protein analysis can prove difficult for low mass resolving power instruments as there are many isotopes, post-translationally modified forms of proteins, and overlapping isotopologues.[71,143] Therefore, samples were analyzed with MALDI-1 using a high mass resolution 15T FT-ICR instrument for sensitive detection of proteins with high mass resolution to differentiate among the numerous isotopologues in the protein data.

Tissue acquisition and treatment

Pancreata from ND donors (ND) (n=6) and T2D donors (n=5) were obtained through agreements with the International Institute for Advancement of Medicine (IIAM), National Disease Research Interchange (NDRI), and local organ procurement organizations. These donors were all screened for criteria reflective of a representative pancreas, including limited ICU/hospital stay, absence of pancreatitis, and no history of congestive heart failure or end-stage renal disease. Pancreata were received within 18 hours from cross-clamp and maintained in cold preservation solution on ice until processing. Pancreata were then cleaned from connective tissue and fat,

measured, and weighed. Multiple cross-sectional slices of the pancreas with 2-3 mm thickness were obtained from the head, body, and distal tail. Pancreatic slices were divided into four quadrants and then snap frozen in liquid nitrogen and stored at -80°C until further use or processed for cryosections. Serial 10 μm cryosections were cut for MALDI IMS and immunohistochemical analysis. Sections were mounted onto Superfrost Plus Gold microscope slides (Fisher Scientific, USA). Briefly, cryosections were air-dried and fixed with 4% paraformaldehyde in 10mM PBS for 10 minutes before permeabilization in 0.2% Triton-X in 10mM PBS. After permeabilization, sections were washed three times in 10mM PBS for 3-5 minutes each, then blocked in 5% normal donkey serum in 10mM PBS for 60-90 minutes in a humidified chamber at room temperature. Sections were incubated overnight with primary antibodies (goat anti-somatostatin, Santa Cruz, sc7819 and mouse anti-glucagon, Abcam, ab10988) diluted in antibody buffer (0.1% Triton-X, 1% BSA in 10mM PBS) in a humidified chamber at 4°C, then washed three times in 10 mM PBS for 10 minutes each. Sections were then incubated with secondary antibodies (donkey anti-goat Cy5, Jackson Immunoresearch, 705-175-147 and donkey anti-mouse Cy3, Jackson Immunoresearch, 715-165-150), prepared in antibody buffer for 90 minutes in a humidified chamber protected from light, at room temperature. Amyloid was visualized using a 2-minute incubation in Thioflavin S (0.5% w/v; #T-1892, Sigma, St. Louis, MO) followed by a brief wash in 70% ethanol. Sections were treated with DAPI (5 mg/mL stock diluted 1:50,000 in 10mM PBS) for 10 minutes and then washed three times in 10mM PBS for 15 minutes each. Slides were mounted using Aqua-Poly/Mount (Polysciences, # 18606-20) before imaging with a Fluorescent ScanScope (Aperio, Leica Biosystems). Islets in the tissue section were hand-annotated based on size (>50 mm) and the presence of multiple endocrine cell types. Islets with any Thioflavin S signal were designated as amyloid-positive.

MALDI IMS analysis

Slides of tissue sections for MALDI IMS stored at -80°C were brought to room temperature in a benchtop vacuum desiccator to reduce condensation during thawing and to reduce subsequent analyte delocalization. Slides were washed with Carnoy's solution protocol to remove salts and lipids.[105] Briefly, washes were of 70% ethanol (30 sec), 100% ethanol (30 sec), Carnoy's solution (6:3:1 ethanol/chloroform/acetic acid, 2 min), 100% ethanol (30 sec), water (30 sec), 100% ethanol (30 sec) and dried on a benchtop vacuum desiccator for 30 minutes. MALDI matrix (2',5'-

dihydroxyacetophenone) was applied using a custom sublimation apparatus to apply a homogeneous coating with a density of approximately 1.7 µg/mm^2. Samples were rehydrated prior to analysis to improve protein sensitivity using a 1 mL solution of 50:50 water/trifluoroacetic acid sealed in a rehydration apparatus and heated at 37°C for two minutes. ND and T2D tissue samples were analyzed by MALDI IMS using a 15T solariX XR FT-ICR instrument equipped with a dual MALDI/ESI interface (Bruker Daltonics, USA). The instrument source was previously modified to allow for proteins to be detected at a more comprehensive *m/z* range.[142] The instrument was calibrated prior to acquisition using a mixture of proteins spotted with a matrix. Mass analysis range was set to *m/z* 1,000 – 30,000 with a 2.31-sec time-domain transient. The laser was operated at a focus setting of "small," tuned for ~50 µm ablation diameter, with laser operation settings of 2000 shots per pixel and a 2,000 Hz frequency. Ion imaging parameters were set to obtain 50 µm spatial resolution. ND and T2D samples were acquired in the same MALDI IMS experiment.

Calibration of data sets was performed after acquisition using FTMS Processing software (Bruker, USA) with the three most intense isotopes of glucagon, insulin, and thymosin β-4 as reference masses. Calibrated data were opened in SCiLS 2021 (Bruker Daltonics, USA) for further processing and ion image generation. Regions of IAPP in the T2D pancreas were outlined in SCiLS software using the *m/z* correlation feature by selecting two isotopes of IAPP, visualizing them in the correlation window, selecting the most intense spectra from the window, and generating a region that includes those spectra. In this way, a new region containing the spectra with an intense IAPP signal can be produced to compare against the location of amyloid plaques in the stained serial section. Additionally, this region of pixels with a high IAPP signal allows for rapid manual determination of other protein signals that localize uniquely with IAPP. No normalization was applied to account for the significant intensity differences between the islet and exocrine regions of tissue. Ion images were exported and manually registered with the serial section of stained tissue using the image transparency feature in PowerPoint to match the location of islets in the stained image and from the IMS data.

RESULTS AND DISCUSSION

Traditional approaches to characterize the localization of biomolecules within a tissue, like immunohistochemistry or immunofluorescence (IF), require the development of antibodies to bind to one protein of interest. Other approaches such as chemical staining can be targeted to bind to

specific morphological structures, such as the β-sheet fibrils of amyloid plaques. The targeted nature of IF and chemical staining allows for very sensitive detection at high spatial resolution, but *a priori* knowledge of the molecular composition of the tissue is needed prior to analysis. Additionally, even though IF stains have been developed for numerous proteins, validation of IF methods remain a challenge.

In **Chapter II**, high spatial resolution technology (combining transmission geometry and microstepping) was developed but here, lower spatial resolution was needed for sensitive detection of species of low intensity. Additionally, **Chapters III**, **IV**, and **V** showed the utility of MALDI-2 for enhancement of some lipid and peptide signals but no enhancement of signal from intact proteins from pancreas tissue was detected, as in the previous section. Therefore, MALDI-1 was used for analysis, and ion images were acquired at 50 μm spatial resolution such that the location of individual islets (~150 μm in diameter) could be visualized by IMS while also maximizing protein signal. In contrast to tissue staining, an untargeted approach such as MALDI IMS allows for the multiplexed detection of hundreds of species within an IMS experiment. To demonstrate these capabilities, serial sections of pancreas tissue from ND and T2D donors were analyzed (**Figure 6.2 B-D**) to compare with results from traditional staining methods (**Figure 6.2 A, E**). Staining of tissue sections allows for specific tagging of cells and plaques at high spatial resolution. Stains include amyloid plaque stained with Thioflavin S, α, β, and δ cells stained using IF, and nuclear DNA stained with DAPI (**Figure 6.2 A**). Staining by IF for α and δ cells allows for the visualization of islets within the tissue as well as the distribution of each cell type (**Figure 6.2 A**). Staining with Thioflavin S provides for visualization of amyloid plaques that are present within T2D donor samples. Thioflavin S is a chemical stain that intercalates between β-sheet fibrils to allow for visualization of mature plaques, but it does not stain unaggregated IAPP that is known to be naturally present at baseline levels (**Figure 6.2 E**, ND donor). [179,197–199] Using the IMS data, we can visualize molecular signals corresponding to certain cell types and structures within the pancreas. Examples are shown in **Figure 6.2 B-D** for the false-color ion images of somatostatin (*m/z* 1639, corresponding to δ cells), glucagon (*m/z* 3484, corresponding to β cells), and IAPP (*m/z* 3904, corresponding to amyloid plaque). Dozens of other protein signals that localized to islet and exocrine tissue were also detected that localized to various regions throughout the pancreas, including to the islets and to exocrine regions but were not shown here. The serial sections of tissue between **Figure 6.2 A, E** and **Figure 6.2 B-D** were aligned for comparison. As expected, the

molecular signatures of somatostatin and glucagon localize to islet regions, where α and δ cells localized (**Figure 6.2 A-D**), whereas IAPP detected by IMS localized to both islets and plaque regions (**Figure 6.2 D, E**) where IAPP is expected to localize.
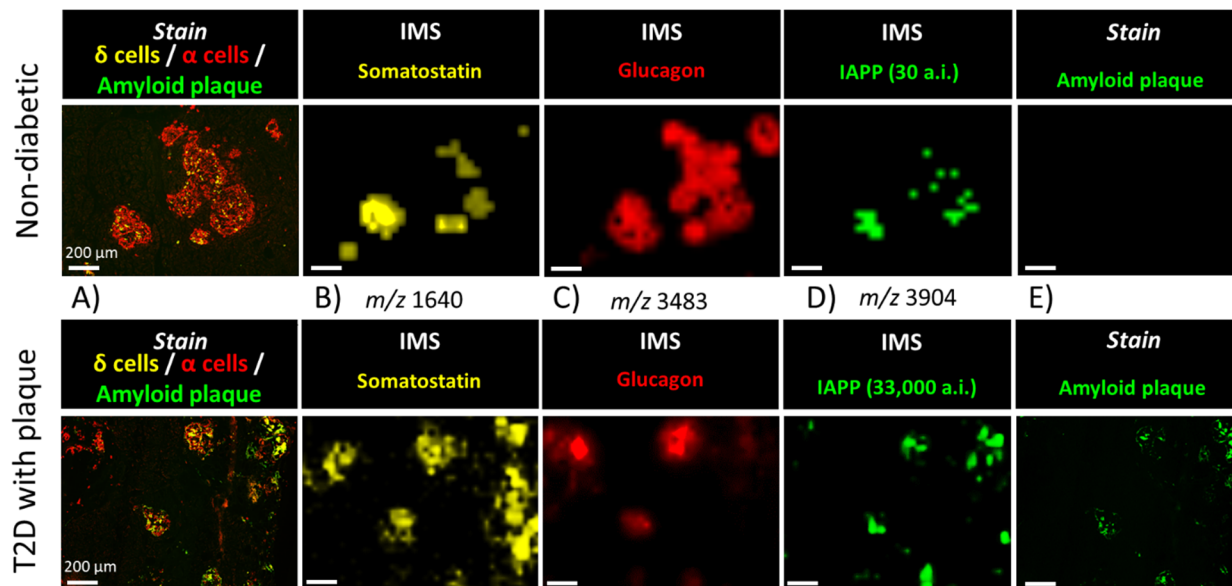
Figure 6.2. Serial sections of the pancreas from ND control (top row) and T2D donors (bottom row) were imaged after chemical and immunofluorescent staining (A, E) and IMS (B-D) for similar tissue regions. Islets are shown in the stained images as combinations of δ cells in yellow and α cells in red and amyloid plaques in green for the T2D donor with plaque. Molecular signals corresponding to these cell types, such as somatostatin (SST) and glucagon (GCG), are among the species detected in the serial section of tissue. The IAPP signal at *m/z* 3904 (D) is detected in low abundance in the ND tissue (30 arbitrary intensity [a.i.]) as well as in very high intensity in the plaque-positive section (33,000 a.i.). IAPP corresponds to amyloid plaque detected in the stained section (A) is displayed separately (E). Ion images of IAPP (in D) were scaled individually because of the wide dynamic range of detection. Ion images for somatostatin and glucagon (B and C) were scaled to imitate islet size represented in stained section. White scale bar length represents 200 μm in all images.

IMS allowed for the sensitive detection of proteins with a wide dynamic range. In islets, unaggregated IAPP is naturally present at baseline levels and is co-secreted in a 1:100 ratio with insulin (**Figure 6.2 E**, ND donor).[179,199] In figure panels 1D and E, the ND and T2D donor signal of IAPP / amyloid plaques for IMS and the stain are shown for comparison. We can detect levels of IAPP present in islets from ND donors (**Figure 6.2 D**, ND donor, 30 arbitrary intensity [a.i.]) where there is no signal from the Thioflavin S stain from the serial section (**Figure 6.2 A, E**). Using IMS, we are also able to detect IAPP at significantly elevated levels (**Figure 6.2 D**, T2D donor, 33,000 a.i.) which correspond to the location of amyloid plaques as determined by staining

of the serial section for the T2D donor (**Figure 6.2 E**, T2D donor). This demonstration of the sensitivity and dynamic range indicates that IMS could be used to characterize the progression of amyloid plaque formation on a molecular level from detection of unaggregated IAPP to IAPP oligomers to mature amyloid plaques.

Post translationally modified forms of IAPP

MALDI IMS allows for regions within the tissue to be selected for comparison of mass spectra. Islet regions were determined by the colocalization of the two-chain form of insulin (*m/z* 5809) and of glucagon (*m/z* 3484) as well as comparison to a serial tissue section that was stained. Islets of similar size were selected from the ND and T2D samples, and the mass spectra were extracted for comparison (**Figure 6.3 A, B**). Numerous protein signals increase in intensity in the T2D donor compared to the ND donor. For the islet from the ND donor (**Figure 6.3 A**), the IAPP signal was detected at a relatively low level, which matches the ion image shown in **Figure 6.2 D**. For the ND donor, no post-translationally modified forms of IAPP were detected (**Figure 6.3 A**). In contrast, the islet in the T2D donor showed a 1000-fold increase in the IAPP signal (**Figure 6.3 B**). The detection of IAPP in islets containing no amyloid plaque, as determined by IHC staining, indicates that IMS is very sensitive and allows for the detection of endogenous IAPP in islets from ND donor tissue. Many post-translationally modified forms of IAPP were detected at levels higher than that in the ND islet (**Figure 6.3 B**), including oxidation, formylation, double oxidation, and the acetylated forms of IAPP. These identities were determined by accurate mass measurements (≤ 5 ppm error) as well as localization to the same pixel regions of IAPP (**Figure 6.3 C**). Even though the post-translationally modified forms of IAPP were not detected in the ND donor, they may be present below the limit of detection of the instrument. These data show that IMS allows for the untargeted detection of numerous post-translationally modified forms of IAPP in the T2D pancreatic tissue that is not detected in the ND tissue.

We are also able to compare the molecular differences between plaque-positive and plaque-negative islets within T2D donor pancreatic tissue using MALDI IMS. One example is demonstrated in **Figure 6.4** between islets designated as plaque-positive and plaque-negative. A section of tissue was stained for amyloid plaque, δ cells, and α cells (**Figure 6.4 A**) and was used for manual annotation of islets based on the presence or absence of amyloid plaque (fluorescence of Thioflavin S). Islets were outlined in green if there was any plaque, as detected using Thioflavin

S, whereas islets with no plaque were outlined in red (**Figure 6.4 A**). Annotations were overlaid onto the MALDI IMS data of a serial section with IAPP signal displayed in green (*m/z* 3904, **Figure 6.4 B**). To account for the wide dynamic range of IAPP detected in plaque-negative vs. plaque-positive islets, the intensity of the plaque-negative islet in the MALDI ion image was scaled to allow for visualization of the IAPP signal present in all islets (**Figure 6.4 B**). Spectra (**Figure 6.4 C**) of the ion image regions outlined in white from **Figure 6.4 B** show the *m/z* signal corresponding to the protein envelope of IAPP from a plaque-negative and a plaque-positive islet. Similar to the difference in IAPP signal between ND and T2D donors using MALDI IMS, in some islets, IAPP signal was detected using IMS in islet regions where no plaque was detected as determined using the stained serial section of tissue for the T2D donor. In contrast, the IAPP signal from a plaque-positive islet region is significantly greater (175-fold). This sensitive detection of IAPP using MALDI IMS and the wide dynamic range provided allows for fine characterization of islets with and without amyloid plaques. Based on MALDI IMS results and comparison to stained tissue, elevated levels of IAPP in islets where there is no amyloid plaque formation may indicate that these islets may have formed plaque over time but are perhaps in an earlier stage of plaque development.
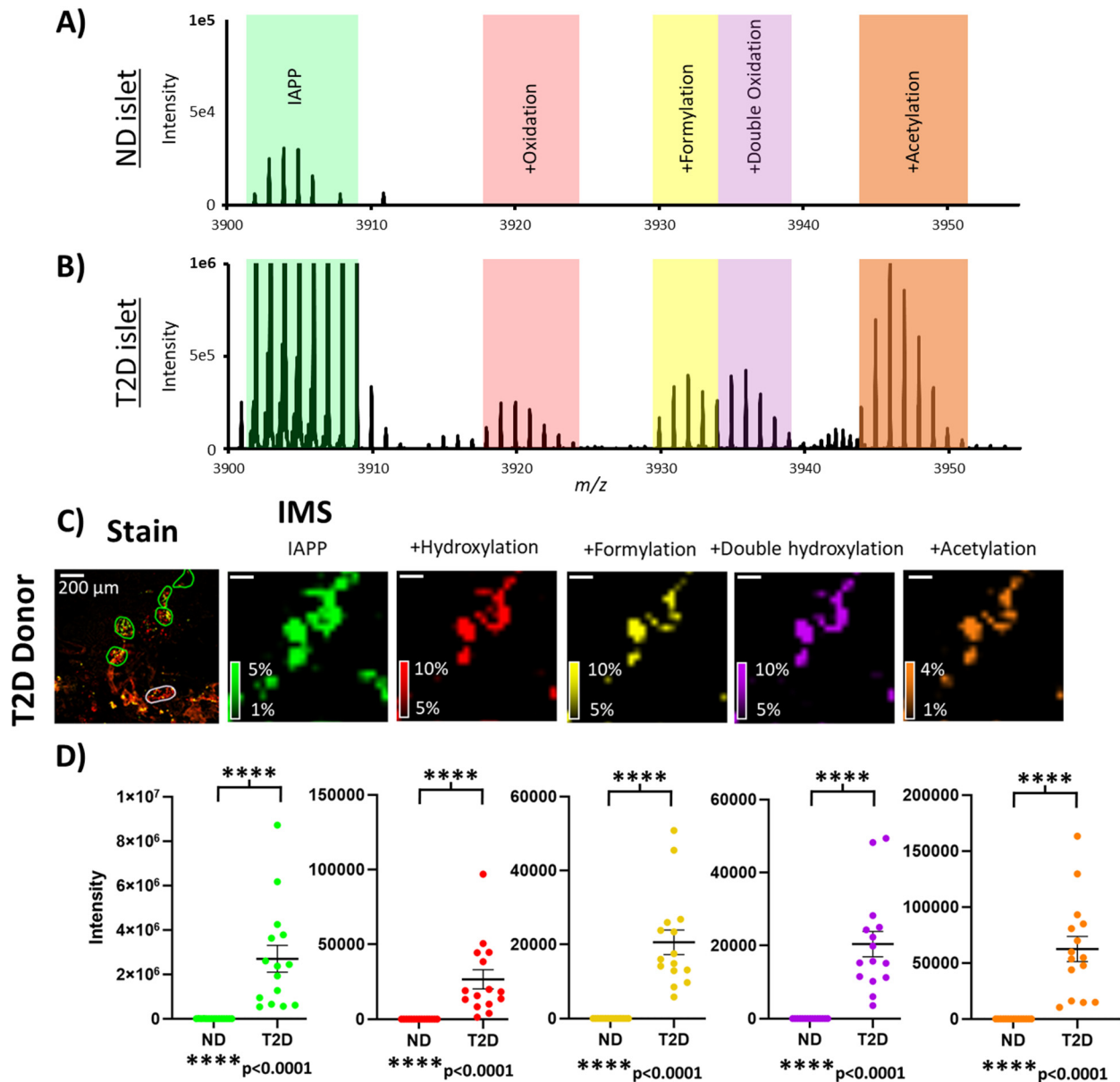
Figure 6.3. Averaged mass spectra of pancreatic islets from the IMS analysis of ND and T2D donors showing IAPP and some PTMs. IAPP is detected by MALDI IMS in low abundance, and no post-translationally modified forms are detected in the ND donor islets (A). For islets of T2D donors with amyloid plaque (B), the IAPP signal was 850-fold greater (3×10^4 vs. 2.6×10^7). Additionally, multiple post-translationally modified forms of IAPP are detected (B). MALDI IMS data were compared to a serial section of tissue annotated with islets circled (C). Each panel of the IMS is a separate ion channel obtained from a single IMS acquisition. Islets in the IHC stain are annotated as IAPP plaque-positive (green outline) or plaque-negative (pink outline). Average intensities of each islet are shown for numerous post-translationally modified forms of IAPP for ND and T2D donors (D). Note that IAPP was detected in the ND donor, but the intensity was significantly lower than in T2D donor islets. Five islets were selected from each tissue section that was analyzed in technical triplicate. Error bars are represented as SEM, and significance was calculated using the Mann-Whitney U test.

126
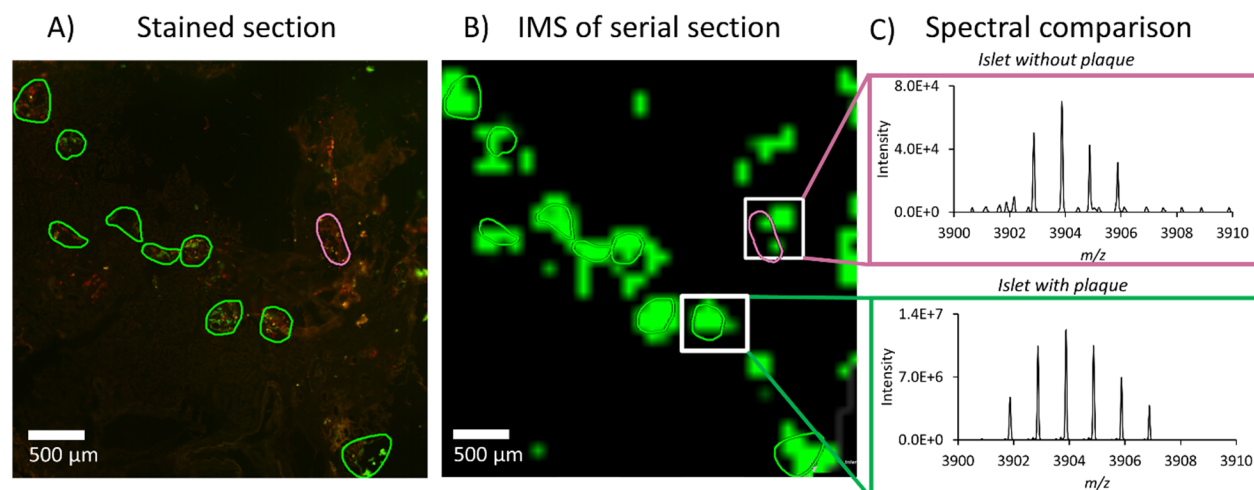
Figure 6.4. IHC stain of pancreas section from a T2D donor (A) with islets annotated as plaque-positive (green outline) or plaque-negative (pink outline). If any plaque signal was detected in an islet, it was designated as plaque-positive. A serial section of tissue was analyzed using IMS, and the results were overlaid onto the annotated regions (B) where the intensity of the IMS region of the plaque-negative islet was scaled to allow for visualization of IAPP in all islets. Spectra of selected regions (C) show the *m/z* signal corresponding to the IAPP monomer, averaged over the respective regions outlined in white. Interestingly, in some islets, IAPP signal was detected using IMS in regions where no plaque was detected from the IHC of a serial section. This wide dynamic range and ability to detect IAPP monomers allow for fine characterization of islets with and without amyloid plaques.
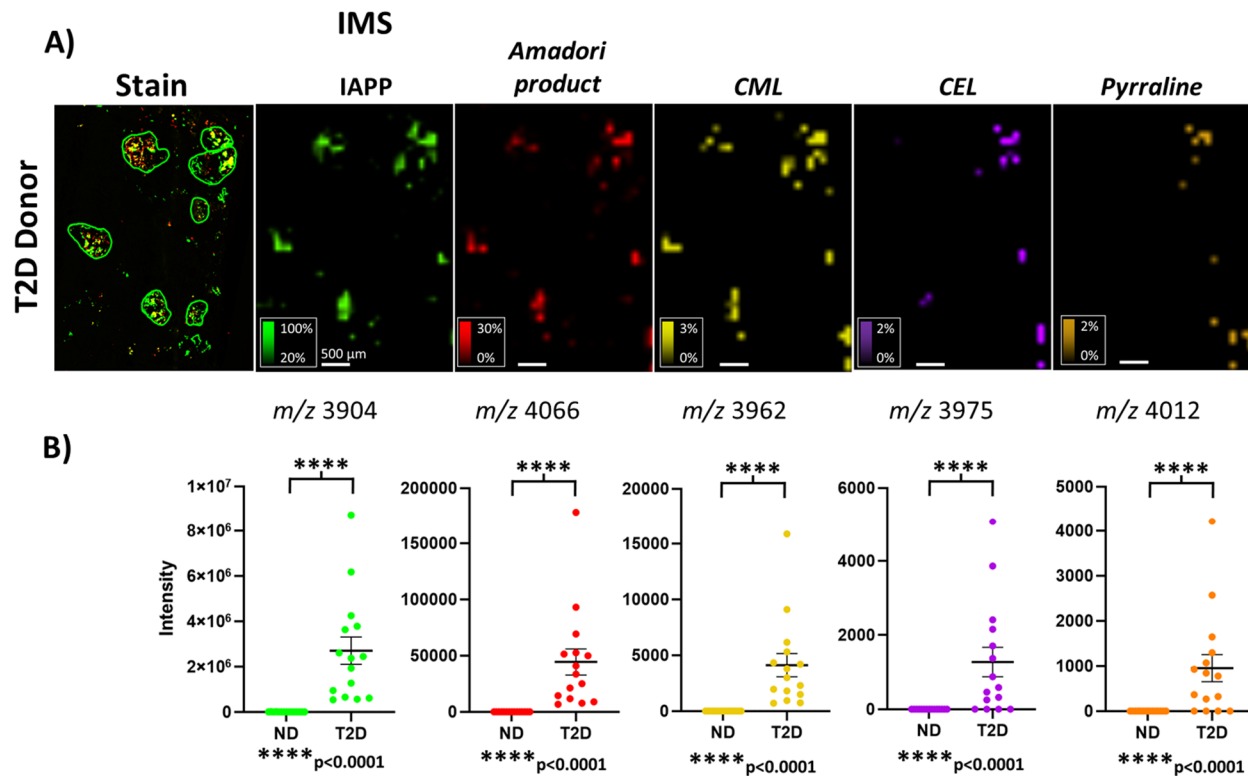
Figure 6.5. IAPP and advanced glycation end products thereof (italicized) in pancreatic tissue from a T2D donor. Tissue was stained for amyloid plaque, α cells, and δ cells (**A, Stain**), and a serial section was analyzed by MALDI IMS. Individual ions are shown corresponding to IAPP and modified forms, including the Amadori product and the AGEs CML, CEL, and pyrraline, identified by accurate mass measurements (**A, IMS**). Here, only the T2D donor results were shown as there was no signal of the modified forms of IAPP for the ND donor. The average intensity from five islets from a ND donor and T2D donor analyzed in technical triplicate were selected for intensity comparison (**B**). Error bars are represented as SEM, and significance was calculated using the Mann-Whitney *U* test.

Spectral differences and ion images for ND and T2D donors

Proteins were identified based on accurate mass measurements (≤ 4 ppm error) and localization to islet regions. In the ND donor, only IAPP is detected, and no other PTMs are detected. For the T2D donor, the IAPP signal is greatly elevated, and multiple PTMs are detected. Of those PTMs, many are related to advanced glycation end products. The Amadori product, an early precursor to AGEs, was detected at *m/z* 4066 with high intensity and localized to IAPP signal as illustrated by the IMS pixels outlined in green (**Figure 6.5 A**). Advanced glycation end products such as CML and pyrraline were detected within 4 ppm mass error. The benefit of high resolving power instrumentation was demonstrated here where the peaks of each isotope were resolved, and the full isotopic envelope could be visualized. The AGE CML was also detected with 3.84 ppm error and

localized to regions of IAPP. The isotopic distribution was different from the theoretical distribution, but it seems there were other interfering species within a similar *m/z* as the isotopes for CML that were not separated at this mass resolution.

Some AGEs may be isobaric or isomeric and cannot readily be identified using high mass resolving power alone. We can deduce structures based on recent literature that has demonstrated that the only reactive residue where AGEs of IAPP form is on the N-terminal lysine *in vitro*.[77,78] Therefore, AGEs that involve arginine and those that involve linkages between two lysine residues are unlikely. One example of isobaric AGEs is CML which is isobaric with pentosidine, but pentosidine has been shown to be unlikely for IAPP as this would require a linkage between lysine and arginine residues. This leaves CML as the only likely AGE associated with these *m/z* values (**Figure 6.5**). Similarly, pyrraline is isobaric with another AGE, glucosepane. Glucosepane is another example of an AGE that forms a linkage between two amino acid residues, here, lysine and arginine. Previous *in vitro* analysis of IAPP has shown that lysine is the only residue that participates in glycation, so glucosepane is, therefore, an unlikely AGE to form with IAPP. Another AGE that we would expect to detect would be CEL, and it appears to be present in these samples but in very low intensity. Some of the ions in that general *m/z* range localize to the regions of IAPP outlined, but we cannot definitively say that CEL was detected in these experiments.

CONCLUSIONS

MALDI IMS can be used for the detection of proteins within the pancreas in an untargeted manner while maintaining the spatial distribution of islet-specific signals. This analytical approach is ideal to study the accumulation and modification of proteins in plaques that form within the islet of diabetic tissues. IAPP was detected as baseline levels in the ND donor as well as elevated levels in plaque-containing islets. Multiple proteoforms of IAPP were detected, including the Amadori product, CML, and pyrraline. These species, identified by accurate mass measurements, were shown to localize to regions of IAPP and of amyloid plaque in a serial section and are elevated in the T2D compared to the ND donor, specifically those islets containing plaque. These results confirm previous literature reports of AGEs localized to islets in the T2D pancreas. They demonstrate the sensitivity and wide dynamic range of MALDI IMS. They also indicate that IAPP may be a source of AGEs that can bind to the receptor for AGEs (RAGE) to induce further β cell death and islet dysfunction.[200–202]

Acknowledgements

CHAPTER VII

CONCLUSIONS AND PERSPECTIVES

OVERVIEW

Obtaining sensitive, high spatial resolution MALDI IMS data is an important part of understanding the molecular differences between healthy and diseased tissue. The research presented in this thesis establishes many technological developments for high spatial resolution and high sensitivity MALDI IMS. First, microstepping drivers and transmission geometry optics were combined on a TOF instrument to allow for high spatial resolution MALDI IMS while maintaining a high acquisition rate. Second, transmission geometry optics combined with MALDI-2 post-ionization was implemented in a custom-built ion source on an Orbitrap platform to obtain high sensitivity, high spatial resolution, and high mass resolution data to elucidate complex mixture contained within tissue sections. Third, the enhancement of lipids using MALDI-2 was evaluated for multiple matrices and pancreata from a non-diabetic (ND) and a type 2 diabetic (T2D) donor were analyzed to find molecular differences between the two. Fourth, MALDI-2 was shown to enhance tryptic peptide signal from tissue for enhanced proteomic coverage compared to MALDI alone. Finally, MALDI-2 did not enhance protein signals from pancreatic tissue. MALDI analysis of intact proteins from ND and T2D pancreata was performed and multiple proteoforms of islet amyloid polypeptide were discovered that have not previously been characterized by spatial proteomic analysis.

High spatial resolution MALDI IMS combined with high throughput was accomplished by the implementation of microstepping drivers with a transmission geometry source on a TOF instrument. Microstepping drivers allowed for the use of existing instrument stage motors for high precision. A retriggerable monostable multivibrator was implemented to ensure stage signal fidelity – bypassing further source modifications and obviating the need for other expensive, high-precision motors. Source modifications to allow for transmission geometry laser optics enabled high spatial resolution imaging capabilities down to 1 μm spatial resolution with routine operation at 2 μm spatial resolution without oversampling (typical ablation diameter of 1.5 μm). Although the TOF instrument provided for a high rate of acquisition (80 Hz), the mass resolution was poor (~4000).

Transmission geometry laser optics were installed on a Spectroglyph MALDI source attached to an Orbitrap Elite. The ion source was also equipped with a MALDI-2 post-ionization laser, which allowed for significant signal enhancement of some lipids compared to MALDI alone. For the first time, we demonstrated the utility of combining transmission geometry laser optics with MALDI-2 on a high mass resolving power instrument. This allowed for high mass resolution (up to 480,000 at m/z 400) and high spatial resolution (1 μm ablation diameter), combined with the enhanced sensitivity with MALDI-2 (7-fold) for some lipid classes.

MALDI-2 signal enhancement of lipids was demonstrated previously but a lipid class dependence was observed. A series of samples including an equimolar mixture of lipids, sections of many tissue homogenates, and tissue sections were analyzed in positive ion mode on the Orbitrap Elite system. The front-side source was used to analyze tissue sections at 20 μm spatial resolution to compare optimal MALDI-1 signal to signal enhancement with MALDI-2. I determined that DHB had the best performance out of all the matrices tested (including DHA, CHCA, and norharmane) based on number of protonated lipids matched to a database within 2 ppm mass error in positive ion mode. With DHB, 125 lipids were identified from a section of rat kidney with MALDI-2 compared with just 72 using standard MALDI alone. The performance of DHB with MALDI-2 was also evaluated in a pilot study using pancreatic tissue from ND and T2D donors analyzed on a timsTOF platform modified with a MALDI-2 laser for post-ionization. The difference in number of lipids matched to a database within 5 ppm mass error between MALDI-1 and MALDI-2 for the T2D donor was 74 and 102, respectively.

MALDI-2 had been shown extensively to enhance lipid signal but its utility for other biomolecules remained unexplored. Tryptic peptides from tissue sections were analyzed using MALDI-2 and CHCA matrix on the Orbitrap Elite system with compelling results. As with lipids, the mass spectrum immediately changed, most peptides increased in signal, and many larger peptides ($< m/z$ 1500) were then detectable. These were the first experiments to show that MALDI-2 can also be used to enhance tryptic peptide signals. Human kidney sections were analyzed to compare performance of MALDI-1 versus MALDI-2 and the resulting peak lists were compared to peptides identified by LC-MS/MS. Protein identification from MALDI-1 and MALDI-2 data was performed by matching two peptides from the MALDI peak list to peptides identified by LC-MS/MS that related to a single protein, matched to the database within 5 ppm error, and that

localized to similar tissue regions in the ion images. Using the above criteria for identification, MALDI-2 showed a 3x increase in proteins identified using the spatial proteomic approach to MALDI-1. MALDI-2 was established as a superior approach to improve proteomic coverage in a spatially resolved manner compared to MALDI-1 alone.

Finally, the utility of MALDI-2 for enhancement of protein signal was explored to achieve better spatial proteomic comparisons of islets in ND and T2D donor pancreata. Samples were prepared with the same matrix as for tryptic peptides with the idea that signal enhancement would be observed for endogenous peptides from tissue with MALDI-2. Interestingly, no enhancement of endogenous peptides or intact proteins was detected on a timsTOF Pro instrument modified with a MALDI source and MALDI-2 capabilities and operated in qTOF mode. Given the often-convoluted peaks from isotopologues in protein IMS data and that no increase in protein signal was detected with MALDI-2 for pancreas samples, a high mass resolving power instrument, the 15T FT-ICR, was used for intact protein analysis. Samples from six ND and five T2D donors were analyzed in technical triplicate and proteomic differences within the islets and localized to amyloid plaques were compared. Amyloid plaques in the pancreas are primarily composed of islet amyloid polypeptide and multiple proteoforms were discovered that were identified in the T2D donors by accurate mass measurements (<10 ppm error). These results may help inform the mechanism of amyloid plaque formation in T2D patients and aid in forming disease prevention strategies.

FUTURE DIRECTIONS

This work describes many novel advances in instrumentation to improve the spatial resolution, lipidomic coverage, and proteomic coverage in MALDI IMS experimentation. Technological advancements are still needed to accurately describe the molecular underpinnings of many diseases. The current practical limit of spatial resolution for ablation-based detection of biomolecules in an untargeted manner is 2 μm. Even though 2 μm spatial resolution is now readily achievable, a significant amount of chemical information is lost with such small sampling volumes. Additionally, there has been research in recent years in both ultra-high spatial resolution laser optical configurations of front-side and transmission geometry. While transmission geometry allows for the use of commercially available, high numerical aperture objectives to achieve ablation diameter of 1.5 μm from tissue, there is a challenge with sensitivity, especially as one laser shot ablates matrix in one region. Approaches that allow for multiple laser shots in a single

pixel while ablating new material each shot, such as programmed increases in laser energy at each pixel to slightly ablate more and more matrix at the expense of spatial resolution, may solidify transmission geometry as the more viable alternative to achieve ultra-high spatial resolution IMS. The present advantages in sensitivity of front-side geometry in obtaining signal from the sample over hundreds of laser shots is unignorable.

MALDI-2 enhances numerous signals of some lipid classes and of peptides, as demonstrated in this dissertation, yet a more complete understanding of the fundamentals of the MALDI-2 ionization process is required. Recent work by others have suggested that MALDI-2 may reverse ion suppression effects to some degree, but a more rigorous understanding is required to ensure that this issue is not biasing the data in an unexpected way using MALDI-2. Why is it that some lipid classes seem to be enhanced with MALDI-2 but not others, why are some tryptic peptides enhanced with MALDI-2 but not others? A more complete fundamental understanding of the MALDI-2 ionization mechanism (and the MALDI process as well) will help ensure that results using MALDI-2 are superior and will help answer what possible drawbacks are associated with MALDI-2 analysis.

To obtain more meaningful data from tryptic peptide analysis with MALDI-2, further validation of peptide signals detected will be necessary. The different peptide ionization approaches of ESI and MALDI often detect a very different but complementary range of peptides. As such, matching MALDI peak lists to databases of LC-MS/MS seems like a fruitless exercise when many of the peptides detected by MALDI remain unannotated. Therefore, better bottom-up proteomic workflows for annotation of peptides detected by MALDI are needed. This will allow for more complete spatially resolved proteomic analysis. Other technologies such as ultraviolet photodissociation (UVPD) of MALDI and MALDI-2-generated peptides may be developed and implemented with MALDI-2 for unambiguous peptide identification. Finally, computational approaches to search MALDI peak lists based all theoretical peptides generated from all proteins in a sample will allow for more complete annotation of peptides generated using MALDI and MALDI-2. This approach was recently implemented as an open-source bioinformatics workflow by Guo et al. with an informatics toolbox called HIT-MAP.[165] Ultimately, I anticipate that my contributions and future technological advances will be used to study diseases to deepen our understanding of the molecular understanding of health and disease to inform more effective disease prevention and treatment strategies.

REFERENCES

(1)   Caprioli, R. M.; Farmer, T. B.; Gile, J. Molecular Imaging of Biological Samples: Localization of Peptides and Proteins Using MALDI-TOF MS. *Anal. Chem.* **1997**, *69* (23), 4751–4760. https://doi.org/10.1021/AC970888I.

(2)   Norris, J. L.; Caprioli, R. M. Analysis of Tissue Specimens by Matrix-Assisted Laser Desorption/Ionization Imaging Mass Spectrometry in Biological and Clinical Research. *Chem. Rev.* **2013**, *113* (4), 2309–2342. https://doi.org/10.1021/cr3004295.

(3)   Hooke, R. *Micrographia: Or Some Physiological Descriptions Of Minute Bodies Made by Magnifying Glasses with Observations and Inquiries Thereupon*; Jo. Martyn and Ja. Allestry, Printers to the Royal Society: London, 1665.

(4)   Heinrichs, A. Stains and Fluorescent Dyes. *Nat. Cell Biol. 2009 111* **2009**, *11* (1), S7–S7. https://doi.org/10.1038/ncb1939.

(5)   J. J. Thomson. Cathode Rays. *Philos. Mag. J. Sci.* **1897**, *44* (269), 293–316.

(6)   Yamashita, M.; Fenn, J. B. Electrospray Ion Source. Another Variation on the Free-Jet Theme. *J. Phys. Chem.* **1984**, *88* (20), 4451–4459. https://doi.org/10.1021/J150664A002.

(7)   Yamashita, M.; Fenn, J. B. Negative Ion Production with the Electrospray Ion Source. *J. Phys. Chem.* **1984**, *88* (20), 4671–4675. https://doi.org/10.1021/J150664A046.

(8)   Karas, M.; Bachmann, D.; Hillenkamp, F. Influence of the Wavelength in High-Irradiance Ultraviolet Laser Desorption Mass Spectrometry of Organic Molecules. *Anal. Chem.* **1985**, *57*, 2935–2939.

(9)   Karas, M.; Bachmann, D.; Bahr, U.; Hillenkamp, F. Matrix-Assisted Ultraviolet Laser Desorption of Non-Volatile Compounds. *Int. J. Mass Spectrom. Ion Process.* **1987**, *78*, 53–68. https://doi.org/10.1016/0168-1176(87)87041-6.

(10)   Tanaka, K. The Origin of Macromolecule Ionization by Laser Irradiation (Nobel Lecture). *Angew. Chemie Int. Ed.* **2003**, *42* (33), 3860–3870. https://doi.org/10.1002/ANIE.200300585.

(11)   Knochenmuss, R. Ion Formation Mechanisms in UV-MALDI. *Analyst* **2006**, *131* (9), 966. https://doi.org/10.1039/b605646f.

(12)   Dreisewerd, K. The Desorption Process in MALDI. *Chem. Rev.* **2003**, *103*, 395–425. https://doi.org/10.1021/cr010375i.

(13)   Guilhaus, M. Principles and Instrumentation in Time-of-Flight Mass Spectrometry. Physical and Instrumental Concepts. *J. Mass Spectrom.* **1995**, *30* (11), 1519–1532. https://doi.org/10.1002/jms.1190301102.

(14)   Bednařík, A.; Machálková, M.; Moskovets, E.; Coufalíková, K.; Krásenský, P.; Houška, P.; Kroupa, J.; Navrátilová, J.; Šmarda, J.; Preisler, J. MALDI MS Imaging at Acquisition Rates Exceeding 100 Pixels per Second. *J. Am. Soc. Mass Spectrom.* **2019**, *30* (2), 289–298. https://doi.org/10.1007/S13361-018-2078-8.

(15)   Marshall, A. G.; Hendrickson, C. L. Fourier Transform Ion Cyclotron Resonance Detection: Principles and Experimental Configurations. *Int. J. Mass Spectrom.* **2002**, *215* (1–3), 59–75. https://doi.org/10.1016/S1387-3806(01)00588-7.

(16) Zubarev, R. A.; Makarov, A. Orbitrap Mass Spectrometry. *Anal. Chem* **2013**, *85* (11), 5288–5296. https://doi.org/10.1021/ac4001223.

(17) de Hoffmann, E.; Stroobant, V. *Mass Spectrometry: Principles and Applications*, 3rd ed.; Wiley & Sons, 2007.

(18) van Agthoven, M. A.; Lam, Y. P. Y.; O'Connor, P. B.; Rolando, C.; Delsuc, M. A. Two-Dimensional Mass Spectrometry: New Perspectives for Tandem Mass Spectrometry. *Eur. Biophys. J.* **2019**, *48* (3), 213–229. https://doi.org/10.1007/S00249-019-01348-5.

(19) Feenstra, A. D.; Dueñas, M. E.; Lee, Y. J. Five Micron High Resolution MALDI Mass Spectrometry Imaging with Simple, Interchangeable, Multi-Resolution Optical System. *J. Am. Soc. Mass Spectrom.* **2017**, *28* (3), 434–442. https://doi.org/10.1007/s13361-016-1577-8.

(20) Kettling, H.; Vens-Cappell, S.; Soltwisch, J.; Pirkl, A.; Rg Haier, J.; Mü, J.; Dreisewerd, K. MALDI Mass Spectrometry Imaging of Bioactive Lipids in Mouse Brain with a Synapt G2-S Mass Spectrometer Operated at Elevated Pressure: Improving the Analytical Sensitivity and the Lateral Resolution to Ten Micrometers. *Anal. Chem* **2014**, *86*, 3. https://doi.org/10.1021/ac5017248.

(21) Kompauer, M.; Heiles, S.; Spengler, B. Atmospheric Pressure MALDI Mass Spectrometry Imaging of Tissues and Cells at 1.4-Mm Lateral Resolution. *Nat. Methods* **2017**, *14* (1), 90–96. https://doi.org/10.1038/nmeth.4071.

(22)   Zavalin, A.; Todd, E. M.; Rawhouser, P. D.; Yang, J.; Norris, J. L.; Caprioli, R. M. Direct
         Imaging of Single Cells and Tissue at Sub-Cellular Spatial Resolution Using Transmission
         Geometry MALDI MS. *J. Mass Spectrom.* **2012**, *47* (11), 1473–1481.
         https://doi.org/10.1002/jms.3108.

(23)   Zavalin, A.; Yang, J.; Hayden, K.; Vestal, M.; Caprioli, R. M. Tissue Protein Imaging at 1
         Mm Laser Spot Diameter for High Spatial Resolution and High Imaging Speed Using
         Transmission Geometry MALDI TOF MS. *Anal. Bioanal. Chem.* **2015**, *407* (8), 2337–
         2342. https://doi.org/10.1007/s00216-015-8532-6.

(24)   Mowry, C. D.; Johnston, M. V. Simultaneous Detection of Ions and Neutrals Produced by
         Matrix-Assisted Laser Desorption. *Rapid Commun. Mass Spectrom.* **1993**, *7*, 569–575.
         https://doi.org/10.1002/rcm.1290070702.

(25)   Bokhart, M. T.; Manni, J.; Garrard, K. P.; Ekelöf, M.; Nazari, M.; Muddiman, D. C. IR-
         MALDESI Mass Spectrometry Imaging at 50 Micron Spatial Resolution. *J. Am. Soc.
         Mass Spectrom.* **2017**, *28* (10), 2099–2107. https://doi.org/10.1007/s13361-017-1740-x.

(26)   Steven, R. T.; Shaw, M.; Dexter, A.; Murta, T.; Green, F. M.; Robinson, K. N.; Gilmore,
         I. S.; Takats, Z.; Bunch, J. Construction and Testing of an Atmospheric-Pressure
         Transmission-Mode Matrix Assisted Laser Desorption Ionisation Mass Spectrometry
         Imaging Ion Source with Plasma Ionisation Enhancement. *Anal. Chim. Acta* **2019**, *1051*,
         110–119. https://doi.org/10.1016/J.ACA.2018.11.003.

(27)   Niehaus, M.; Soltwisch, J.; Belov, M. E.; Dreisewerd, K. Transmission-Mode MALDI-2
         Mass Spectrometry Imaging of Cells and Tissues at Subcellular Resolution. *Nat. Methods*
         2019, *16* (9), 925–931. https://doi.org/10.1038/s41592-019-0536-2.

(28)   Tsai, S.-T.; Chen, C.-H.; Lee, Y. T.; Wang, Y.-S. Desorption Dynamics of Neutral Molecules in Matrix-Assisted Laser Desorption/Ionization. *Mol. Phys.* **2008**, *106* (4), 239–247. https://doi.org/10.1080/00268970701779671.

(29)   Soltwisch, J.; Kettling, H.; Vens-Cappell, S.; Wiegelmann, M.; Müthing, J.; Dreisewerd, K. Mass Spectrometry Imaging with Laser-Induced Postionization. *Science (80).* **2015**, *348* (6231), 211–215. https://doi.org/10.1021/cr010375i.

(30)   Ellis, S. R.; Soltwisch, J.; Paine, M. R. L.; Dreisewerd, K.; Heeren, R. M. A. Laser Post-Ionisation Combined with a High Resolving Power Orbitrap Mass Spectrometer for Enhanced MALDI-MS Imaging of Lipids. *Chem. Commun.* **2017**, *53* (53), 7246–7249. https://doi.org/10.1039/C7CC02325A.

(31)   Spivey, E. C.; McMillen, J. C.; Caprioli, R. M.; Spraggins, J. M.; Ryan, D. J. Combining MALDI-2 and Transmission Geometry Laser Optics to Achieve High Sensitivity for Ultra-High Spatial Resolution Surface Analysis. *J. Mass Spectrom.* **2019**. https://doi.org/10.1002/jms.4335.

(32)   McMillen, J. C.; Gutierrez, D. B.; Judd, A. M.; Spraggins, J. M.; Caprioli, R. M. Enhancement of Tryptic Peptide Signals from Tissue Sections Using MALDI IMS Postionization (MALDI-2). *J. Am. Soc. Mass Spectrom.* **2021**. https://doi.org/10.1021/JASMS.1C00213.

(33)   Bowman, A. P.; Bogie, J. F. J.; Hendriks, J. J. A.; Haidar, M.; Belov, M.; Heeren, R. M. A.; Ellis, S. R. Evaluation of Lipid Coverage and High Spatial Resolution MALDI-Imaging Capabilities of Oversampling Combined with Laser Post-Ionisation. *Anal. Bioanal. Chem.* **2019**. https://doi.org/10.1007/s00216-019-02290-3.

(34) Thomas, A.; Chaurand, P. Advances in Tissue Section Preparation for MALDI Imaging MS. *Bioanalysis* **2014**, *6* (7), 967–982. https://doi.org/10.4155/bio.14.63.

(35) Yang, J.; Caprioli, R. M. Matrix Sublimation/Recrystallization for Imaging Proteins by Mass Spectrometry at High Spatial Resolution. *Anal. Chem.* **2011**, *83*, 5728–5734. https://doi.org/10.1021/ac200998a.

(36) Fujino, Y.; Minamizaki, T.; Yoshioka, H.; Okada, M.; Yoshiko, Y. Imaging and Mapping of Mouse Bone Using MALDI-Imaging Mass Spectrometry. *Bone reports* **2016**, *5*, 280–285. https://doi.org/10.1016/j.bonr.2016.09.004.

(37) Judd, A. M.; Gutierrez, D. B.; Moore, J. L.; Patterson, N. H.; Yang, J.; Romer, C. E.; Norris, J. L.; Caprioli, R. M. A Recommended and Verified Procedure for in Situ Tryptic Digestion of Formalin-Fixed Paraffin-Embedded Tissues for Analysis by Matrix-Assisted Laser Desorption/Ionization Imaging Mass Spectrometry. *J. Mass Spectrom.* **2019**, *54* (8), 716–727. https://doi.org/10.1002/jms.4384.

(38) Dufresne, M.; Patterson, N. H.; Norris, J. L.; Caprioli, R. M. Combining Salt Doping and Matrix Sublimation for High Spatial Resolution MALDI Imaging Mass Spectrometry of Neutral Lipids. *Anal. Chem.* **2019**. https://doi.org/10.1021/acs.analchem.9b02974.

(39) Angel, P. M.; Baldwin, H. S.; Gottlieb Sen, D.; Su, Y. R.; Mayer, J. E.; Bichell, D.; Drake, R. R. Advances in MALDI Imaging Mass Spectrometry of Proteins in Cardiac Tissue, Including the Heart Valve. *Biochim. Biophys. acta. Proteins proteomics* **2017**, *1865* (7), 927–935. https://doi.org/10.1016/j.bbapap.2017.03.009.

(40)   Powers, T. W.; Neely, B. A.; Shao, Y.; Tang, H.; Troyer, D. A.; Mehta, A. S.; Haab, B.

B.; Drake, R. R. MALDI Imaging Mass Spectrometry Profiling of N-Glycans in Formalin-

Fixed Paraffin Embedded Clinical Tissue Blocks and Tissue Microarrays. *PLoS One*

2014, *9* (9), e106255. https://doi.org/10.1371/journal.pone.0106255.

(41)   Angel, P. M.; Spraggins, J. M.; Baldwin, H. S.; Caprioli, R. Enhanced Sensitivity for High

Spatial Resolution Lipid Analysis by Negative Ion Mode Matrix Assisted Laser

Desorption Ionization Imaging Mass Spectrometry. *Anal. Chem.* **2012**, *84* (3), 1557–1564.

https://doi.org/10.1021/ac202383m.

(42)   Sun, C.; Li, Z.; Ma, C.; Zang, Q.; Li, J.; Liu, W.; Zhao, H.; Wang, X. Acetone Immersion

Enhanced MALDI-MS Imaging of Small Molecule Metabolites in Biological Tissues. *J.*

Pharm. Biomed. Anal. **2019**, *176* (112797), 1–8.

https://doi.org/https://doi.org/10.1016/j.jpba.2019.112797.

(43)   Yang, H.; Ji, W.; Guan, M.; Li, S.; Zhang, Y.; Zhao, Z.; Mao, L. Organic Washes of

Tissue Sections for Comprehensive Analysis of Small Molecule Metabolites by MALDI

MS Imaging of Rat Brain Following Status Epilepticus. *Metabolomics* **2018**, *14* (4), 50.

https://doi.org/10.1007/s11306-018-1348-6.

(44)   Yang, J.; Norris, J. L.; Caprioli, R. Novel Vacuum Stable Ketone-Based Matrices for High

Spatial Resolution MALDI Imaging Mass Spectrometry. *J. Mass Spectrom.* **2018**.

https://doi.org/10.1002/jms.4277.

(45)   Thomas, A.; Charbonneau, J. L.; Fournaise, E.; Chaurand, P. Sublimation of New Matrix Candidates for High Spatial Resolution Imaging Mass Spectrometry of Lipids: Enhanced Information in Both Positive and Negative Polarities after 1,5-Diaminonapthalene Deposition. *Anal. Chem.* **2012**, *84* (4), 2048–2054. https://doi.org/10.1021/ac2033547.

(46)   Ulmer, L.; Mattay, J.; Torres-Garcia, H. G.; Luftmann, H. Letter: The Use of 2-[(2E)-3-(4-Tert-Butylphenyl)-2-Methylprop-2-Enylidene]Malononitrile as a Matrix for Matrix-Assisted Laser Desorption/Ionization Mass Spectrometry. *Eur. J. Mass Spectrom.* **2000**, *6* (1), 49–52. https://doi.org/10.1255/ejms.329.

(47)   Stübiger, G.; Belgacem, O. Analysis of Lipids Using 2,4,6-Trihydroxyacetophenone as a Matrix for MALDI Mass Spectrometry. *Anal. Chem.* **2007**, *79* (8), 3206–3213. https://doi.org/10.1021/ac062236c.

(48)   Beavis, R. C.; Chaudhary, T.; Chait, B. T. Alpha-Cyano-4-Hydroxycinnamic Acid as a Matrix for Matrix-Assisted Laser Desorption Mass Spectrometry. *Org. Mass Spectrom.* **1992**, *27* (2), 156–158. https://doi.org/10.1002/oms.1210270217.

(49)   Strupat, K.; Karas, M.; Hillenkamp, F. 2,5-Dihyroxybenzoic Acid - a New Matrix for Laser Desorption Ionization Mass Spectrometry. *Int. J. Mass Spectrom. Ion Process.* **1991**, *111*, 89–102. https://doi.org/10.1016/0168-1176(91)85050-v.

(50)   Xu, N. X.; Huang, Z. H.; Watson, J. T.; Gage, D. A. Mercaptobenzothiazoles: A New Class of Matrices for Laser Desorption Ionization Mass Spectrometry. *J. Am. Soc. Mass Spectrom.* **1997**, *8* (2), 116–124. https://doi.org/10.1016/s1044-0305(96)00233-4.

(51)   Vermillion-Salsbury, R. L.; Hercules, D. M. 9-Aminoacridine as a Matrix for Negative

          Mode Matrix-Assisted Laser Desorption/Ionization. *Rapid Commun. Mass Spectrom.*

          2002, *16* (16), 1575–1581. https://doi.org/10.1002/rcm.750.

(52)   Shi, C. Y.; Deng, C. H. Recent Advances in Inorganic Materials for LDI-MS Analysis of

          Small Molecules. *Analyst* **2016**, *141* (10), 2816–2826.

          https://doi.org/10.1039/C6AN00220J.

(53)   Schröter, J.; Fülöp, A.; Hopf, C.; Schiller, J. The Combination of 2,5-Dihydroxybenzoic

          Acid and 2,5-Dihydroxyacetophenone Matrices for Unequivocal Assignment of

          Phosphatidylethanolamine Species in Complex Mixtures. *Anal. Bioanal. Chem.* **2018**, *410*

          (9), 2437–2447. https://doi.org/10.1007/s00216-018-0926-9.

(54)   Groessl, M.; Graf, S.; Knochenmuss, R. High Resolution Ion Mobility-Mass Spectrometry

          for Separation and Identification of Isomeric Lipids. *Analyst* **2015**, *140* (20), 6904–6911.

          https://doi.org/10.1039/C5AN00838G.

(55)   Groseclose, M. R.; Castellino, S. A Mimetic Tissue Model for the Quantification of Drug

          Distributions by MALDI Imaging Mass Spectrometry. *Anal. Chem.* **2013**, *85* (21), 10099–

          10106. https://doi.org/10.1021/ac400892z.

(56)   Li, S.; Zhang, Y.; Liu, J.; Han, J.; Guan, M.; Yang, H.; Lin, Y.; Xiong, S.; Zhao, Z.

          Electrospray Deposition Device Used to Precisely Control the Matrix Crystal to Improve

          the Performance of MALDI MSI. *Sci. Rep.* **2016**, *6*, 37903.

          https://doi.org/10.1038/srep37903.

(57) Fuchs, B.; Bischoff, A.; Süß, R.; Teuber, K.; Schürenberg, M.; Suckau, D.; Schiller, J. Phosphatidylcholines and -Ethanolamines Can Be Easily Mistaken in Phospholipid Mixtures: A Negative Ion MALDI-TOF MS Study with 9-Aminoacridine as Matrix and Egg Yolk as Selected Example. *Anal. Bioanal. Chem.* **2009**, *395* (8), 2479–2487. https://doi.org/10.1007/s00216-009-3032-1.

(58) Hankin, J. A.; Barkley, R. M.; Murphy, R. C. Sublimation as a Method of Matrix Application for Mass Spectrometric Imaging. *J. Am. Soc. Mass Spectrom.* **2007**, *18* (9), 1646–1652. https://doi.org/http://dx.doi.org/10.1016/j.jasms.2007.06.010.

(59) Anderson, D. M. G.; Ablonczy, Z.; Koutalos, Y.; Spraggins, J.; Crouch, R. K.; Caprioli, R. M.; Schey, K. L. High Resolution MALDI Imaging Mass Spectrometry of Retinal Tissue Lipids. *J. Am. Soc. Mass Spectrom.* **2014**, *25* (8), 1394–1403. https://doi.org/10.1007/s13361-014-0883-2.

(60) Atkinson, M. A.; Campbell-Thompson, M.; Kusmartseva, I.; Kaestner, K. H. Organisation of the Human Pancreas in Health and in Diabetes. *Diabetologia* **2020**, *63* (10), 1966–1973. https://doi.org/10.1007/S00125-020-05203-7.

(61) Westermark, P.; Andersson, A.; Westermark, G. T. Islet Amyloid Polypeptide, Islet Amyloid, and Diabetes Mellitus. *Physiological Reviews*. American Physiological Society Bethesda, MD July 2011, pp 795–826. https://doi.org/10.1152/physrev.00042.2009.

(62) Takeda, S.; Sato, N.; Rakugi, H.; Morishita, R. Molecular Mechanisms Linking Diabetes Mellitus and Alzheimer Disease: Beta-Amyloid Peptide, Insulin Signaling, and Neuronal Function. *Mol. Biosyst.* **2011**, *7* (6), 1822–1827. https://doi.org/10.1039/c0mb00302f.

(63)   Reznik, Y.; Cohen, O. Insulin Pump for Type 2 Diabetes: Use and Misuse of Continuous
         Subcutaneous Insulin Infusion in Type 2 Diabetes. *Diabetes Care* **2013**, *36*
         (Supplement_2), S219–S225. https://doi.org/10.2337/DCS13-2027.

(64)   Zajac, J.; Shrestha, A.; Patel, P.; Poretsky, L. The Main Events in the History of Diabetes
         Mellitus. *Princ. Diabetes Mellit.* **2010**, 3–16. https://doi.org/10.1007/978-0-387-09841-
         8_1.

(65)   Chatterjee, S.; Khunti, K.; Davies, M. J. Type 2 Diabetes. *Lancet* **2017**, *389* (10085),
         2239–2251. https://doi.org/10.1016/S0140-6736(17)30058-2.

(66)   In't Veld, P.; Marichal, M. Microscopic Anatomy of the Human Islet of Langerhans. *Adv.
         Exp. Med. Biol.* **2010**, *654*, 1–19. https://doi.org/10.1007/978-90-481-3271-3_1.

(67)   Kehm, R.; Rückriemen, J.; Weber, D.; Deubel, S.; Grune, T.; Höhn, A. Endogenous
         Advanced Glycation End Products in Pancreatic Islets after Short-Term Carbohydrate
         Intervention in Obese, Diabetes-Prone Mice. *Nutr. Diabetes* **2019**, *9* (9), 1–5.
         https://doi.org/10.1038/s41387-019-0077-x.

(68)   Macauley, M.; Percival, K.; Thelwall, P. E.; Hollingsworth, K. G.; Taylor, R. Altered
         Volume, Morphology and Composition of the Pancreas in Type 2 Diabetes. *PLoS One*
         2015, *10* (5), e0126825. https://doi.org/10.1371/JOURNAL.PONE.0126825.

(69)   Jurgens, C. A.; Toukatly, M. N.; Fligner, C. L.; Udayasankar, J.; Subramanian, S. L.;
         Zraika, S.; Aston-Mourney, K.; Carr, D. B.; Westermark, P.; Westermark, G. T.; Kahn, S.
         E.; Hull, R. L. β-Cell Loss and β-Cell Apoptosis in Human Type 2 Diabetes Are Related
         to Islet Amyloid Deposition. *Am. J. Pathol.* **2011**, *178* (6), 2632–2640.
         https://doi.org/10.1016/J.AJPATH.2011.02.036.

(70)   Hull, R. L.; Westermark, G. T.; Westermark, P.; Kahn, S. E. Islet Amyloid: A Critical
        Entity in the Pathogenesis of Type 2 Diabetes. *J. Clin. Endocrinol. Metab.* **2004**, *89* (8),
        3629–3643. https://doi.org/10.1210/jc.2004-0405.

(71)   Prentice, B. M.; Hart, N. J.; Phillips, N.; Haliyur, R.; Judd, A.; Armandala, R.; Spraggins,
        J. M.; Lowe, C. L.; Boyd, K. L.; Stein, R. W.; Wright, C. V.; Norris, J. L.; Powers, A. C.;
        Brissova, M.; Caprioli, R. M. Imaging Mass Spectrometry Enables Molecular Profiling of
        Mouse and Human Pancreatic Tissue. *Diabetologia* **2019**, *62* (6), 1036–1047.
        https://doi.org/10.1007/s00125-019-4855-8.

(72)   Gupta, D.; Leahy, J. L. Islet Amyloid and Type 2 Diabetes: Overproduction or Inadequate
        Clearance and Detoxification? *J. Clin. Invest.* **2014**, *124* (8), 3292–3294.
        https://doi.org/10.1172/JCI77506.

(73)   Kakinen, A.; Sun, Y.; Javed, I.; Faridi, A.; Pilkington, E. H.; Faridi, P.; Purcell, A. W.;
        Zhou, R.; Ding, F.; Lin, S.; Ke, P. C.; Davis, T. P. Physical and Toxicological Profiles of
        Human IAPP Amyloids and Plaques. *Sci. Bull.* **2019**, *64* (1), 26–35.
        https://doi.org/10.1016/J.SCIB.2018.11.012.

(74)   Moracci, L.; Crotti, S.; Traldi, P.; Agostini, M.; Cosma, C.; Lapolla, A. Role of Mass
        Spectrometry in the Study of Interactions between Amylin and Metal Ions. *Mass
        Spectrom. Rev.* **2021**. https://doi.org/10.1002/MAS.21732.

(75)   Vitek, M. P.; Bhattacharya, K.; Glendening, J. M.; Stopa, E.; Vlassara, H.; Bucala, R.;
        Manogue, K.; Cerami, A. Advanced Glycation End Products Contribute to Amyloidosis in
        Alzheimer Disease. *Proc. Natl. Acad. Sci. U. S. A.* **1994**, *91* (11), 4766–4770.
        https://doi.org/10.1073/pnas.91.11.4766.

(76)   Jeong, H. R.; An, S. S. A. Causative Factors for Formation of Toxic Islet Amyloid Polypeptide Oligomer in Type 2 Diabetes Mellitus. *Clin. Interv. Aging* **2015**, *10*, 1873. https://doi.org/10.2147/CIA.S95297.

(77)   Hsu, Y. H.; Chen, Y. W.; Wu, M. H.; Tu, L. H. Protein Glycation by Glyoxal Promotes Amyloid Formation by Islet Amyloid Polypeptide. *Biophys. J.* **2019**, *116* (12), 2304–2313. https://doi.org/10.1016/j.bpj.2019.05.013.

(78)   Milordini, G.; Zacco, E.; Percival, M.; Puglisi, R.; Dal Piaz, F.; Temussi, P.; Pastore, A. The Role of Glycation on the Aggregation Properties of IAPP. *Front. Mol. Biosci.* **2020**, *7*, 104. https://doi.org/10.3389/fmolb.2020.00104.

(79)   Ma, L.; Yang, C.; Huang, L.; Chen, Y.; Li, Y.; Cheng, C.; Cheng, B.; Zheng, L.; Huang, K. Glycated Insulin Exacerbates the Cytotoxicity of Human Islet Amyloid Polypeptides: A Vicious Cycle in Type 2 Diabetes. *ACS Chem. Biol.* **2019**, *14* (3), 486–496. https://doi.org/10.1021/acschembio.8b01128.

(80)   Jurchen, J. C.; Rubakhin, S. S.; Sweedler, J. V. MALDI-MS Imaging of Features Smaller than the Size of the Laser Beam. *J. Am. Soc. Mass Spectrom.* **2005**, *16* (10), 1654–1659. https://doi.org/10.1016/j.jasms.2005.06.006.

(81)   Zubair, F.; Prentice, B. M.; Norris, J. L.; Laibinis, P. E.; Caprioli, R. M. Standard Reticle Slide To Objectively Evaluate Spatial Resolution and Instrument Performance in Imaging Mass Spectrometry. *Anal. Chem.* **2016**, *88* (14), 7302–7311. https://doi.org/10.1021/acs.analchem.6b01655.

(82)   Fagerer, S. R.; Römpp, A.; Jefimovs, K.; Brönnimann, R.; Hayenga, G.; Steinhoff, R. F.; Krismer, J.; Pabst, M.; Ibáñez, A. J.; Zenobi, R. Resolution Pattern for Mass Spectrometry Imaging. *Rapid Commun. Mass Spectrom.* **2015**, *29* (11), 1019–1024. https://doi.org/10.1002/rcm.7191.

(83)   Lanni, E. J.; Masyuko, R. N.; Driscoll, C. M.; Dunham, S. J. B.; Shrout, J. D.; Bohn, P. W.; Sweedler, J. V. Correlated Imaging with C $_{60}$ -SIMS and Confocal Raman Microscopy: Visualization of Cell-Scale Molecular Distributions in Bacterial Biofilms. *Anal. Chem.* **2014**, *86* (21), 10885–10891. https://doi.org/10.1021/ac5030914.

(84)   Murray, K. K.; Seneviratne, C. A.; Ghorai, S. High Resolution Laser Mass Spectrometry Bioimaging. *Methods* **2016**, *104*, 118–126. https://doi.org/10.1016/J.YMETH.2016.03.002.

(85)   Buchberger, A. R.; DeLaney, K.; Johnson, J.; Li, L. Mass Spectrometry Imaging: A Review of Emerging Advancements and Future Insights. *Anal. Chem.* **2018**, *90* (1), 240–265. https://doi.org/10.1021/acs.analchem.7b04733.

(86)   Spengler, B.; Hubert, M. Scanning Microprobe Matrix-Assisted Laser Desorption Ionization (SMALDI) Mass Spectrometry: Instrumentation for Sub-Micrometer Resolved LDI and MALDI Surface Analysis. *J. Am. Soc. Mass Spectrom.* **2002**, *13* (6), 735–748. https://doi.org/10.1016/S1044-0305(02)00376-8.

(87)   Zavalin, A.; Yang, J.; Caprioli, R. Laser Beam Filtration for High Spatial Resolution MALDI Imaging Mass Spectrometry. *J. Am. Soc. Mass Spectrom.* **2013**, *24* (7), 1153–1156. https://doi.org/10.1007/S13361-013-0638-5.

(88)   Hillenkamp, F.; Unsöld, E.; Kaufmann, R.; Nitsche, R. A High-Sensitivity Laser
       Microprobe Mass Analyzer. *Appl. Phys.* **1975**, *8* (4), 341–348.
       https://doi.org/10.1007/BF00898368.

(89)   Richards, A. L.; Lietz, C. B.; Wager-Miller, J. B.; Mackie, K.; Trimpin, S. Imaging Mass
       Spectrometry in Transmission Geometry. *Rapid Commun. Mass Spectrom.* **2011**, *25* (6),
       815–820. https://doi.org/10.1002/rcm.4927.

(90)   Schürenberg, M.; Schulz, T.; Dreisewerd, K.; Hillenkamp, F. Matrix-Assisted Laser
       Desorption/Ionization in Transmission Geometry: Instrumental Implementation and
       Mechanistic Implications. *Rapid Commun. Mass Spectrom.* **1996**, *10* (15), 1873–1880.
       https://doi.org/10.1002/(SICI)1097-0231(199612)10:15<1873::AID-RCM719>3.0.CO;2-
       3.

(91)   Goto-Inoue, N.; Hayasaka, T.; Zaima, N.; Setou, M. Imaging Mass Spectrometry Reveals
       Changes of Metabolites Distribution in Mouse Testis during Testicular Maturation. *Surf.
       Interface Anal.* **2012**, *44* (6), 749–754. https://doi.org/10.1002/sia.3869.

(92)   Tadano-Aritomi, K.; Matsuda, J.; Fujimoto, H.; Suzuki, K.; Ishizuka, I. Seminolipid and
       Its Precursor/Degradative Product, Galactosylalkylacylglycerol, in the Testis of Saposin
       A- and Prosaposin-Deficient Mice. *J. Lipid Res.* **2003**, *44* (9), 1737–1743.
       https://doi.org/10.1194/JLR.M300119-JLR200.

(93)   Goto-Inoue, N.; Hayasaka, T.; Zaima, N.; Setou, M. The Specific Localization of
       Seminolipid Molecular Species on Mouse Testis during Testicular Maturation Revealed
       by Imaging Mass Spectrometry. *Glycobiology* **2009**, *19* (9), 950–957.
       https://doi.org/10.1093/glycob/cwp089.

(94) Zhang, Y.; Hayashi, Y.; Cheng, X.; Watanabe, T.; Wang, X.; Taniguchi, N.; Honke, K. Testis-Specific Sulfoglycolipid, Seminolipid, Is Essential for Germ Cell Function in Spermatogenesis. *Glycobiology* **2005**, *15* (6), 649–654. https://doi.org/10.1093/glycob/cwi043.

(95) Bowrey, H. E.; Anderson, D. M.; Pallitto, P.; Gutierrez, D. B.; Fan, J.; Crouch, R. K.; Schey, K. L.; Ablonczy, Z. Imaging Mass Spectrometry of the Visual System: Advancing the Molecular Understanding of Retina Degenerations. *PROTEOMICS - Clin. Appl.* **2016**, *10* (4), 391–402. https://doi.org/10.1002/prca.201500103.

(96) Perry, W. Imaging Mass Spectrometry of Staphylococcus Aureus Infection: Mapping Pathogenic Adaptations That Circumvent Immunity, Dissertation, Vanderbilt University, 2020.

(97) Dilillo, M.; Ait-Belkacem, R.; Esteve, C.; Pellegrini, D.; Nicolardi, S.; Costa, M.; Vannini, E.; De Graaf, E. L.; Caleo, M.; McDonnell, L. A. Ultra-High Mass Resolution MALDI Imaging Mass Spectrometry of Proteins and Metabolites in a Mouse Model of Glioblastoma. *Sci. Rep.* **2017**, *7* (1), 1–11. https://doi.org/10.1038/s41598-017-00703-w.

(98) Karlsson, O.; Hanrieder, J. Imaging Mass Spectrometry in Drug Development and Toxicology. *Arch. Toxicol.* **2017**, *91* (6), 2283–2294. https://doi.org/10.1007/s00204-016-1905-6.

(99) Maccarrone, G.; Nischwitz, S.; Deininger, S.-O.; Hornung, J.; König, F. B.; Stadelmann, C.; Turck, C. W.; Weber, F. MALDI Imaging Mass Spectrometry Analysis—A New Approach for Protein Mapping in Multiple Sclerosis Brain Lesions. *J. Chromatogr. B* **2017**, *1047*, 131–140. https://doi.org/10.1016/J.JCHROMB.2016.07.001.

(100) Meding, S.; Nitsche, U.; Balluff, B.; Elsner, M.; Rauser, S.; Schöne, C.; Nipp, M.; Maak, M.; Feith, M.; Ebert, M. P.; Friess, H.; Langer, R.; Höfler, H.; Zitzelsberger, H.; Rosenberg, R.; Walch, A. Tumor Classification of Six Common Cancer Types Based on Proteomic Profiling by MALDI Imaging. *J. Proteome Res.* **2012**, *11* (3), 1996–2003. https://doi.org/10.1021/pr200784p.

(101) Labas, V.; Spina, L.; Belleannee, C.; Teixeira-Gomes, A.-P.; Gargaros, A.; Dacheux, F.; Dacheux, J.-L. Analysis of Epididymal Sperm Maturation by MALDI Profiling and Top-down Mass Spectrometry. *J. Proteomics* **2015**, *113*, 226–243. https://doi.org/10.1016/J.JPROT.2014.09.031.

(102) Spraggins, J. M.; Rizzo, D. G.; Moore, J. L.; Noto, M. J.; Skaar, E. P.; Caprioli, R. M. Next-Generation Technologies for Spatial Proteomics: Integrating Ultra-High Speed MALDI-TOF and High Mass Resolution MALDI FTICR Imaging Mass Spectrometry for Protein Analysis. *Proteomics* **2016**, *16* (11–12), 1678–1689. https://doi.org/10.1002/pmic.201600003.

(103) Wenke, J. L.; Rose, K. L.; Spraggins, J. M.; Schey, K. L. MALDI Imaging Mass Spectrometry Spatially Maps Age-Related Deamidation and Truncation of Human Lens Aquaporin-0. *Investig. Opthalmology Vis. Sci.* **2015**, *56* (12), 7398. https://doi.org/10.1167/iovs.15-18117.

(104) Gessel, M. M.; Norris, J. L.; Caprioli, R. M. MALDI Imaging Mass Spectrometry: Spatial Molecular Analysis to Enable a New Age of Discovery. *J. Proteomics* **2014**, *107*, 71–82. https://doi.org/10.1016/J.JPROT.2014.03.021.

(105) Seeley, E. H.; Oppenheimer, S. R.; Mi, D.; Chaurand, P.; Caprioli, R. M. Enhancement of Protein Sensitivity for MALDI Imaging Mass Spectrometry After Chemical Treatment of Tissue Sections. *J. Am. Soc. Mass Spectrom.* **2008**, *19* (8), 1069–1077. https://doi.org/10.1016/j.jasms.2008.03.016.

(106) Thomas, A.; Patterson, N. H.; Laveaux Charbonneau, J.; Chaurand, P. Orthogonal Organic and Aqueous-Based Washes of Tissue Sections to Enhance Protein Sensitivity by MALDI Imaging Mass Spectrometry. *J. Mass Spectrom.* **2013**, *48* (1), 42–48. https://doi.org/10.1002/jms.3114.

(107) Lemaire, R.; Stauber, J.; Wisztorski, M.; Van Camp, C.; Desmons, A.; Deschamps, M.; Proess, G.; Rudlof, I.; Woods, A. S.; Day, R.; Salzet, M.; Fournier, I. Tag-Mass: Specific Molecular Imaging of Transcriptome and Proteome by Mass Spectrometry Based on Photocleavable Tag. *J. Proteome Res.* **2007**, *6* (6), 2057–2067. https://doi.org/10.1021/pr0700044.

(108) Thiery-Lavenant, G.; Zavalin, A. I.; Caprioli, R. M. Targeted Multiplex Imaging Mass Spectrometry in Transmission Geometry for Subcellular Spatial Resolution. *J. Am. Soc. Mass Spectrom.* **2013**, *24* (4), 609–614. https://doi.org/10.1007/s13361-012-0563-z.

(109) Qiao, L.; Roussel, C.; Wan, J.; Kong, J.; Yang, P.; Girault, H. H.; Liu, B. MALDI In-Source Photooxidation Reactions for Online Peptide Tagging. *Angew. Chemie Int. Ed.* **2008**, *47* (14), 2646–2648. https://doi.org/10.1002/anie.200703876.

(110) Anna Pashkova; Eugene Moskovets, A.; Karger, B. L. Coumarin Tags for Improved Analysis of Peptides by MALDI-TOF MS and MS/MS. 1. Enhancement in MALDI MS Signal Intensities. *Anal. Chem.* **2004**, *76*, 4550–4557. https://doi.org/10.1021/AC049638+.

(111) Prentice, B. M.; Ryan, D. J.; Grove, K. J.; Cornett, D. S.; Caprioli, R. M.; Spraggins, J. M. Dynamic Range Expansion by Gas-Phase Ion Fractionation and Enrichment for Imaging Mass Spectrometry. *Anal. Chem.* **2020**, *92* (19), 13092–13100. https://doi.org/10.1021/acs.analchem.0c02121.

(112) Li, N.; Wang, P.; Liu, X.; Han, C.; Ren, W.; Li, T.; Li, X.; Tao, F.; Zhao, Z. Developing IR-780 as a Novel Matrix for Enhanced MALDI MS Imaging of Endogenous High-Molecular-Weight Lipids in Brain Tissues. *Anal. Chem.* **2019**, *91* (24), 15873–15882. https://doi.org/10.1021/acs.analchem.9b04315.

(113) Liu, H.; Zhou, Y.; Wang, J.; Xiong, C.; Xue, J.; Zhan, L.; Nie, Z. N-Phenyl-2-Naphthylamine as a Novel MALDI Matrix for Analysis and in Situ Imaging of Small Molecules. *Anal. Chem.* **2018**, *90* (1), 729–736. https://doi.org/10.1021/acs.analchem.7b02710.

(114) Wiegelmann, M.; Soltwisch, J.; Jaskolla, T. W.; Dreisewerd, K. Matching the Laser Wavelength to the Absorption Properties of Matrices Increases the Ion Yield in UV-MALDI Mass Spectrometry. *Anal. Bioanal. Chem.* **2013**, *405* (22), 6925–6932. https://doi.org/10.1007/s00216-012-6478-5.

(115) Karas, M.; Ehring, H.; Nordhoff, E.; Stahl, B.; Strupat, K.; Hillenkamp, F.; Grehl, M.; Krebs, B. Matrix-Assisted Laser Desorption/Ionization Mass Spectrometry with Additives to 2,5-Dihydroxybenzoic Acid. *Org. Mass Spectrom.* **1993**, *28* (12), 1476–1481. https://doi.org/10.1002/oms.1210281219.

(116) Tsai, M.-T.; Lee, S.; Lu, I.-C.; Chu, K. Y.; Liang, C.-W.; Lee, C. H.; Lee, Y. T.; Ni, C.-K. Ion-to-Neutral Ratio of 2,5-Dihydroxybenzoic Acid in Matrix-Assisted Laser Desorption/Ionization. *Rapid Commun. Mass Spectrom.* **2013**, *27* (9), 955–963. https://doi.org/10.1002/rcm.6534.

(117) Knochenmuss, R.; Karbach, V.; Wiesli, U.; Breuker, K.; Zenobi, R. The Matrix Suppression Effect in Matrix-Assisted Laser Desorption/Ionization: Application to Negative Ions and Further Characteristics. *Rapid Commun. Mass Spectrom.* **1998**, *12*, 529–534. https://doi.org/10.1002/(SICI)1097-0231(19980515)12:9<529::AID-RCM188>3.0.CO;2-E.

(118) Spengler, B.; Bahr, U.; Karas, M.; Hillenkamp, F. Postionization of Laser-Desorbed Organic and Inorganic Compounds in a Time of Flight Mass Spectrometer. *Instrum. Sci. Technol.* **1988**, *17* (1–2), 173–193. https://doi.org/10.1080/10739148808543672.

(119) McMillen, J. C.; Spivey, E. C.; Ryan, D. J.; Spraggins, J. M.; Caprioli, R. M. MALDI Spatial Resolution Improvment Using MALDI-2 Post-Ionization. In *MALDI Spatial Resolution Improvment using MALDI-2 Post-Ionization*; Poster presentation at the American Society for Mass Spectrometry: Atlanta, GA, 2019.

(120) Hanley, L.; Wickramasinghe, R.; Yung, Y. P. Laser Desorption Combined with Laser Postionization for Mass Spectrometry. *Annu. Rev. Anal. Chem.* **2019**, *12*, 225–245. https://doi.org/10.1146/annurev-anchem-061318-115447.

(121) Diologent, L.; Bolbach, G.; Focsa, C.; Ziskind, M.; Fournier, I. Laser Induced Post-Desolvation of MALDI Clusters. *Int. J. Mass Spectrom.* **2017**, *416*, 29–36. https://doi.org/10.1016/J.IJMS.2016.12.005.

(122) Niehaus, M.; Soltwisch, J. New Insights into Mechanisms of Material Ejection in MALDI Mass Spectrometry for a Wide Range of Spot Sizes. *Sci. Rep.* **2018**, *8* (1), 7755. https://doi.org/10.1038/s41598-018-25946-z.

(123) Boskamp, M. S.; Soltwisch, J. Charge Distribution between Different Classes of Glycerophospolipids in MALDI-MS Imaging. *Anal. Chem.* **2020**. https://doi.org/10.1021/acs.analchem.9b05761.

(124) Barré, F. P. Y.; Paine, M. R. L.; Flinders, B.; Trevitt, A. J.; Kelly, P. D.; Ait-Belkacem, R.; Garcia, J. P.; Creemers, L. B.; Stauber, J.; Vreeken, R. J.; Cillero-Pastor, B.; Ellis, S. R.; Heeren, R. M. A. Enhanced Sensitivity Using Maldi Imaging Coupled with Laser Postionization (Maldi-2) for Pharmaceutical Research. *Anal. Chem.* **2019**, *91* (16), 10840–10848. https://doi.org/10.1021/acs.analchem.9b02495.

(125) Strohalm, M.; Hassman, M.; Košata, B.; Kodíček, M. MMass Data Miner: An Open Source Alternative for Mass Spectrometric Data Analysis. *Rapid Communications in Mass Spectrometry*. John Wiley & Sons, Ltd March 30, 2008, pp 905–908. https://doi.org/10.1002/rcm.3444.

(126) Huizing, L. R. S.; Ellis, S. R.; Beulen, B. W. A. M. M.; Barré, F. P. Y.; Kwant, P. B.; Vreeken, R. J.; Heeren, R. M. A. Development and Evaluation of Matrix Application Techniques for High Throughput Mass Spectrometry Imaging of Tissues in the Clinic. *Clin. Mass Spectrom.* **2019**, *12*, 7–15. https://doi.org/10.1016/J.CLINMS.2019.01.004.

(127) Berry, K. A. Z.; Hankin, J. A.; Barkley, R. M.; Spraggins, J. M.; Caprioli, R. M.; Murphy, R. C. MALDI Imaging of Lipid Biochemistry in Tissues by Mass Spectrometry. *Chem. Rev.* **2011**, *111*, 6491–6512. https://doi.org/10.1021/cr200280p.

(128) Chumbley, C. W.; Reyzer, M. L.; Allen, J. L.; Marriner, G. A.; Via, L. E.; Barry, C. E.; Caprioli, R. M. Absolute Quantitative MALDI Imaging Mass Spectrometry: A Case of Rifampicin in Liver Tissues. *Anal. Chem.* **2016**, *88* (4), 2392–2398. https://doi.org/10.1021/acs.analchem.5b04409.

(129) Takai, N.; Tanaka, Y.; Saji, H. Quantification of Small Molecule Drugs in Biological Tissue Sections by Imaging Mass Spectrometry Using Surrogate Tissue-Based Calibration Standards. *Mass Spectrom.* **2014**, *3* (1), A0025–A0025. https://doi.org/10.5702/massspectrometry.a0025.

(130) Jadoul, L.; Longuespée, R.; Noël, A.; De Pauw, E. A Spiked Tissue-Based Approach for Quantification of Phosphatidylcholines in Brain Section by MALDI Mass Spectrometry Imaging. *Anal. Bioanal. Chem.* **2015**, *407* (8), 2095–2106. https://doi.org/10.1007/s00216-014-8232-7.

(131) Dufresne, M.; Patterson, N. H.; Norris, J. L.; Caprioli, R. M. Combining Salt Doping and Matrix Sublimation for High Spatial Resolution MALDI Imaging Mass Spectrometry of Neutral Lipids. *Anal. Chem.* **2019**, *91* (20), 12928–12934. https://doi.org/10.1021/acs.analchem.9b02974.

(132) Dufresne, M.; Masson, J. F.; Chaurand, P. Sodium-Doped Gold-Assisted Laser Desorption Ionization for Enhanced Imaging Mass Spectrometry of Triacylglycerols from Thin Tissue Sections. *Anal. Chem.* **2016**, *88* (11), 6018–6025. https://doi.org/10.1021/acs.analchem.6b01141.

(133) Barry, J. A.; Groseclose, M. R.; Fraser, D. D.; Castellino, S. Revised Preparation of a Mimetic Tissue Model for Quantitative Imaging Mass Spectrometry. *Protoc. Exch.* **2018**. https://doi.org/10.1038/protex.2018.104.

(134) Patterson, N. H.; Tuck, M.; Van de Plas, R.; Caprioli, R. M. Advanced Registration and Analysis of MALDI Imaging Mass Spectrometry Measurements through Autofluorescence Microscopy. *Anal. Chem.* **2018**, *90* (21), 12395–12403. https://doi.org/10.1021/acs.analchem.8b02884.

(135) Sarretto, T.; Spotbeen, X.; Gevaert, T.; Joniau, S.; Swinnen, J. V; Trevitt, A. J.; Ellis, S. R.; Trevitt, A. J.; Ellis, S. R.; Joniau, S. Selective Mass Spectrometry Imaging of Aromatic Antioxidants Using Sequential Matrix-Assisted Laser Desorption and Resonant Photoionisation. *Anal. Sens.* **2022**, *2* (1), e202100052. https://doi.org/10.1002/ANSE.202100052.

(136) McMillen, J. C.; Fincher, J. A.; Klein, D. R.; Spraggins, J. M.; Caprioli, R. M. Effect of MALDI Matrices on Lipid Analyses of Biological Tissues Using MALDI-2 Post-Ionization Mass Spectrometry. *J. Mass Spectrom.* https://doi.org/10.1002/JMS.4663.

(137) Jiang, K.; Gachumi, G.; Poudel, A.; Shurmer, B.; Bashi, Z.; El-Aneed, A. The Establishment of Tandem Mass Spectrometric Fingerprints of Phytosterols and Tocopherols and the Development of Targeted Profiling Strategies in Vegetable Oils. *J. Am. Soc. Mass Spectrom.* **2019**, *30* (9), 1700–1712. https://doi.org/10.1007/s13361-019-02242-2.

(138) Altelaar, A. F. M.; Taban, I. M.; McDonnell, L. A.; Verhaert, P. D. E. M.; de Lange, R. P. J.; Adan, R. A. H.; Mooi, W. J.; Heeren, R. M. A.; Piersma, S. R. High-Resolution MALDI Imaging Mass Spectrometry Allows Localization of Peptide Distributions at Cellular Length Scales in Pituitary Tissue Sections. *Int. J. Mass Spectrom.* **2007**, *260* (2–3), 203–211. https://doi.org/10.1016/j.ijms.2006.09.028.

(139) Wisztorski, M.; Desmons, A.; Quanico, J.; Fatou, B.; Gimeno, J.-P.; Franck, J.; Salzet, M.; Fournier, I. Spatially-Resolved Protein Surface Microsampling from Tissue Sections Using Liquid Extraction Surface Analysis. *Proteomics* **2016**, *16* (11–12), 1622–1632. https://doi.org/10.1002/pmic.201500508.

(140) Wang, J.; Ying, G.; Wang, J.; Jung, Y.; Lu, J.; Zhu, J.; Pienta, K. J.; Taichman, R. S. Characterization of Phosphoglycerate Kinase-1 Expression of Stromal Cells Derived from Tumor Microenvironment in Prostate Cancer Progression. *Cancer Res.* **2010**, *70* (2), 471–480. https://doi.org/10.1158/0008-5472.CAN-09-2863.

(141) Ludwig, K.; Habbach, S.; Krieglstein, J.; Klumpp, S.; König, S. MALDI-TOF High Mass Calibration up to 200 KDa Using Human Recombinant 16 KDa Protein Histidine Phosphatase Aggregates. *PLoS One* **2011**, *6* (8), e23612. https://doi.org/10.1371/journal.pone.0023612.

(142) Prentice, B. M.; Ryan, D. J.; Van de Plas, R.; Caprioli, R. M.; Spraggins, J. M. Enhanced Ion Transmission Efficiency up to m/z 24 000 for MALDI Protein Imaging Mass Spectrometry. *Anal. Chem.* **2018**, *90* (8), 5090–5099. https://doi.org/10.1021/acs.analchem.7b05105.

(143) Piga, I.; Heijs, B.; Nicolardi, S.; Giusti, L.; Marselli, L.; Marchetti, P.; Mazzoni, M. R.; Lucacchini, A.; McDonnell, L. A. Ultra-High Resolution MALDI-FTICR-MSI Analysis of Intact Proteins in Mouse and Human Pancreas Tissue. *Int. J. Mass Spectrom.* **2019**, *437*, 10–16. https://doi.org/10.1016/j.ijms.2017.11.001.

(144) Minerva, L.; Boonen, K.; Menschaert, G.; Landuyt, B.; Baggerman, G.; Arckens, L. Linking Mass Spectrometric Imaging and Traditional Peptidomics: A Validation in the Obese Mouse Model. *Anal. Chem.* **2011**, *83* (20), 7682–7691. https://doi.org/10.1021/ac200888j.

(145) Gustafsson, J. O. R.; Oehler, M. K.; McColl, S. R.; Hoffmann, P. Citric Acid Antigen Retrieval (CAAR) for Tryptic Peptide Imaging Directly on Archived Formalin-Fixed Paraffin-Embedded Tissue. *J. Proteome Res.* **2010**, *9* (9), 4315–4328. https://doi.org/10.1021/pr9011766.

(146) Huber, K.; Khamehgir-Silz, P.; Schramm, T.; Gorshkov, V.; Spengler, B.; Römpp, A. Approaching Cellular Resolution and Reliable Identification in Mass Spectrometry Imaging of Tryptic Peptides. *Anal. Bioanal. Chem.* **2018**, *410* (23), 5825–5837. https://doi.org/10.1007/s00216-018-1199-z.

(147) Schober, Y.; Guenther, S.; Spengler, B.; Römpp, A. High-Resolution Matrix-Assisted Laser Desorption/Ionization Imaging of Tryptic Peptides from Tissue. *Rapid Commun. Mass Spectrom.* **2012**, *26* (9), 1141–1146. https://doi.org/10.1002/rcm.6192.

(148) Person, M. D.; Lo, H. H.; Towndrow, K. M.; Jia, Z.; Monks, T. J.; Lau, S. S. Comparative Identification of Prostanoid Inducible Proteins by LC-ESI-MS/MS and MALDI-TOF Mass Spectrometry. *Chem. Res. Toxicol.* **2003**, *16* (6), 757–767. https://doi.org/10.1021/tx020049d.

(149) Maria Nadler, W.; Waidelich, D.; Kerner, A.; Hanke, S.; Berg, R.; Trumpp, A.; Ro, C. MALDI versus ESI: The Impact of the Ion Source on Peptide Identification. *J. Proteome Res.* **2017**, *16*, 1207–1215. https://doi.org/10.1021/acs.jproteome.6b00805.

(150) Lim, H.; Eng, J.; Yates, J. R.; Tollaksen, S. L.; Giometti, C. S.; Holden, J. F.; Adams, M. W. W.; Reich, C. I.; Olsen, G. J.; Hays, L. G. Identification of 2D-Gel Proteins: A Comparison of MALDI/TOF Peptide Mass Mapping to μ LC-ESI Tandem Mass Spectrometry. *J. Am. Soc. Mass Spectrom.* **2003**, *14* (9), 957–970. https://doi.org/10.1016/S1044-0305(03)00144-2.

(151) Heijs, B.; Carreira, R. J.; Tolner, E. A.; De Ru, A. H.; Van Den Maagdenberg, A. M. J. M.; Van Veelen, P. A.; McDonnell, L. A. Comprehensive Analysis of the Mouse Brain Proteome Sampled in Mass Spectrometry Imaging. *Anal. Chem.* **2015**, *87* (3), 1867–1875. https://doi.org/10.1021/ac503952q.

(152) Crank, J. A.; Armstrong, D. W. Towards a Second Generation of Ionic Liquid Matrices (ILMs) for MALDI-MS of Peptides, Proteins, and Carbohydrates. *J. Am. Soc. Mass Spectrom.* **2009**, *20* (10), 1790–1800. https://doi.org/10.1016/j.jasms.2009.05.020.

(153) Cillero-Pastor, B.; Heeren, R. M. A. Matrix-Assisted Laser Desorption Ionization Mass Spectrometry Imaging for Peptide and Protein Analyses: A Critical Review of On-Tissue Digestion. *J. Proteome Res.* **2013**, *13* (2), 325–335. https://doi.org/10.1021/pr400743a.

(154) Angel, P. M.; Mehta, A.; Norris-Caneda, K.; Drake, R. R. MALDI Imaging Mass Spectrometry of N-Glycans and Tryptic Peptides from the Same Formalin-Fixed, Paraffin-Embedded Tissue Section. In *Methods in Molecular Biology*; Sarwal, M. M., Sigdel, T. K., Eds.; New York, NY, 2018; Vol. 1788, pp 225–241. https://doi.org/10.1007/7651_2017_81.

(155) Soltwisch, J.; Heijs, B.; Koch, A.; Vens-Cappell, S.; Ho, J.; Dreisewerd, K. MALDI-2 on a Trapped Ion Mobility Quadrupole Time-of-Flight Instrument for Rapid Mass Spectrometry Imaging and Ion Mobility Separation of Complex Lipid Profiles. *Anal. Chem.* **2020**, *92* (13), 8697–8703. https://doi.org/10.1021/acs.analchem.0c01747.

(156) Heijs, B.; Potthoff, A.; Soltwisch, J.; Dreisewerd, K. MALDI-2 for the Enhanced Analysis of N -Linked Glycans by Mass Spectrometry Imaging . *Anal. Chem.* **2020**, *92* (20), 13904–13911. https://doi.org/10.1021/acs.analchem.0c02732.

(157) Woods, A. S.; Jackson, S. N.; Lewis, E. K.; Egan, T.; Muller, L.; Tabet, J. C.; Schultz, J. A. MALDI/Post Ionization-Ion Mobility Mass Spectrometry of Noncovalent Complexes of Dopamine Receptors' Epitopes. *J. Proteome Res.* **2013**, *12* (4), 1668–1677. https://doi.org/10.1021/pr301004w.

(158) Schreiber, C. L.; Smith, B. D. Molecular Imaging of Aminopeptidase N in Cancer and Angiogenesis. *Contrast Media and Molecular Imaging*. Hindawi Limited 2018. https://doi.org/10.1155/2018/5315172.

(159) Wickström, M.; Larsson, R.; Nygren, P.; Gullbo, J. Aminopeptidase N (CD13) as a Target for Cancer Chemotherapy. *Cancer Science*. March 2011, pp 501–508. https://doi.org/10.1111/j.1349-7006.2010.01826.x.

(160) Gao, J.; Zhao, R.; Xue, Y.; Niu, Z.; Cui, K.; Yu, F.; Zhang, B.; Li, S. Role of Enolase-1 in Response to Hypoxia in Breast Cancer: Exploring the Mechanisms of Action. *Oncol. Rep.* **2013**, *29* (4), 1322–1332. https://doi.org/10.3892/or.2013.2269.

(161) Heawchaiyaphum, C.; Pientong, C.; Phusingha, P.; Vatanasapt, P.; Promthet, S.; Daduang, J.; Teeramatwanich, W.; Kongyingyoes, B.; Chuerduangphui, J.; Ekalaksananan, T. Peroxiredoxin-2 and Zinc-Alpha-2-Glycoprotein as Potentially Combined Novel Salivary Biomarkers for Early Detection of Oral Squamous Cell Carcinoma Using Proteomic Approaches. *J. Proteomics* **2018**, *173*, 52–61. https://doi.org/10.1016/j.jprot.2017.11.022.

(162) Lai, C.-K.; Ng, D. C. M.; Pang, H. F.; Le Blanc, J. C. Y.; Hager, J. W.; Fang, D.-C.; Cheung, A. S.-C.; Chu, I. K. Laser-Induced Dissociation of Singly Protonated Peptides at 193 and 266 Nm within a Hybrid Linear Ion Trap Mass Spectrometer. *Rapid Commun. Mass Spectrom.* **2013**, *27* (10), 1119–1127. https://doi.org/10.1002/rcm.6545.

(163) Potthoff, A.; Dreisewerd, K.; Soltwisch, J. Detailed Characterization of the Postionization Efficiencies in MALDI-2 as a Function of Relevant Input Parameters. *J. Am. Soc. Mass Spectrom.* **2020**, *31* (9), 1844–1853. https://doi.org/10.1021/jasms.0c00072.

(164) Kyte, J.; Doolittle, R. F. A Simple Method for Displaying the Hydropathic Character of a Protein. *J. Mol. Biol.* **1982**, *157* (1), 105–132. https://doi.org/10.1016/0022-2836(82)90515-0.

(165) Guo, G.; Papanicolaou, M.; Demarais, N. J.; Wang, Z.; Schey, K. L.; Timpson, P.; Cox, T. R.; Grey, A. C. Automated Annotation and Visualisation of High-Resolution Spatial Proteomic Mass Spectrometry Imaging Data Using HIT-MAP. *Nat. Commun. 2021 121* **2021**, *12* (1), 1–16. https://doi.org/10.1038/s41467-021-23461-w.

(166) Meding, S.; Martin, K.; Gustafsson, O. J. R.; Eddes, J. S.; Hack, S.; Oehler, M. K.; Hoffmann, P. Tryptic Peptide Reference Data Sets for MALDI Imaging Mass Spectrometry on Formalin-Fixed Ovarian Cancer Tissues. *J. Proteome Res.* **2013**, *12* (1), 308–315. https://doi.org/10.1021/pr300996x.

(167) Thiede, B.; Höhenwarter, W.; Krah, A.; Mattow, J.; Schmid, M.; Schmidt, F.; Jungblut, P. R. Peptide Mass Fingerprinting. *Methods* **2005**, *35* (3), 237–247. https://doi.org/10.1016/j.ymeth.2004.08.015.

(168) Brewer, M.; Allen, J.; Neumann, E.; Fogo, A.; Harris, R.; Gutierrez, D.; De Caestecker, M.; Spraggins, J. *Collection and Post-Surgical Excision of Human Kidney Tissue through the Cooperative Human Tissue Network*; 2019. https://doi.org/10.17504/protocols.io.7gehjte.

(169) Allen, J.; Brewer, M.; Neumann, E.; Gutierrez, D.; Decaestecker, M.; Spraggins, J. *Freezing Fresh Tissue V.2*; 2019. https://doi.org/10.17504/protocols.io.6wghfbw.

(170) Anderson, D.; Neumann, E.; Allen, J.; Brewer, M.; Gutierrez, D.; Spraggins, J. *Cryostat Sectioning of Tissues for 3D Multimodal Molecular Imaging*; 2019. https://doi.org/10.17504/protocols.io.7ethjen.

(171) Anderson, D. M. G.; Lambert, W.; Calkins, D. J.; Ablonczy, Z.; Crouch, R. K.; Caprioli, R. M.; Schey, K. L. Imaging MS of Rodent Ocular Tissues and the Optic Nerve. In *Methods in Molecular Biology*; Humana Press Inc., 2017; Vol. 1618, pp 15–27. https://doi.org/10.1007/978-1-4939-7051-3_3.

(172) Allen, J.; Spraggins, J.; Gutierrez, D. *Automated, Rapid Preparation of Tissue Sections for Proteomic Analysis V.2*; 2019. https://doi.org/10.17504/protocols.io.67nhhme.

(173) Gutierrez, D.; Allen, J.; Jenkins, Z.; Spraggins, J. *LC-MS/MS Label-Free Proteomic Data Acquisition V.3*; 2020. https://doi.org/10.17504/protocols.io.bft3jnqn.

(174) Gutierrez, D.; Allen, J.; Jenkins, Z.; Spraggins, J. *LC-MS/MS Label-Free Proteomic Data Analysis Parameters V.2*; 2020. https://doi.org/10.17504/protocols.io.bfshjnb6.

(175) Deutsch, E. W.; Csordas, A.; Sun, Z.; Jarnuczak, A.; Perez-Riverol, Y.; Ternent, T.; Campbell, D. S.; Bernal-Llinares, M.; Okuda, S.; Kawano, S.; Moritz, R. L.; Carver, J. J.; Wang, M.; Ishihama, Y.; Bandeira, N.; Hermjakob, H.; Vizcaíno, J. A. The ProteomeXchange Consortium in 2017: Supporting the Cultural Change in Proteomics Public Data Deposition. *Nucleic Acids Res.* **2017**, *45* (D1), D1100–D1106. https://doi.org/10.1093/nar/gkw936.

(176) Perez-Riverol, Y.; Csordas, A.; Bai, J.; Bernal-Llinares, M.; Hewapathirana, S.; Kundu, D. J.; Inuganti, A.; Griss, J.; Mayer, G.; Eisenacher, M.; Pérez, E.; Uszkoreit, J.; Pfeuffer, J.; Sachsenberg, T.; Yilmaz, Ş.; Tiwary, S.; Cox, J.; Audain, E.; Walzer, M.; Jarnuczak, A. F.; Ternent, T.; Brazma, A.; Vizcaíno, J. A. The PRIDE Database and Related Tools and Resources in 2019: Improving Support for Quantification Data. *Nucleic Acids Res.* **2019**, *47* (D1), D442–D450. https://doi.org/10.1093/nar/gky1106.

(177) Matthiesen, R.; Bunkenborg, J. Introduction to Mass Spectrometry-Based Proteomics. In *Methods in Molecular Biology*; Humana Press Inc., 2020; Vol. 2051, pp 1–58. https://doi.org/10.1007/978-1-4939-9744-2_1.

(178) Cooper, G. J.; Willis, A. C.; Clark, A.; Turner, R. C.; Sim, R. B.; Reid, K. B. Purification and Characterization of a Peptide from Amyloid-Rich Pancreases of Type 2 Diabetic Patients. *Proc. Natl. Acad. Sci.* **1987**, *84* (23), 8628–8632. https://doi.org/10.1073/PNAS.84.23.8628.

(179) Kumar Bishoyi, A.; Roham, P. H.; Rachineni, K.; Save, S.; Hazari, M. A.; Sharma, S.; Kumar, A. Human Islet Amyloid Polypeptide (HIAPP)-a Curse in Type II Diabetes Mellitus: Insights from Structure and Toxicity Studies. *Biol. Chem.* **2021**, *402* (2), 133–153. https://doi.org/10.1515/hsz-2020-0174.

(180) Asthana, S.; Mallick, B.; Alexandrescu, A. T.; Jha, S. IAPP in Type II Diabetes: Basic Research on Structure, Molecular Interactions, and Disease Mechanisms Suggests Potential Intervention Strategies. *Biochim. Biophys. Acta - Biomembr.* **2018**, *1860* (9), 1765–1782. https://doi.org/10.1016/J.BBAMEM.2018.02.020.

(181) Kapurniotu, A.; Bernhagen, J.; Greenfield, N.; Al-Abed, Y.; Teichberg, S.; Frank, R. W.; Voelter, W.; Bucala, R. Contribution of Advanced Glycosylation to the Amyloidogenicity of Islet and Amyloid Polypeptide. *Eur. J. Biochem.* **1998**, *251* (1–2), 208–216. https://doi.org/10.1046/j.1432-1327.1998.2510208.x.

(182) Ma, Z.; Westermark, P.; Westermark, G. T. Amyloid in Human Islets of Langerhans: Immunologic Evidence That Islet Amyloid Polypeptide Is Modified in Amyloidogenesis. *Pancreas* **2000**, *21* (2), 212–218. https://doi.org/10.1097/00006676-200008000-00015.

(183) Gill, V.; Kumar, V.; Singh, K.; Kumar, A.; Kim, J. J. Advanced Glycation End Products (AGEs) May Be a Striking Link Between Modern Diet and Health. *Biomolecules* **2019**, *9* (888), 1–21. https://doi.org/10.3390/BIOM9120888.

(184) Argirov, O. K.; Lin, B.; Olesen, P.; Ortwerth, B. J. Isolation and Characterization of a New Advanced Glycation Endproduct of Dehydroascorbic Acid and Lysine. *Biochim. Biophys. Acta - Gen. Subj.* **2003**, *1620* (1–3), 235–244. https://doi.org/10.1016/S0304-4165(03)00002-3.

(185) Akagawa, M.; Sasaki, D.; Kurota, Y.; Suyama, K. Formation of α-Aminoadipic and γ-Glutamic Semialdehydes in Proteins by the Maillard Reaction. In *Annals of the New York Academy of Sciences*; New York Academy of Sciences, 2005; Vol. 1043, pp 129–134. https://doi.org/10.1196/annals.1333.016.

(186) Nevin, C.; McNeil, L.; Ahmed, N.; Murgatroyd, C.; Brison, D.; Carroll, M. Investigating the Glycating Effects of Glucose, Glyoxal and Methylglyoxal on Human Sperm. *Sci. Reports 2018 81* **2018**, *8* (1), 1–12. https://doi.org/10.1038/s41598-018-27108-7.

(187) Singh Jaggi, A.; Parkash Singh, V.; Bali, A.; Singh, N. Advanced Glycation End Products and Diabetic Complications. *Korean J Physiol Pharmacol* **2014**, *18*, 1–14. https://doi.org/10.4196/kjpp.2014.18.1.1.

(188) Thorpe, S. R.; Baynes, J. W. CML: A Brief History. *Int. Congr. Ser.* **2002**, *1245* (C), 91–99. https://doi.org/10.1016/S0531-5131(02)00881-6.

(189) Abedini, A.; Cao, P.; Plesner, A.; Zhang, J.; He, M.; Derk, J.; Patil, S. A.; Rosario, R.; Lonier, J.; Song, F.; Koh, H.; Li, H.; Raleigh, D. P.; Schmidt, A. M. RAGE Binds Preamyloid IAPP Intermediates and Mediates Pancreatic β Cell Proteotoxicity. *J. Clin. Invest.* **2018**, *128* (2), 682–698. https://doi.org/10.1172/JCI85210.

(190) Fritz, G. RAGE: A Single Receptor Fits Multiple Ligands. *Trends Biochem. Sci.* **2011**, *36* (12), 625–632. https://doi.org/10.1016/J.TIBS.2011.08.008.

(191) Sirangelo, I.; Iannuzzi, C. Understanding the Role of Protein Glycation in the Amyloid Aggregation Process. *Int. J. Mol. Sci. 2021, Vol. 22, Page 6609* **2021**, *22* (12), 6609. https://doi.org/10.3390/IJMS22126609.

(192) Orci, L.; Baetens, D.; Rufener, C.; Amherdt, M.; Ravazzola, M.; Studer, P.; Malaisse-Lagae, F.; Unger, R. H. Hypertrophy and Hyperplasia of Somatostatin-Containing D-Cells in Diabetes. *Proc. Natl. Acad. Sci.* **1976**, *73* (4), 1338–1342. https://doi.org/10.1073/PNAS.73.4.1338.

(193) Mukherjee, A.; Morales-Scheihing, D.; Salvadores, N.; Moreno-Gonzalez, I.; Gonzalez, C.; Taylor-Presse, K.; Mendez, N.; Shahnawaz, M.; Gaber, A. O.; Sabek, O. M.; Fraga, D. W.; Soto, C. Induction of IAPP Amyloid Deposition and Associated Diabetic Abnormalities by a Prion-like Mechanism. *J. Exp. Med.* **2017**, *214* (9), 2591–2610. https://doi.org/10.1084/JEM.20161134.

(194) Kertesz, V.; Van Berkel, G. J. Fully Automated Liquid Extraction-Based Surface Sampling and Ionization Using a Chip-Based Robotic Nanoelectrospray Platform. *J. Mass Spectrom.* **2010**, *45* (3), 252–260. https://doi.org/10.1002/JMS.1709.

(195) Liotta, L. A.; Pappalardo, P. A.; Carpino, A.; Haymond, A.; Howard, M.; Espina, V.; Wulfkuhle, J.; Petricoin, E. Laser Capture Proteomics: Spatial Tissue Molecular Profiling from the Bench to Personalized Medicine. *Expert Rev. Proteomics* **2021**, *18* (10), 845–861. https://doi.org/10.1080/14789450.2021.1984886.

(196) Goltsev, Y.; Samusik, N.; Kennedy-Darling, J.; Bhate, S.; Hale, M.; Vazquez, G.; Black, S.; Nolan, G. P. Deep Profiling of Mouse Splenic Architecture with CODEX Multiplexed Imaging. *Cell* **2018**, *174* (4), 968-981.e15. https://doi.org/10.1016/J.CELL.2018.07.010.

(197) Schwartz, P.; Kurucz, J.; Kurucz, A. Morphologische Und Pathogenetische Untersuchungen Über Veränderungen Im Greisenalter. *Zentralblatt für Allg. Pathol. u. Pathol. Anat.* **1964**, *106*, 320–332.

(198) Schwartz, P. *Amyloidosis; Cause and Manifestation of Senile Deterioration*; Thomas, 1970.

(199) Chen, Y.-C.; Taylor, A. J.; Verchere, C. B. Islet Prohormone Processing in Health and Disease. *Diabetes, Obes. Metab.* **2018**, *20*, 64–76. https://doi.org/10.1111/dom.13401.

(200) Abedini, A.; Derk, J.; Schmidt, A. M. The Receptor for Advanced Glycation Endproducts Is a Mediator of Toxicity by IAPP and Other Proteotoxic Aggregates: Establishing and Exploiting Common Ground for Novel Amyloidosis Therapies. *Protein Sci.* **2018**, *27* (7), 1166–1180. https://doi.org/10.1002/pro.3425.

(201) Costal, F.; Oliveira, E.; Raposo, A.; Machado-Lima, A.; Peixoto, E.; Roma, L.; Santos, L.; Faria, J. B. L.; Carpinelli, A. R.; Giannella-Neto, D.; Passarelli, M.; Correa-Giannella, M. L. Dual Effect of Advanced Glycation End Products in Pancreatic Islet Apoptosis. *Diabetes. Metab. Res. Rev.* **2013**, *29* (4), 296–307. https://doi.org/10.1002/DMRR.2390.

(202) Lim, M.; Park, L.; Shin, G.; Hong, H.; Kang, I.; Park, Y. Induction of Apoptosis of β Cells of the Pancreas by Advanced Glycation End-Products, Important Mediators of Chronic Complications of Diabetes Mellitus. *Ann. N. Y. Acad. Sci.* **2008**, *1150* (1), 311–315. https://doi.org/10.1196/ANNALS.1447.011.

Josiah C. McMillen

Vanderbilt University, Nashville, TN   *May 2022*
   Ph.D., Analytical Chemistry
   Dissertation: MALDI Technology Development to Enable High Spatial Resolution Imaging Mass
   Spectrometry and to Improve Lipidomic and Proteomic Coverage
   Advisor: Dr. Richard M. Caprioli, GPA: 3.8

Purdue University Fort Wayne, Fort Wayne, IN   *May 2016*
   B.S. in Chemistry with American Chemical Society Certification in Biochemistry
   Advisor: Dr. Ronald S. Friedman, GPA: 3.5

Indiana University Fort Wayne, Fort Wayne, IN   *May 2016*
   B.A. in French
   Advisor: Dr. Laurie L. Corbin

TECHNICAL EXPERIENCE

Mass spectrometers:
- 15 Tesla solariX FTICR (Bruker)
- rapifleX MALDI TOF/TOF (Bruker)
- Autoflex MALDI TOF/TOF (Bruker)
- Orbitrap Elite (Thermo) with MALDI / MALDI-2 source (Spectroglyph)
- SimulTOF MALDI 200 and 300

Sample preparation:
- Cryostat/cryosectioning (Leica, Thermo)
- TM Sprayer (HTX Technologies)
- Autofluorescence imaging (Zeiss Axioscan)
- Hematoxylin and Eosin stains of tissue (Leica)
- Immunofluorescence staining for validation of peptide IMS (Zeiss Axioscan)

Software:
- flexImaging, flexControl (Bruker)
- SCiLS (Bruker)
- ImageInsight (Spectroglyph)
- mMass
- Xcalibur (Thermo)
- Prism (GraphPad)
- Microsoft Office

RELEVANT RESEARCH EXPERIENCE

Vanderbilt University (Graduate Dissertation Research)   *2016 – Present*
Developed technology and sample preparation approaches to enable sensitive molecular imaging of
tissues using matrix-assisted laser desorption/ionization imaging mass spectrometry (MALDI IMS)
for high spatial resolution applications.
- First to demonstrate signal enhancement of tryptic peptides, generated *in situ* from tissue sections, using MALDI-2 post-ionization for spatially resolved, more comprehensive proteomic coverage.
- Discovered the presence of truncated protein and post-translationally modified forms of intact islet amyloid polypeptide in pancreata of plaque-containing diabetic donors (compared with non-diabetic donors) tentatively identified via accurate mass measurements.
- Characterized MALDI matrix performance after acquiring 96 ion images from five tissue types coated with four MALDI matrices, analyzed with MALDI and MALDI-2 in technical triplicate.

National Renewable Energy Laboratory   *June – December 2015*
- Evaluated performance of ZSM-5 catalyst for upgrading pine pyrolysis vapors using molecular beam mass spectrometry. Mentor: Dr. Calvin Mukarakate
- Analyzed lipid content of algae at different harvest and storage times using LC-MS/MS. Mentor: Dr. Brenna A. Black

SELECTED TEACHING, LEADERSHIP EXPERIENCE

Vanderbilt University
Mass Spectrometry Workshop Assistant (*Mass Spectrometry Research Center)*   *April 2017, 2018, 2019*
- Advanced Imaging Mass Spectrometry Laboratory Course – "MALDI TOF Instrumentation and Applications".
- Taught MALDI IMS skills to 98 scientists (principal investigators, postdocs, graduate students, and technicians).

President, Graduate Honor Council   *May 2019 – September 2020*
- Organized panel hearings among the accused, the professor, and honor council panel to evaluate possible honor code violations.

Vice President, Graduate Honor Council   *May 2018 – September 2019*
- Interviewed students and faculty and compiled reports for the honor council panel.
- Acted as a student advocate during panel hearings.

PUBLICATIONS

- **Josiah C. McMillen**, Danielle B. Gutierrez, Audra M. Judd, Jeffrey M. Spraggins, Richard M. Caprioli. "Enhancement of Tryptic Peptide Signals from Tissue Sections using MALDI IMS Post-ionization (MALDI-2)" *Journal of the American Society for Mass Spectrometry*. **2021**, https://doi.org/10.1021/jasms.1c00213.
- **Josiah C. McMillen**, Jarod A. Fincher, Dustin R. Klein, Jeffrey M. Spraggins, Richard M. Caprioli. "Effect of MALDI Matrices on Lipid Analyses of Biological Tissues using MALDI-2 Post-Ionization Mass Spectrometry" *Journal of Mass Spectrometry*. **2020**, 55: e4663.
- **Josiah C. McMillen**, William J. Perry, Kavya Sharman, Katerina V. Djambazova, Richard M. Caprioli. (2020) Matrix-Assisted Laser Desorption/Ionization Imaging Mass Spectrometry: Technology and Applications. In: Sindona G., Banoub J.H., Di Gioia M.L. (eds) Toxic Chemical and Biological Agents. NATO Science for Peace and Security Series A: Chemistry and Biology. Springer, Dordrecht.
- Eric C. Spivey, **Josiah C. McMillen**, Daniel J. Ryan, Jeffrey M. Spraggins, Richard M. Caprioli. "Combining MALDI-2 and transmission geometry laser optics to achieve high sensitivity for ultra-high spatial resolution surface analysis" *Journal of Mass Spectrometry*. **2019**, 54, 366-370.
- Boone M. Prentice, **Josiah C. McMillen**, Richard M. Caprioli. "Multiple TOF/TOF events in a single laser shot for multiplexed lipid identifications in MALDI imaging mass spectrometry" *International Journal of Mass Spectrometry*. **2019,** 437; 30-37.

PRESENTATIONS (presenter underlined)

- <u>Angela Kruse</u>, **Josiah C. McMillen**, John T. Walker, Audra Judd, N. Heath Patterson, Danielle Gutierrez, Jeremy L. Norris, Jeffrey M. Spraggins, Alvin C. Powers, Richard M. Caprioli, "Spatially targeted proteomics and multimodal imaging distinguish molecular signatures of amyloid plaque-containing islets from type 2 diabetic donors" *US HUPO*, Charleston, SC, February 2022.

- Angela Kruse, **Josiah C. McMillen**, John T. Walker, Audra Judd, N. Heath Patterson, Danielle Gutierrez, Jeremy L. Norris, Jeffrey M. Spraggins, Alvin C. Powers, Richard M. Caprioli, "Spatially targeted proteomics and multimodal imaging distinguish molecular signatures of amyloid plaque-containing islets from type 2 diabetic donors" *69th ASMS Conference on Mass Spectrometry and Allied Topics*, Philadelphia, PA, October 2021.
- **Josiah C. McMillen**, Jarod A. Fincher, Jeffrey M. Spraggins, Richard M. Caprioli, "Lipid Analysis using Selected Matrices with MALDI-2 Post-Ionization for Advanced Imaging Applications" *Vanderbilt Institute of Chemical Biology Symposium* poster and flash talk, Nashville, TN, August 2020.
- **Josiah C. McMillen**, Jarod A. Fincher, Jeffrey M. Spraggins, Richard M. Caprioli, "Lipid Analysis using Selected Matrices with MALDI-2 Post-Ionization for Advanced Imaging Applications" *68th ASMS Conference on Mass Spectrometry & Allied Topics*, Houston, TX, June 2020.
- Dustin Klein, Emilio S. Rivera, **Josiah C. McMillen**, James E. Cassat, Henning Peise, Jens Hoehndorf, Eric C. Spivey, Eric P. Skaar, Richard M. Caprioli, Jeffrey M. Spraggins, "MALDI-2 Analysis of *Staphylococcus aureus*-infected Tissue" *68th ASMS Conference on Mass Spectrometry & Allied Topics*, Houston, TX, June 2020.
- Jarod A. Fincher, Martin Dufresne, **Josiah C. McMillen**, Jeffrey M. Spraggins, Demis D. John, Biljana Stamenic, Richard M. Caprioli, "Enhanced Ionization of Lipids for High Spatial Resolution Imaging Mass Spectrometry from Matrix-Coated Silicon Nanopost Arrays by MALDI-2" *68th ASMS Conference on Mass Spectrometry & Allied Topics*, Houston, TX, June 2020.
- **Josiah C. McMillen**, Eric C. Spivey, Jeffrey M. Spraggins, Richard M. Caprioli, "Laser Post-Ionization for High Spatial Resolution Imaging Mass Spectrometry" *NATO SPS Advanced Study Institute G5535 "Detection, Diagnosis, and Health Concerns of Toxic Chemical and Biological Agents",* poster and oral presentations, Cetraro, Italy, October 2019.
- **Josiah C. McMillen**, Eric C. Spivey, Daniel J. Ryan, Jeffrey M. Spraggins, Richard M. Caprioli, "MALDI Spatial Resolution Improvement using MALDI-2 Post-Ionization". *67th ASMS Conference on Mass Spectrometry & Allied Topics*, Atlanta, GA, June 2019.
- Eric C. Spivey, **Josiah C. McMillen**, David M. Anderson, Daniel J. Ryan, Jeffrey M. Spraggins, John P. Wikswo, Richard M. Caprioli, Jeremy L. Norris, "Co-Registered, Cellular-Resolution Mass Spectrometry and Fluorescence Imaging for the Multi-Omic Targeting of Rare Cell Types". *67th ASMS Conference on Mass Spectrometry & Allied Topics*, Atlanta, GA, June 2019.
- **Josiah C. McMillen**, Daniel J. Ryan, John T. Walker, Heather A. Nelson, Marcela Brissova, Christopher V. Wright, Jeremy L. Norris, Boone M. Prentice, Alvin C. Powers, Richard M. Caprioli, "Increased Levels of Human Islet Amyloid Polypeptide in Plaques Revealed by Imaging Mass Spectrometry" *Human Islet Research Network Conference*, Washington, D.C., April 2019.
- **Josiah C. McMillen**, Boone M. Prentice, Eric C. Spivey, David M. Anderson, Richard M. Caprioli, "Sub-Cellular Lipid Imaging Mass Spectrometry Via Transmission Geometry" *Vanderbilt Institute of Chemical Biology Symposium*, Nashville, TN, August 2018.
- **Josiah C. McMillen**, Boone M. Prentice, Eric C. Spivey, Andre Zavalin, Richard M. Caprioli, "Transmission Geometry Instrument Modifications and Laser Energy Characterization for High Spatial Resolution MALDI Imaging Mass Spectrometry" *66th ASMS Conference on Mass Spectrometry & Allied Topics*, San Diego, CA, June 2018.
- **Josiah C. McMillen**, Calvin Mukarakate, Mengze Xu, Krstiina Iisa, Mark Nimlos, "Upgrading Pine Pyrolysis Vapors Using Down Selected Catalysts" *Indiana University – Purdue University Co-operative Education Presentation*, Fort Wayne, IN, October 2015.
- **Josiah C. McMillen**, Brenna A. Black, "Application of Analytical Methods for the Dynamic Lipid Profiling in Microalgae," *Science Undergraduate Laboratory Internship (SULI) Poster Session*, Golden, CO, August 2015.

- **Josiah C. McMillen**, "Quantitative Proteomics: An Introduction to Complete Proteomic Analysis" *Indiana University – Purdue University Fort Wayne (IPFW) Chemistry Department Senior Seminar*, Fort Wayne, IN, April 2015.
- Mohammad M. Qasim, <u>Swatabdi R. Kamal</u>, <u>Kali Fridholm</u>, <u>Tim Byers</u>, **Josiah C. McMillen**, "Exceptional Stability of Kidney Bean Inhibitor to Temperature and Pepsin Digestion," *2013 IPFW Student Research and Creative Endeavor Symposium,* Fort Wayne, IN, April 2013.
- <u>Swatabdi R. Kamal</u>, **Josiah C. McMillen**, Mohammad M. Qasim, "Stability of Red Kidney Bean Serine Protease Inhibitor to Heat and Pepsin Digestion," *Indiana University Undergraduate Research Conference (IUURC)*, Indiana University, Indianapolis, IN, November 2012.